JSCSEN 78(7)909–1077(2013)

ISSN 1820-7421(Online)

Journal of the Serbian Chemical Society

eVersion electronic

VOLUME 78

No 7

BELGRADE 2013

Available on line at

СХД
1897

www.shd.org.rs/JSCS/

Journal of the Serbian Chemical Society
eVersion electronic
JSCS-info@shd.org.rs • www.shd.org.rs/JSCS

J. Serb. Chem. Soc. Vol. 78, No. 7 (2013)

CONTENTS

Organic Chemistry

Biochemistry and Biotechnology

Inorganic Chemistry

Theoretical Chemistry

Physical Chemistry

Electrochemistry

Analytical Chemistry

Chemical Engineering

Environmental

Published by the Serbian Chemical Society
Karnegijeva 4/III, 11000 Belgrade, Serbia
Printed by the Faculty of Technology and Metallurgy
Karnegijeva 4, P.O. Box 35-03, 11120 Belgrade, Serbia

Journal of the Serbian Chemical Society
JSCS-info@shd.org.rs • www.shd.org.rs/JSCS

J. Serb. Chem. Soc. *78* (7) 909–916 (2013) UDC 547.814.5+66.095.25:547.288.1+546.151
JSCS–4468 *Original scientific paper*

Cyclization of 2′-hydroxychalcones to flavones using ammonium iodide as an iodine source – an eco-friendly approach

PRAMOD S. KULKARNI[1], DASHARATH D. KONDHARE[1], RAVI VARALA[2]*
and PUDUKULATHAN K. ZUBAIDHA[1]

[1]*School of Chemical Sciences, Swami Ramanand Teerth Marathwada University, Nanded, Maharashtra – 431 606, India and* [2]*Department of Chemistry, AP-IIIT Basar, Rajiv Gandhi University of Knowledge Technologies, Mudhole, Adilabad, Andhra Pradesh - 504 107, India*

(Received 1 September, revised 30 October 2012)

Abstract: Ammonium iodide on exposure to air decomposes to ammonia and iodine. The *in situ* generated iodine was used for the cyclization of 2′-hydroxychalcones to the corresponding flavones under solvent-free conditions in good to excellent yields. This method could serve as an attractive alternative to the existing methods for synthesis of flavones and the use of toxic molecular iodine is avoided.

Keywords: flavones; 2′-hydroxychalcone; ammonium iodide; solvent-free; *in situ* iodine.

INTRODUCTION

There are a number of environmental implications for the use of large volumes of organic solvents since they are utilized in larger quantities than the solutes they carry and are transferred into the environment through evaporation and leakage. Due to the increasing concern for the harmful effects of organic solvents on the environment and human body, organic reactions that are conducted without conventional organic solvents have aroused the attention of organic chemists. Many organic reactions have been reported to proceed efficiently under solvent-free conditions and some showed enhanced selectivity.[1]

Therefore, the synthetic endeavors of more and more chemists are devoted toward nature-friendly syntheses[2a] and to reduce the drastic prerequisites of reactions. Thus, a paradigm shift from using solvents toward solvent-free reactions not only simplifies organic syntheses but also improves process conditions for large-scale syntheses. Therefore, it is now often claimed that "the best solvent is no solvent".[2b]

---

* Corresponding author. E-mail: ravivarala@gmail.com
doi: 10.2298/JSC120901119K

Flavonoids are a group of low molecular weight compounds mainly occurring in the plant kingdom and flavones constitute a major class among the flavonoids. This class of molecules has been extensively investigated and 4000 chemically unique flavonoids have been isolated from plants.[3] They continue to attract a great deal of attention as they possess biological activities, such as antioxidant effects,[4] antiviral,[5] and leishmanicidal activity,[6] ovipositor stimulant of phytoalexins,[7] anti-HIV,[8] vasodilator,[9] bactericidal,[10] DNA cleavage,[11] anti-inflammatory,[12] antimutagenic,[13] anti-allergic[14] and anticancer.[15–18] Especially, flavones (2-phenylchromones) exhibit a wide variety of activities.[19]

The main known synthetic methods for obtaining flavones are oxidative cyclization of 2′-hydroxychalcones,[20] the cyclodehydration of 1-(2-hydroxyphenyl)-3-phenyl-1,3-propanedione[21] and *via* an intermolecular Wittig reaction.[22] Reagents that have been used for the oxidation of 2′-hydroxychalcones and flavanones to obtain flavones are SeO_2–pentan-1-ol,[20] Pd–C/vacuum,[22] I_2–DMSO,[23] SeO_2–DMSO,[24] 2,3-dichloro-5,6-dicyanobenzoquinone (DDQ)–dioxane,[25] $NaIO_4$––DMSO,[26] nickel peroxide–dioxane,[27] H_2O_2–NaOH,[28] Dowex H^+–2-propanol,[23a,29] SeO_2–dioxane,[30] SeO_2–3-methyl-1-butanol (isoamyl alcohol),[31] Br_2––NaOH,[32] $Tl(NO_3)_3 \cdot 3H_2O$[33] and I_2–triethylene glycol.[34]

Most of these methods are of limited use as they suffer from low yields and often afford a mixture of products containing flavones, flavanones and aurones.[18] Furthermore, these procedures require prolonged reaction times, use of harsh organic solvents, high temperatures, expensive catalysts or hazardous reaction conditions. Hence, there is scope for the development of new methods for the synthesis of flavones using easily available, inexpensive and eco-friendly reagents.

Synthesis of flavones from 2′-hydroxychalcone using iodine in dimethyl sulfoxide is reported in the literature.[23] However, molecular iodine is highly corrosive, toxic and expensive, making its use somewhat unattractive. In order to overcome the problems associated with molecular iodine, herein, for the first time, the oxidative cyclization of 2′-hydroxychalcones to flavones by *in situ* generated iodine from ammonium iodide in the presence of air under solvent-free conditions is reported. However, the use of ammonium iodide in organic synthesis is very rare; it is used in the iodination of aromatic compounds with ozone as the oxidizing agent.[35] Recently there was a report on the use of ammonium iodide and H_2O_2 in organic synthesis for iodination of ketones and aromatic compounds, and dethioacetalization.[36] In continuation of ongoing interest in the development of novel synthetic methodologies, particularly of carbon–carbon and carbon–heteroatom bond formation of biologically relevant heterocycles,[37] brief findings are reported herein on the use of ammonium iodide in the oxidative cyclization of 2′-hydroxychalcone to flavones.

EXPERIMENTAL

2′-Hydroxychalcones (**1a**–**q**) were prepared by base-catalyzed condensation between 2-hydroxyacetophenone and the appropriate benzaldehyde using a literature procedure.[38] 2-Hydroxyacetophenone, substituted benzaldehydes, ammonium iodide and solvents were purchased from Loba Chemicals, Merck and Sigma–Aldrich. Progress of the reaction was monitored by TLC. All the yields were calculated after purification of the products by column chromatography using EtOAc:petroleum ether (1:4, boiling range 40–60 °C) on silica gel. The melting points of the compounds were determined in open capillary tubes and are uncorrected. The IR spectra were recorded on a Perkin-Elmer FTIR-1710 spectrophotometer. The ^{1}H-NMR and ^{13}C-NMR spectra were recorded at room temperature on Bruker AC-250 spectrometers using TMS as an internal standard.

*General procedure for the preparation of flavones (**2a**–**q**)*

A mixture of 1.0 mmol of **1** (2′-hydroxychalcone) and ammonium iodide (0.1 mmol) was heated in air under neat condition at 120 °C for 1 h. After completion of the reaction, the reaction mixture was cooled to room temperature and poured into 20 mL water. The formed precipitate was filtered, washed with 10 % sodium thiosulfate (3×10 mL) and then with 5 mL ice-cold ethanol. The crude product obtained was purified by column chromatography (silica gel, ethyl acetate–petroleum ether (1:4)) to give pure flavone (**2**).

RESULTS AND DISCUSSION

Ammonium iodide gradually turns yellow on standing in moist air, owing to decomposition with liberation of iodine[39] and this was utilized for the oxidative cyclization of 2′-hydroxychalcones to their corresponding flavones (Scheme 1).

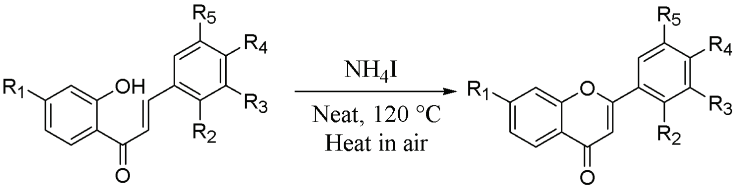

1 **2**

Scheme 1. Synthesis of flavones using NH_4I.

For this purpose, 2′-hydroxychalcones (**1a**–**q**) were synthesized using easily accessible starting materials, substituted 2-hydroxyacetophenones and electronically divergent benzaldehydes in good to excellent yields in presence of base.[38] It was observed that 1-(2-hydroxyphenyl)-3-phenylprop-2-en-1-one (1 mmol, **1a**) when heated with a solution of ammonium iodide (10 mol %) in DMSO at 120 °C becomes transformed to the corresponding flavone (**2a**) in 1 h in good yield (88 %). The reaction was monitored by TLC and the structure of product was confirmed by spectroscopic data. The ^{1}H-NMR spectra of **2a** showed a singlet at 6.86 due to 1H of 3H, *i.e.*, pyrone ring, which is the characteristic singlet for flavones. Such observed ^{1}H-NMR data and the complete absence of a peak near 12.73 ppm due to an *ortho*-hydroxy group is in agreement with the oxidation of the chalcone into the corresponding flavone. Among the solvents screened for optimum conditions for the transformation, DMSO was found to be the most suitable, as is obvious from the data presented in Table I. Of the tested solvents, ethanol (reflux) and diethylene glycol (120 °C) gave poor or no yields. The same reaction was explored under neat conditions and, to our utmost satisfaction, product **2a** was obtained in a good isolated yield (92 %).

TABLE I. Cyclization of 2′-hydroxychalcone in different solvents using ammonium iodide; reaction conditions: 2′-hydroxychalcone (1 mmol), NH_4I (0.1 mmol)

Entry	Solvent	Time, h	Yield[a], %	Product
1	DMSO	1	88	Flavone (**2a**)
2	DMF	4	72	Unidentified compound
3	EtOH	12	10	Flavone (**2a**)
4	Diethylene glycol	12	0	No reaction
5	Solvent free	1	92	Flavone (**2a**)

[a]Isolated yield

In the absence of NH_4I, only the starting materials were isolated from the reaction mixture, even after 12 h. This indicates that the reagent exhibits high catalytic activity in this transformation. In order to evaluate the most appropriate reagent loading, the above test reaction was performed using 5, 10 and 20 mol % of NH_4I under solvent-free conditions. It was found that 10 mol % of the reagent showed maximum yield in the minimum time at 120 °C. Further increasing of the reagent loading did not affect the yield.

Having optimized the reaction parameters (10 mol % NH_4I, heating at 120 °C in open air under neat conditions), this methodology was extended to the other 2′-hydroxychalcones and the results are presented in Table II. The substituents on B ring of 2′-hydroxychalcones were varied from electron donating to electron withdrawing and in all the cases, the studied the transformation went smoothly to yield the corresponding flavones in good yield.[40] Contrary to previously reported methods, this procedure tolerates a wide range of substituents, such as methyl, chloro, methoxy, bromo, hydroxyl, *N*,*N*-dimethylamino and nitro. Generally, it was observed that oxidation of substrates with unprotected hydroxyl groups on the aromatic rings gave poor yields. However, it was found that this new reagent is equally suitable and efficient for the oxidation of such derivatives (entries 15 and 16).

The mechanism of this reaction is still not clear. However, the reaction pathway shown in Scheme 2 is tentatively proposed. Initially, electrophilic addition of iodine to the enone to form **3**, followed by elimination of HI with oxidative cyclization yielding **5**. A *β*-elimination of HI from **5** gave flavone **2**. In support of this mechanism, the model reaction on a relatively larger scale (10 mmol) was performed and during the course of reaction, the pH of aqueous layer was measured. The pH was found to be acidic, confirming thereby the elimination product to be HI.

TABLE II. Cyclization of 2′-hydroxychalcone to flavones using NH_4I under solvent free conditions; reaction conditions: 2′-hydroxychalcone (1 mmol), NH_4I (0.1 mmol) under neat condition

Entry	Chalcone	R^1	R^2	R^3	R^4	R^5	Flavone	Yield^{a}, %	M.p., °C
1	**1a**	H	H	H	H	H	**2a**	92	97^{40a}
2	**1b**	H	H	H	OMe	H	**2b**	89	157^{40a}
3	**1c**	H	H	OMe	OMe	OMe	**2c**	82	174^{40a}
4	**1d**	H	H	H	Cl	H	**2d**	94	189^{40b}
5	**1e**	H	H	H	Me	H	**2e**	79	110^{40c}
6	**1f**	H	H	OMe	OMe	H	**2f**	82	154^{40d}
7	**1g**	H	H	OMe	H	H	**2g**	78	132^{40e}
8	**1h**	H	Cl	H	H	H	**2h**	74	118^{40f}
9	**1i**	H	Cl	H	Cl	H	**2i**	81	172^{40i}
10	**1j**	H	H	H	NO_2	H	**2j**	75	242^{40j}
11	**1k**	OMe	H	H	OMe	H	**2k**	79	143^{40k}
12	**1l**	H	OMe	H	OMe	H	**2l**	84	95^{40k}
13	**1m**	H	H	H	Br	H	**2m**	91	177^{40l}
14	**1n**	H	H	Br	H	H	**2n**	93	115^{40m}
15	**1o**	OH	H	H	H	H	**2o**	71	240^{40g}
16	**1p**	OH	H	H	OMe	H	**2p**	67	264^{40h}
17	**1q**	H	H	H	NMe_2	H	**2q**	72	192^{40n}

[a] Isolated yield after purification

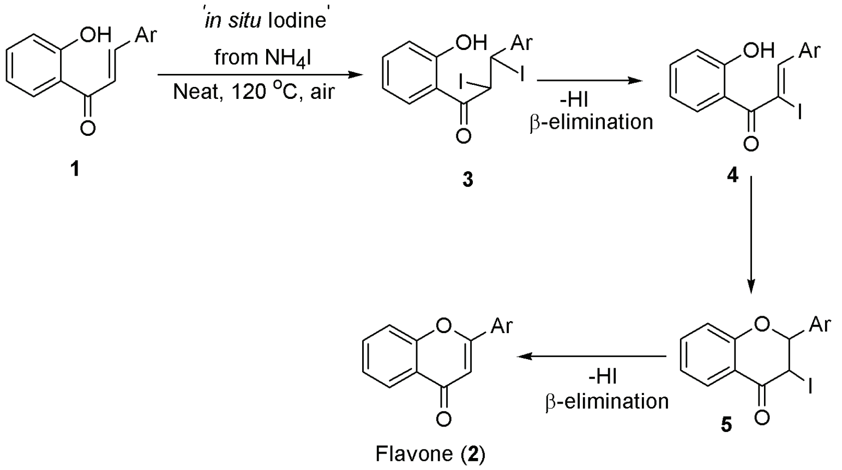

Scheme 2. Possible mechanism of flavone synthesis using NH_4I *via* oxidative cyclization.

CONCLUSIONS

In conclusion, an efficient general method for the conversion of 2′-hydroxychalcones to the corresponding flavones using *in situ* generated iodine is reported. The products were obtained in a shorter time, in high yields, and employed a less hazardous and inexpensive reagent than molecular iodine. Other attributes include its applicability to substrates bearing electron donating and electron withdrawing as well as a free hydroxyl group on the B ring of chalcones. Thus, this methodology would serve as attractive alternative to the use of toxic molecular iodine.

Acknowledgement. One of the authors D. D. Kondhare would like to thank DST-New Delhi for the financial assistance provided by an Inspire Fellowship. Dr. Ravi Varala thanks Prof. Rajendra Sahu (Director, IIIT Basar) and Prof. R. V. Raja Kumar (Vice Chancellor, RGUKT) for their encouragement. We thank the referees for their healthy suggestions.

ИЗВОД

ЦИКЛИЗАЦИЈА 2′-ХИДРОКСИХАЛКОНА ДО ФЛАВОНА УПОТРЕБОМ АМОНИЈУМ-ЈОДИДА КАО ИЗВОРА ЕЛЕМЕНТАРНОГ ЈОДА – ЕКОЛОШКИ ПРИХВАТЉИВ ПРИСТУП

PRAMOD S. KULKARNI[2], DASHARATH D. KONDHARE[2], RAVI VARALA[1] и PUDUKULATHAN K. ZUBAIDHA[2]

[1]*School of Chemical Sciences, Swami Ramanand Teerth Marathwada University, Nanded, Maharashtra - 431 606, India* и [2]*Department of Chemistry, AP-IIIT Basar, Rajiv Gandhi University of Knowledge Technologies, Mudhole, Adilabad, Andhra Pradesh – 504 107, India*

Амонијум-јодид се у присуству ваздуха разлаже на амонијак и елементарни јод. Генерисан *in situ* у реакционој смеши, јод омогућава циклизацију 2′-хидроксихалкона до одговарајућих флавона, у одсуству раставарача, у одличном приносу. Поступак се може користити као добра алтернатива постојећим методама синтезе флавона.

(Примљено 1. септембра, ревидирано 30. октобра 2012)

REFERENCES

1. For reviews, see a) F. Toda, *Acc. Chem. Res.* **28** (1995) 480; b) K. Tanaka, F. Toda, *Chem. Rev*. **100** (2000) 1025; c) W.-Y. Liu, Q.-H. Xu, Y.-M. Liang, B.-H. Chen, W.-M. Liu, Y.-X. Ma, *J. Organomet. Chem*. **637** (2001) 719; d) J.-M. Yang, D.-G. Gu, Z. L. Shen, S. Y. Wang, *J. Organomet. Chem.* **690** (2005) 2989; e) Z.-L. Shen, S.-J. Ji, *Synth. Commun*. **39** (2009) 775
2. a) P. Anastas, T. Williamson, *Green Chemistry, Frontiers in Benign Chemical Synthesis and Procedures*, Oxford Science Publications, Oxford, 1998; b) K. Tamaka, *Solvent-free Organic Synthesis*, Wiley–VCH, Weinheim, 2003
3. *The Flavonoids: Advances in Research Since 1986*, J. B. Harborne, Ed., Chapman and Hall, London, 1993
4. a) J. Grassmann, S. Hippeli, E. F. Elstner *Plant Physiol. Biochem*. **40** (2002) 471; b) S. Miura, J. Watanble, M. Sano, T. Tomita, T. Osawa, Y. Hara, I. Tomita, *Biol. Pharm. Bull*. **18** (1995) 1
5. a) I. Sánchez, F. Gómez-Garibay, J. Taboada, B. H. Ruiz, *Phytother. Res.* **14** (2000) 89; b) E. A. Bae, M. J. Han, M. Lee, D. H. Kim *Biol. Pharm. Bull.* **23** (2000) 1122
6. M. J. Chan-Bacab, L. M. Petia-Rodriguez, *Nat. Prod. Prep.* **18** (2001) 674
7. J. B. Harborne, *Nat. Prod. Rep*. **16** (1999) 509
8. H. Wu, X. H. Wang, Y. H. K. H. Yic Leeb, *Bioorg. Med. Chem. Lett*. **13** (2003) 1813

9. F. Pérez-Vizcaino, M. Ibarra, A. L. Cogolludo, J. Duarte, F. Zaraozá-Arnáez, G. López-López, J. Tamargo, *J. Pharmacol. Exp. Ther.* **301** (2002) 66
10. a) H. X. Xu, S. F. Lee, *Phytother. Res.* **15** (2001) 39; b) J. M. T. Hamilton Miller *Antimicrob. Agents Chemother.* **39** (1995) 2375
11. A. Jain, M. C. Martin, N. Parveen, N. U. Khan, J. H. Parish, S. M. Hadi, *Phytother. Res.* **13** (1999) 609
12. G. M. Shivji, E. Zielinska, S. Kondo, H. Mukhtar, D. N. Sander, *J. Invest. Dermatol*. **106** (1996) 787
13. J. Yamada, Y. Tomita, *Biosci. Biotech. Biochem*. **58** (1994) 2197
14. N. Matsuo, K. Yamada, K. Yamashita, K. Shoji, M. Mori, M. Sugano *In Vitro Cell Div. Biol*. **32** (1996) 340
15. a) C. Han *Cancer Lett.* **114** (1997) 153; b) D. F. Birt, S. Hendrich, W. Wang, *Pharmacol. Therapeut* **90** (2001) 157
16. S. Yano, H. Tachibana, K. Yamada, *J. Agric. Food Chem*. **53** (2005) 1812
17. M. Morimoto, K. Tanimoto, S. Nakano, T. Ozaki, A. Nakano, K. Komai, *J. Agric. Food Chem*. **51** (2003) 389
18. W. Ohmura, S. Doi, M. Aoyama, S. Ohara, *J. Wood Sci*. **46** (2000) 149
19. a) R. B. Isogi Gamill, C. E. Day, P. E. Schurr, *J. Med. Chem*. **26** (1983) 1672; b) A. Yamashita, *J. Am. Chem. Soc.* **107** (1985) 5823; c) W. H. Gerwick *J. Nat. Prod.* **52** (1989) 252
20. a) H. S. Mahal, K. Venkataraman *J. Chem. Soc*. (1935) 866; b) H. S. Mahal, K. Venkataraman, *J. Chem. Soc.* (1936) 569; c) H. H. Lee, C. H. Tan, *J. Chem. Soc*. (1965) 2743; d) H. Miyake, E. Takizawa, M. Sasaki, *Bull. Chem. Soc. Jpn.* **76** (2003) 835
21. G. Kabalka, A. Mereddy, *Tetrahedron Lett*. **46** (2005) 6315
22. a) A. Hercouet, M. L. Corre, *Synthesis* (1982) 597; b) Y. L. Flooch, M. Lefeuvre *Tetrahedron Lett.* **27** (1986) 2755; c) P. K. Bose, P. Chakrabarti, A. K. Sanyal *J. Indian Chem. Soc.* **48** (1971) 1163
23. a) M. D. L. De la Torre, G. L. Marcorin, G. Pirri, A. C. Tome, A. M. S. Silva, J. A. S. Cavaleira, *Tetrahedron Lett*. **43** (2002) 1689; b) A. G. Doshi, P. A. Soni, B. G. Ghiya, *Indian J. Chem., B* **25** (1986) 759
24. J. K. Makrandi, Seema, *Chem. Ind.* (1989) 607
25. K. Lmafuku, M. Honda, J. F. W. Mcomie, *Synthesis* (1987) 199
26. N. Hans, S. K. Grover, *Synth. Commun.* 23 (1993) 1021
27. U. K. Mallik, M. M. Saha, A. K. Mallik. *Indian J. Chem., B* **28** (1989) 970
28. S. Gobbi, A. Rampa, A. Bisi, F. Belluti, L. Piazzi, P. Valen, A. Caputo, A. Zampiron M. Carrara *J. Med. Chem*. **46** (2003) 3662
29. F. A. A. Van Acker, J. A. Hageman, G. R. M. M. Haenen, W. J. F. Vander Vijgh, A. Bast, W. M. P. B. Menge, *J. Med. Chem*. **43** (2000) 3752
30. M. E. Zwaagstra, H. Timmerman, A. C. Van de Stolpe, F. J. J. De Kanter, M. Tamura, Y. Wada, M.-Q. Zhang, *J. Med. Chem.* **41** (1998) 1428
31. T. Akama, Y. Shida, T. Sugaya, H. Ishida, K. Gomi, M. Kasai, *J. Med. Chem*. **39** (1996) 3461
32. J. R. Pfister, W. E. Wymann, M. E. Schuler, A. P. Roszkowski, *J. Med. Chem*. **23** (1980) 335
33. S.-H. Jung, S.-H. Cho, T. H. Dang, J.-H. Lee, J.-H. Ju, M.-K. Kim, S.-H. Lee, J.-C. Ryu, Y. Kim, *Eur. J. Med. Chem*. **38** (2003) 537

34. M. Hideyoshi, T. Eizo, S. Mitsuru, *Bull. Chem. Soc. Jpn*. **76** (2003) 835
35. K. V. V. Krishna Mohan, N. Narender, S. J. Kulkarni, *Tetrahedron Lett.* **45** (2004) 8015
36. a) N. Narender, S. K. Reddy, K. V. V. Krishna Mohan, S. J. Kulkarni, *Tetrahedron Lett*. **48** (2007) 6124; b) N. C. Ganguly, P. Mondal, *Synth. Commun*. **41** (2011) 2374
37. a) K. R. Narayana, R. Varala, P. K. Zubaidha, *Int. J. Org. Chem.* **2** (2012) 287; b) V. B. C. Figueira, A. G. Esqué, R. Varala, C. González-Bello, S. Prabhakar, A. M. Lobo, *Tetrahedron Lett.* **51** (2010) 2029; c) R. Varala, E. Ramu, S. R. Adapa, *Monatsh. Chem.* **139** (2008) 1369; d) R. Enugala, S. Nuvvula, V. Kotra, R. Varala, S. R. Adapa, *Heterocycles* **75** (2008) 2523; e) E. Ramu, R. Varala, N. Sreelatha, S. R. Adapa, *Tetrahedron Lett*. **48** (2007) 7184; f) R. Varala, A. Nasreen, E. Ramu, S. R. Adapa, *Tetrahedron Lett.* **48** (2007) 6972; g) R. Varala, E. Ramu, S. R. Adapa, *Synthesis* **22** (2006) 3825; h) R. Varala, E. Ramu, N. Sreelatha, S. R. Adapa, *Synlett* **7** (2006) 1009 and references cited therein
38. A. H. Blatt, *Organic Synthesis*, Coll. Vol. I, Ed., Wiley, New York, 1956, p. 78
39. A. F. Holleman, E. Wiberg, *Inorganic chemistry*, Academic Press, San Diego, 2001
40. a) D. Nagarathnam, M. Cushman, *Tetrahedron* **28** (1991) 5071; b) A. Nishinaga, H. Ando, K. Maruyama, T. Mashino, *Synthesis* (1992) 839; c) R. S. Varma, R. K. Saini, D. J. Kumar, *Chem. Res. (s)*, (1998) 348; d) K. V. Kumar, P. T. Perumal *Tetrahedron* **63** (2007) 9531; e) J. H. Looker, W. W. Hanneman *J. Org. Chem*. **27** (1962) 381; f) S. Kato, K. Yamamoto, *Biol. Pharm. Bull.* **16** (1993) 90; g) M. Cushman, D. Nagarathnam, *Tetrahedron Lett.* **31** (1990) 6497; h) S. Saxena, J. K. Makrandi., S. K. Grover, *Synthesis* (1985) 697; i) X. Huang, E. Tang, W. M. Xu, J. Cao, *J. Comb. Chem.* **7** (2005) 802; j) P. Kumar, M. S. Bodas, *Org. Lett.* **2** (2000) 3821; k) T. Tanaka, M. Iinuma, M. Mizuno, *Chem. Pharm. Bull.* **34** (1986) 1667; l) L. L. Song, J. W. Kosmeder II, S. Kook Lee, C. Gerhauser, D. Lantvit, R. C. Moon, R. M. Moriarty, J. M. Pezzuto *Cancer Res.* **59** (1999) 578; m) Z. Zhou, P. Zhao, W. Huang, G. Yan, *Adv. Synth. Catal*. **348** (2006) 63; n) S. L. Borsa, M. R. Patel, L. B. Borse, *Int. J. Pharm. Res. Dev.* **3** (2011) 147.

Journal of the Serbian Chemical Society
JSCS-info@shd.org.rs • www.shd.org.rs/JSCS

J. Serb. Chem. Soc. 78 (7) 917–920 (2013) UDC 547.814.5+544.478+547.781/.783+542.913
JSCS–4469 *Short communication*

SHORT COMMUNICATION

An efficient and facile synthesis of flavanones catalyzed by *N*-methylimidazole

PENG WANG[1], JIABIN YANG[1], JIN CAI[2], CHUNLONG SUN[2], LUSHEN LI[1]
and MIN JI[2]*

[1]*School of Biological Science & Medical Engineering, Southeast University, Nanjing 210096, China and* [2] *School of Chemistry & Chemical Engineering, Southeast University, Nanjing 210096, China*

(Received 29 June 2012)

Abstract: The use of *N*-methylimidazole as an efficient catalyst for the cyclization of 2′-hydroxychalcones to the corresponding flavanones in DMSO was investigated. The scope of this process was studied and various flavanones were obtained exclusively in good yields.

Keywords: 2′-hydroxychalcones; flavanones; *N*-methylimidazole.

INTRODUCTION

The flavanone structure is abundant in natural products that possess a broad array of biological activity.[1] Due to their favorable anti-cancer, anti-estrogen and anti-inflammatory properties, flavanones have been investigated as selective estrogen receptor modulators and tumor necrosis factor (TNF)-α inhibitors.[2] Moreover, these kinds of compounds are important intermediates in the synthesis of flavanone glycosides and 2-aryl chromans.[3] These compounds have been synthesized by the cyclization of 2′-hydroxychalcones, that is, by an intramolecular oxa-Michael addition (Scheme 1) using various reagents, such as potassium ferricyanide,[4] iodine,[5] alkali metal carbonates[6] and trifluoroacetic acid.[7] Despite these impressive contributions, more efficient and practical catalytic systems for the synthesis of flavanones are still in high demand.

Recently, several reports referred to *N*-methylimidazole as a co-catalyst for aldol, Claisen and other reactions. Moreover, Lin reported an aza-Michael addition catalyzed by *N*-methylimidazole.[8] Inspired by these findings, herein the use of *N*-methylimidazole as an efficient catalyst that facilitates the cyclization of 2′-hydroxychalcones in high yields is presented.

---

* Corresponding author. E-mail: jimin@seu.edu.cn

doi: 10.2298/JSC120629157W

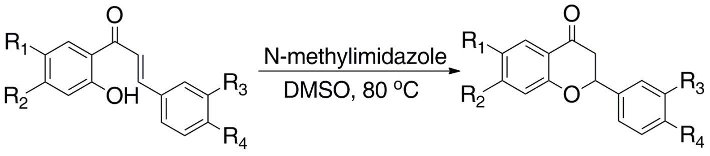

1a-k **2a-k**

Scheme 1. *N*-Methylimidazole catalyzed cyclization of 2′-hydroxychalcones.

RESULTS AND DISCUSSION

First, optimization experiments involving 2′-hydroxychalcone (**1a**) as the test substrate were performed, these focused on the determination of the effect of the solvent and the amount of *N*-methylimidazole. The results are summarized in Table I. The reaction was realized in three different solvents, *viz*., dichloromethane, acetonitrile, and DMSO (Table I, entries 1–3). It was observed that a higher yield of the flavanone **2a** was achieved in DMSO compared with those in the other two solvents, which led DMSO to be chosen for all further studies. The importance of the *N*-methylimidazole was confirmed by the fact that no product **2a** was obtained in the absence of *N*-methylimidazole (Table I, entry 4). Subsequent studies indicated that 20 mol % *N*-methylimidazole was the optimal amount. The product **2a** was obtained in 90 % yield after 6 h in DMSO at 80 °C, while only trace amounts of **2a** were observed at room temperature (Table I, entry 7).

TABLE I. Optimization of the solvent and the amount of *N*-methylimidazole

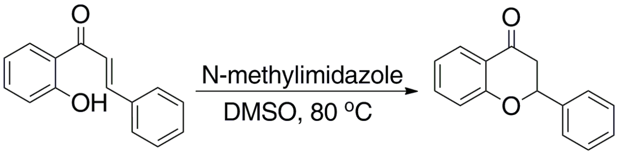

1a **2a**

Entry	Solvent	*N*-methylimidazole (equiv.)	Time, h	Yield[a], %
1	CH_2Cl_2	0.2	6	30
2	CH_3CN	0.2	6	75
3	DMSO	0.2	6	90
4	DMSO	–	6	N.R.
5	DMSO	0.1	12	85
6	DMSO	0.5	6	90
7[b]	DMSO	0.2	12	trace

[a]Isolated yield after column chromatography; [b]at room temperature

To evaluate the scope of the substrate of this methodology, a variety of 2′-hydroxychalcones were examined in the reaction, and the results are summarized in Table II. In all cases, the optimized conditions described previously proved to be applicable. Good to excellent results were achieved for 4-chloro and 4-methyl substituents (Table II, entries 8 and 10). However, the 4-fluoro group significantly decreased the yield (Table II, entry 9). 4-Methoxyl and 3-nitro substitutes afforded the corresponding flavanones in good yields (Table II, entries 7 and 11). Additionally, substitutions at the R_1 or R_2 positions were also tolerated (Table II, entries 2–6).

TABLE II. Scope of the cyclization of 2′-hydroxychalcones; the reactions were carried out with 1 mmol 2′-hydroxychalcones and 0.2 mmol *N*-methylimidazole in DMSO (1 mL) at 80 °C, 6h

Entry	R_1	R_2	R_3	R_4	Product	Yield, %
1	H	H	H	H	**2a**	90
2	CH_3	H	H	H	**2b**	87
3	CH_3	H	H	CH_3	**2c**	76
4	CH_3O	H	H	H	**2d**	89
5	H	CH_3O	H	H	**2e**	90
6	H	CH_3O	H	CH_3O	**2f**	79[a]
7	H	H	NO_2	H	**2g**	86
8	H	H	H	Cl	**2h**	87
9	H	H	H	F	**2i**	65[a]
10	H	H	H	CH_3	**2j**	87
11	H	H	H	CH_3O	**2k**	90[a]

[a] At 100 °C, 8 h

EXPERIMENTAL

Commercial reagents were used as received. Analytical-grade solvents and commercially available reagents were used without further purification. For product purification by flash column chromatography, silica gel (200–300 mesh) and light petroleum ether (PE, b.p. 60–90 °C) are used. The IR spectra were recorded on a Bruker Tensor 37 spectrophotometer as liquid film. The ^{1}H- and ^{13}C-NMR spectra were taken on a Bruker AM-300 spectrophotometer with tetramethylsilane (TMS) as an internal standard and $CDCl_3$ as the solvent. Melting points were measured on a WRS-2A melting point apparatus and are uncorrected. Electron impact-mass spectrometry (EI-MS) was realized on a HP-5988 spectrometer. Elementary analyses were performed on a Vario EL III elementary analysis instrument.

General procedure for the synthesis of flavanones

N-Methylimidazole (0.2 mmol) was added to a solution of 2′-hydroxychalcone **1a** (224 mg, 1 mmol) in DMSO (1 mL). After stirring the reaction mixture at 80 °C for 6 h, it was quenched by adding water and the resulting mixture was extracted with AcOEt, washed with water and brine, and dried over $MgSO_4$. The crude product was purified by flash chromatography on silica gel to afford the desired product. The other flavanones were synthesized in a similar manner.

Characterization of the flavanones

The structures of the synthesized flavanones were confirmed by elemental analysis and spectroscopic methods. The results are given in the Supplementary material to this paper.

CONCLUSIONS

In summary, a facile and efficient cyclization of 2′-hydroxychalcones using *N*-methylimidazole as a catalyst in DMSO is reported. Good yields of flavanones were obtained for a variety of 2′-hydroxychalcones. Extension of this methodology is presently under active study.

SUPPLEMENTARY MATERIAL

Analytic and spectral data for the synthesized flavanones are available electronically from http://www.shd.org.rs/JSCS/, or from the corresponding author on request.

ИЗВОД

ЕФИКАСНА И ЛАКА СИНТЕЗА ФЛАВАНОНА КАТАЛИЗОВАНА *N*-МЕТИЛИМИДАЗОЛОМ

PENG WANG[1], JIABIN YANG[1], JIN CAI[2], CHUNLONG SUN[2], LUSHEN LI[1] и MIN JI[2]

[1]*School of Biological Science & Medical Engineering, Southeast University, Nanjing 210096, China* и
[2]*School of Chemistry & Chemical Engineering, Southeast University, Nanjing, 210096, China*

Испитана је употреба *N*-метил-имидазола као катализатора у реакцији циклизације 2′-хидроксихалкона до одговарајућих флавона у ДМСО-у као растварачу. Изучаван је домет и опсег реакција и добијени су различити флавони у одличном приносу.

(Примљено 29. јуна 2012)

REFERENCES

1. a) L. C. Chang, A. D. Kinghorn, *Bioactive Compounds from Natural Sources: Isolation Characterisation and Biological Properties*, Taylor & Francis, London, 2001; b) Ø. M. Andersen, K. R. Markham, *Flavonoids: Chemistry*, *Biochemistry and Applications*, Taylor & Francis, London, 2006
2. M. M. Biddle, M. Lin, K. A. Scheidt, *J. Am. Chem. Soc.* **129** (2007) 3830
3. a) K. Oyama, T. Kondo, *J. Org. Chem.* **69** (2004) 5240; b) J, H. Kevin *Tetrahedron* **61** (2005) 6860
4. J. K. Makrandi, S. Bala, *Synth. Commun*. **30** (2000) 3555
5. P. D. Lokhande, S. S. Sakate, K. N. Taksande, B. Navghare, *Tetrahedron Lett*. **46** (2005) 1573
6. R. Mondal, A. D. Gupta, A. K. Mallik, *Tetrahedron Lett*. **52** (2011) 5020
7. G. J. Sagrera, G. A. Seoane, *J. Braz. Chem. Soc.* **16** (2005) 851
8. B. K. Liu, Q. Wu, X. Q. Qian, D. S. Lv, X. F. Lin, *Synthesis* (2007) 2653.

Journal of the Serbian Chemical Society
JSCS@tmf.bg.ac.rs • www.shd.org.rs/JSCS
J. Serb. Chem. Soc. 78 (7) S81–S83 (2013)
Supplementary material

SUPPLEMENTARY MATERIAL TO

An efficient and facile synthesis of flavanones catalyzed by *N*-methylimidazole

PENG WANG[1], JIABIN YANG[1], JIN CAI[2], CHUNLONG SUN[2], LUSHEN LI[1]
and MIN JI[2]*

[1]*School of Biological Science & Medical Engineering, Southeast University, Nanjing 210096, China and* [2] *School of Chemistry & Chemical Engineering, Southeast University, Nanjing 210096, China*

J. Serb. Chem. Soc. 78 (7) (2013) 917–920

ANALYTIC AND SPECTRAL DATA FOR THE SYNTHESIZED FLAVANONES

2-Phenylchroman-4-one (**2a**). Yield: 90 %; m.p.: 77–78 °C; Anal. Calcd. for $C_{15}H_{12}O_2$: C, 80.34; H, 5.39 %. Found: C, 80.03, H 5.62 %; IR (KBr, cm^{-1}): 1688 (s). ^{1}H-NMR (300 MHz, $CDCl_3$, δ / ppm): 2.75–3.15 (2H, *m*, J = 13.2 Hz), 5.51 (1H, *dd*, J = 13.2 and 3.0 Hz), 7.04–7.93 (9H, *m*, J = 3.0 Hz); ^{13}C-NMR (75 MHz, $CDCl_3$, δ / ppm): 192.5, 162.1, 139.0, 136.6, 129.3, 129.2, 127.4, 126.6, 122.2, 121.3, 118.5, 80.1, 45.0; EI-MS 224 (M$^+$, 100), 223 (93), 147 (54), 120 (83), 92 (44), 77 (11).

6-Methyl-2-phenylchroman-4-one (**2b**). Yield: 87 %; m.p.: 104–105 °C (lit. 104 °C[1]); Anal. Calcd. for $C_{16}H_{14}O_2$: C, 80.65; H, 5.92 %. Found: C, 80.90; H, 6.17 %; IR (KBr, cm^{-1}): 1700 (s); ^{1}H-NMR (300 MHz, $CDCl_3$, δ / ppm): 2.46 (3H, *s*), 2.90 (2H, *dd*, J = 13.2 and 3.0 Hz), 5.41 (1H, *dd*, J = 13.2 and 3.0 Hz), 7.04–7.90 (8H, *m*); ^{13}C-NMR (75 MHz, $CDCl_3$, δ / ppm): 192.4, 159.8, 137.1, 135.3, 131.0, 128.9, 128.7, 127.8, 127.5, 120.7, 117.6, 71.3, 52.5, 20.5. EI-MS (*m*/*z* (relative abundance, %)): 238 (M$^+$, 100), 104 (23).

6-Methyl-2-(p-tolyl)chroman-4-one (**2c**). Yield: 76 % m.p.: 90–91 °C (lit. 89–90 °C[2]). Anal. Calcd. for $C_{17}H_{16}O_2$: C, 80.93; H, 6.39 %. Found: C, 80.67; H, 6.51 %. IR (KBr, cm^{-1}): 1690 (s); ^{1}H-NMR (300 MHz, $CDCl_3$, δ / ppm): 2.33 (3H, *s*), 2.38 (3H, *s*), 2.96 (2H, *dd*, J = 13.2 and 2.7 Hz), 5.42 (1H, *dd*, J = 13.2 and 2.7 Hz), 6.94–7.72 (7H, *m*); ^{13}C-NMR (75 MHz, $CDCl_3$, δ / ppm): 190.4, 159.8, 138.5, 137.3, 135.9, 130.9, 129.5, 126.6, 126.2, 120.7, 117.9, 79.2, 44.1, 21.5, 20.3. EI-MS (*m*/*z* (relative abundance, %)): 252 (M$^+$, 100), 237 (18), 134 (12), 104 (13).

---

* Corresponding author. E-mail: jimin@seu.edu.cn

*6-Methoxy-2-phenylchroman-4-one (**2d**)*. Yield: 89 %; m.p.: 134–135 °C (lit. 136 °C[1]); Anal. Calcd. for $C_{16}H_{14}O_3$: C, 75.57; H, 5.55 %. Found: C, 75.90; H, 5.72 %; IR (KBr, cm^{-1}): 1676 (s). ^{1}H-NMR (300 MHz, $CDCl_3$, δ / ppm): 2.87 (2H, *dd*, J = 13.3 and 3.0 Hz), 3.75 (3H, *s*), 5.37 (1H, *dd*, J = 13.3 and 3.0 Hz), 6.95–7.50 (8H, *m*); ^{13}C-NMR (75 MHz, $CDCl_3$, δ / ppm): 192.5, 156.8, 154.6, 139.1, 129.2, 129.1, 126.6, 125.8, 121.2, 119.9, 107.7, 80.1, 56.2, 45.1; EI-MS (*m*/*z* (relative abundance, %)): 254 (M^+, 81), 177 (19), 150 (100), 107 (18).

*7-Methoxy-2-phenylchroman-4-one (**2e**)*. Yield: 90 %; m.p.: 90–91 °C (lit. 90–91 °C[3]); Anal. Calcd. for $C_{16}H_{14}O_3$: C, 75.57; H, 5.55 %. Found: C, 75.82; H, 5.80 %; IR (KBr, cm^{-1}): 1679 (s); ^{1}H-NMR (300 MHz, $CDCl_3$, δ / ppm): 2.83 (1H, *dd*, J = 16.9 and 3.1 Hz), 3.05 (1H, *dd*, J = 16.9 and 13.2 Hz), 3.84 (3H, *s*), 5.45 (1H, *dd*, J = 13.2 and 3.0 Hz), 6.51 (2H, *d*, J = 2.4 Hz), 6.63 (1H, *dd*, J = 8.8 and 2.4 Hz), 7.37–7.51 (4H, *m*), 7.89 (1H, *d*, J = 8.8 Hz); ^{13}C-NMR (75 MHz, $CDCl_3$, δ / ppm): 191.0, 166.7, 164.0, 139.2, 129.3, 129.2, 126.7, 115.2, 110.8, 101.3, 80.4, 56.0, 44.7; EI-MS (*m*/*z* (relative abundance, %)): 252 (M^+, 100), 253 (65), 177 (62), 150 (65).

*7-Methoxy-2-(4-methoxyphenyl)chroman-4-one (**2f**)*. Yield: 79 %; m.p.: 94–95 °C (lit. 94–95 °C[3]); Anal. Calcd. for $C_{17}H_{16}O_4$: C, 71.82; H, 5.67 %. Found: C, 71.69; H, 5.84 %; IR (KBr, cm^{-1}): 1679 (s); ^{1}H-NMR (300 MHz, $CDCl_3$, δ / ppm): 2.80 (1H, *dd*, J = 16.9 and 2.9 Hz), 3.06 (1H, *dd*, J = 16.9 and 13.2 Hz), 3.84 (6H, *s*), 5.43 (1H, *dd*, J = 13.2 and 2.9 Hz), 6.48 (1H, *d*, J = 2.4 Hz), 6.62 (1H, *dd*, J = 8.8 and 2.4 Hz), 6.96 (2H, *d*, J = 6.7 Hz), 7.40 (2H, *d*, J = 6.7 Hz), 7.87 (1H, d, J = 8.8 Hz); ^{13}C-NMR (75 MHz, $CDCl_3$, δ / pm): 191.2, 166.7, 163.9, 160.4, 131.2, 129.1, 128.0, 115.2, 114.6, 110.7, 101.3, 80.2, 56.1, 55.8, 44.5; EI-MS 284 (M^+, 100), 283 (57), 177 (30), 134 (98), 121 (45).

*2-(3-Nitrophenyl)chroman-4-one (**2g**)*. Yield: 86 %; m.p.: 143–145 °C (lit. 142 °C[4]); Anal. Calcd. for $C_{15}H_{11}NO_4$: C, 66.91; H, 4.12; N, 5.20 %. Found: C, 66.52; H, 4.33; N, 5.43 %; IR (KBr, cm^{-1}): 1693 (s); ^{1}H-NMR (300 MHz, $CDCl_3$, δ / ppm): 2.96 (1H, *dd*, J = 16.8 and 3.2 Hz), 3.09 (1H, *dd*, J = 16.8 and 12.8 Hz), 5.61 (1H, *dd*, J = 12.8 and 3.2 Hz), 7.12 (2H, *m*), 7.56–7.64 (2H, *m*, J = 8.0 and 1.6 Hz), 7.81 (1H, *m*), 7.95 (1H, *dd*, J = 8.0 and 1.6 Hz), 8.26 (1H, *m*), 8.42 (1H, *t*, J = 2.0 Hz); ^{13}C-NMR (75 MHz, $CDCl_3$. δ / ppm): 190.8, 160.9, 148.6, 141.0, 136.4, 131.9, 130.0, 127.2, 123.6, 122.3, 121.2, 120.7, 118.0, 78.2, 44.5; EI-MS (*m*/*z* (relative abundance, %)): 269 (M^+, 35), 268 (40), 147 (100), 121 (33), 120 (66), 92 (99).

*2-(4-Chlorophenyl)chroman-4-one (**2h**)*. Yield: 87 % m.p.: 84–85 °C (lit. 84–85 °C[2]); Anal. Calcd. for $C_{15}H_{11}ClO_2$: C, 69.64; H, 4.29 %. Found: C, 69.37; H, 4.58 %; IR (KBr, cm^{-1}): 1692 (s); ^{1}H-NMR (300 MHz, $CDCl_3$, δ / ppm): 2.87 (1H, *dd*, J = 17.2 and 3.2 Hz), 3.06 (1H, *dd*, J = 17.2 and 13.2 Hz), 5.48 (1H, *dd*, J = 13.2 and 3.2 Hz), 7.05 (2H, *m*), 7.45 (4H, *m*), 7.52 (1H, *m*), 7.93 (1H, *dd*, J = 8.0 and 2.0 Hz); ^{13}C-NMR (75 MHz, $CDCl_3$, δ / ppm): 191.5, 161.2, 137.1, 136.3, 134.6, 128.9, 127.5, 127.1, 121.9, 120.9, 118.1, 78.9, 44.6; EI-MS (*m*/*z* (relative abundance, %)): 258 (M^+, 70), 257 (100), 223 (28), 147 (65), 120 (67), 92 (75).

*2-(4-Fluorophenyl)chroman-4-one (**2i**)*. Yield; 65 %; m.p.: 79–80 °C (lit. 78–79 °C^5); Anal. Calcd. for $C_{15}H_{11}FO_2$: C, 74.37; H, 4.58 %. Found: C, 74.52; H, 4.85 %; IR (KBr, cm^{-1}): 1695 (s); ^{1}H-NMR (300 MHz, $CDCl_3$, δ / ppm): 2.88 (1H, *dd*, J = 16.8 and 2.8 Hz), 3.08 (1H, *dd*, J = 16.8 and 13.2 Hz), 5.49 (1H, *dd*, J = 13.2 and 2.8 Hz), 7.10 (4H, *m*), 7.47 (2H, *m*), 7.52 (1H, *td*, J = 8.4 and 1.6 Hz), 7.93 (1H, *dd*, J = 8.0 and 2.0 Hz); ^{13}C-NMR (75 MHz, $CDCl_3$, δ / ppm): 191.8, 162.8, 161.4, 136.2, 134.6, 129.9, 127.2, 121.8, 120.9, 118.0, 115.8, 79.0, 44.6. EI-MS (*m*/*z* (relative abundance, %)): 242 (M^+, 56), 241 (86), 147 (43), 122 (40), 121 (36), 120 (68), 92 (100), 63 (23).

*2-(p-Tolyl)chroman-4-one (**2j**)*. Yield: 87 %; m.p.: 82–83 °C (lit. 82–84 °C^6); Anal. Calcd. for $C_{16}H_{14}O_2$: C, 80.65; H, 5.92. Found: C, 80.79; H, 6.16 %; IR (KBr, cm^{-1}): 1696 (s); ^{1}H-NMR (300 MHz, $CDCl_3$, δ / ppm): 2.38 (3H, *s*), 2.88–3.12 (2H, *m*), 5.43 (1H, *dd*, J = 13.8 and 2.0 Hz), 7.03–7.06 (2H, *m*), 7.23 (2H, d, J = 8.0 Hz), 7.36 (d, 2H, J = 8.0 Hz), 7.49 (m, 1H), 7.93 (dd, 1H, J = 8.5 and 2.0 Hz); ^{13}C-NMR (75 MHz, $CDCl_3$, δ / ppm): 192.3, 161.8, 138.9, 136.2, 135.6, 129.6, 127.2, 126, 3, 121.8, 120.9, 118.3, 77.5, 44.6, 21.3; EI-MS (*m*/*z* (relative abundance, %)): 238 (M^+, 100), 237 (86), 161 (56), 134 (32), 104 (23).

*2-(4-Methoxyphenyl)chroman-4-one (**2k**)*. Yield: 90 %; m.p.: 97–98 °C (lit. 98 °C^7); Anal. Calcd. for $C_{16}H_{14}O_3$: C, 75.57; H, 5.55 %. Found: C, 75.72; H, 5.78 %; IR (KBr, cm^{-1}): 1690 (s); ^{1}H-NMR (300 MHz, $CDCl_3$, δ / ppm): 2.86 (1H, *dd*, J = 16.8 and 2.8 Hz), 3.10 (1H, *dd*, J = 16.8 and 13.3 Hz), 3.84 (3H, *s*), 5.43 (1H, *dd*, J = 13.3 and 2.8 Hz), 6.96 (2H, *d*, J = 8.7 Hz), 7.02–7.08 (2H, *m*), 7.41 (2H, *d*, J = 8.7 Hz), 7.46–7.53 (1H, *m*), 7.93 (1H, *dd*, J = 8.3 and 1.7 Hz); ^{13}C-NMR (75 MHz, $CDCl_3$, δ / ppm): 192.7, 162.1, 160.4, 136.5, 131.2, 128.2, 127.4, 122.0, 121.3, 118.5, 114.6, 79.8, 55.9, 44.9; EI-MS (*m*/*z* (relative abundance, %)): 254 (M^+, 65), 253 (48), 147 (16), 134 (100).

REFERENCES

1. R. Mondal, A. D. Gupta, A. K. Mallik, *Tetrahedron Lett.* **52** (2011) 5020
2. J. I. Lee, M. G. Jung, H. J. Jung, *Bull. Korean Chem. Soc.* **28** (2007) 859
3. A. Kasahara, T. Izumi, M. Ooshima, *Bull. Chem. Soc. Jpn.* **47** (1974) 2526
4. S. Fujise, R. Fujii, T. Maeda, K. Takagi, S Nakamura, *Nippon kagaku zasshi* **74** (1953) 827 (in Japanese, English abstract)
5. F. Chimenti, R. Fioravanti, A. Bolasco, P. Chimenti, D. Secci, F. Rossi, M. Yanez, F. Orallo, F. Ortuso, S. Alcaro, R. Cirilli, R. Ferretti, M. L. Sanna, *Bioorg. Med. Chem.* **18** (2010) 1273
6. V. K. Rao, M. S. Rao, A. J. Kumar, *Heterocycl. Chem*. **48** (2011) 1356
7. J. K. Makrandi, S. Bala, *Synth. Commun.* **30** (2000) 3555.

Journal of the Serbian Chemical Society
JSCS-info@shd.org.rs • www.shd.org.rs/JSCS

J. Serb. Chem. Soc. 78 (7) 921–931 (2013)
JSCS–4470

UDC 633.846+541.459:620.28:577.15:
544.478–035.2
Original scientific paper

Magnetic labelled horseradish peroxidase–polymer nanoparticles: a recyclable nanobiocatalyst

AREZOO KHOSRAVI[1], MANOUCHEHR VOSSOUGHI[1,2]*, SAEED SHAHROKHIAN[1,3] and IRAN ALEMZADEH[2]

[1] Institute for Nanoscience and Nanotechnology, Sharif University of Technology, Tehran, Iran, [2] Chemical and Petroleum Engineering Department, Sharif University of Technology, Tehran, Iran and [3] Department of Chemistry, Sharif University of Technology, Tehran, Iran

(Received 30 September, revised 26 November 2012)

Abstract: In this study, the reusability and process stability of nano-reengineered horseradish peroxidase was investigated in a fluorescence-based sensing system for hydrogen peroxide determination as a model application. To this end, dendron macromolecules were attached to the enzyme surface through bio-conjugation techniques. The resulting enzyme–polymer nanoparticles, with an average size of 14(±2) nm, showed significant life time and thermal stability. For enzyme recovery and reusability purposes, the enzyme–polymer nanoparticles were labelled with magnetic nanoparticles with a labelling yield of 90 %. These labelled enzyme molecules showed significant process stability, *i.e.*, up to 7 recycling period in a model sensing system. A linear calibration curve was obtained over a hydrogen peroxide concentrations range from 5×10^{-8} to 1×10^{-5} mol L^{-1}, with a detection limit of 1.3×10^{-9} mol L^{-1} for the sensing system under the optimal conditions.

Keywords: horseradish peroxidase; nano-reengineered enzyme; magnetic nanoparticles; recyclable biocatalyst.

INTRODUCTION

Enzymes, nanometric biocatalysts that play a key role in biochemical reactions of living cells and bio-organisms, offer various applications, including biosensing, bioremediation and chemical synthesis[1–3] due to their specificity.[4,5] Nevertheless, the relatively short lifetime of enzymes and their instability in harsh environments (elevated temperature and organic media) limit their applications.[4] Enzyme stabilization can provide several advantages including: 1) decrease in the amount of enzyme required, 2) life time prolongation and 3) enhancement in the potential for enzyme reuse.[2,6]

---

* Corresponding author. E-mail: vosoughi@sharif.edu
doi: 10.2298/JSC120930133K

There have been several approaches to improve enzyme stability that are mainly categorized into enzyme immobilization (entrapment on solid surfaces or within porous materials,[7,8] trapping in gels,[9] polymers[10] or composite materials[11]), surface modification, protein engineering and reaction medium engineering.[12–14]

The economics of a bio-catalytic process can be enhanced by enzyme reuse. One of the most attractive methods of separating the enzyme molecules from the reaction solution is utilizing magnetic nanoparticles–enzyme conjugates.[15,16] The magnetic nanoparticles can attach to the enzyme surface through conjugation methods or they can play the role of a support for enzyme immobilization. Suspended super-paramagnetic particles in solution can be removed from a reaction mixture using an external magnet, but they do not agglomerate after removal of the external magnetic field.[17]

In the past years, magnetic nanoparticles have been widely used as biomolecule-carriers for the immobilization of various enzymes.[18–21]

However, the activity and stability of enzyme immobilized on these magnetic nanoparticles will greatly depend on the environmental factors, such as pH, temperature and organic solvent.[17] To improve this limitation, Yang and co-workers fabricated magnetic single enzyme nanoparticles through encapsulation of each single glucose oxidase molecule in a thin composite layer of magnetic nanoparticles and polymer.[17] In a previous work, a simple method was proposed for the fabrication of enzyme–polymer nanoparticles using dendritic polymers, which improved the enzyme stability through bio-conjugation of polyester dendron macromolecules to the primary amino groups on the enzyme surface. The approach represents a novel way of modifying and stabilizing enzymes as the fabricated horseradish peroxidase–polymer nanoparticles exhibited significant life-time stability up to 70 days, whereas free horseradish peroxidase (HRP) lost its activity after several days.[22] These enzyme–polymer nanoparticles could readily be labelled with magnetic nanoparticles for further enzyme recovery and reused by employing an external magnetic field for enzyme separation from the reaction mixture.

The present study was aimed at evaluating the process stability and reusability of magnetic-labelled dendritic modified enzymes. As a model application of HRP, a hydrogen peroxide (H_2O_2) sensing system was designed based on the generation of a fluorescent agent from the reaction of homovanillic acid (HVA) and H_2O_2 in the presence of the stabilized HRP.[23,24] This simple and model enzyme-based process was used to investigate the stability and reusability of the labelled modified enzyme. In addition, the sensing conditions were optimized for this nano-reengineered HRP and also the linear range and detection limit of the sensing system were examined. Furthermore, as a real test, the H_2O_2 content of some excipient samples was assessed. Excipients are the inactive part of drug formulations that have some roles, such as binder, filler or dispersing agent, for the active drugs. Drug chemical stability could be significantly decreased by impurities present in formulation excipients. Hydrogen peroxide is one of the impurities that could oxidize drugs. For example, the presence of residual H_2O_2 in poly(vinylpyrrolidone) (PVP) as a pharmaceutical excipient is reported to be the main agent in drug oxidation and deactivation.[25,26]

EXPERIMENTAL

Materials

Horseradish peroxidase (HRP), 3,3′,5,5′-tetramethylbenzidine (TMB), *N*-hydroxysulphosuccinimide (Sulpho-NHS), 2-(4-morpholino)ethanesulphonic acid (MES), 1-ethyl-3-[3-(dimethylamino)propyl]carbodiimide hydrochloride (EDC) and ethylenediamine (EDA) were purchased from Merck (Germany). Polyester-32-hydroxyl-1-carboxyl bis-MPA Dendron (Generation 5, M_w 3617 g mol^{-1}) and HVA were purchased from Sigma–Aldrich (USA). A solution of Fe_3O_4 nanoparticles (7 vol. %) was purchased from PlasmaChem (Germany). All other chemicals were of analytical grade and used without further purification. De-ionised (DI) water (resistivity of 18 MΩ cm) was obtained from a Millipore Milli-Q Water System (Millipore Inc.), and was used for rinsing and for makeup of all aqueous solutions.

Methods

Enzyme–polymer bio-conjugation. As reported in a previous work, a dendritic polymer with a carboxylic group core was conjugated to amine group residues of HRP for stability enhancement.[22] Briefly, the dendron was dissolved in MES buffer (pH 6.0, 0.05 M) at a concentration of 1 mg mL^{-1}. EDC and Sulpho-NHS were added to reach the final concentrations of 2 mM for EDC and 5 mM for Sulpho-NHS. They were mixed and reacted for 15 min at room temperature. Then, an HRP solution (1 mg mL^{-1} in 0.1 M phosphate buffer of pH 7.5) was added and mixed for at least 2 h and subsequently the fabricated HRP–dendron nanoparticles were purified.

Labelling of HRP–dendron nanoparticles with magnetic nanoparticles. The purchased magnetic nanoparticles (MNPs) had oleic acid molecules on their surface as the stabilizer. Ethylenediamine was used for the conjugation of the surface acid groups of the MNPs to the carboxyl groups on the surface of the HRP–polymer nanoparticles. At first, 200 μL of a MNPs solution (7 vol. %) was diluted with 5 mL of PBS buffer (0.10 M). Then, it was activated with EDC and Sulpho-NHS solutions with final concentrations of 2 mM and 5 mM, respectively. Then, 5 mL of HRP–polymer nanoparticles solution was also activated with EDC and Sulpho-NHS. After stirring each mixture for 15 min, 100 μL of ethylenediamine and the enzyme nanoparticles mixture were simultaneously added to the first mixture under mechanical stirring conditions and mixed for 1 h. Then, a strong magnet was used for the separation of MNPs from the mixture. Finally, the separated MNPs (attached to the HRP–polymer nanoparticles) were washed 3 times with DI water to remove excess reactants and then stored in the refrigerator at 4 °C. The HRP concentration was evaluated using the Lowry procedure as modified by Peterson[27] for determination of the HRP labelling yield.

H_2O_2 fluorescence-based nanobiosensor

Homovanillic acid (HVA) was used as a fluorogenic compound for H_2O_2 sensing. HVA itself is not a fluorescent agent but after oxidation with H_2O_2 in the presence of HRP converts to a fluorescent dimer. Therefore, it could be used as a probe in the fluorescence-based H_2O_2 sensors.

Reaction solution (3 mL) was obtained by mixing 2.2 mL phosphate buffer saline (PBS, 0.10 M) of pH 7.5, 0.3 mL HRP solution and 0.2 mL HVA solution. The reaction was started by addition of 0.3 mL of H_2O_2 solution at a pre-defined concentration (or the sample solution) to the above mixture. Then, the assay solution was mixed for 5 min at room temperature. At the end of reaction, the labelled enzyme molecules were removed by magnetic separation. Then, the supernatant pH was adjusted to 10.0 by addition of 0.30 mL of glycine–NaOH buffer solution, which was used for spectrofluorometric measurement at 420 nm with an excitation wavelength of 312 nm.[23]

The affecting parameters on the fluorescence intensity may be enzyme concentration and HVA concentration. From previous investigations on the HRP–polymer nanoparticles activity,[22] a pH of 7.5 and room temperature were selected for the assay because the stabilized HRP has its maximum activity under these conditions. Response surface methodology was used for the optimization of enzyme and HVA concentration by using Design Expert® 8.0.4 software.

Real sample analysis

As a real sample analysis, the amount of H_2O_2 residue in PVP and poly(ethylene glycol) (PEG) as model excipients were determined. For this purpose, 0.1 g of PVP and PEG samples were dissolved in 3 mL of DI water under stirring. 0.3 mL of each sample was added to the sensing reaction tube to determine the amount of H_2O_2 in the excipient samples. The H_2O_2 content of samples were reported as solution concentration in μmol L^{-1} and also in ppm (μg g^{-1}) of the solid form of the sample.

Enzyme recovery and reusability

The stabilized HRP–polymer molecules labelled with MNPs can be separated from the sensing mixture by applying an external magnetic field. To investigate the recovery and reusability of the labelled HRP–polymer nanoparticles, the used bio-catalyst was recovered by magnetic separation and washed 3 times with DI water to remove the reaction solution. The recovered catalyst was reused in a subsequent sensing reaction under the same experimental conditions as described before.

Characterization methods

TEM imaging of the samples were determined by means of a CM120 transmission electron microscope, Philips, the Netherlands, using standard carbon-coated grids and 120 kV as the applied voltage. A Cary Eclipse fluorescence spectrophotometer (Varian, Agilent Technologies, Australia) was used for the spectrofluorometric measurements. For protein concentration assay and enzyme activity assessments (with TMB as the substrate[22]), the Lambda 950 UV–Vis spectrometer (PerkinElmer, USA) was used.

RESULTS AND DISCUSSIONS

HRP–polymer nanoparticles preparation

The HRP molecules were modified by attaching dendron macromolecules to the enzyme surface. Based on previous studies, each fabricated nanoparticle consisted of a single enzyme with five dendron molecules attached to its surface amine groups.[22] Based on TEM images, the average size of the nanoparticles was 14(±2) nm, as shown in Fig. 1a. The life-time and stability analysis revealed that the dendritic modified HRP showed a significant enhancement in its life-time over 70 days storage at 4 °C (Fig. 2a). The thermal activity of the reengineered enzyme at elevated temperatures up to 80 °C was considerably higher in comparison to that of the free HRP, as shown in Fig. 2b. This result may be due to the attached dendron macromolecules being able to effectively preserve the conformation of the HRP biomolecules against thermal induced unfolding and denaturation caused by movements of the protein moiety around haem.[22] The stability results suggest promising applications of this stabilized enzyme in some interesting fields, such as biosensors.

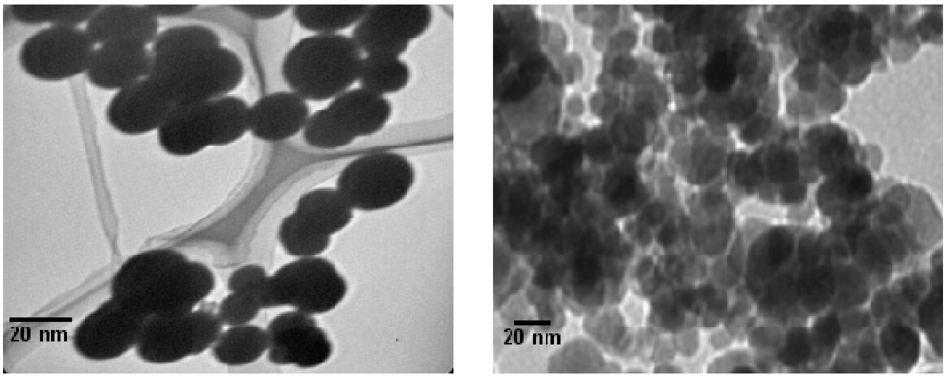

(a) (b)

Fig. 1. TEM images of a) the fabricated HRP–polymer nanoparticles and b) MNPs attached to the HRP–polymer nanoparticles.

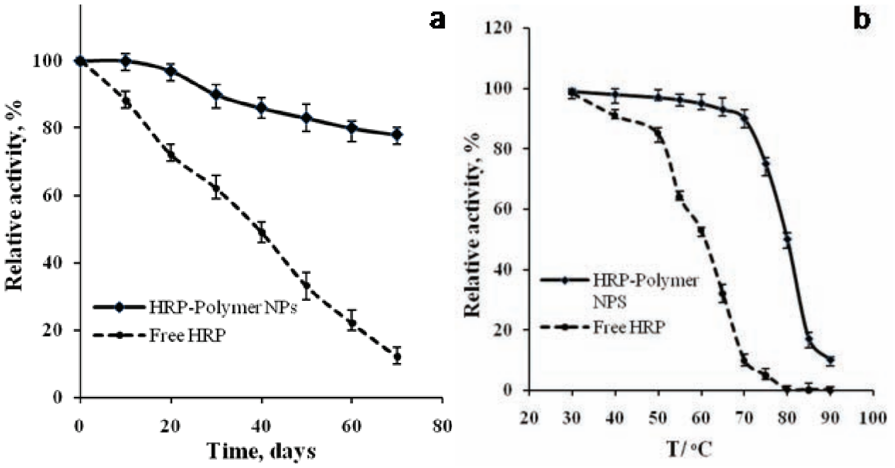

Fig. 2. a) Storage stability and b) thermal stability of the HRP–polymer nanoparticles in contrast to free HRP.

Magnetic labelling of HRP–polymer nanoparticles

The Fe_3O_4 magnetic nanoparticles (MNPs) with an average size of 8 nm were utilized as magnetic labels for the preparation of a recyclable stabilized biocatalyst. Enzyme activity assays revealed a slight loss of enzymatic activity (less than 4 %) due to the labelling process. The average yield of conjugation for MNPs to dendritic stabilized HRP was 90(±2) %. This labelling yield was obtained from HRP concentration assessment after separation of the enzyme from the reaction mixture and then re-dispersing in 5 mL of PBS. A TEM image of MNPs conjugated to HRP–polymer nanoparticles is shown in Fig. 1b.

H_2O_2 sensing system and its spectral characteristics

The H_2O_2 assay was based on the oxidation of HVA to its fluorescent biphenyl dimer (Scheme 1) in the presence of hydrogen peroxide and peroxidase. As shown in Fig. 3, the product shows the excitation and emission maximum wavelengths at 312 and 420 nm, respectively.[23] The blank samples (HRP–HVA and H_2O_2–HVA systems) have no significant fluorescence intensity in comparison with the HRP–HVA–H_2O_2 samples. This means that HVA could be oxidized by H_2O_2 to a strongly fluorescent dimer in the presence of the HRP enzyme as catalyst. Thus, the determination of H_2O_2 could be achieved by using its oxidizing ability, and its concentration is directly proportional to the fluorescence intensity of the HVA dimer. Therefore, the fluorescence intensity of HRP–HVA–H_2O_2 system could be used as the basis of the proposed method for detection of H_2O_2 traces.

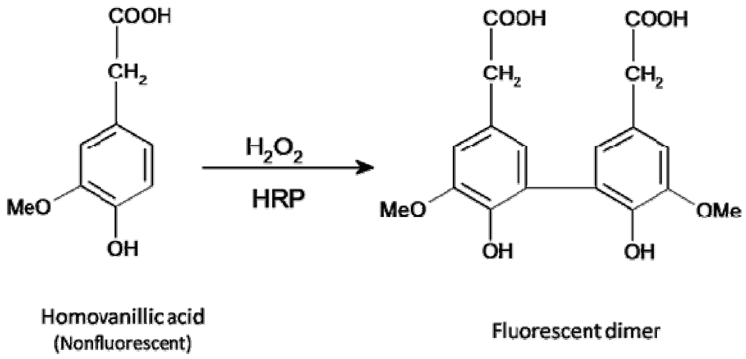

Scheme 1. Oxidation of HVA to a fluorescent dimer by H_2O_2 in the presence of HRP.

Experimental design and optimum conditions

The concentrations of enzyme (labelled HRP–polymer nanoparticles) and HVA were chosen as independent variables and the fluorescence intensity as a dependent output response variable. The composite system was applied for the response surface methodology and optimization of the parameters.

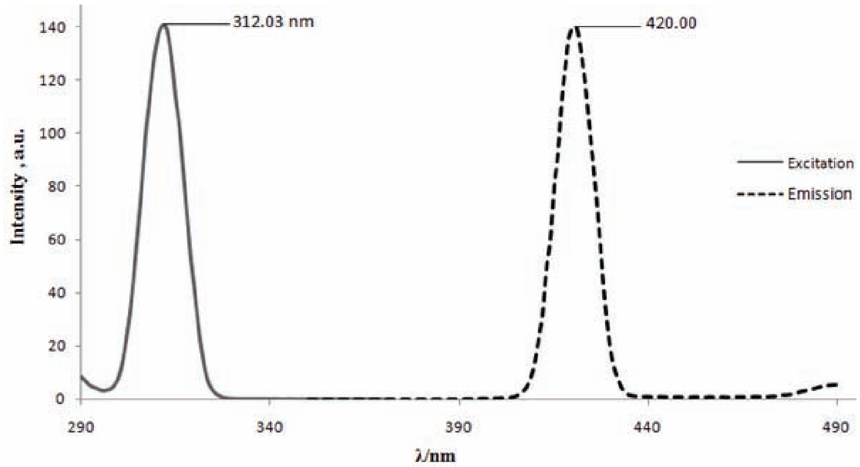

Fig. 3. Excitation and emission spectra of solutions from the systems of HVA/H_2O_2/HRP–polymer nanoparticles (labelled). Experimental conditions: H_2O_2, 2.0×10^{-6} mol L^{-1}; HVA, 100×10^{-6} mol L^{-1}; labelled HRP–polymer nanoparticles, 0.4 mg mL^{-1}; pH of the reaction solution, 7.5; reaction temperature, 25 °C; reaction time, 5 min; pH of detection solution, 10.0.

The response surface plot resulted from a fitted cubic model (with $R^2 = 0.9955$) is shown in Fig. 4. This fitted model showed that the fluorescence intensity of this probing system was increased with an increasing enzyme (labelled HRP–polymer nanoparticles) and HVA concentrations. It is revealed that the rate of increase in the intensity was very low for specific levels of HRP and HVA concentrations. This design suggests optimum concentrations of 0.3 mg mL^{-1} and 70 μM for the enzyme and HVA, respectively. These results are based on the minimum enzyme and HVA concentrations consistent with a sufficiently high fluorescence intensity.

H_2O_2 calibration curve

Under the optimized conditions, this sensing system gave linear responses to H_2O_2 in the range 5×10^{-8}–1×10^{-5} mol L^{-1}. The calibration curves of H_2O_2 detection for different HVA concentrations were obtained by correlating the fluorescence intensity with the H_2O_2 concentration. Figure 5 indicates that the fluorescence of the reaction system responded linearly with H_2O_2 concentration (c, μmol L^{-1}) with an HVA concentration of 70 μM and more. The linear regression equation for H_2O_2 concentration *vs*. the fluorescence intensity under the optimal conditions was $F = 67.97c + 4.24$ with a correlation coefficient (R^2) of 0.997. The detection limit for this probing system was 1.3×10^{-9} mol L^{-1}.

Determination of H_2O_2 in real samples

The application of the prepared sensing system was assessed by the determination of hydrogen peroxide content of 4 excipient samples using the standard addition method for sample analysis. As shown in Table I, when H_2O_2 at three different concentrations was added to the excipient samples, the recoveries of H_2O_2 ranged from 96 to 104 % for all samples and the relative standard deviation (*RSD*) was less than 3.5 %. These results showed that this sensing system had sufficient accuracy and reliability and could also be an effective tool for monitoring the hydrogen peroxide in drug excipients and thus useful in the selection of an appropriate one with a smaller amount of H_2O_2 impurity.

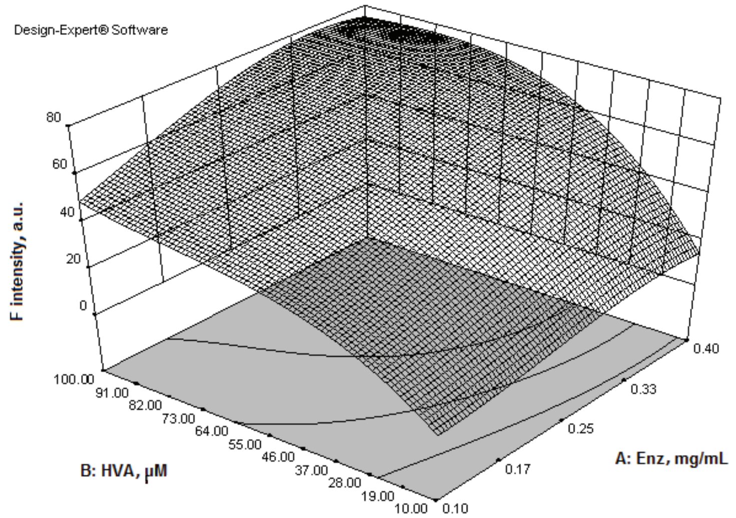

Fig. 4. Surface response plot of the combined effect of concentrations of enzyme and HVA on the fluorescence intensity of the system (enzyme: labelled HRP–polymer nanoparticles).

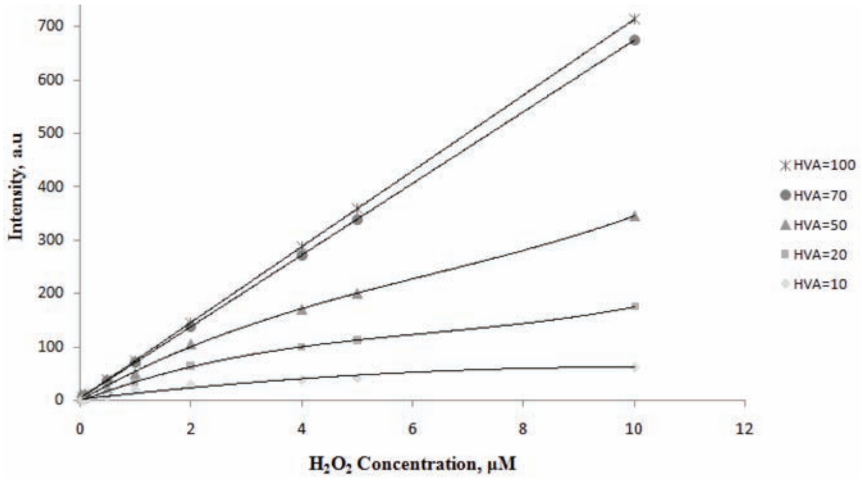

Fig. 5. Calibration curves of HVA-related H_2O_2 detection. (labelled HRP–polymer nanoparticles, 0.3 mg ml^{-1} and reaction time, 5min).

Table I. Determination of the H_2O_2 content in pharmaceutical excipient samples (*n* = 5)

Sample	Added, μmol L^{-1}	Found, μmol L^{-1}	Found, ppm	*RSD*, %	Recovery, %
PVP-A	0	6.170	62.934	3.1	–
	2	8.191		2.6	101
	5	10.970		3.0	96
PVP-B	0	2.642	26.948	2.4	–
	2	4.683		1.9	102
	5	7.795		3.2	103
PEG-A	0	0.094	0.958	1.5	–
	0.1	0.198		1.7	104
	0.5	0.588		2.1	98
PEG-B	0	0.236	2.407	2.0	–
	0.5	0.716		3.5	96
	1	1.203		2.7	98

Enzyme recovery

The magnetic labelled stabilized enzyme could be easily separated and assessed for its remained catalytic activity (Fig. 6a). To demonstrate the reusability of the stabilized enzyme, the used biocatalyst was recovered by magnetic separation and rinsed thoroughly with distilled water to remove the remaining reaction solution. The recovered enzyme was reused in subsequent sensing reactions under optimal conditions. The relative activity of the reused stabilized HRP for seven first cycles is shown in Fig. 6b, which indicates that the nano reengineered HRP (with dendron macromolecules) exhibited a remarkable stability and could be recovered and reused as the decrease in activity after seven sensing cycles was minimal.

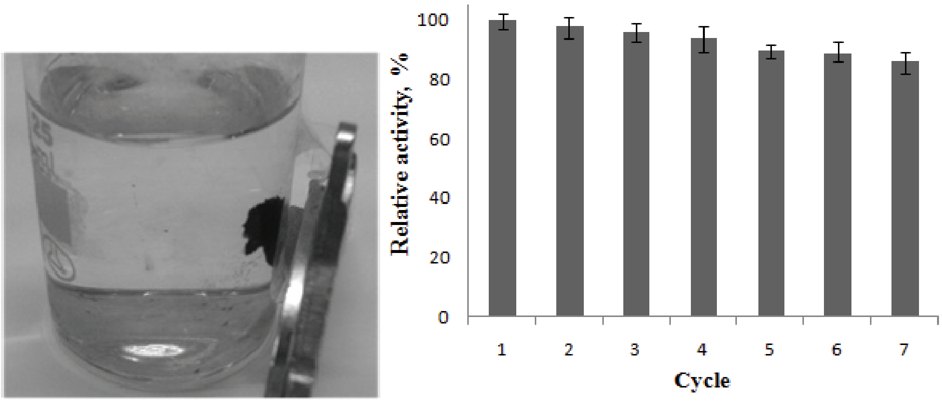

(a) (b)

Fig. 6. a) Magnetic separation of magnetically labelled HRP-polymer nanoparticles and b) relative activity of the reused labelled HRP-polymer nanoparticles.

CONCLUSIONS

The present study introduced a recyclable biocatalyst consisting of nano-reengineered horseradish peroxidase (by means of dendron macromolecule attachment to the enzyme surface) and attached magnetic nanoparticles, as labelling agents providing recyclability. After stabilization, the HRP showed a remarkable life-time and stability. A simple fluorescence based sensing system for H_2O_2 was designed and optimized as a model application for stability and reusability evaluation of fabricated reusable stabilized HRP. The sensing system showed a relatively wide linear response over H_2O_2 concentrations from 5×10^{-8} to 1×10^{-5} mol L^{-1} and was successfully applied to monitoring trace levels of H_2O_2 residues in PVP and PEG excipients, to ensure their safety and efficacy. The significant stability of HRP–dendron nanoparticles was further displayed in the H_2O_2 probing system after 7 recycling times.

ИЗВОД

МАГНЕТНЕ НАНОЧЕСТИЦЕ СА ИМОБИЛИЗОВАНОМ ПЕРОКСИДАЗОМ ИЗ РЕНА – НАНОБИОКАТАЛИЗАТОР ЗА ВИШЕСТРУКУ УПОТРЕБУ

AREZOO KHOSRAVI[1], MANOUCHEHR VOSSOUGHI[1,2], SAEED SHAHROKHIAN[1,3] и IRAN ALEMZADEH[2]

[1]*Institute for Nanoscience and Nanotechnology, Sharif University of Technology, Tehran, Iran,*
[2]*Chemical and Petroleum Engineering Department, Sharif University of Technology, Tehran, Iran и*
[3]*Department of Chemistry, Sharif University of Technology, Tehran, Iran*

У раду је описано испитивање могућности вишеструког коришћења нанsocача са имобилизованом пероксидазом из рена у циљу одређивања водоник-пероксида методом флуоресцентне детекције. Дендронски макромолекули су везани за површину ензима техником биоконјуговања. Настале ензим–полимер наночестице, просечне величине 14(±2) nm, имале су значајан полуживот и термичку стабилност. Да би се ензим могао вишеструко користити, ензим–полимер наночестице су обележене магнетним наночестицама, уз принос од 90 %. Овако обележене ензимске честице су испољиле значајну процесну стабилност и могле су се користити до 7 пута у сензорском модел систему. Добијена је линеарна калибрациона права за концентрације водоник-пероксида у опсегу 5×10^{-8} до 1×10^{-5} mol L^{-1}, уз детекциони лимит од $1,3\times10^{-9}$ mol L^{-1} за сензорски систем под оптималним условима.

(Примљено 30. септембра, ревидирано 26. новембра 2012)

REFERENCES

1. J. B. Kim, *J. Biotechnol.* **150** (2010) 71
2. J. Kim, J. W. Grate, P. Wang, *Chem. Eng. Sci.* **61** (2006) 1017
3. T. Ahuja, I. A. Mir, D. Kumar, Rajesh, *Biomaterials* **28** (2007) 791
4. D. Brady, J. Jordaan, *Biotechnol. Lett.* **31** (2009) 1639
5. P. Wang, *Curr. Opin. Biotechnol.* **17** (2006) 574
6. I. Hegedus, E. Nagy, *Chem. Eng. Sci.* **64** (2009) 1053
7. S. Matsuura, R. Ishii, T. Itoh, S. Hamakawa, T. Tsunoda, T. Hanaoka, F. Mizukami, *Chem. Eng. J.* **167** (2011) 744
8. H. Qiu, L. Lu, X. Huang, Z. Zhang, Y. Qu, *Bioresour. Technol.* **101** (2010) 9415

9. S. Bai, C. Wu, K. Gawlitza, R. Von Klitzing, M. B. Ansorge-Schumacher, D. Wang, *Langmuir* **26** (2010) 12980
10. C. Dhand, M. Das, M. Datta, B. D. Malhotra, *Biosens. Bioelectron.* **26** (2011) 2811
11. A. Pizzariello, M. Stredánsky, S. Miertus, *Bioelectrochemistry* **56** (2002) 99
12. A. Schmid, J. Dordick, B. Hauer, A. Kiener, M. Wubbolts, B. Witholt, *Nature* 409 (2001) 258
13. J. Ge, D. Lu, Z. Liu, *Biochem. Eng. J.* **44** (2009) 53
14. P. Wirth, J. Souppe, D. Tritsch, J.-F. Biellmann, *Bioorg. Chem.* **19** (1991) 133
15. A. Johnson, A. Zawadzka, L. Deobald, R. Crawford, A. Paszczynski, *J. Nanopart. Res.* **10** (2008) 1009
16. M. Alcalde, M. Ferrer, F. J. Plou, A. Ballesteros, *Trends Biotechnol.* **24** (2006) 281
17. Z. Yang, S. Si, C. Zhang, *Biochem. Biophys. Res. Commun.* **367** (2008) 169
18. A. R. Herdt, B.-S. Kim, T. A. Taton, *Bioconjugate Chem.* **18** (2006) 183
19. A. Dyal, K. Loos, M. Noto, S. W. Chang, C. Spagnoli, K. V. P. M. Shafi, A. Ulman, M. Cowman, R. A. Gross, *J. Am. Chem. Soc.* **125** (2003) 1684
20. L. Luo, L. Zhu, Y. Xu, L. Shen, X. Wang, Y. Ding, Q. Li, D. Deng, *Microchim. Acta* **174** (2011) 55
21. F. Šulek, Ž. Knez, M. Habulin, *Appl. Surf. Sci.* **256** (2010) 4596
22. A. Khosravi, M. Vossoughi, S. Shahrokhian, I. Alemzadeh, *Enzyme Microb. Technol.* **50** (2012) 10
23. A. Gomes, E. Fernandes, J. L. F. C. Lima, *J. Biochem. Biophys. Methods* **65** (2005) 45
24. C. Foppoli, R. Coccia, C. Blarzino, M. A. Rosei, *Int. J. Biochem. Cell Biol.* **32** (2000) 657
25. T. Huang, M. E. Garceau, P. Gao, *J. Pharm. Biomed. Anal.* **31** (2003) 1203
26. H. Yue, X. Bu, M.-H. Huang, J. Young, T. Raglione, *Int. J. Pharm.* **375** (2009) 33
27. G. L. Peterson, *Anal. Biochem.* **83** (1977) 346.

Journal of the Serbian Chemical Society
JSCS-info@shd.org.rs • www.shd.org.rs/JSCS

J. Serb. Chem. Soc. 78 (7) 933–945 (2013)
JSCS–4471

UDC 663.551.5:634.22:546.56’47’72’41’23+
543.421(497.11)
Original scientific paper

The contents of heavy metals in Serbian old plum brandies

MIRJANA BONIĆ[1], VELE TEŠEVIĆ[2]*, NINOSLAV NIKIĆEVIĆ[3], JELENA CVEJIĆ[4], SLOBODAN MILOSAVLJEVIĆ[2], VLATKA VAJS[5], BORIS MANDIĆ[2], IVAN UROŠEVIĆ[3], MILOVAN VELIČKOVIĆ[3] and SAŠA JOVANIĆ[1]

[1]Institute of Public Health, Zmaj Jovina 30, 24000 Subotica, Serbia, [2]Faculty of Chemistry, University of Belgrade, Studentski trg 16, 11000 Belgrade, Serbia, [3]Faculty of Agriculture, University of Belgrade, Nemanjina 6, 11080 Zemun, Serbia, [4]Faculty of Medicine, University of Novi Sad, Hajduk Veljkova 3, 21000 Novi Sad, Serbia and [5]Institute for Chemistry, Technology and Metallurgy, University of Belgrade, Njegoševa 12, 11000 Belgrade, Serbia

(Received 5 November 2012, revised 5 February 2013)

Abstract: Seven elements, namely, arsenic, lead, cadmium, copper, zinc, iron and manganese were determined in 31 samples of Serbian plum brandies by application of atomic spectrometry techniques. Flame atomic absorption spectrometry was used for the quantification of copper, iron, zinc, manganese, lead and cadmium, and hydride generation atomic spectrometry absorption for arsenic quantification. The measured concentrations of the heavy metals and arsenic were assessed according to Serbian regulations, official regulations of some other countries and in respect to the content of microelements in other similar distilled alcoholic beverages. The amounts of microelements in the maximal recommended daily and weekly intake of plum brandy were determined. The influence of production (home made or industrial), type of wooden barrel (oak or mulberry), and duration of ageing process on the content of Zn, Cu, Fe and Mn in plum brandies, as well as the coefficient of correlation between the Cu content and pH value were also studied.

Keywords: Šljivovica; plum brandy; atomic absorption spectrometry; aging parameters.

INTRODUCTION

The toxicity of heavy metals is the result of their interactions with the enzymatic systems of animal cells or some constituents of cell membranes. Heavy metals and usual elements from diet (Cu, Zn, Fe, Ca and Se) play an important role in acute and chronic toxicity. The population can be poisoned by heavy metals through ingestion of contaminated or polluted food or water.

---

* Corresponding author. E-mail: vtesevic@chem.bg.ac.rs

doi: 10.2298/JSC121106016B

On the other hand, lack or inadequate quantities of essential trace elements can cause health problems for the populace. Therefore, the concern of food manufacturers and processors is to ensure that a food product does not breach the essentiality / toxicity duality embodied in the various legal requirements or codes of practice for metals in food.[1]

Heavy metals in alcoholic beverages may originate from natural sources (soil, water, raw materials and yeast) and from environmental contamination due to fertilizers, pesticides, industrial processing, and containers.[2]

Knowledge about the inorganic profile of strong alcoholic beverages is of importance for the control of heavy metals ion concentrations, in order to provide quality and safety of the beverage.[3] Mineral contents can indicate differences between alcoholic beverages as to the country of origin, since they are directly associated with soil structure.[3,4]

It is notorious that metal traces affect color, aroma and taste of alcoholic beverages.[5] Copper is one of the key determiners of sensory characteristics of many alcoholic beverages. It contributes to the catalytic conversion of complex sulfur compounds that have odor but subsequently give a majority of alcoholic beverages a better aroma and taste. Copper occurrence in distilled beverages is due to surface corrosion of the copper pot still, which is then converted into copper oxide. This oxide forms deposits or is dissolved and the copper ions can react with some compounds, thereby forming salts.[6]

Distillates containing iron in excess are initially colorless but subsequently under the influence of air oxygen, a yellow or brown deposit is formed, the color of which is derived from iron compounds. It often happens that beverage ageing in wooden barrels has black coloration, which is affected by iron compounds and tannin substances. The presence of higher metal contents imparts the distillates a bitter - astringent taste. Such distillates can be redistilled. Aluminum and zinc, apart from iron and copper, can impart a bitter taste to the beverage.[7]

Plum brandy is primarily produced in Slavic regions of central and eastern Europe, both commercially as well as by many households on an informal, home-made basis. Primary producing nations include the Czech Republic, Lithuania, Slovenia, Slovakia, Bosnia and Herzegovina, Poland, Hungary, Bulgaria, Romania, Croatia, and Serbia.[8] Similar plum brandies are also produced in Switzerland, France, the United States, and Canada, but marketed under other names, such as brandy, *Pflümli*, or *eau de vie*.

Plum brandy, as a distillate of *Prunus* crop plum fermented must, apart from the main constituents – ethanol and water, contains numerous ingredients the amounts of which vary within an average of 0.5–1.0 % depending on the raw material content, the way in which the fermentation was performed and the manner in which the distillation was conducted. Apart from numerous valued components, plum brandy can also contain some undesirable substances. These refer, first of all, to cyanides, ethyl carbamate and methanol.[9]

Various techniques have been used to quantify the contents of trace metals in highly alcoholic beverages, including flame atomic absorption spectrometry, FAAS[2,7,10–17] graphite furnace atomic absorption spectrometry, GFAAS,[7,11,12,15] electrothermal atomization-atomic absorption spectrometry, ETA-AAS,[18,19] flow injection-hydride generation-atomic absorption spectrometry, FI-HG-AAS,[20,21] anodic stripping voltammetry, ASV,[22] differential pulse voltammetry, DPV,[13] differential pulse anodic stripping voltammetry, DPASV,[13] inductively coupled plasma-optical emission spectrometry, ICP-OES,[23–25] inductively coupled plasma-atomic emission spectrometry, ICP-AES,[26,27] inductively coupled plasma mass spectrometry, ICP-MS,[17,28,29] and total reflection X-ray fluorescence spectrometry, TXRF.[30]

Analytical methods frequently require sample pre-concentration and/or pretreatment for the destruction of the organic matrix, such as wet digestion, dry ashing, and microwave oven dissolution.[31]

Plum brandy, the so-called Šljivovica, is the most popular distilled spirit in Serbia. The aim of the present paper was to determine the heavy metal content of samples of old Serbian plum brandy in order to characterize them and evaluate human exposure.

EXPERIMENTAL

Instrumentation

The determination of the As content in plum brandies was performed using an atomic absorption spectrophotometer (AAS) equipped with an air–acetylene burner and a hydride generation unit Shimadzu AA-680, with D_2 correction for background radiation. The contents of Cu, Zn, Fe, Mn, Pb and Cd in the plum brandies were determined using an atomic absorption spectrophotometer (Pye Unicam SP 192). Hollow-cathode lamps were used to determine the heavy metals Cu (wavelength 324.75 nm, slit width 0.4 nm), Zn (wavelength 213.86 nm, slit width 0.4 nm), Fe (wavelength 248.33 nm, slit width 0.4 nm), Mn (wavelength 279.48 nm, slit width 0.4 nm), Pb (wavelength 217.00 nm, slit width 0.4 nm), Cd (wavelength 228.80 nm, slit width 0.4 nm) and the metalloid As (wavelength 193.7 nm, slit width 0.8 nm).

The pH values of the plum brandies were determined using a PHS-3BW pH/mV/ /temperature meter (Shanghai Benson Instrument Co.).

Chemicals and reagents

Distilled or deionized water (conductivity max. 1 μS cm^{-1}) was used. Nitric acid (65 %), ethanol (96 %), magnesium nitrate hexahydrate (10 % ethanolic solution), hydrochloric acid (37 %), potassium iodide (40 %), sodium hydroxide and sodium borohydride solution (1.25 g NaOH and 1 g $NaBH_4$ dissolved in 250 mL H_2O), and ascorbic acid (5 %) were used in the mineralization and preparation of samples. All were of analytical grade and purchased from Merck (Darmstadt, Germany).

Stock standard solutions (1000 mg L^{-1}) of arsenic, lead, cadmium, copper, zinc, iron and manganese were supplied by Carlo Erba (Italy). The working standard solutions were freshly prepared by suitable dilution of the respective stock solutions. The employed glassware was washed in boiling nitric acid (30 %) for a 15 min and thoroughly rinsed with distilled or deionized water before use.

Standard pH buffers (4.01, 7.00 and 10.01) were supplied by Labprocess (Spain).

Samples

Thirty-one Serbian plum brandies of different ages and origin, 25 aged in oak wood casks and 6 aged in mulberry wood casks, were analyzed. The pH and ethanol contents of the samples were determined (Table I).

Table I. Mean values of Cu, Zn, Fe and Mn concentrations in Šljivovica plum brandies of various ages from oak barrels and the coefficient of correlation (*r*) between the parameters

Age groups of Šljivovica plum brandies from oak barrels	Average age of Šljivovica plum brandies, *y*±*SD*	Mean values of the metal concentrations, (*c*±*SD*) / mg L^{-1}			
		Cu	Zn	Fe	Mn
3 years (*n* = 1)[a]	3.0	0.11	0.08	0.67	0.05
8–9 years (*n* = 6)	8.3±0.5	3.05±2.13	0.75±1.35	1.30±2.38	0.05±0.04
11–18 years (*n* = 11)	14.1±2.0	3.54±1.61	0.42±0.37	0.73±0.63	0.26±0.56
23–28 years (*n* = 3)	26.0±2.6	9.04±2.62	0.64±0.08	2.29±0.54	2.63±0.89
r		0.982	0.542	0.833	0.917

[a] *n* – Number of samples in each group

Sample preparation. In 10 mL aliquot of a plum brandy sample was added 10 mL of 10 % an ethanolic solution of magnesium nitrate.[32] The sample was then dried and caramelized by heating carefully to a maximum of 250 °C. Subsequently, the sample was annealed for 12 h in an oven programmed to 450 °C at a rate of 3 °C min^{-1}.

After destruction and annealing the sample was cooled and dressed with a 4 mL solution of HNO$_3$ (1:3). After evaporation to dryness, the sample was re-annealed for 1 h at 450 °C. Thereafter, the residue was quantitatively transferred to a 25-mL volumetric flask with 2 M HCl and made up to the mark with the same solution. This solution was used to determine the contents of metals (Cu, Zn, Fe, Mn, Pb and Cd). For the determination of As, 5.0 mL of solution was taken, 1.0 mL of 40 % KI and 1.0 mL of 0.5 % ascorbic acid in water were added and the mixture was diluted with 2 M HCl to 25 mL in a volumetric flask. The solution was left in the dark for 50 min. prior to AAS analysis by the hydride technique.

Calibration and analytical performance data

For quantification of Zn and Cd, calibration curves were constructed in the concentration range 0.20–2.00 mg L^{-1}, and for Pb, Cu, Zn, Fe and Mn in the range 0.20–8.00 mg L^{-1}, while the calibration curve for As was in the range 0.002–0.010 mg L^{-1}. The correlation coefficients (*r*) of the linear fittings to the calibration points (*n* = 7) were greater than 0.995 for all element. Evaluation of the limits of detection and quantification was performed by 10 measurements of the blank. Considering the standard deviation of the blank (S_{blank}) and the slope of the calibration curve (*b*), limit of detection (*LOD*) and limit of quantification (*LOQ*) were calculated as $3S_{\text{blank}}/b$ and $10S_{\text{blank}}/b$, respectively. The *LOD* and *LOQ*, expressed in mg L^{-1} of plum brandy were, respectively: 0.006 and 0.02 for Zn and Cd, 0.024 and 0.08 for Fe, 0.009 and 0.03 for Mn, 0.012 and 0.04 for Cu, 0.096 and 0.32 for Pb and 0.003 and 0.10 for As.

The accuracy of the method was confirmed by recovery assays. Sample aliquots of 10 mL of the same Serbian old plum brandy (*n* = 5) were fortified with 20 µg of each metal and

1 μg of arsenic. The average recovery for each metal was calculated and the values ranged from 94.2 to 103.0 %, while the average recovery for arsenic was 104.0±5.5 %. Concerning the concentrations of each analyte in analyzed samples, the obtained recoveries were within the expected range: 80–110 %. The precision was obtained from the experiments of accuracy and was expressed as the relative standard deviation (*RSD*). According to the concentrations levels of metals and arsenic in fortified samples of plum brandy, the recommended *RSD* values are lower than 11 and 15 %, respectively.[33] The determined *RSD* values for each metal and arsenic fulfilled thee requirements. The recovery±precision (%) for the studied elements were 103.0±0.7 for Zn, 101.9±1.5 for Cd, 99.7±6.6 for Fe, 100.6±0.5 for Mn, 94.2±9.2 for Cu, 99.0±1.1 for Pb and 104.0±5.5 for As.

Statistical analysis

Software SPSS 10.0 for Windows was applied for the statistical analysis of the results. As, Pb and Cd exhibited a high number of not detected or quantified cases. In order to avoid misleading conclusions, these cases were rejected. Moreover, linear regression analysis was further used to determine a regression equation to predict the age of Šljivovica plum brandies according to their content of heavy metals.

RESULTS AND DISCUSSION

The general characteristics of the 31 samples of Serbian plum brandy and the results of the determination of the metals and As are given in Table II. The alcoholic degree ranged within 36.33–49.48 vol. %, while the pH values ranged from 3.61 to 5.12.

It can be concluded from Table II that 74 % of the analyzed Šljivovica plum brandies ($n = 31$) contained below 0.010 mg L^{-1} of As, while 8 brandies contain it at the limit level of the quantification method (mean 0.01±0.01 mg L^{-1}). Lead was quantified only in Šljivovica sample 23, while it was not detected in the others. The Cd content in all plum brandies was below 0.02 mg L^{-1}. Zn was quantified in approximately 90 % of samples and its content varied from 0.06 to 3.50 mg L^{-1} (mean value of all plum brandies: 0.44±0.63 mg L^{-1}). The Fe concentration in the Serbian plum brandies ranged from 0.20 to 7.31 mg L^{-1} (total mean: 1.17±1.62 mg L^{-1}) and was quantified in approximately 77 % of the samples. Mn content ranged from 0.05 to 3.65 mg L^{-1} (total mean: 0.38±0.87 mg L^{-1}) and was present in approximately 45 % of the samples. The highest average metal contents was observed for Cu, ranging from 0.11–11.17 mg L^{-1} (total mean: 3.81±2.49 mg L^{-1}).

The determinations of heavy metals and arsenic in Serbian plum brandies is of great importance from toxicological and organoleptic points of view The correct knowledge of these parameters is required by the current Serbian regulations for the levels of pesticides, metals and metalloids and other toxic substances, chemotherapeutics, anabolics and other substances in foodstuffs,[34] which govern the maximum allowable concentration (*MAC*, mg L^{-1}) of lead (0.5 mg L^{-1}), zinc (2 mg L^{-1}), arsenic (10 mg L^{-1}) and copper (10 mg L^{-1}) in fruit brandies. In Šljivovica 2, the copper concentration exceeded the prescribed legal level and in Šlji-

TABLE II. Content of metals and arsenic (mg L^{-1}) in samples of plum brandies (Šljivovica)

Sample code	Plum variety	Type of barrel	Type/year of production	Plum brandy age, years	EtOH vol. %	pH value	As[a]	Pb[b]	Cd[a]	Cu	Zn[a]	Fe[a]	Mn[a]
1	Požegača + Crvena ranka	Oak	Homemade/1979.	27	38.96	3.92	0.01	*LOD*	*LOQ*	9.84	0.65	1.96	2.23
2	Požegača	Oak	Homemade/1983	23	37.62	3.88	*LOQ*	*LOD*	*LOQ*	11.17	0.71	2.00	2.02
3	Crvena ranka + Plavac	Oak	Homemade/1993	13	45.99	3.69	*LOQ*	*LOD*	*LOQ*	3.91	*LOQ*	0.83	*LOQ*
4	Mixed varieties	Oak	Industrial/1997	9	42.88	4.55	*LOQ*	*LOD*	*LOQ*	0.94	0.17	*LOQ*	0.09
5	Mixed varieties	Oak	Industrial /1992	14	38.64	3.89	*LOQ*	*LOD*	*LOQ*	5.42	1.00	1.29	1.67
6	Požegača	Mulberry	Homemade/1977	29	43.99	3.85	*LOQ*	*LOD*	*LOQ*	5.55	0.10	0.24	*LOQ*
7	Mixed varieties	Oak	Industrial/1995	11	44.60	4.02	*LOQ*	*LOD*	*LOQ*	4.30	0.79	0.97	0.18
8	Mixed varieties	Oak	Homemade/o.u.y.p.[c]	–	43.80	3.85	*LOQ*	*LOD*	*LOQ*	5.42	0.32	7.31	0.09
9	Požegača	Mulberry	Homemade/1991	15	47.39	3.61	*LOQ*	*LOD*	*LOQ*	2.50	*LOQ*	0.60	0.06
10	Požegača + Trnovača	Oak	Homemade/1991	15	45.56	3.64	*LOQ*	*LOD*	*LOQ*	4.14	0.38	2.11	*LOQ*
11	Mixed varieties	Oak	Homemade/1992	14	43.17	4.37	*LOQ*	*LOD*	*LOQ*	1.08	0.08	*LOQ*	*LOQ*
12	Crvena ranka	Mulberry	Homemade/o.u.y.p.	–	43.83	3.70	*LOQ*	*LOD*	*LOQ*	1.53	0.40	1.36	0.19
13	Mixed varieties	Oak	Industrial/o.u.y.p.	–	43.74	4.93	*LOQ*	*LOD*	*LOQ*	1.64	0.23	*LOQ*	*LOQ*
14	Mixed varieties	Oak	Industrial/1998	8	41.45	4.40	0.02	*LOD*	*LOQ*	6.43	3.50	*LOQ*	*LOQ*
15	Mixed varieties	Oak	Homemade/1992	14	38.50	3.89	*LOQ*	*LOD*	*LOQ*	2.14	0.10	*LOQ*	*LOQ*
16	Požegača	Oak	Homemade/1951	55	40.92	3.73	*LOQ*	*LOD*	*LOQ*	4.45	*LOQ*	1.46	*LOQ*
17	Mixed varieties	Oak	Homemade/1998	8	38.59	4.34	*LOQ*	*LOD*	*LOQ*	0.60	0.34	0.54	0.05
18	Požegača	Oak	Homemade/1991	15	41.17	4.52	*LOQ*	*LOD*	*LOQ*	2.85	0.99	0.86	*LOQ*

TABLE II. Continued

Sample code	Plum variety	Type of barrel	Type/year of production	Plum brandy age, years	EtOH vol. %	pH value	As[a]	Pb[b]	Cd[a]	Cu	Zn[a]	Fe[a]	Mn[a]
19	Mixed varieties	Mulberry	Homemade/o.u.y.p.	–	45.44	3.72	*LOQ*	*LOD*	*LOQ*	3.13	0.19	*LOQ*	*LOQ*
20	Mixed varieties	Oak	Homemade/1995	11	47.85	4.01	*LOQ*	*LOD*	*LOQ*	3.38	0.09	0.45	*LOQ*
21	Mixed varieties	Oak	Homemade/2003	3	41.20	5.12	*LOQ*	*LOD*	*LOQ*	0.11	0.08	0.67	0.05
22	Požegača	Oak	Homemade/o.u.y.p.	–	42.08	4.29	0.01	*LOD*	*LOQ*	1.50	0.20	0.47	0.24
23	Mixed varieties	Mulberry	Homemade/o.u.y.p.	–	36.33	3.62	*LOQ*	0.34	*LOQ*	4.03	0.65	0.97	0.08
24	Požegača + Čačanska rodna	Oak	Homemade/1997	9	49.48	3.48	*LOQ*	*LOD*	*LOQ*	3.52	0.06	0.20	0.07
25	Mixed varieties	Oak	Homemade/1990	16	43.10	3.81	0.01	*LOD*	*LOQ*	5.99	0.32	0.71	1.05
26	Požegača	Oak	Homemade/1978	28	42.67	3.83	*LOQ*	*LOD*	*LOQ*	6.11	0.56	2.92	3.65
27	Crvena ranka	Oak	Homemade/1988	18	45.63	3.94	*LOQ*	*LOD*	*LOQ*	4.57	0.22	0.79	*LOQ*
28	Požegača + Čačanska rodna + Stenli	Oak	Industrial/1992	14	44.47	3.57	0.01	*LOD*	*LOQ*	1.13	0.61	*LOQ*	*LOQ*
29	Požegača	Oak	Homemade/1998	8	45.00	3.68	0.02	*LOD*	*LOQ*	3.07	0.24	6.11	0.07
30	Požegača	Oak	Homemade/1998	8	44.95	3.76	0.01	*LOD*	*LOQ*	3.75	0.20	0.95	*LOQ*
31	Crvena ranka	Mulberry	Homemade/1997	9	44.60	3.88	0.02	*LOD*	*LOQ*	3.80	0.36	0.64	0.09

[a] *LOQ* – concentration of arsenic or metal below the respective limit of quantification; [b] *LOD* – concentrations of lead below the limit of detection; [c] o.u.y.p. – old, unknown year of production

vovica 14, the content of Zn was higher than the *MAC* value. Furthermore, internationalization of Serbian Šljivovica and its acceptance as a competitive brand product has led to the necessity for the fulfillment of certain official regulation of other countries. The Mexican Official Norm regulates the concentrations of four metals/metalloids in alcoholic beverages, namely copper (2.0 mg L^{-1}), lead (0.5 mg L^{-1}), arsenic (0.5 mg L^{-1}) and zinc (1.5 mg L^{-1}).[29] The average content of copper in Serbian Šljivovica is almost 2 times higher than the *MAC* value, but the other elements (Pb, As and Zn) are clearly below their respective *MAC* values. A Colombian norm standard establishes a maximum level of 1 mg L^{-1} for Cu in rum.[30] Only three samples of the Serbian Šljivovica investigated, 4, 17 and 21, are in consonance with these permitted levels. Venezuelan standard norm govern maximum allowable concentrations of iron (2 mg L^{-1}) and copper (4 mg L^{-1}) in whiskey.[30] Except for the four Serbian homemade Šljivovica (8, 10, 26 and 29), the content of Fe in this beverage was below the *MAC* value. Brazilian legislature[2] prescribes an upper limit of 5.0 mg $L^{-1}$for the content Cu of in alcoholic beverages. However, *MAC* values are not prescribed for other toxic metals (Zn, Pb and Cd). The Serbian plum brandies 1, 2, 5, 6, 8, 14, 25 and 26 did not meet the mentioned standards.

Analysis of certain elements in distilled spirits is of special interest due to their toxicity in the case of excessive intake.[21] It is considered that two doses of whiskey (100 mL) is the average daily intake for an adult consuming moderate amounts of alcoholic beverages.[2] When compared with identical dose of Serbian Šljivovica, the average daily intake of Cu would be 0.381±0.249 mg; Zn, 0.044±0.063 mg; Fe, 0.117±0.162 mg; Mn, 0.038±0.087 mg; Pb, 0.034 mg (for Šljivovica 23), As 0.001±0.001 mg and Cd < 0.002 mg. These amounts do not exceed the recommended allowable daily intake of trace elements, which means microgram to low milligram levels. Soufleros *et al*.[7,15] reported that the daily Cu intake in the diet of a healthy adult is from 1 to 3 mg. The World Health Organization (1996) has set an estimated minimum requirement for Cu at 0.6 mg day^{-1} for women and 0.7 mg day^{-1} for men. The amount of 0.300 mg is considered the upper limit level for Pb in the diet of an adult.[7] Hence, it could be concluded that the consumption of Serbian Šljivovica is not harmful from the aspect of heavy metal content to health if the daily intake does not exceed 50–100 mL.

According to the alcohol control database of the WHO, the average annual alcohol consumption for the EU in 2001 is given in as 9.2 L of pure alcohol per person. Information on the distribution is not available.[37] Given an average alcohol content of 43 vol. % for Serbian Šljivovica (Table II) corresponds to an annual Šljivovica consumption per person of approximately 21 L, which means 0.42 L $week^{-1}$ or 0.06 L day^{-1}.

In order to discuss the metal and arsenic intake through Serbian plum brandy consumption, an average intake of each element $person^{-1}$ $week^{-1}$ (AMI) was evaluated taking into account the present results of the content of the corresponding metal and As in Šljivovica, and the estimated alcohol consumption in the EU in 2001. The obtained values for the AMI (mg person^{-1} week^{-1}) were compared with the respective safety limits (mg person^{-1} week^{-1}) for the studied metals and As from the literature.[11] The estimated average metal intake of Cu would be 1.60±1.05 mg person^{-1} week^{-1}; Fe, 0.49±0.68 mg person^{-1} week^{-1}; Mn, 0.16±0.37 mg person^{-1} week^{-1}, Zn, 0.18±0.26 mg person^{-1} week^{-1}, As, 0.004±0.004 mg person^{-1} week^{-1}, Cd, < 0.008 mg person^{-1} week^{-1} and Pb, 0.14 mg person^{-1} week^{-1} (for Šljivovica 23). Literature data of the safety limits for the intake of the metals are Cu, 14–21 mg person^{-1} week^{-1}, Fe, 9800 mg person^{-1} week^{-1}, Cd, 0.49 mg person^{-1} week^{-1}, and Pb, 0.9 mg person^{-1} week^{-1}, and for As, 1.05 mg person^{-1} week^{-1}.[11] It could be noticed that Serbian Šljivovica plum brandy has no significant contribution to the total intake of these elements for moderate drinkers.

Motounet *et al*.[38] found that distillates with the highest Cu content contained the highest concentrations of acids and as a result the lowest pH values. Furthermore, Adam *et al*.[39] quoted that the acidity of the to be distilled liquor may be important as a source of copper (*e.g*., in whisky), since more acidic beverages tend to contain more Cu.[40] The correlation between copper concentration and pH value (Table II) in Serbian Šljivovica was slightly negative (r = –0.34), as shown in Fig. 1.

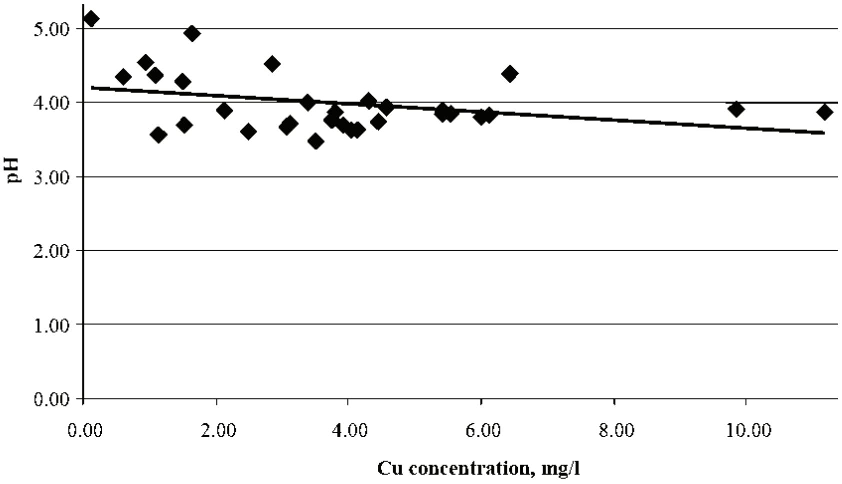

Fig. 1. Correlation between pH value and Cu concentration in Serbian Šljivovica plum brandies.

To examine the effects of commercial and homemade production, as well as the type of barrel (oak and mulberry) used for ageing the plum brandies on the metal concentrations, the plum brandies were arranged into four groups: commercial and homemade, from oak and mulberry barrels. The mean values of metal concentrations (Cu, Zn, Fe and Mn) in the mentioned groups are given in Table III.

TABLE III. Average content of metals±*SD* (mg L^{-1}) in commercial and homemade Serbian Šljivovica plum brandies, and in Šljivovica plum brandies from oak and mulberry barrels

Metal	Commercial Šljivovica (n = 6)	Homemade Šljivovica (n = 25)	Šljivovica from oak barrels (n = 25)	Šljivovica from mulberry barrels (n = 6)
Cu	3.3±2.4	3.9±2.6	3.9±2.7	3.4±1.4
Zn	1.1±1.2	0.3±0.3	0.5±0.7	0.3±0.2
Fe	0.4±0.6	1.4±1.8	1.3±1.8	0.6±0.5
Mn	0.3±0.7	0.4±0.9	0.5±0.9	0.07±0.07

According to *t*-test results, the differences between concentration levels of Cu, Zn, Fe and Mn in plum brandies aged in oak and plum brandies aged in mulberry barrels are not statistically significant, although the average contents of Mn and Fe were few times greater in the brandies aged in oak than in mulberry wood. On the other hand, statistically very significant differences (p = 0.0062) were found between the mean concentration levels of Zn in commercial and homemade Šljivovica.

A potential source of the higher concentration levels of zinc in commercial Šljivovica, except for the pot stills used for distillation and metallic receiving vessels, might also be attributed to contaminated water used to dilute the distillate.[7]

Dugo *et al.*[41] studied the effects of the duration of the ageing process on the contents of heavy metals (Cd, Cu, Pb and Zn) in gold and amber Marsala wines. The authors considered that the increase in metal concentrations with extension of the ageing process in oak barrels might be the result of extraction of inorganic elements, which are normally present in the wood. Rodushkin *et al.*[28] also reported that the concentrations of Ti, U, Al and Co in whiskies from Swedish retail shops showed a significant positive correlation with maturity. The main source of these elements in these whiskies was probably, time-dependent extraction from the oak containers.[28] Therefore, for each age group of the Šljivovica aged in oak barrels (except for "the youngest" comprising one sample) the mean values of the Cu, Zn, Fe and Mn concentrations are given in Table II. The results of the correlations between the mean values of the metal concentrations (Cu, Zn, Fe and Mn) and the average age (3–26) of the Šljivovica plum brandies are listed in Table III and shown in Fig. 2. The correlation coefficients (r values from 0.833 to 0.982) showed that the concentration levels of Cu, Fe and Mn are very well associated with ageing period of Šljivovica.

The linear regression analysis revealed that the concentration of copper is a highly significant predictor of the age of Serbian Šljivovica ($\beta = 0.982$, $p < 0.05$) as described by the following equation:

$$\text{Ageing period (years)} = 2.602\times\text{Concentration of Cu} + 2.610$$

where the concentration of Cu is expressed in mg L^{-1}. The adjusted $R^2 = 0.947$; the F ratio = 54.924; $p < 0.05$ and $DW = 3.100$. The Durbin–Watson test (DW) for autocorrelation was used to detect errors in the linear regression.[40] All these values indicate a very good reliability of the statistical model.

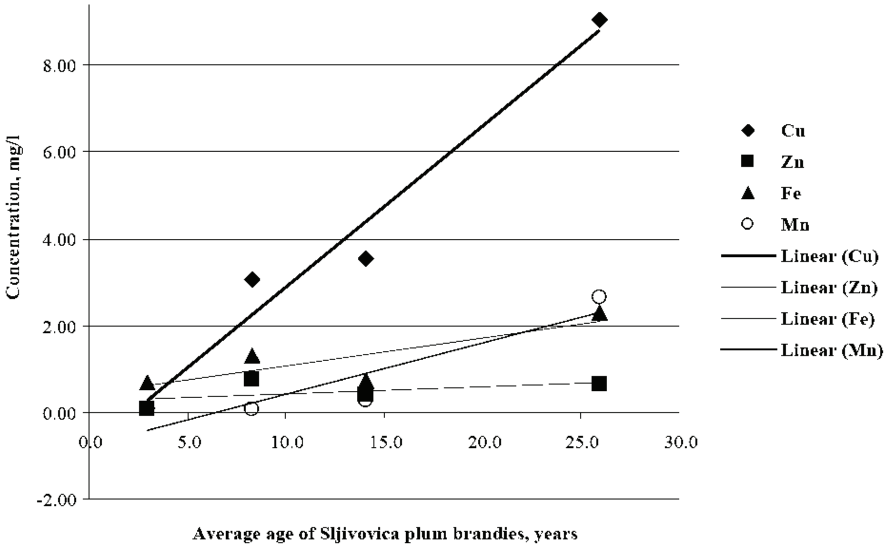

Fig. 2. Correlation between metal concentrations in Serbian Šljivovica plum brandies from oak barrels and average age of the brandies (3–26 years).

CONCLUSIONS

Knowledge about the inorganic profile of Serbian Šljivovica plum brandies is important for the control of heavy metals ion concentrations and as a contribution to the improvement of the quality of this national beverage.

The obtained results lead to the conclusion that the ageing time, *i.e.* ageing process and the origin (homemade or industrial) of Šljivovica plum brandies are the major factors that affect the concentrations of Cu, Mn, Fe and Zn in this Serbian beverage.

Some of the highly toxic elements, namely, Cd, As and Pb were almost absent (below limit level of the quantification method) in this beverage.

Acknowledgement. The authors acknowledge their gratitude to the Ministry of Education, Science and Technological Development of the Republic of Serbia for financial support (Project No. 172053).

ИЗВОД

САДРЖАЈ ТЕШКИХ МЕТАЛА У СТАРИМ СРПСКИМ РАКИЈАМА ШЉИВОВИЦАМА

МИРЈАНА БОНИЋ[1], ВЕЛЕ ТЕШЕВИЋ[2], НИНОСЛАВ НИКИЋЕВИЋ[3], ЈЕЛЕНА ЦВЕЈИЋ[4], СЛОБОДАН МИЛОСАВЉЕВИЋ[2], ВЛАТКА ВАЈС[5], БОРИС МАНДИЋ[2], ИВАН УРОШЕВИЋ[3], МИЛОВАН ВЕЛИЧКОВИЋ[3] и САША ЈОВАНИЋ[1]

[1]Институт за јавно здравље, Змај Јовина 30, 24000 Суботица, [2]Хемијки факултет, Универзитет у Београду, Студентски трг 16, 11000 Београд, [3]Пољопривредни факултет, Универзитет у Београду, Немањина 6, 11080 Земун, [4]Медицински факултет, Универзитет у Новом Саду, Хајдук Вељкова 3, 21000 Нови Сад, и [5]Институт за хемију, технологију и металургију, Универзитет у Београду, Његошева 12, 11000 Београд

Седам елемената: арсен, олово, кадмијум, бакар, цинк, гвожђе и манган су одређивани у 31 узорку српских ракија шљивовица применом технике атомске апсорпционе спектрометрије. Пламена атомска апсорпциона спектрометрија је коришћена за квантификацију бакра, гвожђа, цинка, олова, мангана и кадмијума, а хидридна техника атомске апсорпционе спектрометрије за квантификацију арсена. Измерена концентрација тешких метала и арсена је у складу са прописима Републике Србије, званичним прописима неких других земаља и другим сличним јаким алкохолним пићима. Количина микроелемената у максималном дневном и недељном уносу ракије шљивовице је одређена. Утицај производње (домаћа и индустијска), врсте дрвених буради (храст и дуд), трајање процеса сазревања на садржај цинка, бакра, гвожђа и мангана у шљивовицама, као и коефицијент корелације између садржаја бакра и pH је такође испитиван.

(Примљено 5. новембра 2012, ревидирано 5. фебруара 2013)

REFERENCES

1. P. Szefer, J. O. Nriagu, *Mineral Component in Foods*, CRC Press, Boca Raton, USA, 2007, p. 132
2. Y. Li. J. C. Van Loon, R. R. Barefoot, *Fresenius J. Anal. Chem.* **345** (1993) 467
3. R. F. Nascimento, C. W. B. Bezerra, S. M. B. Furuya, M. S. Schultz, L. R. Polastro, B. S. Lima Neto, D. W. Franco, *J. Food Compos. Anal.* **12** (1999) 17
4. S. Frias, J. E. Conde, J. J. Rodriguez-Bencomo, F. Garcia-Montelongo, J. P. Perez-Trujillo, *Talanta* **59** (2003) 335
5. E. A. Neves, A. Oliveira, A. P. Fernandes, J. A. Nobrega, *Food Chem.* **101** (2007) 33
6. R. Prado-Ramirez, V. Gonzales-Alvarez, C. Pelayo-Ortiz, N. Casillas, M. Estarron, H. E. Gomez-Hernandez, *Int. J. Food Sci. Tech.* **40** (2005) 701
7. E. H. Soufleros, A. S. Mygdalia, P. Natskoulis, *Food Chem.* **86** (2004) 625
8. W. Pokhlebkin, *The Raw Materials and Production Techniques of Other Principal Spirits of the World, A history of vodka*, Appendix 5, Verso Books, London, UK, 1992, p. 206
9. N. Nikicevic, V. Tesevic, *J. Agr. Sci.* **50** (2005) 49
10. F. F. Lopez, C. Cabrera, M. L. Lorenzo, M. C. Lopez, *Sci. Total Environ.* **220** (1998) 1
11. A. M. Camean, I. M. Moreno, M. Lopez-Artiguez, M. Repetto, A. G. Gonzalez, *Sci. Aliment.* **20** (2000) 433
12. A. M. Camean, I. M. Moreno, M. Lopez-Artiguez, M. Repetto, A. G. Gonzalez, *Talanta* **54** (2001) 53
13. V. S. Ijeri, A. K. Srivastava, *Anal. Sci.* **17** (2001) 605
14. S. M. Bettin, W. D. Isique, D. W. Franco, M. L. Andersen, S. Knudsen, L. H. Skibsted, *Eur. Food Res. Technol.* **215** (2002) 169
15. E. H. Soufleros, A. S. Mygdalia, P. Natskoulis, *J. Food Compos. Anal.* **18** (2005) 699

16. R. R. Madrera, B. S. Valles, A. G. Hevia, O. G. Fernandez, N. F. Tascon, J. J. M. Alonso, *J. Agr. Food Chem.* **54** (2006) 9992
17. D. W. Lachenmeier, D. Nathan-Maister, T. A. Breaux, E. M. Sohnius, K. Schoeberl, T. Kuballa, *J. Agr. Food Chem.* **56** (2008) 3073
18. C. Mena, C. Cabrera, M. L. Lorenzo, M. C. Lopez, *Sci. Total Environ.* **181** (1996) 201
19. M. Olalla, M. C. Gonzalez, C. Cabrera, M. C. Lopez, *J. AOAC Int.* **83** (2000) 189
20. C. Mena, C. Cabrera, M. L. Lorenzo, M. C. Lopez, *J. Agr. Food Chem.* **45** (1997) 1812
21. S. Chanthai, N. Suwamat, C. Ruangviriyachai, P. Danvirutai, *ASEAN Food J.* **14** (2007) 181
22. P. J. S. Barbeira, N. R. Stradiotto, *Talanta* **44** (1997) 185
23. R. V. Reche, A. F. L. Neto, A. A. Da Silva, C. A. Galinaro, R. Z. De Osti, D. W. Franco, *J. Agr. Food Chem.* **55** (2007) 6603
24. O. M. Sampaio, R. V. Reche, D. W. Franco, *J. Agr. Food Chem.* **56** (2008) 1661
25. S. G. Ceballos-Magana, J. M. Jurado, M. J. Martin, F. Pablos, *J. Agr. Food Chem.* **57** (2009) 1372
26. R. Kokkinofta, P. V. Petrakis, T. Mavromoustakos, C. R. Theocharis, *J. Agr. Food Chem.* **51** (2003) 6233
27. D. R. Cardoso, L. G. Andrade-Sobrinho, A. F. Leite-Neto, R. V. Reche, W. D. Isique, M. M. C. Ferreira, B. S. Lima-Neto, D. W. Franco, *J. Agr. Food Chem.* **52** (2004) 3429
28. I. Rodushkin, F. Odman, P. K. Appelblad, *J. Food Compos. Anal.* **12** (1999) 243
29. C. R. Flores, J. A. L. Figueroa, K. Wrobel, K. Wrobel, *Eur. Food Res. Technol.* **228** (2009) 951
30. T. Capote, L. M. Marco, J. Alvarado, E. D. Greaves, *Spectrochim. Acta, Part B* **54** (1999) 1463
31. F. Salvo, L. L. Pera, G. D. Bella, M. Nicotina, G. Dugo, *J. Agr. Food Chem.* **51** (2003) 1090
32. M. T. Friend, C. A. Smith, D. Wishart, *At. Absorpt. Newsletter* **16** (1977) 46
33. H. Ludwig, *Validation and Qualification in Analytical laboratories*, 2nd ed., Informa healthcare, 2007 (http://www.labcompliance.com/tutorial/methods/default.aspx)
34. Official Gazette of FRY, No. 5/1992.
35. J. D. Bogden, L. M. Klevay, *Clinical Nutrition of the Essential Trace Elements and Mineral*: *The Guide for Health Professionals*, Humana Press, New Jersey, USA, 2000, p. 231
36. L. M. Gaetke, C. K. Chow, *Toxicology* **189** (2003) 147
37. S. S. Sadhra, A. D. Wheatley, H. J. Cross, *Sci. Total Environ.* **374** (2007) 223
38. P. Motounet, J. L. Escudier, C. Jouret, *Symposium International sur les eaux-de-vie traditionelles d'origine viticole*, (1991), Paris, France, 1991, p. 105
39. T. Adam, E. Duthie, J. Feldmann, *J. Inst. Brew.* **108** (2002) 459
40. J. G. Ibanez, A. Carreon-Alvarez, M. Barcena-Soto, N. Casillas, *J. Food. Compos. Anal.* **21** (2008) 672
41. G. Dugo, L. La Pera, T. M. Pellicano, G. Di Bella, M. D'Imperio, *Food Chem.* **91** (2005) 355.

Journal of the Serbian Chemical Society
JSCS-info@shd.org.rs • www.shd.org.rs/JSCS
J. Serb. Chem. Soc. *78* (7) 947–957 (2013)
JSCS–4472
UDC 542.9+547.57+547.551+546.732’742’562+
543.429.22:615.28–188
Original scientific paper

New complexes of Co(II), Ni(II) and Cu(II) with the Schiff base 2,2′-[(3,3′-dimethyl[1,1′-biphenyl]-4,4′-diylbis-(nitrilomethylidyne)]bis[6-methoxyphenol]

IONELA ALAN[1]*, ANGELA KRIZA[1], OLGUTA DRACEA[2] and NICOLAE STANICA[3]

[1] University of Bucharest, Faculty of Chemistry, Inorganic Chemistry Department, 23 Dumbrava Rosie Street, 020462 Bucharest, Romania, [2] “Cantacuzino” National Institute for Research in Microbiology and Immunology, 103 Spl. Independentei, 050096 Bucharest, Romania and [3] Ilie Murgulescu Institute of Physical Chemistry, Romanian Academy, 202 Spl. Independentei, 77208 Bucharest, Romania

(Received 13 June, revised 3 November 2012)

Abstract: The new 2,2′-[(3,3′-dimethyl[1,1′-biphenyl]-4,4′-diylbis(nitrilomethylidyne)]bis[6-methoxyphenol] (H_2L) Schiff base and its complexes with Co(II), Ni(II) and Cu(II) of the type [M(HL)Cl(H_2O)] (M = Co(II) or Cu(II)), $[M_2L(H_2O)_4]X_2$ (M = Co(II), X = ClO_4 and M = Cu(II), X = NO_3) and $[M_2L(CH_3COO)_2]$ (M=Co(II), Ni(II), Cu(II)) were synthesised. The ligand and complexes were characterized by elemental analysis, conductivity measurements, magnetic moments at room temperature, IR, NMR, UV–Vis-NIR, EPR spectra and thermogravimetric analysis. Mole ratios of 1:1 or 1:2 between the ligand and metal were determined from the elemental analysis results. Except for the perchlorate complex that behaved as an electrolyte, the other complexes are non-electrolytes. The spectral data suggested tetrahedral, pseudo-tetrahedral or square-planar stereochemistry, which was confirmed by the magnetic behaviour of complexes. The antimicrobial tests indicated fungicide effects for both the ligand and the complexes.

Keywords: Schiff base; *o*-tolidine; *o*-vanillin; EPR spectra; antimicrobial activity.

INTRODUCTION

Complexes with Schiff bases derived from aromatic diamines and aromatic aldehydes have been intensively studied due to their possible application in various fields.[1–6]

These complexes are also interesting as models for enzymes involved in several biochemical processes.[7,8] Many Schiff bases of this type and their com-

---

* Corresponding author. E-mail: ionelaalan@yahoo.com

doi: 10.2298/JSC120613121A

plexes with various metal ions were found to exhibit fungicidal, bactericidal, antimalarial and anticancer properties.[9,10]

Following previous research,[11] in this paper, data is presented concerning the synthesis and characterisation of Co(II), Ni(II), Cu(II) complexes with a new Schiff base obtained through *o*-tolidine (3,3′-dimethylbenzidine) condensation with *o*-vanillin (2-hydroxy-3-methoxybenzaldehyde) (Fig. 1). It is noteworthy that only a few papers with Schiff bases derived from *o*-tolidine are mentioned in the literature.[12,13]

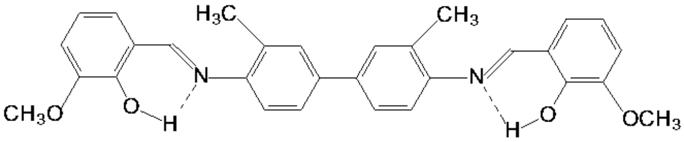

Fig. 1. Structure of the ligand (H_2L).

EXPERIMENTAL

Materials

Metal salts (Sigma–Aldrich), *o*-vanillin (Merck), *o*-tolidine (ICN Biomedicals) and triethylamine (Fluka) were used in the syntheses.

Synthesis of the ligand

The 2,2′-[(3,3′-dimethyl[1,1′-biphenyl]-4,4′-diylbis(nitrilomethylidyne)]bis[6-methoxyphenol] (H_2L) Schiff base was obtained by mixing an ethanolic solution of *o*-tolidine (0.01 mol in 50 mL ethanol) with an ethanolic solution of *o*-vanillin (0.02 mol in 50 mL ethanol), in the presence of acetic acid. The mixture was refluxed for 2 h. After cooling, the obtained precipitate was filtered, washed with and recrystallized from tetrahydrofuran. The yield was 72 %. The reddish–orange crystalline product was stable at room temperature and was non-hygroscopic.

Synthesis of the complexes

A solution of ligand (H_2L) (0.01 mol) in 50 mL tetrahydrofuran was mixed with an equal volume of an ethanolic solution containing 0.01 mol Co(II) or Cu(II) chloride to obtain complexes **1** and **5** according to the reaction:

$$MCl_2 + H_2L + H_2O \rightarrow [M(LH)Cl(H_2O)] + HCl \quad (1)$$

Complexes **2** and **6** were synthesised using a solution of 0.01 mol ligand in 50 mL tetrahydrofuran and either 50 mL of an ethanolic solution of Co(II) perchlorate (0.02 mol) or of Cu(II) nitrate (0.02 mol), respectively, according to:

$$2MX_2 + H_2L + 4H_2O \rightarrow [M_2L(H_2O)_4]X_2 + 2HX \quad (2)$$

The complexes **3**, **4** and **7** were synthesised using 50 mL of a tetrahydrofuran solution of ligand (0.01 mol) and a solution of 0.02 mol of Co(II), Ni(II) or Cu(II) acetate, respectively, in 50 mL of ethanol, according to:

$$2M(CH_3COO)_2 + H_2L \rightarrow [M_2L(CH_3COO)_2] + 2CH_3COOH \quad (3)$$

In all cases, the reaction mixture was refluxed at least 4 h and afterwards concentrated to half of the initial volume. The obtained precipitate was filtered, washed, and dried in a vacuum desiccator over anhydrous $CaCl_2$. The obtained complexes were solid, coloured, stable under atmospheric conditions and non-hygroscopic.

Techniques

The contents of the metal were determined volumetrically by complexometric methods for Ni(II) and Co(II) and by an iodometric method for Cu(II). The contents of N, C and H were measured with an ECS-40-10-Costeh microdosimeter, following drying at 105 °C. The melting points were determined using a Stuart Scientific SMP3 apparatus and no correction was applied. The molar conductivities were determined in acetone (**1**, **2** and **4**), ethanol (**3**) or DMF (**5** and **6**) (10^{-3} M) at room temperature using a Consort C533 conductometer. The IR spectra were recorded in KBr pellets, using a BioRad FTS-135 Fourier transform spectrometer in the range 4000–400 cm^{-1}. The electronic spectra were recorded on a Jasco V670 spectrophotometer, by the diffuse reflectance technique. The NMR spectra for the ligand were recorded in DMSO-d_6 on a Varian Gemini 300BB instrument operating at 300 MHz for ^1H and 75 MHz for ^{13}C. The magnetic susceptibilities were determined by the Faraday method and were corrected for atomic diamagnetism. The EPR spectra were recorded using a MiniScope MS200 type spectrometer. This was operated in the X-band (9.3 to 9.6 GHz) and it was provided with a rectangular TE_{102} resonance cavity. The thermogravimetric analysis was realised using a current Labsys 1200 Setaram derivatograph under a synthetic air flow of 16.67 $cm^3 min^{-1}$ at a heating rate of 10 °C min^{-1}. The microbial strains, isolated from various pathological products, were identified using a VITEK I automatic system. The VITEK cards for identifying and testing the antibiotic sensitivity (GNS-522) were inoculated and incubated according to the directions of the producer. The results were interpreted using the AMS R09.1 program.

Antimicrobial activity

The complexes **1**–**7** were tested to determine their *in vitro* antimicrobial activity using qualitative and quantitative analysis methods.[14] Reference microbial species were used for the tests. These included: the Gram-positive strain *Staphylococcus aureus* 1263, Gram-negative bacteria (*Klebsiella pneumoniae* 1204, *Escherichia coli* IC 13147 and *Pseudomonas aeruginosa* 1246) and the fungal strain *Candida albicans* LS, isolated from various clinical samples. The quality control was performed by the simultaneous testing of the antimicrobial activity on the above-mentioned strains and on the reference strains: *Klebsiella pneumoniae* IC 13420, *E. coli* IC 13529, *S. aureus* IC 13204, *P.aeruginosa* IC 13202 and *C. albicans* IC 249.

The qualitative screening of the action of the synthesized compounds on the bacteria and fungi was realised by two diffusion methods, adapted to the diffusimetric method. The first method consisted of impregnating filter paper disks with a solution a compound in DMSO (1000 μg mL^{-1}). The second method consisted of the qualitative determination of the antimicrobial effect of a compound spot distributed on a microbial culture-seeded medium.

The used solvent dimethyl sulphoxide (DMSO) was also tested using the same two methods in order to emphasize the potential antimicrobial activity.

For the quantitative determination of the antimicrobial activity of the ligand and of the complexes, the binary microdilution method in a liquid medium was applied (yeast extract–peptone–glycerol (YPG) medium for the fungi), using 96-well plates, in order to determine the minimal inhibitory concentration (*MIC*) values. In this manner, binary serial dilutions of stock solutions of the test compounds in DMSO (1000 µg mL^{-1}) and of a fluconazole solution (concentration 128 µg mL^{-1}), as a control solution for the fungi, were obtained.

For the qualitative and quantitative screening, the plates were incubated for 24 h at 37 °C for the bacteria and for 48 h at 28 °C for the fungi. The results were obtained by macroscopic observation.

RESULTS AND DISCUSSION

The tetradentate ligand 2,2′-[(3,3′-dimethyl[1,1′-biphenyl]-4,4′-diylbis(nitrilomethylidyne)]bis[6-methoxyphenol] (H_2L), having a divergent ON–NO donor atom set, was synthesized by 1:2 condensation of *o*-tolidine with *o*-vanillin in ethanol. The analytic and spectral data for H_2L are presented in the Supplementary material to this paper.

The seven complexes of the prepared ligand with Co, Ni and Cu are given in Table I, together with their solubilities in several organic solvents. The complexes **1**–**7** were characterised based on chemical and thermal analyses, IR, UV–Vis–NIR and EPR spectral data, as well as magnetic moments at room temperature and molar conductivity.

TABLE I. The prepared complexes **1–7** and their solubility is some organic solvents

Compound	No.	Soluble in
H_2L		THF, DMSO, CH_2Cl_2
$[Co(LH)Cl(H_2O)]$	**1**	Acetone, DMSO, CH_2Cl_2
$[Co_2L(H_2O)_4](ClO_4)_2$	**2**	Acetone, DMSO, CH_2Cl_2
$[Co_2L(CH_3COO)_2]$	**3**	Acetone, DMSO, EtOH
$[Ni_2L(CH_3COO)_2]$	**4**	Acetone, DMF, DMSO
$[Cu(HL)Cl(H_2O)]$	**5**	DMF, DMSO
$[Cu_2L(H_2O)_4](NO_3)_2$	**6**	DMF, DMSO
$[Cu_2L(CH_3COO)_2]\cdot H_2O$	**7**	DMSO

The physical, analytical and spectral data of the complexes are given in the Supplementary material to this paper.

NMR spectra of the ligand

The formation of the Schiff base was confirmed by the ^{1}H-NMR and ^{13}C-NMR spectra of the ligand. In the ^{1}H-NMR spectrum, signals for methylene protons are present at 2.42 (CH_3) and 3.83 ppm (OCH_3) and the aromatic protons appear between 7.48 and 7.70 ppm for the fragment derived from the amine. The aromatic protons from the fragment derived from the 3-methoxysalicylaldehyde generate a doublet signal in the range of 6.93 and 7.26 ppm, while the signal of the proton from the azomethine group appears as singlet at 8.96 ppm. In addition, the ^{13}C-NMR spectrum contains signals which are characteristic for carbon atoms derived from both the amine and the aromatic aldehyde, noting that the characteristic signal for the azomethinic carbon appears at 162.87 ppm. The signals located at 18.03 and 55.91 ppm in the ^{13}C-NMR spectrum correspond to the carbon atoms from methyl group of the amine and to the methoxy group of the 3-methoxysalicylaldehyde, respectively.

IR spectra

The most important bands in the IR spectra of the ligand (H_2L) and complexes **1**–**7** are presented in the Supplementary material to this paper. The Schiff base spectrum exhibits two very intense bands, one at 1615 cm^{-1}, which can be attributed to the stretching vibration of the azomethine group ν(C=N), and another one at 1253 cm^{-1}, corresponding to the phenolic group ν(C–O).[15] The bands at 3439 and 2780 cm^{-1} may be due to the vibration of intermolecular hydrogen bonds.[15,16]

The stretching frequencies ν(C=N) and ν(C–O) show significant shifts towards lower values within the IR spectra of complexes **1**–**7** compared to the corresponding band in the spectrum of H_2L. This means that both the azomethine nitrogen and the phenolic oxygen atoms are involved in the coordination.[17]

In the spectra of complexes **1** and **5**, the bands corresponding to the azomethine group appear split into two intense bands, one shifted to higher values and one to lower values, as compared to the corresponding band of the ligand, which suggests that the two groups are not identical within the complexes. Moreover, in the spectra of **1** and **5**, a band at about 2780 cm^{-1}, which is also present in the spectrum of the ligand, appears, which is probably due to the existence of intermolecular hydrogen bonds. However, this band is absent in the spectra of complexes **2**–**4**, **6** and **7**. These features of the IR spectra of the complexes **1** and **5**, supported by the elemental analysis data, suggest that only one azomethine group is involved in coordination.[12,16]

In the spectrum of complex **2**, a very intense band at 1102 cm^{-1} (ν_3) and a weak one at 623 cm^{-1} (ν_4) indicate that the perchlorate ion is present as a free ion.[18] For complexes **3**, **4** and **7**, the $\Delta\nu = \nu_{asym}(COO) - \nu_{sym}(COO)$ values are 107, 113 and 101 cm^{-1}, respectively. According to the literature,[15,19] values lower than 164 cm^{-1} suggest that the acetate group is coordinated in a bidentate form. In the spectrum of complex **6**, a very intense band appears at 1384 cm^{-1}, which can be assigned to the ν_3 vibration mode of nitrate present as a free ion.[15,20]

In the spectra of all complexes, the broader bands that appear in the region 3330–3450 cm^{-1} can be assigned to ν(OH) for water molecules. The presence of some water molecules coordinated in complexes **1**, **2**, **5** and **6** is supported by the presence of a new band in the range of 700–900 cm^{-1}, which can be assigned to $\delta_w(H_2O)$.[21] New bands of low intensity in the range 400–600 cm^{-1} can be assigned to the stretching vibrations ν(M–O) and ν(M–N).[22]

UV–Vis–NIR spectra and magnetic moments

The UV–Vis–NIR spectral data for the ligand and the complexes are given in the Supplementary material to this paper. The electronic spectrum of the ligand exhibited three bands at 42,500, 25,000 and 19,800 cm^{-1}, which can be assigned to $\pi \rightarrow \pi^*$ intraligand transitions.[23] These bands also appeared in the spectra of the complexes.

The spectrum of complex **1**, in addition to a $\pi \rightarrow \pi^*$ transition at 25,970 cm^{-1}, showed bands at 15,380 and at 8,130, 7,220 cm^{-1}, which can be assigned to d–d transitions $^4A_2 \rightarrow {}^4T_1(P)$ and $^4A_2 \rightarrow {}^4T_1(F)$, respectively, for Co(II) in a tetrahedral environment. The spectrum of complex **2** also contained a $\pi \rightarrow \pi^*$ transition at 25,970 cm^{-1} with further bands at 17,240 and 13,700 and at 8,700 and 7,170 cm^{-1} resulting from d–d transitions. The corresponding transitions for complex **3** appeared at 20,000, 18,520, 10,580 and 7,200 cm^{-1}, respectively. It should be mentioned that the bands occurring in the visible and infrared regions, and assigned to the spin-allowed transitions for a $3d^7$ ion were split into two components. Due to the different nature of donor atoms that generate a distorted tetrahedral stereochemistry, a decrease of the symmetry and an increase in the ^4T levels degeneracy occurs. The values of spectral parameters $10Dq$, B and β for the Co complexes, presented in Table II, are in agreement with a pseudo-tetrahedral stereochemistry. It can be noticed that the values of the spectral parameters for the cobalt complexes are similar. The values of the magnetic moments of Co(II) complexes, presented in Table II, were between 4.11 and 4.84 μ_B, which are characteristic for Co(II) with a pseudo-tetrahedral geometry.[23,24]

TABLE II. Crystal field parameters and magnetic moments for complexes **1**–**4**

Compound	Crystal field parameters			μ_{eff} / μ_B
	$10Dq$ / cm^{-1}	B	β	
$[Co(HL)Cl(H_2O)]$ (**1**)	4494	734	0.75	4.11
$[Co_2L(H_2O)_4](ClO_4)_2$ (**2**)	4720	722	0.74	4.57
$[Co_2L(CH_3COO)_2]$ (**3**)	4589	853	0.87	4.84
$[Ni_2L(CH_3COO)_2]$ (**4**)	–	–	–	Dia.

For complex **4**, in addition to the $\pi \rightarrow \pi^*$ intraligand transition at 35,710 cm^{-1}, the two bands at 19,230 and 15,750 cm^{-1} can be assigned to the $^1A_{1g} \rightarrow {}^1B_{1g}$ and $^1A_{1g} \rightarrow {}^1B_{2g}$ transitions, respectively. This spectrum suggests the presence of a square-planar stereochemistry for the Ni(II) ion, which was confirmed by the diamagnetic behaviour of this compound.[23,25]

The spectra of the Cu(II) complexes **5**–**7** showed a $\pi \rightarrow \pi^*$ transition at 25,640, 25,640 and 25,970 cm^{-1}, respectively, and in the visible range, a wide and asymmetric band centred at 12,660, 14,285 and 13,245 cm^{-1}, respectively, corresponding to the $d_{xy} \rightarrow d_{z^2,x^2-y^2}$ transition. In the case of compounds **6** and **7**, a shoulder appears at lower wavenumbers corresponding to the $d_{xy} \rightarrow d_{xz,yz}$ transition. The presence of absorption maxima at lower energy indicates a large number of oxygen atoms in the donor atoms set together with nitrogen atoms, for a pseudo-tetrahedral stereochemistry.[26] The magnetic moment values for complexes **5**–**7** were, respectively, 2.12, 1.97 and 2.03 μ_B, which are characteristic of metal ions with a d^9 configuration and one unpaired electron.[23,27]

EPR spectra

The EPR spectra of the Cu complexes as powders were recorded both at room temperature (293 K) and at liquid nitrogen temperature (77 K). The signals obtained did not show any significant differences at these temperatures; hence, the geometry around the copper ion was not affected by cooling. The EPR signals of these samples measured at room temperature are specific for Cu(II) ions with a tetrahedral or pseudo-tetrahedral geometry.

The signal of sample **5** was wide (about 300 G) and centred at g_0 = 2.117 and on cooling, its width decreased to 270 G and g_0 = 2.123[28] (Fig. 2).

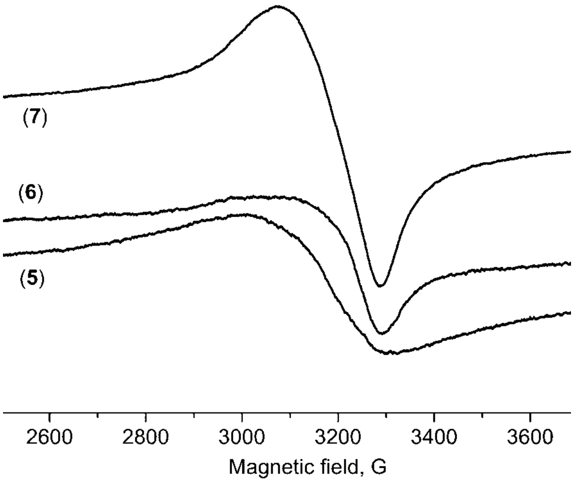

Fig. 2. EPR spectra of complexes **5**–**7** powders.

Complexes **6** and **7** exhibited an asymmetric signal (Fig. 2), significantly expanded in the lower field area, which indicates axial distortion with a tendency of resolving the hyperfine structure, due to the interaction of the unpaired electron with the nuclear spin of copper.

This tendency, determined by the nuclear electron-spin interaction, was more noticeable in the spectrum of sample **6**, especially at 77 K, when the signal was more intense, but the split value could not be determined (probably $A_{//} \approx 150$ G). The asymmetry was also well emphasized in the derivative signals (d^2 represents the second derivative of the absorption curve).[29] The g_0 parameter, corresponding to the spectrum intersection with the baseline, had a value (2.102±0.01) for **6** and (2.092±0.001) for **7**, both at room temperature and at 77 K (Fig. 3). The peak widths were within the range 200 to 250 G.[30,31]

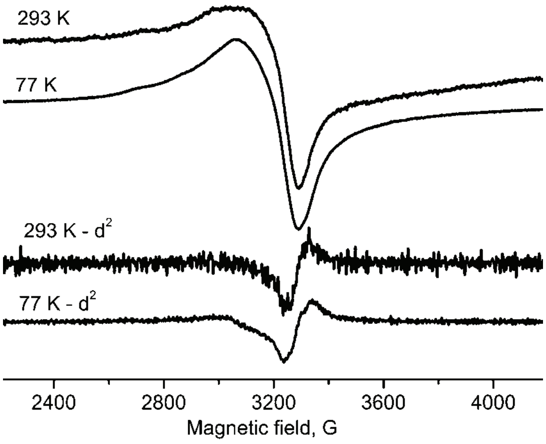

Fig. 3. The EPR spectra of the sample **6** powder registered at 293 K and 77 K with the signal derivative (d^2).

Thermal analysis

Thermal decomposition the complexes **1** and **7** under air was studied in order to determine the presence and nature of water molecules. The thermogravimetric curves show two major decomposition stages (Table III).

TABLE III. Thermal analysis data for the complexes **1** and **7**

Compound	Temperature range °C	Mass loss, % Exp.	Mass loss, % Calcd.	Processes
[Co(HL)Cl(H$_2$O)] (**1**)	100–180	3.40	3.08	Dehydration
	180–590	86.13	86.15	Oxidative degradation of the ligand
	590–800	12.47	12.77	Residue Co$_3$O$_4$
[Cu$_2$L(CH$_3$COO)$_2$]·H$_2$O (**7**)	50–150	2.65	2.91	Dehydration
	150–490	86.64	85.98	Oxidative degradation of the ligand
	490–800	10.71	11.11	Residue CuO

The first stage corresponds to the elimination of crystallisation water and of coordinated water.

The second stage includes all the processes comprising the detachment of the ligand and of other groups from the metal ion, the removal of chlorine and ligand oxidation, finally resulting in the formation of the metal oxide as a residue.[32]

Based on these data, the water molecule can be considered as coordinated in complex **1** while it is crystallization water in complex **7**.[33]

Antimicrobial activity

The results showed that the ligand and the complexes have no antibacterial activity, but they are fungicidal. The ligand and complexes **2**, **3**, **6** and **7** exhibited the best inhibitory activity over the *Candida albicans* species. Therefore, the quantitative antimicrobial activity (*MIC* values in µg mL^{-1}) for the most active compounds were determined by measuring the diameters of the inhibition zone generated by the compounds on both the standard and clinically isolated multidrug resistant fungal strains.[34] The solvent (DMSO) had no antimicrobial activity, this fact representing a great advantage in the testing the complexes and the ligand, which are insoluble in water.[35]

The ligand and complexes **2** and **3** had a pronounced ability to destroy the fungi (*MIC* = 62.5 µg mL^{-1}), while complexes **6** and **7** exhibited poor fungicidal activity (*MIC* > 500 µg mL^{-1}). The *MIC* values of the Co(II) complexes were lower than those of the Cu(II) complexes, which suggests an influence of the metal ion on the capacity to inhibit the growth of the fungi.

CONCLUSIONS

The 2,2′-[(3,3′-dimethyl[1,1′-biphenyl]-4,4′-diylbis(nitrilomethylidyne)]bis-[6-methoxyphenol] (H_2L) ligand containing two donor centres was synthesised and characterised by spectral data. The ligand has tetradentate dianionic behaviour (N_2O_2) in all the complexes, except for the Co(II) and Cu(II) chloride complexes, where the ligand behaves as a bidentate monoanionic species (NO), according to the IR data. The ligand is able to coordinate the metal ions in a tetrahedral, pseudo-tetrahedral or square planar geometry, as indicated by the electronic, EPR and magnetic data. The antimicrobial activity of the complexes was tested and it was found that the ligand and its complexes have fungicidal activity. The structural formulas suggested for the complexes **1**–**7** are presented in Figs. 4–6, respectively.[36]

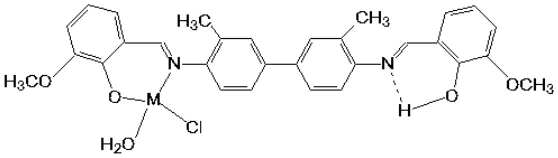

Fig. 4. Structural formulas proposed for the complexes [M(HL)Cl(H_2O)], where M = Co(II) (**1**) and Cu(II) (**5**).

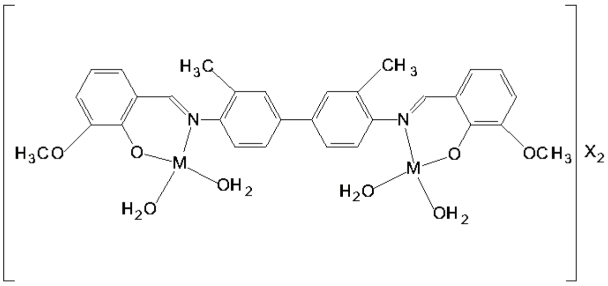

Fig. 5. Structural formulas proposed for the complexes [$M_2L(H_2O)_4$]X_2 , where M = Co(II), X = ClO_4 (**2**) and M = Cu(II), X = NO_3 (**6**).

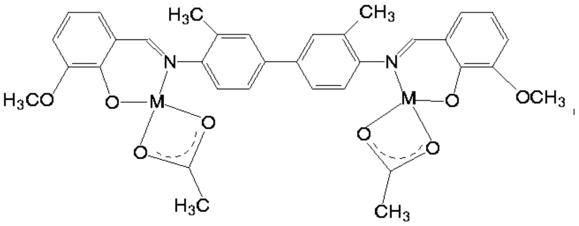

Fig. 6. Structural formulas proposed for the complexes $[M_2L(CH_3COO)_2]$, where M = Co(II) (**3**), Ni(II) (**4**) and Cu(II) (**7**).

SUPPLEMENTARY MATERIAL

Physical, analytic and spectral data for the ligand and complexes are available electronically from http://www.shd.org.rs/JSCS/, or from the corresponding author on request.

Acknowledgements. The authors would like to thank Dr Laura Almajan (1968–2012), University of Medicine and Pharmacy, Faculty of Pharmacy, Organic Chemistry Department, for providing the NMR spectra.

ИЗВОД

НОВИ КОМПЛЕКСИ CO(II), Ni(II) И Cu(II) СА ШИФОВОМ БАЗОМ 2,2′-[(3,3′-ДИМЕТИЛ[1,1′-БИФЕНИЛ]-4,4′-ДИИЛБИС(НИТРИЛОМЕТИЛИДИН)]-БИС[6-МЕТОКСИФЕНОЛ]

IONELA ALAN[1], ANGELA KRIZA[1], OLGUTA DRACEA[2] и NICOLAE STANICA[3]

[1]*University of Bucharest, Faculty of Chemistry, Inorganic Chemistry Department, 23 Dumbrava Rosie Street, 020462 Bucharest, Romania,* [2]*"Cantacuzino" National Institute for Research in Microbiology and Immunology, 103 Spl. Independentei, 050096 Bucharest, Romania и* [3]*Ilie Murgulescu, Institute of Physical Chemistry, Romanian Academy, 202 Spl. Independentei, 77208 Bucharest, Romania*

У овом раду, синтетисана је Шифова база, 2,2′-[(3,3′-диметил[1,1′-бифенил]-4,4′-диилбис(нитрилометилидин)]бис[6-метоксифенол] (H_2L), као и одговарајући комплекси Co(II), Ni(II) или Cu(II) опште формуле $[M(HL)Cl(H_2O)]$ (M = Co(II) и Cu(II)), $[M_2L(H_2O)_4]X_2$ (M = Co(II), X = ClO_4 и M = Cu(II), X = NO_3) и $[M_2L(CH_3COO)_2]$ (M = Co(II), Ni(II) или Cu(II)). Поред елементалне микроанализе, мерења проводљивости и магнетног момента на собној температури, за карактеризацију лиганда и комплекса су употребљене IR, NMR, UV–Vis–NIR и EPR спектроскопске методе, као и термогравиметријска анализа. Применом елементалне микроанализе одређен је у испитиваним комплексима 1:1 и 1:2 молски однос између лиганда и јона метала. Комплекс кобалта(II) са перхлоратом као контра-анјоном је електролит, док су остали испитивани комплекси неелектролити. На основу спектроскопских података, претпостављена је тетраедарска, псеудо-тетраедарска и квадратно-планарна геометрија синтетисаних комплекса. Антимикробна испитивања су показала да лиганд и одговарајући комплекси имају фунгицидну активност.

(Примљено 13. јуна, ревидирано 3. новембра 2012)

REFERENCES

1. A. Blagus, D. Cincic, T. Friscic, B. Kaitner, V. Stilinovic, *Maced. J. Chem. Chem. Eng.* **29** (2010) 117

2. K. Anuradha, R. Rajavel, *Int. J. Pharm. Technol.* **3** (2011) 2217
3. A. Ourari, L. Baameur, M. A. Khan, G. Bouet, *Electrochem. Commun.* **10** (2008) 1736
4. P. Roy, M. Nandi, M. Manassero, M. Ricco, M. Mazzani, A. Bhaumik, P. Banerejee, *Dalton Trans.* **54** (2009) 9543
5. A. Ourari, M. Khelafi, D. Aggoun, G. Bouet, M. A. Khan, *Adv. Phys. Chem.* **10** (2011) 1155
6. M. Shakiir, S. Khanam, M. Azam, M. Aatif, F. Firdaus, *J. Coord. Chem.* **64** (2011) 3158
7. T. Nakamura, K. Niwa, M. Fujiwara, T. Matsushita, *Chem. Lett.* **10** (1999) 1067
8. B. Dede, F. Karpicin, M. Cengiz, *J. Hazard Mat.* **163** (2009) 1148
9. Z. Susu, F. Alanyali, O. Artagan, S. Yuksel, *Int.. J. Pharm.* **7** (2011) 278
10. N. Raman, S. Parameswari, *Microbiology* **35** (2007) 65
11. I. Alan, A. Kriza, N. Stanica, C. Draghici, L. G. Almajan, *Rev. Chim.* **10** (2011) 975
12. M. A. Ali, H. A. Ayman, A. M. Tarek, H. M. Bassem, *J. Appl. Sci. Res.* **3 (**2007) 109
13. M. A. Ali, H. A. Ayman, A. M. Tarek, H. M. Bassem, *Transition Met. Chem.* **32** (2007) 461
14. O. Dracea, C. Larion, M. C. Chifiriuc, I. Raut, C. Limban, G. M. Niţulescu, C. D. Bădiceanu, A. M. Israil, *Rom. Arch. Microb. Imunol.* **67 (**2009) 92
15. K. Nakamoto, *Infrared and Raman spectra of inorganic coordination compounds*, Part B-*Application in coordination, organometallic and bioinorganic chemistry*, Wiley, New York, 2009
16. R. Srinisavan, I. Sougandi, K. Velevan, R. Venkastan, V. Babu, P. S. Rao, *Polyhedron* **23** (2004) 1115
17. J. Liu, B. Wu, B. Zhang, Y. Liu, *Turk J. Chem.* **30** (2006) 41
18. K. Rathore, K. R. R. Singh, H. B. Singh, *E-J. Chem.* **7** (2010) 566
19. A. Kriza, M. Dianu, C. Andronescu, A. Rogozea, M. Musuc, *J. Therm. Anal. Calorim.* **100 (**2010) 929
20. G. Rajendran, C. Amritha, R. J. Anto, *J. Serb. Chem. Soc.* **75** (2010) 749
21. M. Tatucu, P. Rotaru, I. Rau, C. Spinu, A. Kriza, *J. Therm. Anal. Calorim.* **100** (2010) 1107
22. Bi. B. Mahapatra, A. K. Sarangi, *Bangladesh J. Sci. Ind. Res.* **46**(2) (2011) 259
23. A. B. P. Lever, *Inorganic Electronic Spectroscopy*, 2nd ed., Elsevier, Amsterdam, 1984
24. A. Kriza, M. Dianu, G. Dianu, N. Stanica, *Anal. Univ. Buc.* **I–II** (2005) 123
25. A. A. El-Sherif, *Inorg. Chim. Acta* **362** (2009) 4991
26. T. Rosu, A. Gulea, E. Pahontu, A. Cotovaia, *Rev. Chim.* **58** (2007) 475
27. A. Cukurovali, I. Yilmaz, H. Ozmen, *Transition Met. Chem.* **26** (2001) 619
28. J. B. Gispert, *Coordination Chemistry*, Wiley–VCH, Weinheim, Germany, 2008
29. F. A. Cotton, G. Wilkinson, *Advanced Inorganic Chemistry*, 5th ed, Wiley, New York, 1988
30. E. B. Seena, M. R. P. Kurup, *Polyhedron* (2007) 829
31. B. J. Hathaway, D. E. Billing, *Coord. Chem. Rev.* **5** (1970) 143
32. R. Olar, M. Badea, M. Marinescu, R. Mardale, *J. Therm. Anal. Calorim.* **8** (2011) 53
33. S. A. Abouel-Enein, *J. Therm. Anal. Calorim.* **91** (2008) 929
34. C. E. Stecoza, M. T. Căproiu, C. Drăghici, M. C. Chifiriuc, O. N. Drăcea, *Rev. Chim.* **60** (2009) 137
35. C. Limban, A. V. Missir, I. C. Chiriţă, G. M. Niculescu, C. Drăghici, M. T. Căproiu, M. C. Chifiriuc, O. Drăcea, *Rev. Chim.* **58** (2009) 637
36. R. C. Maurya, J. Chourasia, P. Sharma, *Indian J. Chem.* **47** (2008) 517.

Journal of the Serbian Chemical Society
JSCS@tmf.bg.ac.rs • www.shd.org.rs/JSCS
J. Serb. Chem. Soc. 78 (7) S84–S85 (2013)
Supplementary material

SUPPLEMENTARY MATERIAL TO

New complexes of Co(II), Ni(II) and Cu(II) with the Schiff base 2,2′-[(3,3′-dimethyl[1,1′-biphenyl]-4,4′-diylbis-(nitrilomethylidyne)]bis[6-methoxyphenol]

IONELA ALAN[1]*, ANGELA KRIZA[1], OLGUTA DRACEA[2] and NICOLAE STANICA[3]

[1] *University of Bucharest, Faculty of Chemistry, Inorganic Chemistry Department, 23 Dumbrava Rosie Street, 020462 Bucharest, Romania,* [2] *"Cantacuzino" National Institute for Research in Microbiology and Immunology, 103 Spl. Independentei, 050096 Bucharest, Romania and* [3] *Ilie Murgulescu Institute of Physical Chemistry, Romanian Academy, 202 Spl. Independentei, 77208 Bucharest, Romania*

J. Serb. Chem. Soc. 78 (7) (2013) 947–957

PHYSICAL, ANALYTIC AND SPECTRAL DATA FOR THE LIGAND

2,2′-[(3,3′-dimethyl[1,1′-biphenyl]-4,4′-diylbis(nitrilomethylidyne)]bis[6-methoxyphenol] (H_2L). Reddish orange; Yield: 72 %; m.p.: 219.5 °C; Anal. Calcd. for $C_{30}H_{28}N_2O_4$: C, 74.98; H, 5.87; N, 5.82 %. Found: C, 74.44; H, 5.41; N, 5.89 %; IR (KBr, cm^{-1}): 3439 (O–H), 1615 (C=N), 1253 (C–O); ^{1}H-NMR (300 MHz, DMSO-d_6, δ / ppm): 8.96 (2H, *s*, –CH=N), 7.70 (2H, *d*, J = 2.2 Hz, aromatic), 7.66 (2H, *dd*, aromatic, J = 8.3 Hz), 7.48 (2H, *d*, aromatic, J = 8.3 Hz), 7.26 (2H, *dd*, J = 7.8 Hz, aromatic), 7.15 (2H, *dd*, J = 7.8 Hz, aromatic), 6.93 (2H, *t*, J = 7.8 Hz, aromatic,), 3.83 (6H, *s*, OCH_3), 2.42 (6H, *s*, CH_3); ^{13}C-NMR (75 MHz, DMSO-d_6, δ / ppm): 162.87 (C-1, C-1′), 119.36 (C-2, C-2′), 145.80 (C-3, C-3′), 148.00 (C-4, C-4′), 115.58 (C-5, C-5′), 118.65 (C-6, C-6′), 124.02 (C-7, C-7′), 150.90 (C-9, C-9′), 132.29 (C-10, C-10′), 132.15 (C-11, C-11′), 137.94 (C-12, C-12′), 128.67 (C-13, C-13′), 125.24 (C-14, C-14′), 18.03 (CH_3), 55.91 (OCH_3); UV–Vis (bulk, λ_{max} / cm^{-1}): 42,500, 25,000, 19,800.

PHYSICAL, ANALYTIC AND SPECTRAL DATA FOR THE COMPLEXES **1**–**7**

*[Co(HL)Cl(H_2O)] (**1**)*. Green; Yield: 65 %; m.p.: 310 °C; Anal. Calcd. for $C_{30}H_{29}Cl\,CoN_2O_5$: C, 60.08; H, 4.93; Co, 9.95; N, 4.73 %. Found: C, 60.55; H, 4.92; Co, 9.69; N, 4.95 %; FTIR (KBR, cm^{-1}): 3648 (O–H), 1636 (C=N), 1605 (C=N), 1243 (C–O), 570 (Co–O), 423 (Co–N); UV–Vis (bulk, λ_{max} / cm^{-1}): 25,970, 15,380, 8,130, 7,220; Λ_M (acetone, 10^{-3} M, Ω^{-1} cm^2 mol^{-1}): 10.4.

---

* Corresponding author. E-mail: ionelaalan@yahoo.com

*$[\mathrm{Co_2L(H_2O)_4}](\mathrm{ClO_4})_2$ (**2**)*. Green; Yield: 60 %; Anal. Calcd. for $\mathrm{C_{30}H_{34}Cl_2Co_2N_2O_{16}}$: C, 41.54; H, 3.95; Co, 13.58; N, 3.22 %. Found: C, 41.78; H, 4.34; Co, 13.42; N, 3.56 %; FTIR (KBr, cm^{-1}): 3444 (O–H), 1608 (C=N), 1245 (C–O), 1102, (anion), 623 (anion), 570 (Co–O), 446 (Co–N); UV-Vis (bulk, λ_{max} / cm^{-1}): 25,970, 17,240, 13,700, 8,700, 7,170; Λ_M (acetone, 10^{-3} M, Ω^{-1} cm^2 mol^{-1}): 105.

*$[\mathrm{Co_2L(CH_3COO)_2}]$ (**3**)*. Greenish brown; Yield: 62 %; m.p.: >330 °C; Anal. Calcd. for $\mathrm{C_{34}H_{32}Co_2N_2O_8}$: C, 57.15; H, 4.51; Co, 16.49; N, 3.92 %. Found: C, 56.83; H, 4.64; Co, 16.74; N, 4.12 %; FTIR (KBr, cm^{-1}): 3421 (O–H), 1606 (C=N), 1541 (anion), 1434 (anion), 1243 (C–O), 550 (Co–O), 422 (Co–N); UV–Vis (bulk, λ_{max} / cm^{-1}): 20,000, 18,520, 10,580, 7,200; Λ_M (EtOH, 10^{-3} M, Ω^{-1} cm^2 mol^{-1}): 18.1.

*$[\mathrm{Ni_2L(CH_3COO)_2}]$ (**4**)*. Brown; Yield: 56 %; m.p.: >330 °C; Anal. Calcd. for $\mathrm{C_{34}H_{32}N_2Ni_2O_8}$: C, 57.19; H, 4.51; N, 3.92; Ni, 16.44 %. Found: C, 56.83; H, 4.64; N, 4.12 4.62; Ni, 16.74 %; FTIR (KBr, cm^{-1}): 1609 C=N), 1547 (anion), 1434 (anion), 1237 (C–O), 537 (Ni–O), 421 (Ni–N); UV–Vis (bulk, λ_{max} / cm^{-1}): 35,710, 19,230, 15,750; Λ_M (acetone, 10^{-3} M, Ω^{-1} cm^2 mol^{-1}): 2.8.

*$[\mathrm{Cu(HL)Cl(H_2O)}]$ (**5**)*. Dark brown; Yield: 71 %; m.p.: 297 °C; Anal. Calcd. for $\mathrm{C_{30}H_{29}ClCuN_2O_5}$: C, 60.39; H, 4.89; Cu, 10.65; N, 4.69 %. Found: C, 60.75 60.75; H, 4.62; Cu, 9.87 9.87; N, 4.15 %; FTIR (KBr, cm^{-1}): 3498 (O–H), 1618 (C=N), 1594 (C=N), 1242 (C–O), 578 (Cu–O), 435 (Cu–N); UV–Vis (bulk, λ_{max} / cm^{-1}): 25,64, 12,660; Λ_M (DMF, 10^{-3} M, Ω^{-1} cm^2 mol^{-1}): 10.2.

*$[\mathrm{Cu_2L(H_2O)_4}](\mathrm{NO_3})_2$ (**6**)*: Light brown; Yield: 53 %; m.p.>330 °C; Anal. Calcd. for $\mathrm{C_{30}H_{34}Cu_2N_4O_{14}}$: C, 44.94; H, 4.27; Cu, 15.85; N, 6.98 %. Found: C, 44.72; H, 4.23; Cu, 15.43; N, 6.36 %; FTIR (KBr, cm^{-1}): 3441 1610 (C=N), 1384 (anion), 1243 (C–O), 578 (Cu–O), 466 (Cu–N); UV–Vis (bulk, λ_{max} / cm^{-1}): 25,640, 12,660, 10,200; Λ_M (DMF, 10^{-3} M, Ω^{-1} cm^2 mol^{-1}): 123.0.

*$[\mathrm{Cu_2L(CH_3COO)_2}]$ (**7**)*. Light brown; Yield: 59 %; m.p.: >330 °C; Anal. Calcd. for $\mathrm{C_{34}H_{32}Cu_2N_2O_8}$: C, 56.42; H, 4.45; Cu, 17.56; N, 3.87 %. Found: C, 56.88; H, 4.72; Cu, 16.98; N, 4.11 %; FTIR (KBr, cm^{-1}): 3443 (O–H), 1605 (C=N), 1543 (anion), 1442 (anion), 1242 (C–O), 596 (Cu–O), 437 (Cu–N); UV–Vis (bulk, λ_{max} / cm^{-1}): 25,970, 13,245, 11,695.

Journal of the Serbian Chemical Society
JSCS-info@shd.org.rs • www.shd.org.rs/JSCS

J. Serb. Chem. Soc. 78 (7) 959–971 (2013) UDC 544.275–128+546.264.31:66.081+001.891
JSCS–4473 *Original scientific paper*

Investigations of CO_2 capture by 1-(3-aminopropyl)-3-ethyl imidazolium tetrafluoroborate ionic liquid

LIJUAN YANG[1], YI ZHAO[1]* and WEI SUN[2]

[1]*North China Electric Power University, College of Environmental Science and Engineering, Baoding 071003, China and* [2]*North China Electric Power University, Department of Power Engineering, Baoding 071003, China*

(Received 18 October 2012)

Abstract: CO_2 capture by 1-(3-aminopropyl)-3-ethylimidazolium ($[Apeim]^+$) tetrafluoroborate ($[BF_4]^-$) ionic liquid (IL) was systematically explored at the B3LYP/6-311++G** and mp2/6-311++G** levels. The stable geometries of the ILs and the capture products were optimized, the energies of these geometries were obtained and corrected by zero-point-vibration-energy and basis set superposition error correction. The results show that the interactions between $[Apeim]^+$ and $[BF_4]^-$ are mainly displayed as hydrogen bonds, but the interaction energies exceed –328 kJ mol^{-1}. Further analysis found that the interactions are reinforced by charge dispersion and charge redistribution of the ion-pair, and that electrostatic attraction contributes a great deal to the interaction energies. This IL system capturing CO_2 belongs to the class of physical absorption with a 1:1 molar absorption ratio; the absorption energy is nearly –18 kJ mol^{-1} and thus, this IL may require low energy consumption when regenerated from IL–CO_2.

Keywords: ionic liquid; CO_2 capture; absorption; charge redistribution.

INTRODUCTION

Nowadays, CO_2 capture is an urgent issue in the academic circles. On the one hand, as one of the main greenhouse gases, the dramatic increase in the emission of CO_2 is becoming a potential hazard to the environment. On the other hand, CO_2 is also widely used in many fields as a raw material. Due to the unique properties (negligible vapor pressures, high thermal stabilities, excellent CO_2 solubility, and designability),[1–11] ionic liquids (ILs) may offer a new opportunity for developing novel capture technologies that are capable of reversibly capturing CO_2 with high efficiency. However, many problems have not been solved for the limitations of the experimental technology, such as the structures, the interactions between cations and anions, the mechanisms for capturing CO_2,

---

Corresponding author. E-mail: zhaoyi9515@163.com

doi: 10.2298/JSC121018120Y

etc. These problems have become a bottleneck in the design of functional ILs for special purpose. Therefore, it is necessary and important to perform studies on series of ILs to solve the above-mentioned problems by using theoretical methods, which will reduce the experimental blindness and help in the design and synthesis of functional ILs with satisfactory properties.

The focus of the present work was 1-(3-aminopropyl)-3-ethylimidazolium ($[\text{Apeim}]^+$) tetrafluoroborate ($[BF_4]^–$) IL and its reactions with CO_2. Computational quantum chemistry methods were used for optimizing the possible stable geometries of the ILs and the capture products. By employing natural bond orbital (NBO) calculations, the influence of charge redistribution on interaction force between the ion-pair, as well as between the IL and $CO_{2.}$ In addition, the interaction characteristics and the absorbing interaction mechanism were investigated using the atom in molecular theory (AIM) and the electron density topological theory.

THEORETICAL METHODS

Bearing in mind that the DFT method can yield reliable characteristics for geometries with low computational cost, all the geometry optimization works were performed to a minimum for all initial geometries with full freedoms and with no constraints for the symmetry of their initial structure, except for $[BF_4]^-$ for T_d, and frequency analysis was employed to check the correctness of the minimum points at the B3LYP /6-311++G(d,p) level. However, B3LYP may not be able to offer sound and reliable energy results when describing systems with very weak interactions, such as ILs capturing CO_2, thus the single point energy of stable geometries were computed at the MP2/6-311++G** level. *ZPE* corrections for the total energy (E_t) and the relative energies (E_r) were obtained based on B3LYP/6-311++G(d,p) frequency results. The interaction characteristics and mechanisms were predicted by adopting NBO and AIM calculations and electron density topological analysis. All the computation works were completed by employing Gaussian 03[12] and AIM 2000[13] programs.

RESULTS AND DISCUSSION

In order to find the stable geometries of the IL and the capture products resulting from the absorption of CO_2 by the IL, the possible geometries of the IL were guessed. First, the geometries of $[BF_4]^–$ and $[\text{Apeim}]^+$ were optimized, and the optimized $[BF_4]^–$ were placed in the possible positions around the optimized geometry of $[\text{Apeim}]^+$, and then, eight geometries of the IL were guessed totally. Subsequently, optimization calculations for these guessed geometries were performed and two stable conformers, named ^{A}IL and ^{B}IL are shown in Fig. 1. Finally, the geometries of the capture products were predicted when CO_2 was introduced into the possible positions around ^{A}IL and ^{B}IL, and the optimization calculations found two stable geometries, which are named ^{A}IL–CO_2 and ^{B}IL––CO_2 (shown in Fig. 2). All the geometry optimizations were performed with all the degrees of freedom relaxed and no symmetry constraints, except for the isolated $[BF_4]^–$ for T_d.

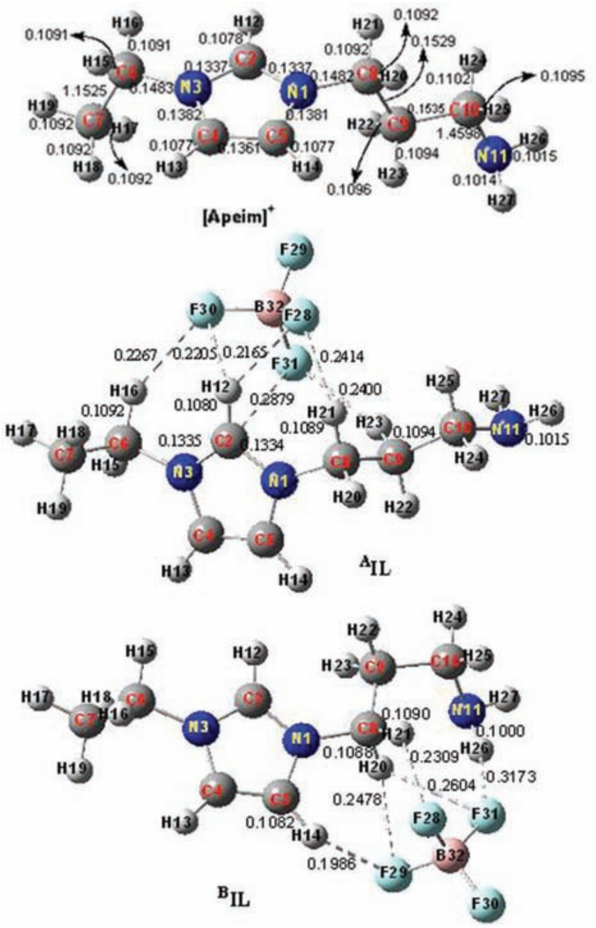

Fig. 1. Geometry of the isolated cation of the IL with atomic numbering and bond lengths in nm. A solid line denotes a normal chemical bond; a dot line denotes a hydrogen bond or a weak chemical bond.

Energies of the stable species

The total energies (E_t), relative energies(E_r), zero-point energy (*ZPE*) and basis set superposition error (*BSSE*) of all species are given in Table I. The total energy of isolated [Apeim]$^+$ and [BF$_4$]$^–$ and the total energy of isolated ^{A}IL and CO$_2$ were set as zero point datum marks of energy.

The energy change (ΔE(IL)) between an IL and the isolated ions is commonly used to estimate the interaction energy between the ion-pair of an IL, which, in the present case, can be calculated from $\Delta E(\text{IL}) = E([\text{BF}_4]^-) + E([\text{Apeim}]^+) - E(\text{IL})$. It could be observed that $\Delta E(^A\text{IL})$ is 359.69 kJ mol^{-1} and $\Delta E(^B\text{IL})$ is 328.19 kJ mol^{-1}, which indicates that $\Delta E(^A\text{IL})$ is only 31.5 kJ mol^{-1} greater than that of $\Delta E(^B\text{IL})$. Hence, it could be predicted that both ^{A}IL and ^{B}IL are stable geometries and that ^{A}IL may be the main geometry of the [Apeim][BF$_4$] IL. Whereas, it can be observed from Fig. 1 that the interactions between [[Apeim]$^+$ and [BF$_4$]$^-$ are mainly displayed as hydrogen bonds (HBs) and the energy of these HBs is far less than the value of ΔE(IL), so there must be other stronger interaction forces between the ion-pair besides these HBs, and it is necessary to perform further NBO and AIM investigations.

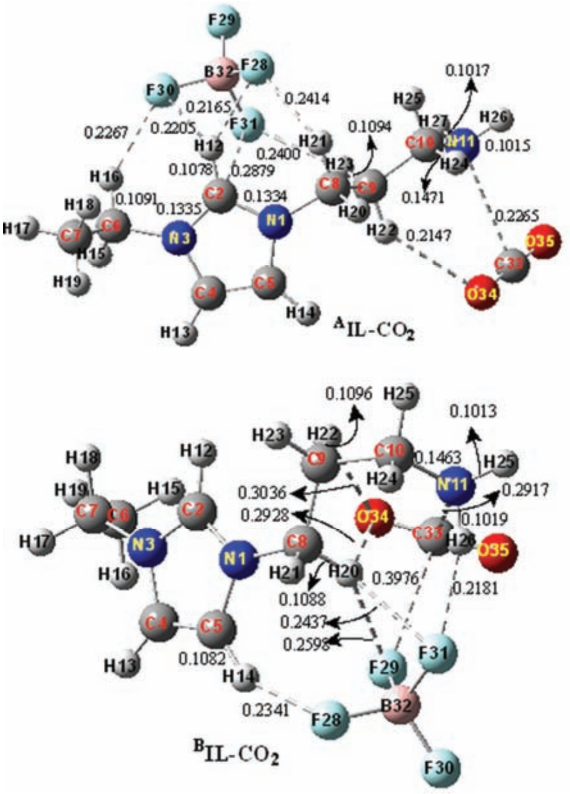

Fig. 2. Geometry of ^{A}IL–CO$_2$ and ^{B}IL–CO$_2$ with atomic numbering and bond lengths in nm. A solid line denotes a normal chemical bond; a dot line denotes a hydrogen bond or a weak chemical bonds.

TABLE I. The energies of all species corrected by *ZPE* and *BSSE*

Species	*ZPE*	*BSSE*	E_t	E_r
	a.u.	a.u.	a.u. mol^{-1}	kJ mol^{-1}
[Apeim]$^+$ + [BF$_4$]$^-$	0.2564	0.0000	–900.7603	0.0000
^{A}IL	0.2583	0.0024	–900.8973	–359.69
^{B}IL	0.2585	0.0023	–900.8853	–328.19
^{A}IL +CO$_2$	0.2700	0.0024	–1089.0918	0.0000
^{A}IL–CO$_2$	0.2706	0.0026	–1089.0999	–21.01
^{B}IL +CO$_2$	0.2702	0.0023	–1089.0797	31.76
^{B}IL–CO$_2$	0.2709	0.0034	–1089.0923	–1.26

Table I also shows that the relative energies of ^{A}IL–CO$_2$ and ^{B}IL–CO$_2$ are –21.01 and 31.76 kJ mol^{-1}, respectively, *i.e.*, ^{A}IL capturing CO$_2$ is an exothermic reaction while ^{B}IL capturing CO$_2$ is an endothermic reaction. Thus, the relative energy of ^{A}IL–CO$_2$ is 52.77 kJ mol^{-1} lower than that of ^{B}IL–CO$_2$ and furthermore, ^{A}IL is the most likely geometry; hence, ^{A}IL–CO$_2$ is the most likely stable product of this IL capturing CO$_2$. ΔE(IL–CO$_2$) was also used to estimate the interaction energy between IL and CO$_2$, calculated according to ΔE(IL–CO$_2$) = = E(IL) + E(CO$_2$) – E(IL–CO$_2$). ΔE (^{A}IL–CO$_2$) is 20.01 kJ mol^{-1}, which means that the interaction between ^{A}IL and CO$_2$ is a strong intermolecular interaction force, the reaction of ^{A}IL capturing CO$_2$ is physical absorption and IL–CO$_2$ is a molecular complex. It could be further speculated that the desorption of CO$_2$ from ^{A}IL–CO$_2$ might be a low energy consumption process. For the sake of simplification, ^{A}IL together with ^{A}IL–CO$_2$ are used as examples to illustrate the research details throughout this paper.

Geometry structures of the ionic liquid

The geometries given in Fig. 1 show that there are five hydrogen bonds (HBs) and a weak bond of F31···C2 between the ion-pair in ^{A}IL. The five HBs are F28···H12–C2 (0.2165 nm), F28···H21–C8 (0.2414 nm), F30···H16–C6 (0.2267 nm), F30···H12–C2 (0.2205 nm) and F31···H23–C9 (0.2400 nm). The HB strength order is F28···H12–C2 > F30···H12–C2 > F30···H16–C6 > > F28···H21–C8 > F31···H23–C9. Obviously, the bond length could be a simple criterion for the formation of HBs or weak chemical bonds when classic HBs or weak chemical bonds are investigated, and the shorter the bond length, the stronger is the bond. The bond lengths of the five HBs are slightly shorter than the van der Waals radii (Pauling) of F and H (0.245 nm)[14], that is to say, they pertain to normal HBs. The bond length of F31···C2 (0.2879 nm) is much longer than a normal F–C chemical bond, which means that it is a very weak. However, the interaction energy between the ion-pair in ^{A}IL is far beyond the bond energy of the five HBs and F31···C2. It could be observed from Fig. 1 that the C2–H12 bond length is lengthened resulting from the electrons on the H atom transferring to form the HB or another weak chemical bond, this phenomenon being called an "electron transfer effect". Moreover, the C2–N1 and C2–N3 bond lengths are shortened by 0.0003 and 0.0002 nm, respectively, in spite of C2 involvement in F31···C2 formation. These abnormal bond length changes depart from the "electron transfer effect". In addition, another particular phenomenon is that H12 participates in the formation of two HBs, *i.e.*, F30···H12–C2 and F28···H12–C2, simultaneously despite the saturation characteristic of a HB.

Geometries of the molecular complexes

It can be seen from Fig. 2 that ^{A}IL–CO$_2$ is produced when CO$_2$ is absorbed by ^{A}IL and the molar absorption ratio is 1:1. The main interactions between ^{A}IL and CO$_2$ are through the C33···N11 (0.2265 nm) and O34···H22–C9 (0.2147 nm) bonds. The bond lengths of these two chemical bonds are shorter than the van der Waals radii of the corresponding two atoms. Additionally, C10–N11, N11–H26 and N11–H27 participate in the formation of C33···N11 and they are elongated by the “electron transfer effect”. The C9–H22 bond is abnormally shortened, although it is involved in the formation of the C10–H26···O38 HB. This particular phenomenon possibly influences the absorption of CO_2 by ^{A}IL. Therefore, it was essential to determine the reasons for these abnormal phenomena by using NBO and AIM research.

Frequency analysis

The frequency calculations suggest that the two optimized geometries of the IL and the two capture products have no imaginary vibration frequency, which confirmed their stability. The interactions between cation and anion resulted in the breakage of T_d symmetry in $[BF_4]^-$ and a shift of the vibration frequencies, which are consistent with the bond strength changes.

The NBO analysis

In order to reveal how the charge population affects the interaction forces between the ion-pair, as well as between the IL and CO_2, NBO atomic charges were calculated and analyzed. The NBO net charges of atoms and group fragments are given in Tables II and III, respectively. Here, ^{A}IL and ^{A}IL–CO_2 are considered.

TABLE II. The net integral atomic charges in all stable species

Atom	Cation	^{A}IL	^{A}IL–CO_2	^{B}IL	^{B}IL–CO_2	$[BF_4]^-$	
N1	–0.34404	–0.35775	–0.35546	–0.33081	–0.32983	B	1.33356
C2	0.29607	0.32491	0.32493	0.27236	0.28145	F	–0.58339
N3	–0.35099	–0.36037	–0.36168	–0.36669	–0.36724	F	–0.58339
C4	–0.00877	–0.01895	–0.02289	–0.03748	–0.03488	F	–0.58339
C5	–0.00410	–0.02061	–0.02134	0.01462	0.01487	F	–0.58339
C6	–0.16613	–0.17909	–0.17901	–0.16426	–0.16321	CO_2	
C7	–0.58896	–0.58095	–0.58031	–0.58466	–0.58438	C	0.99076
C8	–0.16354	–0.16242	–0.16145	–0.19660	–0.18859	O	–0.49538
C9	–0.40064	–0.41316	–0.42047	–0.40706	–0.41165	O	–0.49538
C10	–0.17975	–0.17647	–0.17471	–0.17147	–0.17216	–	
N11	–0.84167	–0.84403	–0.85638	–0.87076	–0.88013	–	
H12	0.23630	0.27921	0.28054	0.22692	0.22765	–	
H13	0.24574	0.22713	0.22774	0.23053	0.22943	–	
H14	0.24523	0.22997	0.23247	0.29558	0.29032	–	
H15	0.22086	0.20377	0.20338	0.21133	0.20896	–	
H16	0.21553	0.25894	0.25852	0.20730	0.20628	–	
H17	0.21250	0.21861	0.21855	0.21063	0.21067	–	
H18	0.21443	0.20878	0.20912	0.20998	0.21471	–	
H19	0.23457	0.19838	0.19838	0.21871	0.21653	–	
H20	0.22006	0.19693	0.19742	0.25522	0.26627	–	

TABLE II. Continued

Atom	Cation	^{A}IL	^{A}IL–CO$_2$	^{B}IL	^{B}IL–CO$_2$	[BF$_4$]$^-$
H21	0.21526	0.24130	0.24235	0.25503	0.22318	–
H22	0.20094	0.19589	0.20497	0.20054	0.20738	–
H23	0.21524	0.24133	0.24157	0.18781	0.19170	–
H24	0.16436	0.17229	0.17368	0.16834	0.16705	–
H25	0.18832	0.17168	0.17477	0.18433	0.18599	–
H26	0.3550	0.35272	0.35744	0.39004	0.39408	–
H27	0.36816	0.35385	0.35852	0.35529	0.35817	–
F28	–	–0.58795	–0.58899	–0.58497	–0.58436	–
F29	–	–0.53967	–0.53958	–0.58687	–0.58917	–
F30	–	–0.58580	–0.58571	–0.54363	–0.54143	–
F31	–	–0.57938	–0.57888	–0.58416	–0.58078	–
B32	–	1.33093	1.33156	1.33484	1.33664	–
C33	–	–	1.00935	–	1.02160	–
O34	–	–	–0.52348	–	–0.54636	–
O35	–	–	–0.49491	–	–0.47876	–

TABLE III. The net integral charges of the main groups

Species	[Apeim]$^+$	^{A}IL	^{A}IL–CO$_2$	^{B}IL	^{B}IL–CO$_2$
Ethyl	0.34280	0.32844	0.32863	0.30903	0.30956
Imidazole	0.31544	0.30354	0.30431	0.30503	0.31177
Aminopropyl	0.34174	0.32991	0.33771	0.35071	0.34129
[BF$_4$]$^-$	–	–0.96187	–0.96160	–0.96479	–0.95910
CO$_2$	–	–	–0.00904	–	–0.00352

Theoretically, the unit charge of isolated [Apeim]$^+$ should belong to the N3 atom, but from Table III it can be seen that some of the unit positive charge disperses over the whole cation, with +0.34280 charge transferring to the ethyl, +0.34174 charge transferring to the aminopropyl group, and the remaining +0.31544 charge disperses over the imidazole ring. The unit negative charge disperses over the whole [BF$_4$]$^–$, which leads to an increase in the net negative charges of the F atoms (see Table II), which is beneficial for the HBs.

It could be observed from the charge data of the isolated ions and ^{A}IL in Table III that the negative charge of [BF$_4$]$^–$ becomes –0.96205 when ^{A}IL is formed; in other words, the unit negative charge of [BF$_4$]$^–$ disperses over the whole ^{A}IL, with –0.03813 electrons transferring from [BF$_4$]$^–$ to [Apeim]$^+$, which results in the positive charges of imidazole, ethyl and aminopropyl decreasing by 0.01190, 0.01436 and 0.01183, respectively. Additionally, the atomic positive charges in ^{A}IL must decrease and the atomic negative charges must increase after receiving the electrons coming from [BF$_4$]$^–$. The atomic charges given in Table II suggest that most of the atomic charges changes accord with the above theoretical deduction, yet some deviate. For example, the atomic positive charge of C2, H12, H16, H17, H21, H23 and H24 are increased by 0.02884, 0.04291, 0.04341, 0.00611, 0.02604, 0.02609 and 0.00793, respectively, the atomic negative charge of C7, C8 and C10 are decreased abnormally by 0.0080, 0.0011 and 0.0033, respectively. These abnormal atomic charge changes imply that the unit positive charge of $[Apeim]^+$ must redistribute together with the dispersing of the unit negative charge of $[BF_4]^–$. Furthermore, the charge dispersion and distribution may have some influence on the interactions between the ion-pair, as well as between IL and CO_2, which will be discussed in the next paragraph.

It is obvious that F31···C2 is a very weak chemical bond and the bond length of the five C–H···F HBs in ^{A}IL are much longer than that of a normal C—H···F HB (about 0.163 nm), which means that each of the hydrogen-bonding energy in ^{A}IL should be smaller than that of a normal C—H···F HB (about 28 kJ mol$^{–1}$), whereas it is directly opposite. All these extraordinary phenomena may be due to the electrostatic attraction force between the ion-pair. The atomic charge of F in isolated $[BF_4]^–$ is –0.58339 (Table II), which is so large that it can easily form a strong HB. Moreover, the charges of F28 and F30 in ^{A}IL become –0.58795 and –0.58580; the atomic positive charges of H12, H16 and H21 change from 0.23630 to 0.27921, from 0.21553 to 0.25894 and from 0.21526 to 0.24130, respectively. Both the increasing of negative charge of the F atom and the positive charges of the H atoms are propitious to strengthening the electrostatic attraction between F and H, so the hydrogen-bonding energies of the five HBs are far beyond those of normal HBs. The strengthened electrostatic attraction force is displayed as HBs and it is the reason of the involvement of F28 and F30 in two HBs simultaneously. Additionally the atomic negative charge of F31 (–0.57938) in ^{A}IL is slightly smaller than in a single $[BF_4]^–$, but it is enough to form an HB, and the positive charge of H23 becomes larger (from 0.21524 to 0.24133), therefore, F31···H23–C9 can be formed. Overall, all the atomic positive charges of H involved in HB formation are increased, which is beneficial to reinforce the interaction forces between the ion-pair and stabilize the IL system.

The atomic charge changes caused by charge dispersion and redistribution can also explain the abnormal shortening of the C2–N1 and C2–N3 bonds. Both the atomic positive charge of C2 (changes from 0.29607 to 0.32491) and the atomic negative charges of N1 (changes from –0.34404 to –0.35775) and N3 (changes from –0.35099 to –0.36037) contribute to the strengthening of the C2––N1 and C2–N3 bonds, and the strengthening effect exceeds the weakening effect caused by the “electron transfer effect”. Thus, the comprehensive result is that C2–N1 and C2–N3 bonds are strengthened. In addition, some of the other normal chemical bonds are either strengthened or weakened because of the atomic charge changes, but these changes are not remarkable.

^{A}IL is the main geometry and ^{A}IL–CO_2 is the main product of CO_2 capture by IL. Thus in this part, ^{A}IL–CO_2 is taken as an example to discuss the charge distributions and their consequences for CO_2 capture by ^{A}IL.

Table III shows that –0.00904 electrons transfer from ^{A}IL to CO_2 when ^{A}IL combines with CO_2. The charge change of $[BF_4]^-$ is only –0.00027. In other words, the –0.00904 electron mostly comes from $[Apeim]^+$, which should theoretically result in increasing atomic positive charges or decreasing atomic negative charges in $[Apeim]^+$. However, the atomic negative charges of N3, C4, C5, C9 and N11 are somewhat increased and the atomic positive charge of H15, H16, H17 and F28 are somewhat decreased (Table II). Hence, the charge must redistribute over the whole ^{A}IL–CO_2 system for a secondary time during the process of ^{A}IL combination with CO_2, which results in some changes in the atomic charges in $[Apeim]^+$ and the second charge redistribution contributes further to reinforcement of the absorptive interaction force. For instance, the atomic negative charge of N11 is increased by –0.00124, the positive charge of C33 (1.00935) is greater than that of the C atom (0.99076) in an isolated CO_2 molecule. Both these atomic charge changes on N11 and C33 are beneficial to the electrostatic attraction force between the two atoms. The atomic charge of H22 changes from 0.19589 to 0.20497, and the atomic charge of O34 (–0.52348) is greater than that of an isolated CO_2 molecule; thus the reinforced electrostatic attraction between O34 and H22 reinforce the combination interactions between ^{A}IL and CO_2.

The above analysis suggests that the charge dispersion and redistribution are beneficial by reinforcing both the interactions between the ion-pair and the combination interaction force between ^{A}IL and CO_2. In order to research the energy contribution of electrostatic attraction force, the orbital interaction energy of these weak chemical bonds in ^{A}IL and ^{A}IL–CO_2 were calculated. The results show that the total orbital interaction energy of the six weak chemical bonds in ^{A}IL are less than 10 kJ mol^{-1}; hence, most of the interaction energy comes from a non-orbital interaction force, which proves the prediction that electrostatic interaction force plays a dominant role in this IL system. In a word, when attempts are made to change the physical or chemical properties of an ionic liquid, the electrostatic attraction force has to be considered. The total orbital interaction energy of the two weak chemical bonds between ^{A}IL and CO_2 are 1.65 kJ mol^{-1}, *i.e.*, most of the interaction energy between ^{A}IL and CO_2 is non-orbital interaction energy and electrostatic attraction may play a dominant role in CO_2 capture by ^{A}IL. Thus, this is a further evidence that CO_2 capture by ^{A}IL is a physical absorption process and the interactions between ^{A}IL and CO_2 are strong intermolecular interactions. Therefore, in future studies, it is vital that a series of research on how to influence the charge distribution be realized, which could aid in the design of functionalized ILs to satisfy the set requirements.

Electronic density topological analyses

Based on the Bader[13] theory of Atoms in Molecules (AIM), if there is a bond critical point（BCP) between two atoms in a molecule, they must form a chemical bond. The values $\rho(r_c)$ (the electron density at the BCP), $\nabla^2\rho(r_c)$ (Laplacian value of the electron density) and ε (the ellipticity value of a bond) are used to characterize the properties of a bond. The larger the $\rho(r_c)$ value, the stronger is the bond. A $\nabla^2\rho(r_c)$ value close to zero means a weak bond; a $\nabla^2\rho(r_c)$ value less than zero means a covalent bond, and the smaller the $\nabla^2\rho(r_c)$ value, the stronger is the covalence of the bond; a $\nabla^2\rho(r_c)$ value larger than zero suggests an ionic bond, and the larger the $\nabla^2\rho(r_c)$ value, the stronger is the ionic nature of the bond. The ε value is used to characterize the σ or π nature of a bond, the greater the ε value, the more obvious is the π character of the bond; conversely, the σ character of the bond is stronger. In this section, the AIM theory was employed to analyze further the characteristics of the interaction between the ion-pair and between the IL and CO_2.

The AIM molecular graphs of ILs and ILs–CO_2 are drawn by AIM200 program package (Fig. 3), the little red dots between two atoms represent the BCPs, the bond parameters at the BCPs were calculated and are listed in parentheses beside the little red dots, and they are ρ values, $\nabla^2\rho(r_c)$ values and ε values from the top down. In this section, the electron density topological theory was applied in discussing and predicting the interaction characteristics in the IL, as well as the absorption characteristics between the IL and CO_2.

As shown in the AIM structure of ^{A}IL, the BCPs of the five HBs prove their formation. According to their $\rho(r_c)$ values, the bond strength order is F28···H12–C2 > F30···H12–C2 > F30···H16–C6 > F28···H21–C8 > F31···H23–C9, which agrees with the conclusion drawn from the bond lengths. The $\rho(r_c)$ values of F28···H12–C2 and F30···H12–C2 are greater than 0.015, indicating two strong H-bonds; the $\rho(r_c)$ values of the other three HBs are about 0.01, which indicates they are normal HBs. All the $\nabla^2\rho(r_c)$ values of these five HBs are close to zero and their ε values at the BCPs are very small; thus, the five HBs are weak chemical bonds of typical σ bond characteristics. The $\rho(r_c)$ and $\nabla^2\rho(r_c)$ values of F31···C2 are 0.0100 and 0.0400, respectively, hence F31···C2 is a weak chemical bond. However F31···C2 has some π characteristics as indicated by its larger ε value (0.9127). It could be predicted that the π electrons on C2 and F31 contribute a great deal to the F31···C2 bond. The AIM analysis proved that the interaction forces between the ion-pair are weak chemical bonds, with electrostatic attraction playing dominant role in reinforcing the interaction forces.

Two new BCPs between O34 and H22, as well as between C33 and N11 in the AIM geometry of ^{A}IL–CO_2 confirmed the formation of O34···H22–C9 and C33···N11 bonds. The $\rho(r_c)$ value of the C33···N11 bond is 0.0105 and that of O34···H22–C9 bond is 0.0059, and the $\nabla^2\rho(r_c)$ values of for these bonds are close to zero. Thus, both the $\rho(r_c)$ and $\nabla^2\rho(r_c)$ values indicate that the two bonds belong to molecular interactions and that ^{A}IL–CO_2 may be a bimolecular complex; therefore, the reaction of ^{A}IL and CO_2 is physical absorption. The

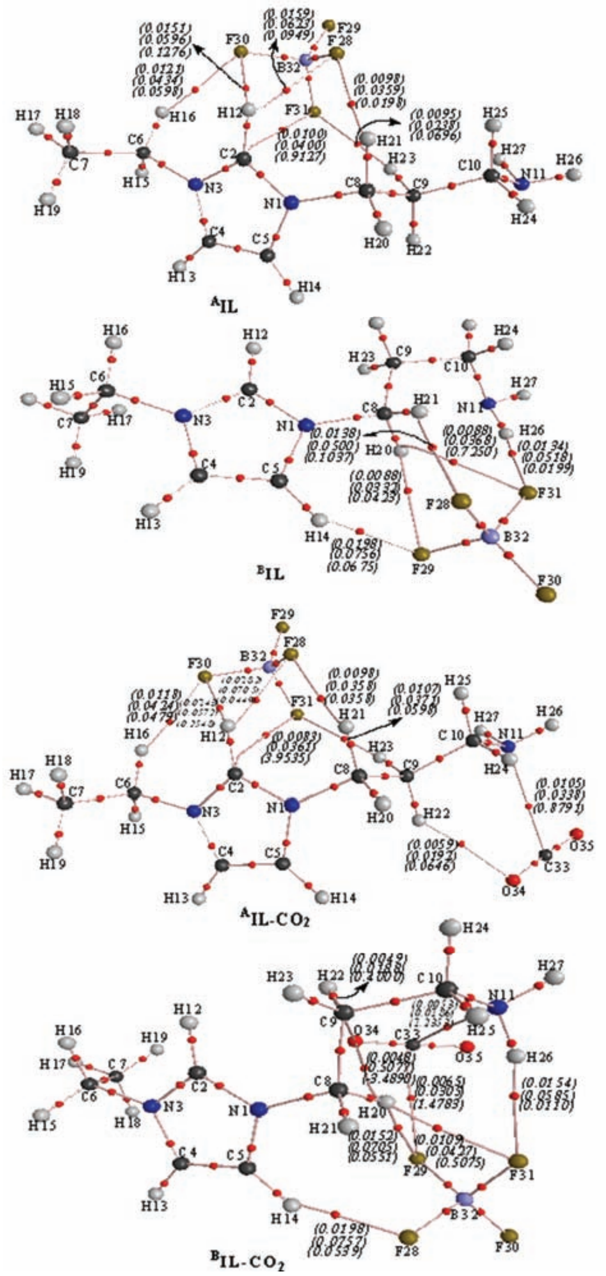

Fig. 3. AIM structures of ^{A}IL, ^{B}IL, ^{A}IL–CO$_2$ and ^{B}IL–CO$_2$. The little red balls denote the BCP. Some bond parameters at the BCPs, *i.e.*, the ρ values, $\nabla^2\rho(r_c)$ values and ε values from the top down, are listed in parentheses beside the little red dots.

O34···H22–C9 bond has typical σ characteristics according to its ε value. The ε value of the C33···N11 bond (0.8791) implies greater π characteristics and it could be inferred that π electron interactions contribute a great deal to the C33···N11 bond. In addition, the weak chemical bonds between the ion-pair in ^{A}IL–CO_2 changed somewhat owing to geometry changes and the secondary charge redistribution effect, but the changes are negligible and have little effect on the absorbing interaction.

CONCLUSIONS

The CO_2 capture by the [Apeim][BF_4] ionic liquid has been systematically discussed at the electron level and the conclusions could be summarized as follows:

1. Two stable geometries, named ^{A}IL and ^{B}IL, were optimized, ^{A}IL is the main geometry and the interaction energy between ion-pair is nearly 360 kJ mol^{-1}. CO_2 capture by ^{A}IL is physical absorption and the molar absorbing ratio is 1:1, the absorbing energy is about 20 kJ mol^{-1}. Thus ^{A}IL may absorb CO_2 effectively and the energy consumption for its regeneration is low.

2. Electrostatic attractive forces resulting from charge dispersion and redistribution of [Apeim]$^+$ and [BF_4]$^-$ help in the stabilization of this IL system and reinforce the absorbing interaction forces between IL and CO_2.

3. Electrostatic attractive forces play a dominant role in the interactions between the ion-pair. The main absorption mechanism is the π electron interaction between C33 and N11, and a weak hydrogen bond between CO_2 and [Apeim]$^+$.

Acknowledgements. This project was supported by the Fundamental Research Funds for the Central Universities of North China Electric Power University (Project No. 11ML64).

ИЗВОД

ИСПИТИВАЊЕ ЈОНСКЕ ТЕЧНОСТИ 1-(3-АМИНОПРОПИЛ)-3-ЕТИЛ-ИМИДАЗОЛИЈУМ-ТЕТРАФЛУОРОБОРАТА КОЈА ВЕЗУЈЕ CO_2

LIJUAN YANG[1], YI ZHAO[1] и WEI SUN[2]

[1]North China Electric Power University, College of Environmental Science and Engineering, Baoding 071003, China и [2]North China Electric Power University, Department of Power Engineering, Baoding 071003, China

1-(3-Аминопропил)-3-етил-имидазолијум ([Apeim]$^+$) тетрафлуороборат ([BF_4]$^-$) је јонска течност (IL) која везује CO_2. Ово једињење је систематски проучавано на нивоу B3LYP/6-311++G** и mp2/6-311++G**. Геометрије за IL и продукте везивања CO_2 су оптимизоване и њихове енергије одређене. Резултати показују да се интеракција између [Apeim]$^+$ и [BF_4]$^-$ углавном остварује преко водоничних веза, али да енергија интеракције превазилази –328 kJ mol^{-1}. Даљом анализом смо нашли да је интеракција појачана дисперзијом наелектрисања и њеном редистрибуцијом, као и да електростатичко привлачење знатно доприноси енергији интеракције. Овај IL систем за везивање CO_2 спада у класу физичке сорпције са молским односом 1:1 и апсорпционом енергијом око –18 kJ mol^{-1}. Због тога би регенерација ове IL из IL–CO_2 захтевала малу потрошњу енергије.

(Примљено 18. октобра 2012)

REFERENCES

1. S. M. Mahurin, J. S. Yeary, S. N. Baker, De-en Jiang, S. Dai, G. A. Baker, *J. Membr. Sci*. **401** (2012) 61
2. X. F. Wei, D. J. Zhang, C. B. Liu, *J. Mol. Struct*. **909** (2009) 1
3. V. Kempter, B. Kirchner, *J. Mol. Struct*. **972** (2010) 22
4. O. Acevedo, *J. Mol. Graphics Modell*. **28** (2009) 95
5. R. Q. Lü, Z. G. Cao, G. P. Shen, *J. Nat. Gas Chem*, **16** (2007) 428
6. A. H. Jalili, A. Mehdizadeh, M. Shokouhi, A. N. Ahmadi, M. Hosseini-Jenab, F. Fateminassab, *J. Chem. Thermodyn*. **42** (2010) 1298
7. R. Modelli, A. Sali, P. Galletti, *Chemosphere* **73** (2008) 1322
8. A. R. Sampaio de Sousa, R. Silva, F. H. Tay, A. L. Simplício, S. G. Kazarian, C. M. M. Duarte. *J. Supercrit. Fluids* **48** (2009) 120
9. M. Kobayashi, M. Terada, Y. Terayama, M. Kikuchi, A. Takahara, *Isr. J. Chem*. **52** (2012) 364
10. W. Li, C. S. Qi, X. M. Wu, H. Rong, L. F. Gong, *J. Mol. Struct*. **85** (2008) 534
11. S. Hanioka, T. Maruyama, T. Sotani, M. Teramoto, H. Matsuyama, K. Nakashima, M. Hanaki, F. Kubota, M. Goto, *J. Membr. Sci*. **314** (2008) 1
12. Gaussian 03, revision B.05, Gaussian, Inc., Wallingford, CT, 2004
13. R. F. W. Bader, *Atoms in molecules: a quantum theory*, *International series of monographs in chemistry*, Oxford University Press, Oxford, UK, 1990
14. S. Z. Hu, C. H. Zhou, Q. R. Cai, *Acta Phys. Chim. Sin*. **19** (2003) 1073.

Journal of the Serbian Chemical Society
JSCS-info@shd.org.rs • www.shd.org.rs/JSCS
J. Serb. Chem. Soc. *78* (7) 973–986 (2013) UDC 544.2+544.15:544.174.21.3+544.354–128
JSCS–4474 *Original scientific paper*

Ab initio study of vibronic transitions between $X^2\Pi$ and $1^2\Sigma^+$ electronic states of HCP^+

LJILJANA STOJANOVIĆ*#

Faculty of Physical Chemistry, Studentski Trg 12, 11158 Belgrade, Serbia

(Received 15 November, revised 25 November 2012)

Abstract: The ground and low-lying excited doublet electronic states of the HCP^+ were studied by means of the multireference configuration interaction method. The vibronic energy levels of the $X^2\Pi$ state of Σ, Π, Δ, and Φ symmetry, up to the 2500 cm^{-1}, have been calculated variationally, employing previously developed *ab initio* methods that take into account vibronic and spin–orbit interactions. The vibronic wave functions were used to estimate transition moments between vibronic energy levels of the $X^2\Pi$ and $1^2\Sigma^+$ electronic states. The results were compared to available experimental and theoretical data.

Keywords: excited states; Renner–Teller effect; phosphaethyne cation.

INTRODUCTION

The HCP^+ was detected for the first time in a photoelectron spectroscopy experiment on the HCP molecule, when the CP stretching progressions between the ground $X^2\Pi$ and the first excited $1^2\Sigma^+$ state were observed.[1] King *et al*. later recorded electron-impact $1^2\Sigma^+ \rightarrow X^2\Pi$ emission spectra. In their first study,[2] short progressions in the CP stretching vibrations were reported, and the ground state spin–orbit coupling constant and the CP stretching frequency were derived from the spectrum. In a subsequent study,[3] bands of the high-resolution emission spectrum were analyzed and rotational constants of the ground and the first excited state, as well as an improved value of the spin–orbit coupling constant, were derived. Finally, in the latest study,[4] the authors reported the $1^2\Sigma^+ \rightarrow X^2\Pi$ emission spectrum with resolved transitions to $v_2'' = 1$ and 2 bending vibrational levels. They were able for the first time to analyze vibronic, spin–orbit, and Fermi resonance structures of the ground state. In the latest study[5] of this ion by Clouthier *et al*., the laser-induced fluorescence (LIF) spectrum between first two states involving all vibrational modes was recorded and a set of vibrational cons-

---

[*] Correspondence, E-mail: stojanovicmljiljana@gmail.com
[#] Serbian Chemical Society member.
doi: 10.2298/JSC121115128S

tants and ground and excited state geometric parameters were derived from the spectrum.

The HCP^+ has also been the subject of several theoretical studies. Initially, they were mainly concerned with the geometries and properties of the potential energy surfaces of the ground and the first excited state.[6–8] Karna and Grein performed the first systematic study of the excited states.[9] They optimized, using the multireference configuration interaction method, the geometries and calculated the vertical excitation energies and stretching frequencies of the nine lowest-lying doublet and quartet electronic states. Later, Temelso *et al*. studied the ground and the first excited state using coupled cluster methods with different basis sets.[10]

The vibronic structure of the $X^2\Pi$ state of HCP^+ was investigated theoretically in two thorough studies. In the first of them, Tarroni *et al*. calculated the MRCI potential energy surfaces of the ground state components and employed a full-dimensional vibrational treatment to calculate the spin–rovibronic energy levels of the ground state employing the Handy–Carter Hamiltonian as the kinetic energy operator.[11] They performed detailed analysis of the Fermi resonance between the bending (v_2) and CP stretching modes (v_3), and concluded that the used effective model Hamiltonian that describes a Fermi interaction was inapplicable when the bending and CP stretching modes are multiply excited ($v_2 + + 2v_3 > 3$). The obtained results well reproduced the experimental findings, except that in some cases the ordering of the levels was different from the experimentally derived one.

Clouthier *et al*. also performed a Renner–Teller analysis of the ground state vibrational energy levels.[5] They were able to fit the majority of the levels up to 4500 cm^{-1} (with the exception of several levels) using their previously developed model that includes vibronic, spin–orbit, and Fermi resonance interactions.

In the present study, computation of the bending potential curves of the ground and the nine lowest-lying doublet electronic states of HCP^+ was performed. The obtained bending potential energy curves of the $X^2\Pi$ state were employed in the calculation of the vibronic energy levels using previously developed variational methods with Hamiltonians that incorporate terms describing vibronic and spin–orbit coupling. Finally, the vibronic transition moments between the $X^2\Pi$ and $1^2\Sigma^+$ states were computed employing calculated vibronic wave functions and electronic dipole transition moments.

COMPUTATIONAL AND THEORETICAL METHODS

Electronic ab initio *methods*

The ground and lowest-lying doublet electronic states of the linear HCP^+ were studied by means of the internally contracted MRCI method[12] with a state average complete active space self-consistent field (SA-CASSCF)[13] reference wave function using the Dunning aug-cc-pVTZ basis[14]. The full valence CASSCF computations were performed, *i.e*., the configuration state functions were formed by distribution of all nine valence electrons within the active space composed of eight orbitals in the $C_{\infty v}$ symmetry group - (5–9)σ and (2–4)π (in the C_{2v} subgroup, it is composed of 11 orbitals - (5–9)a_1, (2–4)b_1, and (2–4)b_2). All computations were performed using the MOLPRO program package.[15]

The geometries of the ground $X^2\Pi$ and $1^2\Sigma^+$ states were optimized at the MRCI level of theory with CASSCF reference functions. In the case of the $X^2\Pi$ state, the reference function was obtained by averaging with equal weights both state components (1^2B_1 and 1^2B_2), whereas the 1^2A_1 CASSCF wave function was used as the reference for the geometry optimization of the $1^2\Sigma^+$ state.

The vertical excitation energies from the ground to the nine lowest-lying doublet states and the bending potential curves of all studied states were computed at the MRCI-optimized bond lengths of the $X^2\Pi$ state within the C_s symmetry group using the MRCI/FV-SA-CASSCF method by averaging with equal weights all the states. The electronic transition moments between the ground and excited CASSCF electronic states were computed as functions of the bending coordinate at the MRCI bond lengths of the ground state.

The spin–orbit coupling constant of the $X^2\Pi$ state was also computed at its MRCI optimized geometry as the difference between the energies of the two spin components obtained by diagonalization of the sum of the Breit–Pauli operator and the electronic operator in the basis of the MRCI components of the state.

In addition, the harmonic vibration frequencies of all three vibrational modes in the $X^2\Pi$ and $1^2\Sigma^+$ states were computed.

Vibronic ab initio *methods*

The Hamiltonian used in this study included operators describing electronic motion, bending vibrations, rotation around axis of the smallest moment of inertia (*z*-axis), and spin–orbit interaction in its phenomenological form ($A_{\mathrm{SO}}\hat{L}_z\hat{S}_z$):[16]

$$\hat{H} = \hat{H}_{\mathrm{e}} + \hat{T}_{\mathrm{b}} + \hat{T}_{\mathrm{r}}^{z} + \hat{H}_{\mathrm{SO}}. \tag{1}$$

This model neglects possible couplings between the bending and stretching modes and rotations around axes perpendicular to the axis of the smallest moment of inertia, although Fermi resonance between the CP stretching and bending mode was previously detected.[4] The general form of the kinetic energy operator for bending vibrations and rotation about the z-axis in atomic units is:

$$\hat{T}_{\mathrm{b}} + \hat{T}_{\mathrm{r}}^{z} = -\frac{1}{2}\left(T_1(\rho)\frac{\partial^2}{\partial\rho^2} + T_2(\rho)\frac{\partial}{\partial\rho} + T_0(\rho)\right) - A(\rho)\frac{\partial^2}{\partial\varphi^2} \tag{2}$$

where ρ is the angle supplementary to the instantaneous bond angle θ, φ is the angle between the molecular plane and the space-fixed plane, which is chosen such that it contains the axis that corresponds to the smallest moment of inertia of the molecule. $T_2(\rho)$, $T_1(\rho)$, $T_0(\rho)$ and $A(\rho)$ are the functions of the bending coordinate. The bending operator derived by Hougen, Bunker, and Johns (HBJ),[17] which allows the handling of large amplitude bending vibrations, was used in this study. The last term of Eq. (2) couples two adiabatic components of the degenerate state, and, hence, the problem should be solved in a two-dimensional electronic basis. In order to avoid singularities of the Hamiltonian matrix elements, a diabatic basis, formed by the unitary transformation of the adiabatic one, was used. The matrix form of the Hamiltonian in the diabatic basis (vibronic Hamiltonian) is:

$$\begin{pmatrix} \begin{gathered}\frac{V^{+}+V^{-}}{2}-\frac{1}{2}\left(T_{1}\frac{\partial^{2}}{\partial\rho^{2}}+T_{2}\frac{\partial}{\partial\rho}+T_{0}\right)+\\ A(K^{2}+\frac{C^{++}+C^{--}}{2}-2KB^{+-})+\Sigma B^{+-}A_{\mathrm{SO}}\end{gathered} & \frac{V^{+}-V^{-}}{2} \\ \frac{V^{+}-V^{-}}{2} & \begin{gathered}\frac{V^{+}+V^{-}}{2}-\frac{1}{2}\left(T_{1}\frac{\partial^{2}}{\partial\rho^{2}}+T_{2}\frac{\partial}{\partial\rho}+T_{0}\right)+\\ A(K^{2}+\frac{C^{++}+C^{--}}{2}+2KB^{+-})-\Sigma B^{+-}A_{\mathrm{SO}}\end{gathered} \end{pmatrix} \quad (3)$$

where $V^{\pm}$ are adiabatic potentials, K is quantum number corresponding to the total orbital angular momentum. C^{++} and C^{--} are diagonal matrix elements of the square of the electronic orbital angular momentum ($\hat{L}_{z}{}^{2}$), and B^{+-} is the off-diagonal matrix element of $\hat{L}_{z}{}^{2}$.

The vibronic Schrödinger Equation was solved variationally using previously developed methods.[18–24] The vibronic wave functions were expanded in the sine basis, and all terms of the Hamiltonian (Eq. (3)) were expanded in sine or cosine bases, depending on their parity. The matrix elements of the vibronic Hamiltonian were than computed as the sums of simple trigonometric integrals, and the obtained matrix was diagonalized.

To explain the effect of spin–orbit and vibronic coupling on the ordering of the vibronic levels, another variational approach was used. All terms of the Hamiltonian were expanded in the polynomial form, and Laguerre polynomials (labeled by the two quantum numbers v and l, $|v,l\rangle$) were used as the basis for expansion of the wave function. In this case, the Bunker–Landsberg (BL) Hamiltonian was used as the kinetic energy operator for the bending vibrations. However, in the case when the bond lengths are constant, as in the present study, the BL Hamiltonian reduces to the Hougen–Bunker–Johns (HBJ) Hamiltonian.

Vibronic transition moments between the $X^2\Pi$ and $1^2\Sigma^+$ states

Perpendicular vibronic transitions between the $X^2\Pi$ and $1^2\Sigma^+$ states, which correspond to the selection rule $\Delta K = \pm 1$, are allowed within the framework of the $C_{\infty v}$ point group. When the symmetry is lowered to C_s, because of bending, parallel vibronic transitions, that correspond to the $\Delta K = 0$ selection rule, become allowed.[20] The vibronic transition intensities are proportional to the squares of the vibronic transition moments. Their forms, in the cases of parallel and perpendicular transitions, were especially derived for the present study:

$$\begin{aligned} W(K'=K'') &\propto \frac{1}{2\pi}\left|\langle m_{\Sigma^{+}}|R_{z}^{++}|n_{\Pi^{+}}\rangle+\langle m_{\Sigma^{+}}|R_{z}^{++}|n_{\Pi^{-}}\rangle\right|^{2} \\ W(K'=K''+1) &\propto \frac{1}{2}\frac{1}{2\pi}\left|\langle m_{\Sigma^{+}}|R_{x}^{++}-R_{y}^{+-}|n_{\Pi^{+}}\rangle+\langle m_{\Sigma^{+}}|R_{x}^{++}+R_{y}^{+-}|n_{\Pi^{-}}\rangle\right|^{2} \\ W(K'=K''-1) &\propto \frac{1}{2}\frac{1}{2\pi}\left|\langle m_{\Sigma^{+}}|R_{x}^{++}+R_{y}^{+-}|n_{\Pi^{+}}\rangle+\langle m_{\Sigma^{+}}|R_{x}^{++}-R_{y}^{+-}|n_{\Pi^{-}}\rangle\right|^{2} \end{aligned} \quad (4)$$

$|n_{\Pi^{\pm}}\rangle$ and $|m_{\Sigma^{+}}\rangle$ are vibronic wave functions of the Π and Σ states, respectively, and $R^{+\pm}_{(x,y,z)}$ are the Cartesian components of the electronic transition moments between the components of the Π and Σ states. The first sign (+) in the superscript denotes the symmetry of the Σ^+ state, and the second sign (+ or –) denotes the symmetry of the component of the Π state. The molecule is placed such that the y-axis of the space-fixed system is perpendicular to the molecular plane at bent geometries.

The electronic transition moments were calculated as matrix elements of the dipole moment operator in the adiabatic electronic basis. The electronic wave functions were determined up to the phase factor in *ab initio* calculations, resulting in ambiguity of the sign of the computed electronic transition moments. In the case of perpendicular transitions, the values of vibronic transition moments depend on the sign of the electronic transition moments (Eq. (4)). For this reason, the correct sign of the electronic transition moments should be determined. The electronic transition moments, as electronic wave functions themselves, are monotonic functions of the molecular coordinates. Secondly, their sign at linear geometry could be determined using asymptotic dependences of the electronic functions and components of the dipole moment operator on the coordinate α (which is coordinate conjugate to the electronic angular momentum), which are of the following forms:[25]

$$\begin{gathered}\Psi^0_{\Pi^+} \propto \cos\alpha,\ \Psi^0_{\Pi^-} \propto \sin\alpha,\ \Psi^0_{\Sigma^+} \propto 1 \\ R_{ex} \propto \cos\alpha,\ R_{ey} \propto \sin\alpha\end{gathered} \tag{5}$$

The asymptotic values of the electronic transition moments are then:

$$\begin{gathered}R^{++}_{ex} = \left\langle \Psi_{\Sigma^+} \middle| R_{ex} \middle| \Psi_{\Pi^+} \right\rangle \propto \frac{1}{\pi}\int_0^{2\pi} \cos\alpha\ \cos\alpha d\alpha = 1 \\ R^{+-}_{ey} = \left\langle \Psi_{\Sigma^+} \middle| R_{ey} \middle| \Psi_{\Pi^-} \right\rangle \propto \frac{1}{\pi}\int_0^{2\pi} \sin\alpha\ \sin\alpha d\alpha = 1\end{gathered} \tag{6}$$

Both R^{++}_{ex} and R^{+-}_{ey} have positive values at linear geometry and during bending vibrations they change such that their dependence on bending coordinate is monotonic. The dependence of *ab initio* electronic transition moments on the bending coordinate is shown in Fig. 1.

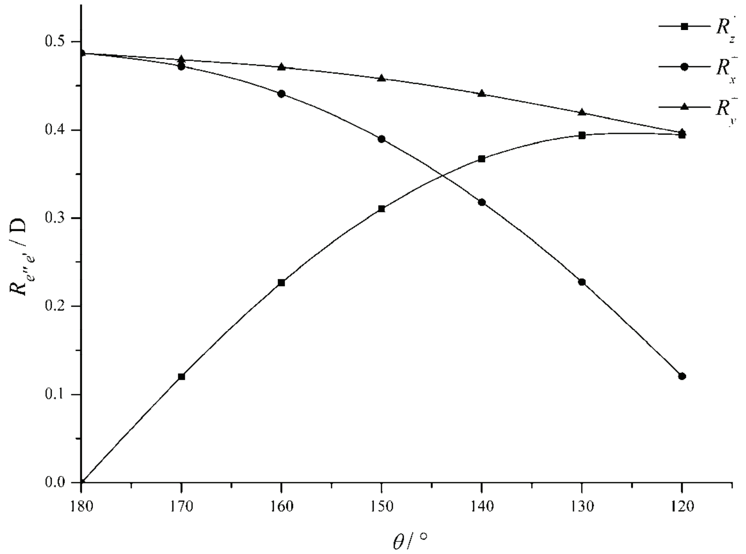

Fig. 1. MRCI bending potential energy curves of the lowest-lying doublet electronic states of HCP$^+$. Symmetric (A') electronic states are represented by full lines, and antisymmetric states (A'') by dashed lines.

To calculate vibronic transition moments, electronic transition moments fitted in trigonometric series and vibronic wave functions obtained by diagonalization of vibronic Hamiltonian were used. In this way, the vibronic transition moments are again represented as the sums of the simple trigonometric integrals.

RESULTS AND DISCUSSION

Electronic states

The computed MRCI bending energy curves of the lowest-lying doublet electronic states of HCP^+ are presented in Fig. 2. Degenerate electronic states are characterized by a lifting of the orbital degeneracy upon bending, *i.e.*, by the Renner–Teller (RT) effect. The $X^2\Pi$ and $1^2\Phi$ state are characterized by weak RT effects, where both state components have minima at linear geometries. The other states are examples of strong RT effects: one component of the $2^2\Pi$ and the $3^2\Pi$ state have minima at linear geometry, whereas in the cases of the $1^2\Delta$ and $2^2\Delta$ states, both of the components have minima at nonlinear geometries. In the case of a weak RT effect, the splitting of the potential energy curves upon bending in the vicinity of linear geometry follows the theoretically predicted dependence, $\rho^{2\Lambda}$, *i.e.*, the $X^2\Pi$ state shows a large splitting, whereas the splitting of the $1^2\Phi$ state is negligible.

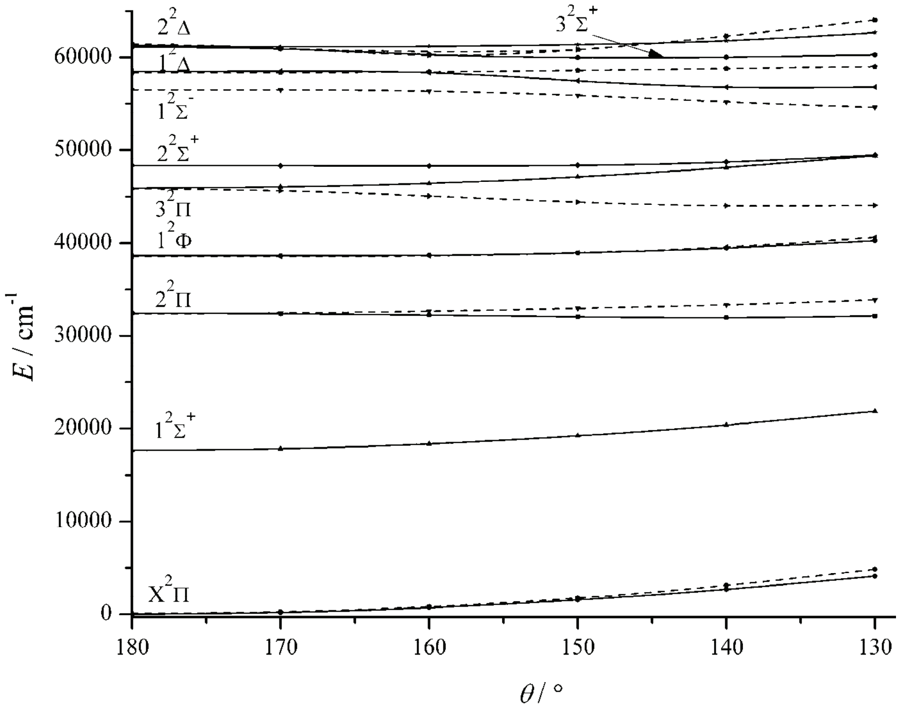

Fig. 2. Magnitudes of spin–orbit splittings of some non-unique levels in the $X^2\Pi$ state.

The electronic configuration of the X$^2\Pi$ state is $(5\sigma)^2(6\sigma)^2(7\sigma)^2(2\pi)^3$. According to the present results, the $1^2\Sigma^+$ state is formed by excitation of an electron from the 7σ to the 2π orbital, and the $2^2\Pi$, $1^2\Phi$, and $3^2\Pi$ states by excitation from the 2π to the 3π orbital. When an electron is promoted from the 7σ to the 3π orbital, three doublet states are formed, *i.e.*, $1^2\Sigma^-$, $1^2\Delta$, and $2^2\Delta$. The $7\sigma^1\ 2\pi^3\ 3\pi^1$ configuration can also give rise to quartet of states. The $2^2\Sigma^+$ and $3^2\Sigma^+$ states have more complex electronic structure - they can be approximately represented by linear combinations of three electronic configurations, $\ldots(5\sigma)^2(6\sigma)^1(7\sigma)^2(2\pi)^4$, $\ldots(5\sigma)^2(6\sigma)^2(7\sigma)^1(2\pi)^3(3\pi)^1$ and $\ldots(5\sigma)^1(6\sigma)^2(7\sigma)^2(2\pi)^4$ (Table I). Karna and Grein[9] found that the configurations obtained by excitation of an electron from the 7σ to the 4π orbital contribute significantly to some excited states ($2^2\Pi$, $1^2\Delta$ and $1^2\Sigma^-$). The present calculations were performed such that 4π orbital was also a part of the active space, but the configuration state functions in which it was occupied by an electron gave negligible contributions to the wave functions of the mentioned states. Differences in the electronic configurations explain the significant discrepancies in the vertical excitation energies in cases of the $2^2\Pi$ and $1^2\Sigma^-$ states (Table I). Unfortunately, no experimental results are available for these states. The calculated excitation energies of the other excited states are in plausible accordance with the available theoretical results.

TABLE I. Electronic configurations of the ten lowest-lying doublet electronic states of HCP$^+$, vertical excitation energies, electronic transition moments and oscillator strengths for transitions from the ground X$^2\Pi$ state to the corresponding excited states

State ($C_{\infty v}$)	Dominant configurations	T_e / cm^{-1}	$\lvert R_{e''e'}\rvert$ / D	f
X$^2\Pi$	$\ldots(5\sigma)^2(6\sigma)^2(7\sigma)^2(2\pi)^3$	0.00	1.545209 (z)	–
$1^2\Sigma^+$	$\ldots(5\sigma)^2(6\sigma)^2(7\sigma)^1(2\pi)^4$	17507[b] 18067 16776	0.464382 (x,y)	0.0071
$2^2\Pi$	$\ldots(5\sigma)^2(6\sigma)^2(7\sigma)^2(2\pi)^2(3\pi)^1$	32159 26939	0.623049 (z)	0.0236
$1^2\Phi$	$\ldots(5\sigma)^2(6\sigma)^2(7\sigma)^2(2\pi)^2(3\pi)^1$	38508	Forbidden	
$3^2\Pi$	$\ldots(5\sigma)^2(6\sigma)^2(7\sigma)^2(2\pi)^2(3\pi)^1$	45769	0.358802 (z)	0.0028
$2^2\Sigma^+$	$c_1\lvert\Psi_1\rangle+c_2\lvert\Psi_2\rangle+c_3\lvert\Psi_3\rangle$ [a]	48120 49119	0.487279 (x,y)	0.0215
$1^2\Sigma^-$	$\ldots(5\sigma)^2(6\sigma)^2\ (7\sigma)^1(2\pi)^3(3\pi)^1$	57414 60572	0.482024 (x,y)	0.0251
$1^2\Delta$	$\ldots(5\sigma)^2(6\sigma)^2\ (7\sigma)^1(2\pi)^3(3\pi)^1$	58244 57669	0.700384 (x,y)	0.2149
$3^3\Sigma^+$	$c_1'\lvert\Psi_1\rangle+c_2'\lvert\Psi_2\rangle+c_3'\lvert\Psi_3\rangle$ [a]	60849	0.592387 (x,y)	0.0402
$2^2\Delta$	$\ldots(5\sigma)^2(6\sigma)^2\ (7\sigma)^1(2\pi)^3(3\pi)^1$	61129	1.054598 (x,y)	0.5115

[a] The vectors $\lvert\Psi_1\rangle, \lvert\Psi_2\rangle$ and $\lvert\Psi_3\rangle$ denote the electronic configurations $(5\sigma)^2(6\sigma)^1(7\sigma)^2(2\pi)^4$, $(5\sigma)^2(6\sigma)^2(7\sigma)^2(2\pi)^3$ and $(5\sigma)^1(6\sigma)^2(7\sigma)^2(2\pi)^4$, respectively; [b] The first values of T_e in the cells were obtained in this study, the second values (where available) are theoretical values obtained by Karna and Grein[9] and the third result for the $1^2\Sigma^+$ state is an experimental value

In order to inspect the character of the excited states, the vertical ionization energy from the ground state of the HCP$^+$ ion to the X$^1\Sigma^+$ state of the HCP^{2+} was computed. It is found that the vertical ionization energy, expressed in wave numbers, was $IP_V = 156800$ cm^{-1}. The energetic terms of the Rydberg states can be calculated by application of the Rydberg Formula, $T_n = IP - R / (n - \Delta)^2$,[26] where IP is the ionization energy, R is the Rydberg constant, n is the principal quantum number, and Δ is the quantum defect of the state in question. It could be estimated that the lowest-lying Rydberg states (for $n - \Delta = 1$) of the HCP$^+$ could be expected at approximately 47000 cm^{-1} above the minimum of the ground state. There is a possibility that the $2^2\Sigma^+$, $1^2\Sigma^-$, $1^2\Delta$, $3^2\Sigma^+$ and $2^2\Delta$ states are Rydberg states because their vertical excitation energies surpass the given value. In order to inspect this, calculations of the vertical excitation energies were performed with aug-cc-pVTZ basis sets augmented by one set of diffuse *s* and *p* orbitals built in an even tempered manner from the exponents of the two most diffuse *s* and *p* functions[27] (exponents of additional diffuse functions are: hydrogen *s* (0.006212) and *p* (0.026815); carbon *s* (0.015080) and *p* (0.0101536); phosphorous *s* (0.015856) and *p* (0.009702)). The excitation energies of all the studied states obtained with the augmented set differed negligibly from those obtained with aug-cc-pVTZ set. Hence, it was concluded that the studied electronic states do not have marked Rydberg character.

By inspecting the calculated values of the electronic transition moments at linear geometry (Table I), it could be concluded that the most probable are transitions to the $1^2\Delta$ and $2^2\Delta$ states. The transition moments to other states are of smaller magnitude.

The dimensionless quantity that expresses the strength of the transition between two quantum states, oscillator strength, is defined as:

$$f_{12} = \frac{2}{3}(E_2 - E_1)\sum_{m_2}\sum_{\alpha=\mathrm{x,y,z}}\left|\langle 1m_1|R_\alpha|2m_2\rangle\right|^2 \tag{7}$$

where E_1 and E_2 are the energies of the $|1m_1\rangle$ and $|2m_2\rangle$ quantum states, which can have several degenerate sub-states labeled by m_1 and m_2. R_α are the Cartesian components of the electronic transition operator between states. All quantities in Eq. (7) are expressed in atomic units. The calculated values of the oscillator strengths for transitions between the ground and studied excited states are presented Table I. The most intensive transitions to $2^2\Delta$ and $1^2\Delta$ are expected. The oscillator strengths for other transitions are at least one order of magnitude smaller.

Vibronic structure of the X$^2\Pi$ state

The bending potential curves of the X^{2}A' and 1^2A'' components of the X$^2\Pi$ state are fitted in a polynomial form as the functions of the coordinate ρ:

$$\begin{aligned} E(X\,^2A') &= 0.026135\rho^2 - 0.002018\rho^4 \\ E(1^2\,A'') &= 0.027678\rho^2 - 0.001252\rho^4 \end{aligned} \tag{8}$$

where the energies are expressed in hartrees and the angles in radians.

The most important molecular parameters of the X$^2\Pi$ state obtained in this study using *ab initio* methods and the available experimental and theoretical values are given in Table II. The calculated parameters are compared with the corresponding experimental values.

TABLE II. Molecular parameters of HCP$^+$ in the X$^2\Pi$ state

Parameter	MRCI/CASSCF/ aug-cc-pVTZ (this work)	Emission spectrum study[3,4]	LIF spectrum study[5a]
r_{HC} / Å	1.0839	1.11(4)	1.077(2)
r_{CP} / Å	1.6129	1.596(5)	1.6013(3)
ω_1 / cm^{-1}	3144	–	2986.0 (3124.8)
ω_2 / cm^{-1}	639	–	717.5 (642.7)
ω_3 / cm^{-1}	1277	1150.0	1282.0 (1156.0)
A_{SO} / cm^{-1}	–129.3	–146.97	–148.4
ε	–0.0313	–	(–0.034(2))
$\varepsilon\omega_2$/ cm^{-1}	–20.0	–26.(4)	–22.0

The X$^2\Pi$ state is characterized by a relatively large value of the spin–orbit coupling constant (A_{SO} = –148.4 cm^{-1}), which is approximately seven times larger than the product of the Renner parameter and the bending frequency ($\varepsilon\omega_2$ = = 22 cm^{-1}). According to this, it would be expected that the spin–orbit interaction determines the ordering of the vibronic levels.

The computed bending vibronic levels up to ≈2500 cm^{-1} of Σ (K = 0), Π (K = 1), Δ (K = 2), and Φ (K = 3) symmetries of the X$^2\Pi$ electronic states, the available experimental values and the compositions of the vibronic wave functions in terms of Laguerre polynomials are given in Table III. The theoretical values obtained variationally by Biczysko and Tarroni[11] are also given. They were able to reproduce satisfactorily the energies, but the order of some levels was different from the experimental assignment. For example, this was the case with the close-lying (0,2,0)$\mu\Pi_{3/2}$ and (0,2,0)$\mu\Pi_{1/2}$ levels. Only the results obtained with the first described variational method (with expansions in trigonometric basis) are presented. They are in satisfactory agreement with experimental and theoretical results. The second method based on the expansion in Laguerre polynomials gives excellent results for the low-lying vibronic levels, but significant deviations from the available experimental values occur for the higher levels. The second method is here used to obtain the approximate compositions of the vibronic wave functions in terms of Laguerre polynomials.

The magnitude of the spin–orbit splittings of the unique levels (represented with one Laguerre polynomial) is equal to the spin–orbit constant (for example,

$(0,0,0)\Pi_{3/2}$ and $(0,0,0)\Pi_{1/2}$, $(0,1,0)\Delta_{3/2}$ and $(0,1,0)\Delta_{5/2}$). On the other hand, the obtained spin components of the non-unique levels, which are approximately described as linear combinations of two Laguerre polynomials, are very close to each other. In the absence of spin–orbit coupling, the contribution of both polynomials is approximately equal. When spin–orbit coupling is taken into account, the contribution of one Laguerre polynomial becomes dominant and of the other one much smaller, because relatively strong spin–orbit interaction "tends" to decouple relatively weakly coupled vibronic levels. The signs of the expansion coefficients are such that when one vibronic level is combined with $\Sigma = 1/2$ or $\Sigma = -1/2$, the energies of both obtained spin components are shifted in the same direction compared to the case when spin–orbit interaction is not taken into account (Fig. 3). For this reason, the obtained spin components are very similar in energies in some cases and the magnitude of their splitting depends on the strength of the vibronic coupling. Hence, the level of sophistication in treatment of kinetic energy and anharmonic resonances can significantly influence the structure of the spectrum.

TABLE III. Energies obtained in this study for the lowest vibronic levels in the $X^2\Pi$ state, and the available theoretical and experimental values

Level	Composition	E / cm^{-1}		
		Calculated (this work)	Experimental[4]	Calculated[11]
$(0,0,0)\Pi_{3/2}$	$\|0,0\rangle$ (u)	0.0	0.0	0.0
$(0,0,0)\Pi_{1/2}$	$\|0,0\rangle$ (u)	148.3	148.1	148.2
$(0,1,0)\mu\Sigma^+$	$0.986\|1,1\rangle+0.163\|1,-1\rangle$	632.6	633.4	631.6
$(0,1,0)\Delta_{5/2}$	$\|1,1\rangle$ (u)	636.8	648.3	642.6
$(0,1,0)\kappa\Sigma^-$	$-0.162\|1,1\rangle+0.986\|1,-1\rangle$	790.4	786.5	787.0
$(0,1,0)\Delta_{3/2}$	$\|1,1\rangle$ (u)	785.1	796.0	790.1
$(0,2,0)\mu\Pi_{3/2}$	$0.975\|2,0\rangle-0.219\|2,2\rangle$	1240.8	1260.9	1257.3
$(0,2,0)\mu\Pi_{1/2}$	$-0.282\|2,0\rangle+0.959\|2,2\rangle$	1262.1	1256.0	1259.2
$(0,2,0)\Phi_{7/2}$	$\|2,2\rangle$ (u)	1271.5		1290.9
$(0,2,0)\kappa\Pi_{1/2}$	$0.958\|2,0\rangle+0.280\|2,2\rangle$	1408.4	1426.8	1418.8
$(0,2,0)\Phi_{5/2}$	$\|2,2\rangle$ (u)	1420.0		1437.5
$(0,2,0)\kappa\Pi_{3/2}$	$0.217\|2,0\rangle-0.975\|2,2\rangle$	1429.8		1433.5
$(0,3,0)\mu\Sigma^+$	$0.937\|2,0\rangle-0.348\|4,2\rangle$	1868.7		1871.8
$(0,3,0)\mu\ \Delta_{3/2}$	$-0.404\|3,1\rangle+0.915\|3,3\rangle$	1909.3		1887.3
$(0,3,0)\mu\ \Delta_{5/2}$	$0.966\|3,1\rangle-0.254\|3,3\rangle$	1875.3	1896.1	1889.2
$(0,3,0)\kappa\Sigma^-$	$-0.345\|2,0\rangle+0.935\|4,2\rangle$	2056.1		2053.7
$(0,3,0)\kappa\ \Delta_{3/2}$	$0.912\|3,1\rangle+0.401\|3,3\rangle$	2055.3		2058.1
$(0,3,0)\kappa\ \Delta_{5/2}$	$0.251\|3,1\rangle+0.966\|3,3\rangle$	2089.5		2086.9
$(0,4,0)\mu\Pi_{3/2}$	$0.923\|4,0\rangle-0.383\|4,2\rangle$	2494.8		2490.9
$(0,4,0)\mu\Pi_{1/2}$	$-0.459\|4,0\rangle+0.888\|4,2\rangle$	2509.6	2492.5	2492.3

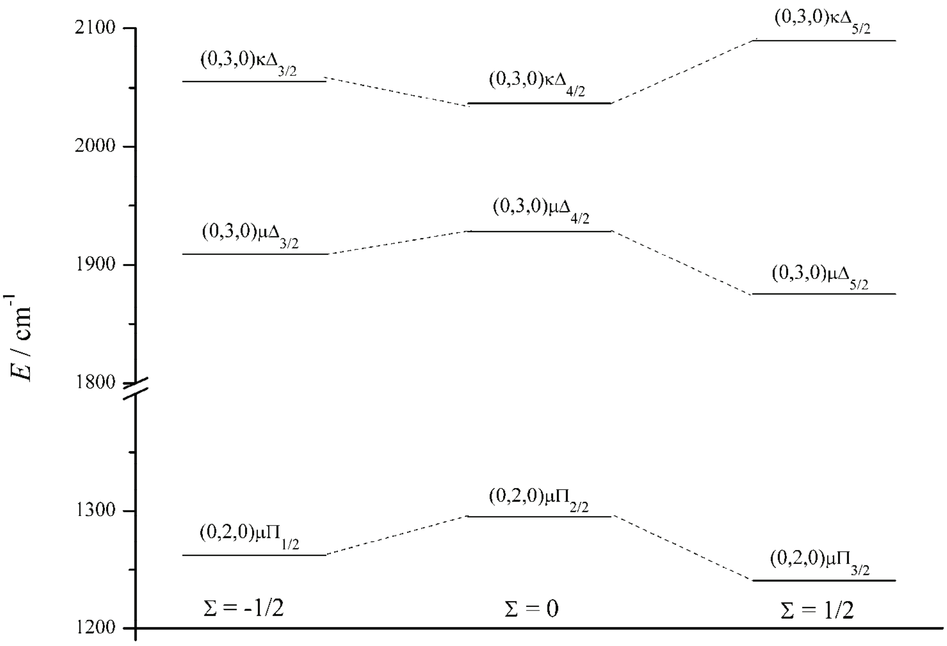

Fig. 3. Dependence of the electronic transition moments between the $X^2\Pi$ and $1^2\Sigma^+$ states on the bending coordinate.

Vibronic transitions between the $X^2\Pi$ and $1^2\Sigma^+$ states

The squared values of the vibronic transition moments between low-lying vibronic levels of the $X^2\Pi$ and $1^2\Sigma^+$ states are given in Table IV. According to the results, vibronic transitions corresponding to the $\Delta K = 0$ selection rule are of low intensity. The reason for this is that the *z*-component of the electronic transition moment, which induces these transitions, is zero at linear geometry and becomes large only when molecule is significantly bent.

On the other hand, several intensive perpendicular transitions ($\Delta K = \pm 1$) occur. The most intensive ones arise from unique levels of the $X^2\Pi$ state, particularly from the lowest unique $K'' = 1$ level, $|0,0\rangle$ to the lowest $K' = 1$ level of the $1^2\Sigma^+$ state, which is also described by a $|0,0\rangle$ polynomial. Also, the transition between unique $K'' = 2$ $|1,1\rangle$ level to the $|1,1\rangle$ level of the $1^2\Sigma^+$ state is intensive. Several intensive transitions from non-unique levels of the $X^2\Pi$ state composed predominantly of one Laguerre polynomial to vibronic levels of the $1^2\Sigma^+$ state described by the same Laguerre polynomial exist. For example, the transition between the first $K'' = 0$ level, which is approximately described as $-0.163|1,-1\rangle + 0.986|1,1\rangle$ and the first K' = 1 level composed of $|1,1\rangle$ polynomial is intensive.

TABLE IV. Squared vibronic transition moments in D^2 between the vibronic levels of the $X^2\Pi$ and $1^2\Sigma^+$ states for the case $\Sigma = -1/2$. The vibronic levels of the $X^2\Pi$ state are placed vertically and the levels of the $1^2\Sigma^+$ state are placed horizontally. The compositions of the vibronic levels in terms of Laguerre polynomials are given for each level

$K'' = 0$	$K' = 0$				
	$\|0,0\rangle$	$\|2,0\rangle$	$\|4,0\rangle$	$\|6,0\rangle$	$\|8,0\rangle$
$0.163\|1,-1\rangle+0.986\|1,1\rangle$	0.709–2	0.629–2	0.189–4	0.871–6	0.166–5
$0.986\|1,-1\rangle-0.162\|1,1\rangle$	0.165–1	0.145–1	0.521–4	0.204–5	0.377–5
$0.348\|3,-1\rangle+0.937\|3,1\rangle$	0.145–4	0.771–2	0.612–2	0.237–4	0.233–5
$0.935\|3,-1\rangle-0.345\|3,1\rangle$	0.735–4	0.322–1	0.250–1	0.148–3	0.873–5
$0.483\|5,-1\rangle+0.875\|5,1\rangle$	0.708–6	0.696–5	0.420–2	0.378–2	0.180–5
$K'' = 1$	$K' = 0$				
	$\|0,0\rangle$	$\|2,0\rangle$	$\|4,0\rangle$	$\|6,0\rangle$	$\|8,0\rangle$
$\|0,0\rangle$	0.225+0	0.116–6	0.450–5	0.306–6	0.281–7
$-0.282\|2,0\rangle+0.959\|2,2\rangle$	0.834–4	0.217–1	0.104–3	0.558–6	0.152–4
$0.958\|2,0\rangle+0.280\|2,2\rangle$	0.961–3	0.180+0	0.340–3	0.399–5	0.451–6
$-0.459\|4,0\rangle+0.888\|4,2\rangle$	0.803–4	0.360–3	0.492–1	0.806–3	0.122–3
$0.884\|4,0\rangle+0.454\|4,2\rangle$	0.270–4	0.736–3	0.134+0	0.318–3	0.574–4
$K'' = 1$	$K' = 2$				
	$\|2,2\rangle$	$\|4,2\rangle$	$\|6,2\rangle$	$\|8,2\rangle$	$\|10,2\rangle$
$\|0,0\rangle$	0.488–3	0.656–4	0.994–4	0.873–4	0.491–3
$-0.282\|2,0\rangle+0.959\|2,2\rangle$	0.173+0	0.109–2	0.948–4	0.173–4	0.334–1
$0.958\|2,0\rangle+0.280\|2,2\rangle$	0.214–1	0.425–3	0.200–4	0.286–4	0.152–2
$-0.459\|4,0\rangle+0.888\|4,2\rangle$	0.177–2	0.142+0	0.128–2	0.197–4	0.704–4
$0.884\|4,0\rangle+0.454\|4,2\rangle$	0.141–1	0.983–2	0.476–1	0.626–4	0.700–5
$K'' = 0$	$K' = 1$				
	$\|1,1\rangle$	$\|3,1\rangle$	$\|5,1\rangle$	$\|7,1\rangle$	$\|9,1\rangle$
$0.163\|1,-1\rangle+0.986\|1,1\rangle$	0.120+0	0.702–1	0.892–2	0.165–2	0.346–3
$0.986\|1,-1\rangle-0.162\|1,1\rangle$	0.544–2	0.614–3	0.249–3	0.113–5	0.231–6
$0.986\|1,-1\rangle-0.162\|1,1\rangle$	0.306–1	0.822–1	0.560–1	0.616–2	0.238–2
$0.935\|3,-1\rangle-0.345\|3,1\rangle$	0.569–2	0.941–2	0.962–3	0.124–2	0.403–4
$0.483\|5,-1\rangle+0.875\|5,1\rangle$	0.142–1	0.112–1	0.588–1	0.576–1	0.164–2
$K'' = 1$	$K' = 1$				
	$\|1,1\rangle$	$\|3,1\rangle$	$\|5,1\rangle$	$\|7,1\rangle$	$\|9,1\rangle$
$\|0,0\rangle$	0.778–2	0.364–2	0.544–3	0.713–4	0.819–5
$-0.282\|2,0\rangle+0.959\|2,2\rangle$	0.524–2	0.120–1	0.366–7	0.159–5	0.750–8
$0.958\|2,0\rangle+0.280\|2,2\rangle$	0.155–2	0.397–1	0.214–2	0.464–3	0.143–3
$-0.459\|4,0\rangle+0.888\|4,2\rangle$	0.883–3	0.265–2	0.687–2	0.459–5	0.275–4
$0.884\|4,0\rangle+0.454\|4,2\rangle$	0.243–3	0.669–2	0.622–1	0.320–2	0.156–3
$K'' = 2$	$K' = 1$				
	$\|1,1\rangle$	$\|3,1\rangle$	$\|5,1\rangle$	$\|7,1\rangle$	$\|9,1\rangle$
$\|1,1\rangle$	0.125+0	0.705–1	0.914–2	0.166–2	0.334–3
$-0.404\|3,1\rangle+0.915\|3,3\rangle$	0.488–2	0.157–1	0.114–1	0.498–3	0.398–3
$0.912\|3,1\rangle+0.401\|3,3\rangle$	0.309–1	0.756–1	0.448–1	0.684–2	0.198–2
$-0.550\|5,1\rangle+0.834\|5,3\rangle$	0.642–2	0.554–2	0.276–1	0.282–1	0.155–3
$0.828\|5,1\rangle+0.543\|5,3\rangle$	0.141–1	0.983–2	0.476–1	0.307–1	0.369–2

In conclusion, all intensive vibronic transitions between the $X^2\Pi$ and $1^2\Sigma^+$ states correspond to the selection rules $\Delta K = \pm 1$ and $\Delta v = 0$. They occur between levels whose wave functions overlap significantly, which is the case between unique levels of the $X^2\Pi$ state or non-unique levels of similar composition as the unique ones and vibrational levels of the $1^2\Sigma^+$ state composed of the same Laguerre polynomial.

CONCLUSIONS

The low-lying doublet excited states of HCP$^+$ were studied by means of the internally contracted MRCI method. The computed bending potentials of the $X^2\Pi$ state were employed in variational calculations of the vibronic energy levels using the model Hamiltonian that neglects coupling between stretching and bending modes. The applied method gave results for the vibronic levels that were in accordance with the experimental values up to 2500 cm^{-1}. The obtained wave functions were utilized for the calculation of the vibronic transition moments between the $X^2\Pi$ and $1^2\Sigma^+$ states. According to the results, the most intensive are perpendicular transitions with the selection rule $\Delta v = 0$ between unique levels of the $X^2\Pi$ state or non-unique levels of similar composition as the unique ones and vibrational levels of the $1^2\Sigma^+$ state.

Acknowledgments. The author gratefully acknowledges Professor Fiedrich Grein for sending a copy of his paper on the HCP$^+$ and Professor Miljenko Perić for support and for allowing the use of his programs for solving the vibronic Schrödinger Equation. This study was financially supported by the Ministry of Education, Science and Technological Development of the Republic of Serbia (Project No. 172040).

ИЗВОД

AB INITIO ПРОУЧАВАЊЕ ВИБРОНСКИХ ПРЕЛАЗА ИЗМЕЂУ $X^2\Pi$ И $1^2\Sigma^+$ СТАЊА HCP$^+$

ЉИЉАНА СТОЈАНОВИЋ

Факултет за физичку хемију, Универзитет у Београду, Студентски трг 12, 11158 Београд

Дублетна нисколежећа електронска стања HCP$^+$ су проучавана помоћу методе мултиреферентне интеракције конфигурација. Енергије вибронских нивоа $X^2\Pi$ стања Σ, Π, Δ, и Φ симетрија до 2500 cm^{-1} су израчунате применом варијационих метода које узимају у обзир вибронску и спин–орбитну интеракцију. Израчунате вибронске таласне функције су искоришћене у прорачунима момената прелаза између вибронских нивоа $X^2\Pi$ и $1^2\Sigma^+$ електронских стања. Добијене вредности су упоређене са доступним експерименталним и теоријским резултатима.

(Примљено 15. новембра, ревидирано 25. новембра 2012)

REFERENCES

1. D. C. Frost, S. T. Lee, C. A. McDowell, *Chem. Phys. Lett*. **23** (1973) 472
2. M. A. King, H. W. Kroto, J. F. Nixon, D. Klapstein, J. P. Maier, O. Marthaler, *Chem. Phys. Lett*. **82** (1981) 543

3. M. A. King, D. Klapstein, H. W. Kroto, J. P. Maier, J. F. Nixon, *J. Mol. Struct*. **80** (1982) 23
4. M. A. King, R. Kuhn, J. P. Mayer, *Mol. Phys*. **60** (1987) 867
5. F. X. Sunahori, X. Zhang, D. J. Clouthier, *J. Chem. Phys*. **127** (2007) 104312
6. F. T. Chau, Y. W. Tang, X. Song, *J. Mol. Struct*. *(THEO-CHEM)* **280** (1993) 233
7. P. J. Bruna, G. Hirsch, R. J. Buenker, S. D. Peyerimhoff, in *Molecular Ions: Geometric and Electronic Structures*, NATO ASI Ser. B, vol. 90, J. Berkowitz and K.-O. Groeneveld, Eds., Plenum Press, New York, 1983, p. 309
8. P. Botschwina, P. Sebald, *J. Mol. Spectrosc*., **100** (1983) 1
9. S. P. Karna, F. Grein, *Chem. Phys. Lett*. **169** (1990) 161
10. B. Temelso, N. A. Richarson, L. Sari, Y. Yamaguchi, H. F. Schaefer, *J. Theor. Comput. Chem*. **4** (2005) 707
11. M. Biczysko, R. Tarroni, *Phys. Chem. Chem. Phys*. **4** (2002) 708
12. a) H.-J. Werner, P. J. Knowles, *J. Chem. Phys*. **89** (1988) 5803; b) P. J. Knowles, H.-J. Werner, *Theor. Chim. Acta* **84** (1992) 95
13. a) H.-J. Werner, P. J. Knowles, *J. Chem. Phys*. **82** (1985) 5053; b) P. J. Knowles, H.-J. Werner, *Chem. Phys. Lett*. **115** (1985) 259
14. T. H. Dunning, Jr., *J. Chem. Phys*. **90** (1989) 1007
15. MOLPRO, a package of *ab initio* programs designed by H.-J. Werner and P. J. Knowles, version 2006.1, http://www.molpro.net
16. M. Perić, S. D. Peyerimhoff, in *The Role of Degenerate States in Chemistry*, *Advances in Chemical Physics*, Vol. 124, M. Baer, G. D. Billing, Eds., Wiley, New York, 2002, p. 583
17. J. T. Hougen, P. R. Bunker, J. W. C. Johns, *J. Mol. Spectrosc*. **34** (1970) 136
18. M. Perić, S. D. Peyerimhoff, R. J. Buenker, *Mol. Phys*. **49** (1983) 379
19. M. Perić, S. D. Peyerimhoff, R. J. Buenker, *Int. Rev. Phys. Chem*. **4** (1985) 85
20. M. Perić, R. J. Buenker, S. D. Peyerimhoff, *Mol. Phys*. **59** (1986) 1283
21. M. Perić, B. Ostojić, J. Radić-Perić, *Phys. Rep*. **290** (1997) 283
22. S. Jerosimić, Lj. Stojanović, M. Perić, *J. Chem. Phys*. **133** (2010) 024307
23. M. Perić, B. Engels, S. D. Peyerimhoff, in *Quantum Mechanical Electronic Structure Calculations with Chemical Accuracy*, S. R. Langhoff, Ed., Kluwer, Dordrecht, 1995, p. 261
24. S. Jerosimić, M. Perić, *J. Chem. Phys*. **129** (2008) 144305
25. Lj. Stojanović, S. Jerosimić, M. Perić, *Chem. Phys*. **379** (2011) 57
26. M. Perić, S. D. Peyerimhoff, in *The Role of Rydberg States in Spectroscopy and Photochemistry*, C. Sándorfy, Ed., Kluwer, Dordrecht, The Netherlands, 1999, p. 137
27. R. Vetter, T. Ritschel, L. Zülicke, K. Peterson, *J. Phys. Chem., A* **107** (2003) 1405.

Journal of the Serbian Chemical Society
JSCS-info@shd.org.rs • www.shd.org.rs/JSCS

J. Serb. Chem. Soc. 78 (7) 987–995 (2013)
JSCS–4475

UDC 546.831–31:53.085.2+543.57
Original scientific paper

The influence of chemical and thermal treatment on the point of zero charge of hydrous zirconium oxide

JOVAN B. STANKOVIĆ[1], SLOBODAN K. MILONJIĆ[2]*# and SLAVICA P. ZEC[2]

[1]*High Medical School, Cara Dušana 254, Belgrade, Serbia and* [2]*The Vinča Institute of Nuclear Sciences, University of Belgrade, Belgrade, Serbia*

(Received 10 October, revised 16 December 2012)

Abstract: Two zirconia samples were prepared by precipitation from aqueous zirconium oxychloride and zirconyl sulfate solutions with potassium hydroxide. The prepared zirconia samples were amorphous. The pH_{pzc} values of the zirconia samples, determined in NaCl and $NaNO_3$ solutions, were 6.6±0.1 and 6.9±0.1, respectively. After prolonged hydration of zirconia in doubly distilled water, the pH_{pzc} decreased to 4.7±0.3. Crystallization into tetragonal (metastable) + monoclinic zirconia appeared at 691 K. Above 873 K, the tetragonal metastable phase changes to a monoclinic phase. It was shown that crystallite sizes of zirconia treated at 673–1273 K increased from 9.5 to 40.5 nm, respectively. The increase in temperature from 385 to 1070 K increased the pH_{pzc} of zirconia samples from 6.6 to 9.0, respectively.

Keywords: zirconium oxide; point of zero charge; thermal analysis; surface properties.

INTRODUCTION

Inorganic sorbents, especially metal oxides, can withstand high temperatures and high radiation doses. One of them is hydrous zirconium oxide used for the removal of corrosion products from nuclear reactor cooling systems, and as a catalyst support or membrane for various catalysts. Furthermore, zirconium oxide has been widely used, both pure and in mixtures with other oxides or compounds, for the preparation of both traditional and advanced ceramic materials. Finally, zirconium oxide has been used as a column packing material for gas chromatography and high-performance liquid chromatography.

In the last three decades, many experimental and theoretical attempts have been made to explain the chemical behavior of the oxide/aqueous interface. Solid oxides in aqueous suspensions are, in general, electrically charged. The main

---

* Corresponding author. E-mail: smiloni@vinca.rs
\# Serbian Chemical Society member.
doi: 10.2298/JSC121010149S

reasons for this are amphoteric association and dissociation of protons and hydroxyl groups existing on the oxide surface.[1,2] Therefore, the double layer at an oxide/aqueous interface can be investigated by studying the equilibrium distribution of these ions (called potential determining ions) between the surface and the bulk of the solution.

One of the main characteristics of aqueous metal oxide suspensions is the point of zero charge (pH_{pzc}), which represents the suspension pH value at which an immersed oxide surface has zero net charge or the sum of surface positive and negative charges is zero (for hydrous zirconium oxide):

$$\sum[(=\mathrm{ZrO}^-)+(=\mathrm{ZrO_2}^+)]=0 \qquad (1)$$

Addition of hydrous zirconium oxide to the solution of higher pH than pH_{pzc} leads to a decrease in formed suspension pH. Similar, but opposite effect, will occur if the oxide is added to the solution of lower pH than pH_{pzc}. Such effects are the result of the charge formed on the oxide interface[3,4] accompanied by the sorption of ions from the solution. The sorption of cations occurs in the region of pH above pH_{pzc}, while that of anions in the region of pH below pH_{pzc}.

In the present study, a ZrO_2/H_2O system was investigated with the aim of determining the influence of different sample preparations and physicochemical treatments on the point of zero charge of hydrous zirconium oxide.

EXPERIMENTAL

Hydrous zirconium oxide samples were prepared by precipitation from aqueous zirconium oxychloride ($ZrOCl_2\cdot 8H_2O$) solution (sample 1) and zirconium sulfate ($Zr(SO_4)_2\cdot H_2O$) solution (sample 2) (concentration 0.71 mol dm^{-3}) with potassium hydroxide (3.0 mol dm^{-3}), similar to the procedure described previously.[5,6] All chemicals, obtained from various commercial sources, were of A. R. quality and used “as received”.

The resultant precipitates were filtered and thoroughly washed with doubly distilled water until neutral reaction. Then, the precipitates were dried in air at 383 K for 72 h and lightly crushed.

Thermal analysis experiments (TGA and DTA) were performed in air (Dupont 1090 instrument) up to 875 K at a heating rate of 10–20 K min^{-1}. In addition, the obtained graphs were converted into digital form/format using the Graph digitizer program.

The calcinations of the samples was performed (in a Pt crucible) in a drying oven or in a Heraous ceramic furnace (depending on the calcinations temperature) for 4 h.

Structural characterization of the dry and calcined samples was performed by X-ray diffraction (XRD) analysis (Siemens Kristalloflex 4 with a GM counter). The XRD patterns were transformed from graphical form into digital data using the Graph Digitizer program. The apparent crystallite sizes of the prepared zirconia powders were calculated from the full-width at half-maximum height of the (111) XRD peaks using the Scherrer formula[7] corrected for instrumental broadening, the method most frequently used in the literature:

$$D = 0.89\lambda/(\beta_{1/2}\cos\theta) \qquad (2)$$

where D is the crystallite diameter, nm, 0.89 is a constant, λ is the wavelength for CuK$_\alpha$ (equal to 0.15405 nm), $\beta_{1/2}$ is the half-width of the maximum intensity peak of the XRD pattern and θ is the Bragg angle.

The point of zero charge (pH$_{pzc}$) was determined by the batch equilibration technique.[8,9] The samples of hydrous zirconium oxide (0.500 g) with 50 cm^3 of NaCl or NaNO$_3$ solution were shaken in PVC vials for 4 h at 294 K. The initial pH values of the NaCl or NaNO$_3$ solution (in the pH range from 2.5 to 10.5) were adjusted by the addition of a small amount of HCl or NaOH (concentration of 0.1 mol dm^{-3}) solution, keeping the ionic strength constant.

RESULTS AND DISCUSSION

The dependence of the pH$_f$ of the filtered solutions, after equilibration with hydrous zirconium oxide, on the initial pH$_i$ gives a smooth curve with a plateau at a pH that represents the pH$_{pzc}$ (as was shown in previous papers[6,8,9]). The obtained pH$_{pzc}$ value (sample 1) was 6.6±0.1 (obtained using NaCl solutions of three different ionic strengths).[6] In addition, the obtained value for sample 2 was also pH$_{pzc}$ 6.6±0.1. The same pH$_{pzc}$ value for both samples indicates that the prepared samples had the same surface stoichiometry. This pH$_{pzc}$ value is in good agreement with the results of other authors[10–13] (pH$_{pzc}$ 6.4–6.7). The pH$_{pzc}$ value of 4.0 reported by Milonjić *et al*.[9] refers to a hydrous zirconium oxide sample prepared by precipitation with ammonia. It is obvious that the surface stoichiometry of the oxide was changed by this synthesis procedure.

Most likely, the nature of the cations of the precipitating reagent could cause a change in the surface stoichiometry, and even in the surface purity and water content of the zirconia sample.

In the next experiment, a NaNO$_3$ electrolyte was used instead of a NaCl one. The dependence pH$_f$ *vs*. pH$_i$ (0.001, 0.01, and 0.1 mol dm^{-3} NaNO$_3$) for sample 1 is shown in Fig. 1 (pH$_{pzc}$ 6.9±0.1). Good agreement between the obtained pH$_{pzc}$ values (determined using 0.1 mol dm^{-3} NaCl and NaNO$_3$ solutions) denotes that there was no specific sorption of Na$^+$, Cl$^-$ and NO$_3^-$ on hydrous zirconium oxide.

The hydrous zirconium oxide already used in determination of the pH$_{pzc}$ (sample 1) was collected, thoroughly washed with distilled water until neutral, dried at 385 K for 24 h (sample denoted as sample 1-U), and reused in pH$_{pzc}$ determination experiments (from now on, all experimental data were obtained using 0.1 mol dm^{-3} NaCl solution). A decrease in the pH$_{pzc}$ was found (pH$_{pzc}$ 4.6±0.3).

To determine the effect of sorbed ions (possibly present on the oxide surface) on pH$_{pzc}$, a desorption experiment was performed using sample 1-U. The experiment was performed with dilute HNO$_3$ (0.1 mol dm^{-3}) at a solid/liquid ratio of 5 g:100 cm^3 and an equilibration time of 2 h. The desorption procedure was performed three times. Finally, after filtration, the zirconium sample 1-U was thoroughly washed with distilled water until neutral and dried at 385 K for

24 h. The pH_{pzc} of so-treated sample was 4.7±0.3. The obtained pH_{pzc} value is in good agreement with the pH_{pzc} value of the same sample 1-U determined before desorption. This means that the eventually sorbed ions (Na^+ or NO_3^-) have no influence on the pH_{pzc} value of the ZrO_2 sample.

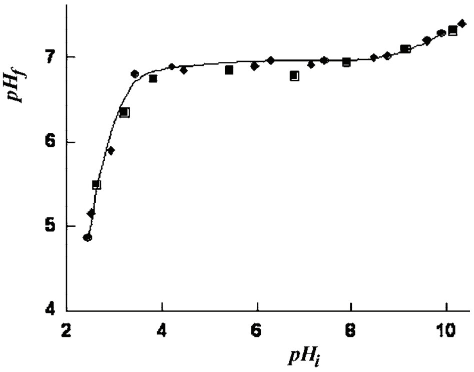

Fig. 1. pH_f *vs*. pH_i of zirconia (sample 1) suspensions. • – 0.001, □ – 0.01, ♦ – 0.10 mol dm^{-3} $NaNO_3$.

To explain the obtained pH_{pzc} value, the zirconia powder was further investigated. Fresh samples (sample 1) were placed in PVC bottles filled with doubly distilled water and equilibrated for various times (from 50 to 400 h). Then, the samples were filtrated, thoroughly washed with distilled water until neutral, dried at 383 K for 24 h, and used for pH_{pzc} determination.

The obtained pH_{pzc} values are shown in Fig. 2. A decrease in the pH_{pzc} of the zirconia samples with increasing hydration time is evident. A smooth curve with a plateau at pH_{pzc} 4.7±0.3 indicates the influence of the hydrolysis/hydration time on the pH_{pzc} of the hydrous zirconium oxide. Most likely, the differences in pH_{pzc} in the present experiments were caused by the sorption or formation of simple zirconium hydrolytic complexes on the surface, which changed the surface stoichiometry. This is in accordance with the results of other authors for several oxides. Kanungo and Parida[14] showed that the pH_{pzc} of MnO_2 increases with decreasing water content in the oxide. In the case of MnO_2[15] and RuO_2,[16] the pH_{pzc} values underwent significant changes in the acid direction on passing from “dry” crystalline forms to hydrous oxides. Moreover, hydroxides were reported to present pH_{pzc} values more acidic than the corresponding “dry” oxides (CuO, Fe_2O_3 and Al_2O_3).[17]

Parks[18] indicated that one of the mechanisms of the formation of charges on oxide surfaces in aqueous solutions is the sorption of metal hydroxocomplexes derived from hydrolysis of the solid material, as might have been the case in the present investigations.

When used as a sorbent, hydrous zirconium oxide exposed to high temperatures undergoes some kind of thermal decomposition and transformation. The thermogravimetric (TG) and differential thermogravimetric (DTG) results for

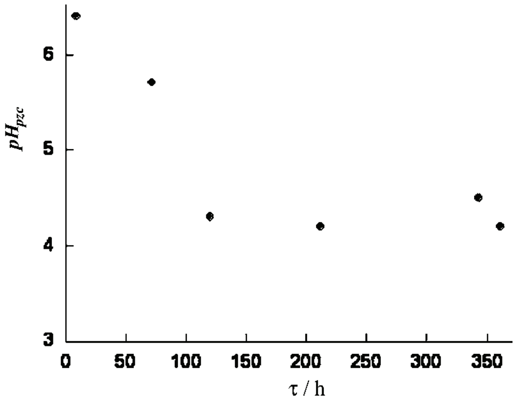

Fig. 2. The dependence of the pH_{pzc} of zirconia (sample 1) on the time of equilibration with deionized water.

fresh sample 1 are illustrated in Fig. 3. The sample lost about 20 % of structure water ($ZrO_2 \cdot nH_2O$, n between 1 and 2), which corresponds to the loss of 1.5–1.6 molecules of H_2O. The ZrO_2 sample contained adsorbed water, which was totally removed at around 500 °C. This is in good agreement with the result of Ardizzone *et al.*[19] The total mass loss between 100 and 500 °C was 14.4 mass %. This corresponds to the synthesized ZrO_2 having the composition ($ZrO_2 \cdot 1.2H_2O$) after drying in air at 110 °C for 72 h. The mass loss is considered to be the result of the removal of water (both physisorbed and chemisorbed at the surface of the particles). On the DTG curve presented in Fig. 3, three peaks are evident, *i.e.*, one large peak centered at 110 °C and two small ones centered at 207 and 461 °C. A differential thermal analysis (DTA) curve of zirconia sample 1 is given in Fig. 4. The first broad endothermic peak observed on the DTA curve at about 130 °C could be attributed to desorption of water molecules adsorbed on the zirconia surface. The subsequent sharp exothermic peak observed at about 410 °C was due to phase transformation (*i.e.*, crystallization) of the zirconia.

The XRD data for untreated zirconium particles and samples thermally treated at different temperatures are shown in Fig. 5. The X-ray diffraction pat-

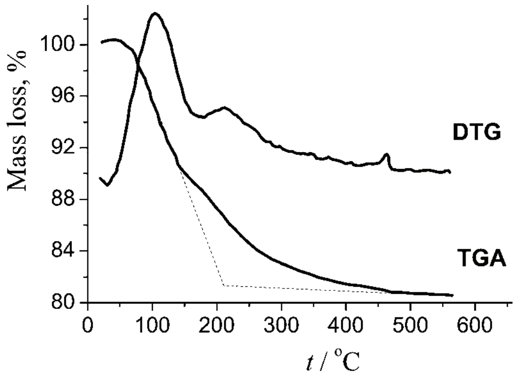

Fig. 3. The TG and DTG curves for zirconia (sample 1).

tern of the prepared, thermally untreated (385 K), sample shows no peaks except a broad, weak one at 2*θ* 25–35°. This indicates that the prepared zirconium particles were amorphous. Amorphous precipitates usually transform into the metastable tetragonal phase upon thermal treatment, then into a mixture of tetragonal and monoclinic phases and finally into the monoclinic phase.

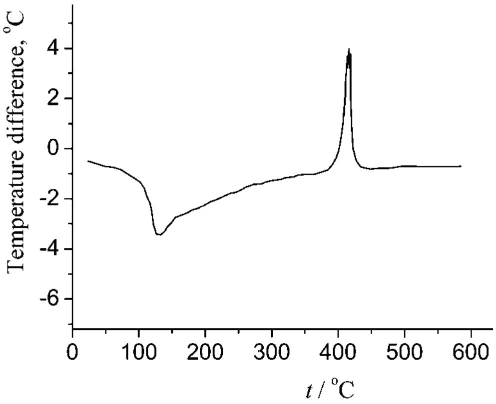

Fig. 4. The differential thermal analysis curves for zirconia (sample 1).

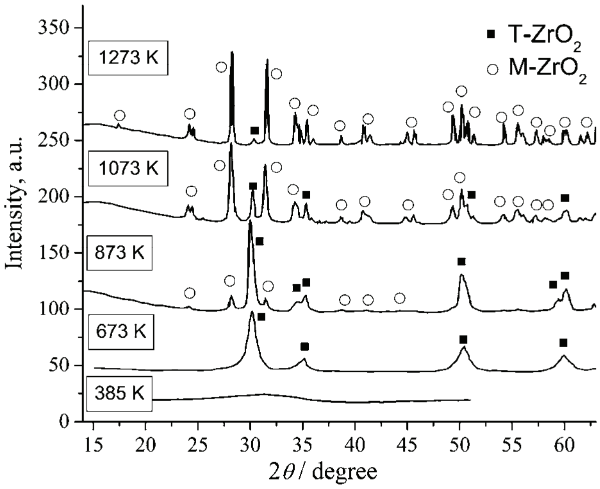

Fig. 5. XRD Patterns of zirconia (sample 1) treated at various temperatures.

Crystallization into tetragonal (metastable) ZrO_2 appeared at 691 K (Figs. 4 and 5). Samples calcinated at 873 and 1073 K were a mixture of monoclinic and metastable tetragonal phases. The sample calcinated at 1273 K (or above) was monoclinic. This is in good agreement with the recently published result of Bortun *et al.*[20] The broad peak[21] at 2*θ* 30° (Fig. 5) consists of two peaks, one for the monoclinic and one for the tetragonal phase (at a temperature above 720 to 870 K these peaks are distinguishable).[21,22] Above 873 K, the tetragonal metastable phase changes to the monoclinic one.[22]

The calculated crystallite diameters of the ZrO_2 samples (treated at 673, 873, 1073 and 1273 K) are plotted against calcination temperatures in Fig. 6. The crystallite size of the tetragonal phase (samples thermally treated at 673 and 873 K) was calculated from the characteristic peak 2θ 30.5° (for the (111) reflection, data PDF 14-534), whereas the crystallite size of the monoclinic phase (samples thermally treated at 1073 and 1273 K) was calculated from the characteristic peak 2θ 28.4° (for the (–111) reflection, data PDF 36-420). It is evident that the size of crystallites (*D*) in the ZrO_2 samples increases from about 9 nm after thermal treatment at 673 K to about 40 nm after calcinations at 1273 K. The obtained results are in good agreement with those previously reported by other authors.[19,21,24,28]

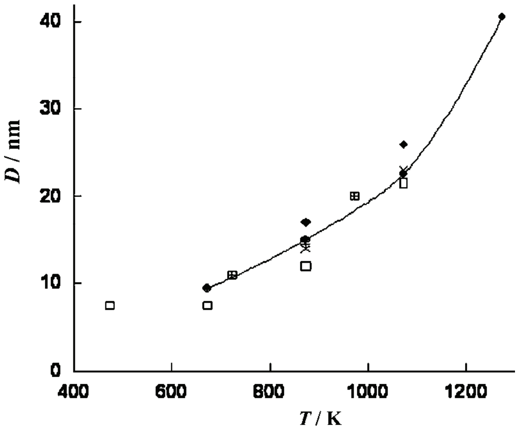

Fig. 6. Effects of treatment temperature on the crystallite size of zirconia (sample 1): • – present results, □ – [17], ♦ – [20], × – [21], + – [22].

The increase in thermal treatment temperature from 385 to about 1070 K increased the pH_{pzc} of sample 1 from 6.6±0.1 to 9.0±0.3. The pH_{pzc} 9.0±0.3 corresponds to crystalline, totally dehydrated, zirconium oxide. According to the data presented, the point of zero charge of hydrous zirconium oxide depended far more on the degree of hydration than on the crystal structure of the oxide. The obtained results are in accordance with the literature data reviewed by Ardizzone and Trasatti.[29] They observed a shift of pH_{pzc}/pH_{iep} in the alkaline direction when going from the hydroxide to the crystalline oxide. The pH_{pzc} values of RuO_2 obtained by calcination of different precursors in the presence of oxygen, at various temperatures, were between 4 (calcined at 300 °C) and 6 (calcined at 500–700 °C).[29] However, Kosmulski,[30] analyzing some literature data, concluded that the (hydro)oxides of some metals at certain degrees of oxidation show consistent pH_{pzc} values that are rather insensitive to the degree of their hydration and crystallographic forms.

CONCLUSIONS

Two zirconia samples were prepared by precipitation from aqueous zirconnium oxychloride and zirconyl sulfate solutions with potassium hydroxide (sample 1 and 2, respectively). The pH_{pzc} values of the zirconia samples, determined from NaCl and $NaNO_3$ solutions, were 6.6±0.1 and 6.9±0.1, respectively. This implies that there is no difference in surface properties of prepared zirconia samples and no specific sorption of Na^+, Cl^- and NO_3^- on hydrous zirconium oxide. After prolonged (100 h) hydration of zirconia in doubly distilled water, the pH_{pzc} decreased to 4.7±0.3. The prepared zirconia samples were amorphous. Crystallization into tetragonal (metastable) + monoclinic zirconia appeared at 691 K. Above 873 K, the tetragonal phase changed to a monoclinic one. It was shown that crystallite sizes of zirconia treated at 673–1273 K increased from 9.5 to 40.5 nm, respectively. The increase in temperature from 385 to 1070 K increased the pH_{pzc} of zirconia samples from 6.6 to 9.0, respectively. The pH_{pzc} value of 9.0 corresponds to totally dehydrated crystalline zirconia.

Acknowledgements. We are grateful to Prof. N. Petranović of the Faculty of Physical Chemistry, University of Belgrade, for the thermal analyses (TGA and DTA) of hydrous zirconium oxide. The research was financially supported by the Ministry of Education, Science and Technological Development of the Republic of Serbia, Project No. 45012.

ИЗВОД

УТИЦАЈ ХЕМИЈСКОГ И ТЕРМИЧКОГ ТРЕТМАНА НА ТАЧКУ НУЛТОГ НАЕЛЕКТРИСАЊА ХИДРАТИСАНОГ ЦИРКОНИЈУМ(IV)-ОКСИДА

ЈОВАН Б. СТАНКОВИЋ[1], СЛОБОДАН К. МИЛОЊИЋ[2] и СЛАВИЦА П. ЗЕЦ[2]

[1]*Виша медицинска школа, Цара Душана 254, Београд и* [2]*Институт за нуклеарне науке "Винча", Универзитет у Београду, Београд*

Таложењем из воденог раствора цирконијум-оксихлорида или цирконил-сулфата са калијум-хидроксидом припремљена су два узорка цирконијум(IV)-оксида. Припремљени узорци цирконијум(IV)-оксида су аморфни. Тачке нултог наелектрисања, pH_{tnn}, припремљених узорака цирконијум(IV)-окисида, одређене из раствора натријум-хлорида и натријум-нитрата, износиле су 6,6±0,1 и 6,9±0,1, редом. После дуже хидратације цирконијум(IV)-оксида у дестилованој води, pH_{tnn} опада до вредности 4,7±0,3. Кристализација цирконијум(IV)-оксида у тетрагоналну (метастабилну) + моноклиничну фазу дешава се при 691 K. Изнад 873 K, тетрагонална метастабилна фаза прелази у моноклиничну. Показано је да величина кристалита цирконијум(IV)-оксида, третираног при 673–1273 K, расте од 9,5 до 40,5 nm, редом. Повишење температуре од 385 до 1070 K води до померања pH_{tnn} од 6,6 до 9,9, редом.

(Примљено 10. октобра, ревидирано 16. децембра 2012)

REFERENCES

1. J. A. Davis, R. O. James, J. O. Leckie, *J. Colloid Interface Sci.* **63** (1978) 480

2. R. O. James, G. A. Parks, *Characterization of Aqueous Colloids by Their Electrical Double-Layer and Intrinsic Surface Chemical Properties*, in: *Surface and Colloid Science*, Vol. 12, E. Matijević, Ed., Wily Interscience, New York, 1982, p. 119
3. A. G. Kokarev, V. A. Kolesnikov, L. M. Tubin, A. A. Korobanov, *Elektrokhimiya* **16** (1982) 466
4. S. M. Ahmed, *Can. J. Chem*. **44** (1966) 1663
5. L. M. Zaitsev, V. N. Zabelin, V. V. Sakharov, N. D. Polishchuk, V. M. Klyuchnikov, I. A. Aproksin, *Zh. Neorg. Khim*. **17** (1972) 60
6. J. B. Stanković, S. K. Milonjić, M. M. Kopečni, T. S. Ćeranić, *J. Serb. Chem. Soc.* **51** (1986) 95
7. B. D. Cullity, *Elements of X-ray Diffraction*, Addison Wesley Pub., USA, 1956
8. S. K. Milonjić, A. Lj. Ruvarac, M. V. Šušić, *Thermochim. Acta* **11** (1975) 261
9. S. K. Milonjić, Z. E. Ilić, M. M. Kopečni, *Colloids Surf.* **6** (1983) 167
10. K. C. Ray, S. Khan, *Indian J. Chem*. **13** (1975) 577
11. M. Kosmulski, *J. Dispersion Sci. Technol*. **23** (2002) 529
12. J. Randon, A. Larbot, C. Guizard, L. Cot, M. Lindheimer, S. Partyka, *Colloids Surf.* **52** (1991) 241
13. A. Pettersson, G. Marino, A. Pursiheimo, J. B. Rosenholm, *J. Colloid Interface Sci*. **228** (2000) 73
14. S. B. Kanungo, K. M. Parida, *J. Colloid Interface Sci*. **98** (1984) 252
15. T. W. Healy, A. P. Hearring, D. W. Furstenau, *J. Colloid Interface Sci*. **21** (1968) 435
16. S. Ardizzone, A. Daghetti, L. Franceschi, S. Trasatti, *Colloids Surf.* **35** (1989) 85
17. R. H. Yoon, T. Salmon, G. Donnay, *J. Colloid Interface Sci*. **70** (1979) 483
18. G. A. Parks, *Chem. Rev*. **65** (1965) 177
19. S. Ardizzone, M. G. Cattania, P. Lazzari, P. Lugo, *Colloids Surf.*, *A* **90** (1994) 45
20. A. Bortun, M. Bortun, J. Pardini, S. A. Khainakov, J. R. García, *Mater. Res. Bull*. **45** (2010) 142
21. T. Mitsuhashi, M. Ichihara, V. Tatsuke, *J. Am. Ceram. Soc.* **57** (1974) 97
22. T. Sato, F. Ozawa, T. Nakamura, H. Watanabe, S. Ikoma, *Thermochim. Acta* **34** (1979) 210
23. B. D. Cullity, *Elements of X-ray Diffraction*, Addison Wesley Pub., USA, 1956
24. S. Ardizzone, G. Bassi, G. Liborio, *Colloids Surf.* **51** (1990) 207
25. M. A. Blesa, A. J. G. Maroto, S. I. Passagio, N. E. Figliolia, G. Rigotti, *J. Mater. Sci*. **20** (1985) 4601
26. E. Crucean, B. Rand, *Trans. J. Brit. Ceram. Soc.* **78** (1979) 58
27. Y. Murase, E. Kato, *J. Am. Ceram. Soc.* **66** (1983) 196
28. R. Gopalan, C.-H. Chang, Y. S. Lin, *J. Mater. Sci*. **30** (1995) 3075
29. S. Ardizzone, S. Trasatti, *Adv. Colloid Interface Sci*. **64** (1996) 173
30. M. Kosmulski, *Adv. Colloid Interface Sci*. **152** (2009) 14.

Journal of the Serbian Chemical Society
JSCS-info@shd.org.rs • www.shd.org.rs/JSCS

J. Serb. Chem. Soc. 78 (7) 997–1011 (2013)
JSCS–4476

UDC 546.655+546.62–034:621.793:
620.193+543.552
Original scientific paper

Electrochemical methods for corrosion testing of Ce-based coatings prepared on AA6060 alloy by the dip immersion method

BORE V. JEGDIĆ[1#], LJILJANA S. ŽIVKOVIĆ[2#], JOVAN P. POPIĆ[3#],
JELENA B. BAJAT[4#] and VESNA B. MIŠKOVIĆ-STANKOVIĆ[4*#]

[1]Institute Goša, Milana Rakića 35, Belgrade, Serbia, [2]The Vinča Institute of Nuclear Sciences, University of Belgrade, P. O. BOX 522, 11001 Belgrade, Serbia, [3]ICTM-Department of Electrochemistry, University of Belgrade, Njegoševa 12, Belgrade, Serbia and [4]Faculty of Technology and Metallurgy, University of Belgrade, Karnegijeva 4, P. O. Box 3503, 11120 Belgrade, Serbia

(Received 12 December 2012, revised 17 January 2013)

Abstract: Dip-immersion is a simple and cost-effective method for the preparation of Ce-based conversion coatings (CeCCs), a promising alternative to toxic chromate coatings, on metal substrates. In this work, CeCCs were prepared on Al-alloy AA6060 from an aqueous solution of cerium chloride at room temperature. The effect of immersion time and post-treatment in phosphate solution on the microstructure and corrosion properties of the coatings was studied. The longer the immersion time was, the thicker but more non-homogeneous and cracked were the CeCCs. The post-treatment contributed to a sealing of the cracks, as proven by an increase in the corrosion resistance compared with the as-deposited coatings. The CeCCs prepared at longer deposition times and post-treated showed much better corrosion protection than those prepared at shorter deposition times. A detailed electrochemical impedance spectroscopy (EIS) study was undertaken to follow the evolution of the corrosion behaviour of the CeCCs with time of exposure to an aggressive chloride environment (3.5 % NaCl). For the sake of comparison, the EIS properties of bare AA6060 were also investigated. Linear voltammetry was performed to complete the study. The results confirmed the formation of protective CeCCs on the surface of AA6060. However, even CeCCs prepared at longer deposition times and post-treated provided short term protection in the aggressive environment, due to the small thickness of the coating.

Keywords: cerium; conversion coatings; aluminium alloy; EIS; linear voltammetry.

---

* Corresponding author. E-mail: vesna@tmf.bg.ac.rs

[#] Serbian Chemical Society member.

doi: 10.2298/JSC121212009J

INTRODUCTION

Conversion coatings containing hexavalent chromium (chromate) have been widely used for decades as part of the corrosion protection system on aluminium alloys. However, chromates are prohibited in many fields due to their toxicity, and replacements that show promise have been extensively investigated.[1–6] Cerium-based conversion coatings (CeCCs) are among the most promising alternatives because of their anti-corrosion efficiency, environmentally benign nature and low cost. The effectiveness of cerium salts as corrosion inhibitors was highlighted in 1984. Hinton *et al*.[7,8] reported that immersing an Al-alloy in a $CeCl_3$-containing solution for several days produced a yellowish Ce-based film that provided significant corrosion protection. Its deposition was driven by the natural electrochemical interactions between the Al matrix and inclusions of intermetallic compounds (IMCs) that make up structural alloys.[9] Wilson and Hinton[10] patented a comercially attractive process for the preparation of CeCCs in the order of minutes, using H_2O_2 to accelerate the deposition kinetics.

The deposition mechanism involves both anodic oxidation of Al, Eq. (1), and cathodic reduction of soluble oxygen and/or added H_2O_2, Eqs. (2 and 3), respectively, as follows:[11–15]

$$Al \rightarrow Al^{3+} + 3e^- \tag{1}$$

$$2H_2O + O_2 + 4e^- \rightarrow 4OH^- \tag{2}$$

$$H_2O_2 + 2e^- \rightarrow 2OH^- \tag{3}$$

The generation of hydroxide ions at cathodic sites leads to a strong local increase in the pH near the alloy surface, which promotes formation of a $Ce(OH)_3$ precipitate or/and soluble ionic complexes, such as $Ce(OH)_2^+$. When H_2O_2 is added, the deposition of Ce(IV) is more favourable than Ce(III):[14,15]

$$Ce^{3+} + 3OH^- \rightarrow Ce(OH)_3 \tag{5}$$

$$2Ce^{3+} + 3OH^- + H_2O_2 \rightarrow 2Ce(OH)_2^+ \tag{6}$$

$$2Ce(OH)_2^+ + 2OH^- \rightarrow Ce(OH)_4 \tag{7}$$

$$Ce(OH)_4 \rightarrow CeO_2 \cdot 2H_2O \tag{8}$$

An inhibition effect was achieved by the insoluble Ce-oxide/hydroxide layer formed at the cathodic sites, which suppresses the oxygen reduction reaction (Eq. (2)), thereby providing cathodic inhibition.[8,16]

The number of variables that influence the rate of CeCC deposition is large and includes solution chemistry (cerium salt used – chloride or nitrate, additives such as gelatine, glycerol to reduce cracking), concentrations of cerium and H_2O_2, pH, temperature, time of immersion, *etc*. In addition, the surface composition and electrochemical behaviour of the range of alloys, as a function of alloying elements, add to the complexity of the deposition mechanism. The most common alloys studied are those rich in copper, AA2024 and AA7075, widely used in aerospace and military applications.[7–10,17–29] According to the island growth model, precipitation of Ce-species commences on cathodically strong, Cu-containing IMCs,[7,8,27–29] and the deposited film subsequently proceeds to grow over the Al matrix. It was shown later[30,31] that, although the cathodic features of Cu enhance the deposition, its presence is not necessarily required. The deposition of Ce was also observed to occur on low Cu alloys (AA5xxx and AA6xxx), on IMCs of cathodic nature with respect to the matrix.[32–35]

A limited number of studies report on the formation of CeCCs on AA6xxx.[11,28,35–39] However, owing to the attractive combinations of properties, the AA6xxx series is of particular interest in the aerospace and automotive industry as potential replacements for the expensive AA2xxx and AA7xxx.[39,40] The benefits include medium strength, formability and weldability, due to the Mg_2Si intermetallics formed when silicium and magnesium are added in appropriate amounts. They are also heat treatable.

CeCCs can be prepared by different chemical methods, such as spontaneous immersion, spraying and electrolytic routes. Major steps in the coating process are pre-treatment (acid or alkaline) of the substrate surface,[12,20–24] deposition and subsequent post-treatment.[12,25,26] Declaroy and Petitjean[11] showed that any etching sequence of AA6xxx must finish with an alkaline pre-treatment for successful CeCC deposition.

In this work experimental parameters for the preparation of ceria-based layers on the AA6060 by the dip immersion method were studied. In particular, the time of immersion of the substrate in the conversion solution was investigated, as well as the effect of subsequent post-treatment of the deposited coatings on their microstructure and corrosion properties. Electrochemical methods: linear voltammetry and electrochemical impedance spectroscopy (EIS) were applied for the corrosion testing. The time-dependent EIS behaviour of the CeCCs and of alkali etched AA6060, as the substrate, on exposure to an aggressive chloride environment (3.5 % NaCl) were detailed and compared with the aim of estimating the quality of CeCCs and the duration of protection.

EXPERIMENTAL

Pre-treatment of the substrate and coating deposition

Cerium conversion coatings were prepared on (50 mm×25 mm×0.8 mm) panels of commercial AA6060 alloy used as a substrate. Prior to deposition, the panels were abraded with SiC papers # 600 and #1000, ultrasonically desmutted in acetone for 2 min, rinsed with distilled water and then degreased and etched in alkaline solution (NaOH 7.5 g dm^{-3}, $Na_3PO_4 \cdot 12H_2O$, 45 g dm^{-3} Na_2SiO_3, 4 g dm^{-3}, ethoxylate nonylphenol 13 g dm^{-3}) at 70 °C for 2 min and rinsed again. The pre-treated panels were immersed for 5 and 20 min in the Ce-containing solution for deposition. An aqueous solution (0.05 M) of $CeCl_3 \cdot 6H_2O$ (Alfa Aesar), acidified to pH 2, was used, with the addition of 24 ml of 30 % H_2O_2 (Fisher Scientific). The coated samples were subjected for 5 min to a post-treatment in a phosphate solution (2.5 % Na_3PO_4, pH 4.5) at 85 °C. The post-treated coatings were rinsed in deionised water and dried in air. All solutions were prepared with analytical grade chemicals and deionised water.

Electrochemical measurements

Electrochemical measurements were performed in an aqueous 0.5 mol dm^{-3} NaCl solution under ambient conditions using a Gamry Reference 600 Potentiostat/Galvanostat/ZRA. The classic three-electrode cell arrangement was used. The working electrode was a coated or bare AA6060 panel situated in a special holder. The counter electrode was a platinum mesh with a surface area considerably greater than that of the working electrode. The reference electrode was a saturated calomel electrode (SCE). The cell assembly was located at a Faraday cage to prevent electrical interferences. The electrochemical impedance spectroscopy (EIS) measurements were performed at the open-circuit potential (OCP), over a frequency range from 300 kHz to 10 mHz, using a 10 mV amplitude sinusoidal voltage. The impedance spectra were analyzed using Gamry Elchem Analyst fitting procedure. The linear sweep voltammetry data were collected at a potential sweep rate of 0.5 mV s^{-1}, starting from the OCP, after a constant value was achieved (up to 30 min). Cathodic and anodic polarizations were performed independently.

Scanning electron microscopy with energy dispersive spectroscopy

A scanning electron microscope (SEM) JEOL JSM-5800, operated at 20 keV, equipped for energy dispersive spectroscopy (EDS) measurements, was used to analyze the morphology and composition of the CeCCs.

RESULTS AND DISCUSSION

The CeCCs microstructure

After 5 min of immersion in the conversion solution, the entire substrate surface underwent a noticeable change in colour, from initial metallic grey to light yellow. The colour turned evenly to dark yellow as the immersion time was increased to 20 min. The change in colour could be taken as an indication of different film thicknesses as a consequence of different deposition times. The CeCCs microstructure was characterized by SEM, a commonly used technique for morphology studies.[3,4,9,41] SEM images of the as-deposited CeCCs, prepared at short and longer deposition times, are presented in Fig. 1.

As can be seen, the films covered, were adherent and had a rather rough surface. Polishing marks were noticeable after 5 min immersion, but they were no longer visible after the longer deposition time. The plan view of the coatings, illustrated in Fig. 2a for the CeCC deposited over 20 min, exhibited an inhomogeneous structure of deposited layers, with numerous defects and cracks. The cracks were more pronounced in the sample prepared at the longer deposition. However, the CeCCs microstructure visibly changed after the post-treatment: the majority of the cracks were effectively sealed, rendering a coating surface with fewer imperfections, as seen for the CeCC after 20 min deposition (Fig. 2b).

The EDS analysis (not shown) performed for CeCCs prepared at 5 and 20 min immersion confirmed a low amount of cerium deposited over the alloy substrate. The weak Ce signals recorded at 0.9 and 4.9 keV were more pronounced for the CeCC prepared for a longer time, *i.e.*, the amount of Ce increased from 1.24 at. % for CeCC deposited for 5 min to 1.97 at. % Ce for the coating deposited for 20 min, which is in accordance with visual observations of the thicknesses of the coatings. After post-treatment in heated phosphate solution, a strong P signal appeared at 2 keV. Since the P content was quantified as 4.51 at. % (more than twice the Ce one) it is reasonable to believe that it allowed a conversion of the entire amount of Ce(CC) to the $CePO_4$ compound (see "Effect of post-treatment").

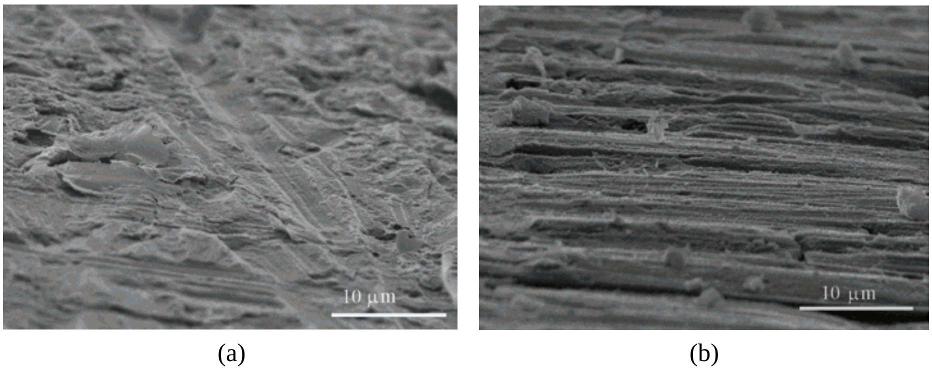

(a) (b)

Fig..1. SEM microphotographs of CeCCs deposited for a) 5 min and b) 20 min (tilted view).

Electrochemical properties of the CeCCs

The electrochemical properties of the CeCCs exposed to 0.5 mol dm^{-3} NaCl were examined by EIS, a commonly used method in corrosion testing.[9,31,34,38,42,43] The method was applied to measure the corrosion resistance of the coatings and to study the effect of the post-deposition treatment. A study was also undertaken to follow the evolution of the EIS properties of CeCC as well as those of alkali-etched AA6060, as the substrate for the deposition of CeCCs, with time of exposure to the corrosive agent. In addition, potentiodynamic measurements were performed to complete the corrosion behaviour study.

Effect of deposition time

The Nyquist plots in complex plane of CeCCs prepared by immersion in cerium-containing deposition solution for different periods (5 and 20 min), and of alkali-etched AA6060, as a reference, after 1 h of exposure to 0.5 mol·dm^{-3} NaCl solution are depicted in Fig. 3. No significant difference in the impedance plots was observed for CeCCs deposited for 5 and 20 min. A possible reason for the similar behaviour could be the cracked surface of the coatings. An increase in thickness, *i.e.*. increase in deposition time, led to further crack propagation. However, the impedance values measured for both CeCCs were almost three times higher than that of bare AA6060.

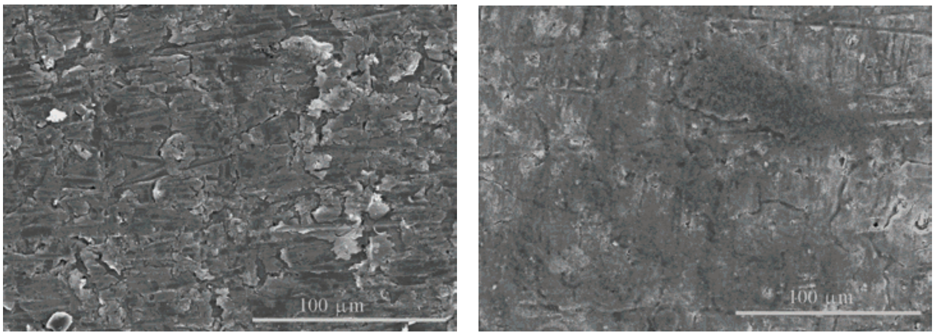

(a) (b)

Fig. 2. SEM microphotographs of CeCCs deposited for 20 min, a) without and b) with post-treatment (plan view).

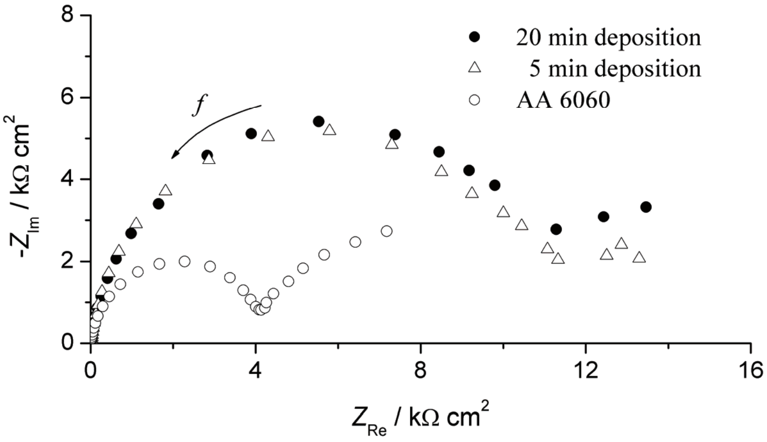

Fig. 3. Nyquist plots for CeCCs deposited for different deposition times and alkali-etched AA 6060, after 1 h of exposure to a 0.5 mol dm^{-3} NaCl solution.

Effect of post-treatment

The purpose of the post-treatment of CeCCs was to improve the corrosion resistance. As reported earlier,[18] immersion of the coatings into a heated phosphate solution immediately after deposition sealed the present cracks, eliminated cerium-peroxide/hydroxide species and altered the chemical composition by converting most of the CeCCs to $CePO_4 \cdot H_2O$, all of which increased the corrosion protection. This study also confirmed (Fig. 2) that the post-treatment induced a change in the microstructure of the CeCCs. Accordingly, the post-deposition sealing of the cracks significantly increased the impedance of the coatings, as illustrated in Fig. 4 for the CeCC prepared in a 20 min deposition; the impedance of the post-treated sample was around 4 times higher than that of the as-deposited one. A similar trend was also registered for the CeCCs deposited for 5 min (Figs. 3 and 4). Although both post-treated CeCCs (5 and 20 min deposition) had higher values of impedance in comparison with that of alkali-etched AA6060, the longer deposition offered much better corrosion protection than the shorter deposition (Fig. 4).

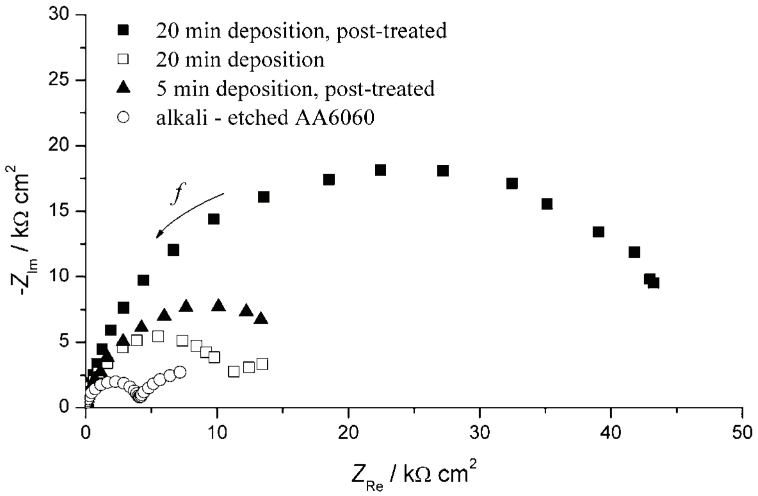

Fig. 4. Nyquist plots for CeCCs, 20 min deposition without and with post-treatment, and 5 min deposition with post-treatment, after 1 h of exposure to a 0.5 mol dm^{-3} NaCl solution.

Polarization measurements

The potentiodynamic polarization measurements gave further information on the behaviour of CeCCs in the corrosive agent (0.5 mol dm^{-3} NaCl). As it was shown that the post-treatment of CeCCs increased the corrosion protection of AA6060, only the post-treated samples were tested. The cathodic and anodic polarization curves registered for the CeCCs deposited for 5 and 20 min and for alkali-etched AA6060, as a reference, are shown in Fig. 5. As can be seen, smaller cathodic currents were measured for the CeCCs than for AA6060, since the CeCCs decreased the cathodic current density of oxygen reduction. The CeCC deposited for 20 min reduced the current more than the one deposited for 5 min, as a result of the diminution of the cathodic sites.[2,44] The retarding effect of CeCCs on the anodic process of the alloy is more easily observed if the anodic curves are presented in a linear rather than in a semi logarithmic form (Fig. 5b). At a fixed potential, for instance –0.575 V, the anodic current densities were 2.73, 1.04 and 0.23 mA cm^{-2} for AA6060 and CeCCs deposited for 5 and 20 min, respectively. This clearly indicates a reduced anodic activity of the CeCCs on AA6060, which was especially pronounced for the sample deposited for 20 min and post-treated. The results confirmed that the CeCCs affected both the cathodic and anodic behaviour of AA6060.

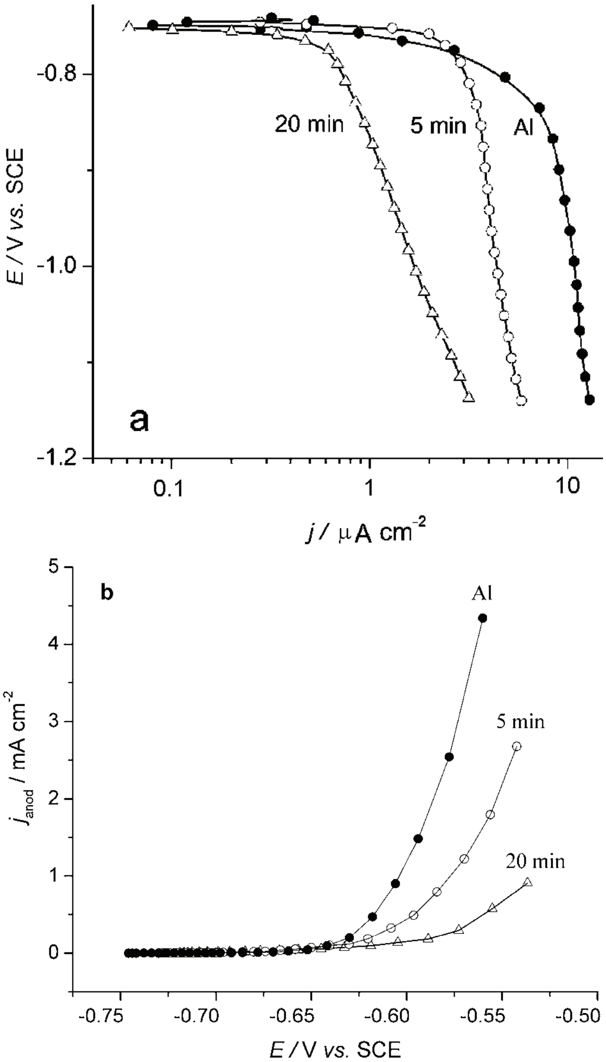

Fig. 5. Cathodic (a) and anodic (b) polarization curves for CeCCs deposited for 5 and 20 min and post-treated, and alkali-etched AA6060 in 0.5 mol dm^{-3} NaCl solution.

Time dependence of the EIS characteristics of CeCC and alkali etched AA6060

For an extensive EIS study, the CeCC deposited for 20 min and post-treated was submitted to a long-time immersion in a 0.5 mol dm^{-3} NaCl solution, since it showed the best protective properties. The evolution in corrosion behaviour of

CeCC, over a month period, is presented in the Bode module and phase plots, Figs. 6a and 6b.

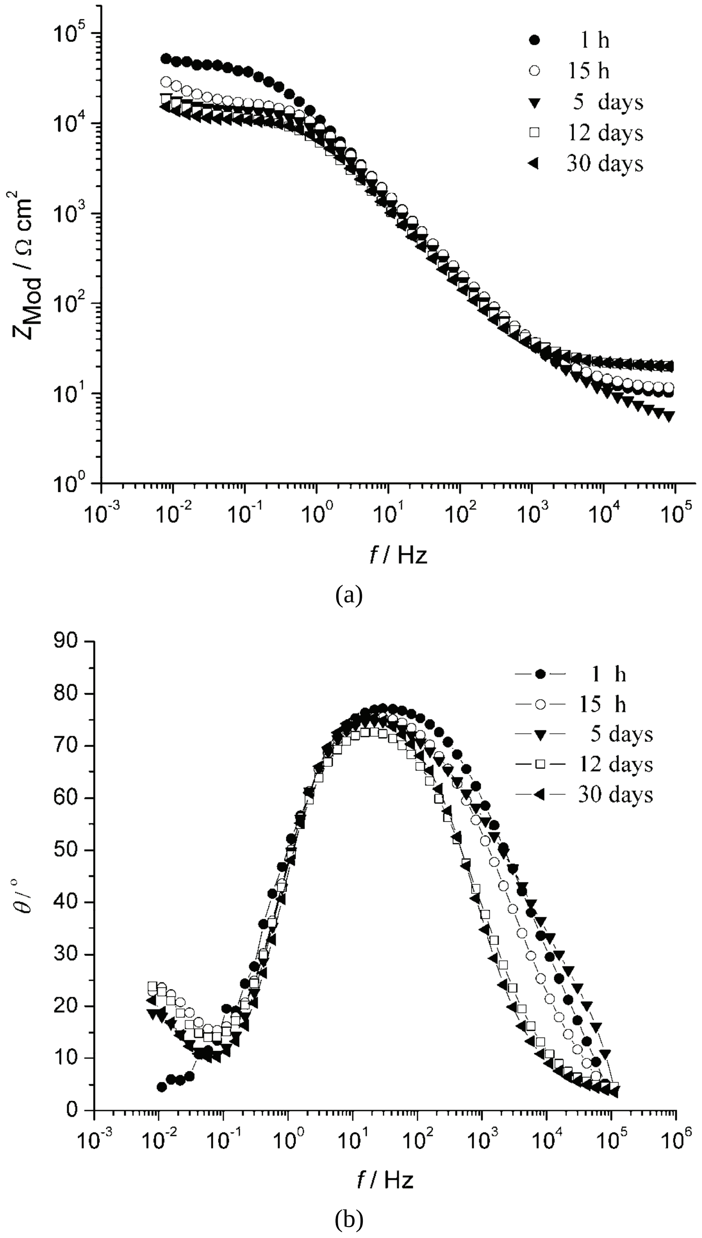

(a)

(b)

Fig. 6. Bode module (a) and phase plots (b) for CeCC deposited for 20 min and post-treated after different times of exposure in 0.5 mol dm^{-3} NaCl solution.

The highest Z_{mod} value (50 kΩ cm^2) was measured at the beginning of exposure (1 h), corresponding to a high pore resistance value of the coating. After 15 h immersion, there was a significant decrease in Z_{mod}. A much smaller change was registered after 5 days, followed by a small, gradual decrease up to 12 days of exposure. In the next 13–30 days, the Z_{mod} attained an almost constant value (15 kΩ cm^2), which was more than 3 times smaller than the initial one. Two time constants could be seen in the EIS spectra, Fig. 6b. The first time constant, appearing at higher frequencies, is associated with the CeCC, while the other one refers to the AA6060 substrate.

The EIS data were fitted using the equivalent electrical circuits shown in Fig. 7. The circuits consist of electrolyte resistance, R_Ω, CeCC pore resistance, R_p, coating capacitance, C_c, charge-transfer resistance, R_{ct}, and CPE, a constant phase element which represents all frequency dependent electrochemical phenomena, namely the double layer capacitance, C_{dl}, and diffusion processes.

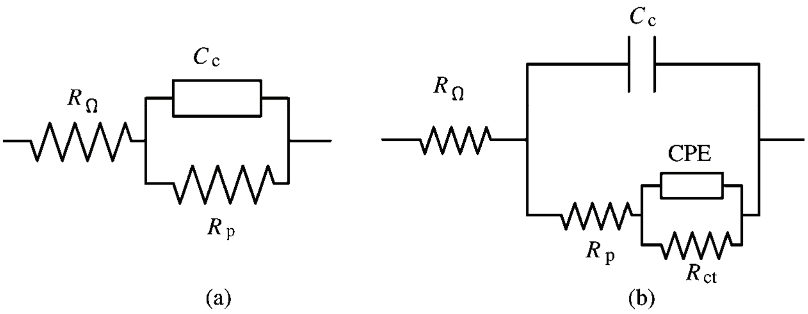

Fig. 7. Equivalent electrical circuits for CeCCs on the AA6060 alloy.

The results obtained are summarized in Fig. 8, which presents the evolution of CeCCs pore resistance and CPE with time. Fig. 8a shows that the highest value of the pore resistance (R_p > 45 kΩ cm^2) was measured for the CeCC just after its immersion in the aggressive chloride solution. The result is in accordance with the cross-sectional SEM observation (inset in Fig. 8a), which indicates a small average thickness (2 μm) of the coating. After 15 h exposure, the R_p value had decreased significantly (≈20 kΩ cm^2). During the following 15 days, the value gradually decreased. From 20 days to the end of tests, the R_p value was nearly unchanged (≈10 kΩ cm^2). The value of the double-layer capacitance (more correctly, constant phase element, CPE) showed a tendency to increase during 20 days of immersion in NaCl solution and then gradually reached a constant value (Fig. 8b).

An EIS study of AA6060, used as the substrate, was also conducted (Figs. 9a and 9b). Prior to the CeCCs deposition, the substrate underwent alkaline etching, as detailed in the Experimental section. This treatment is known to induce the formation of an alumina gel layer on the surface. This non-insulating layer was proven necessary for the deposition of Ce-species on the AA6xxx series, allowing faradic processes to occur. Hughes *et al.*[45] claim that the transfer of OH^- through the hydrated alumina layer assists the progress of the precipitation of cerium species. This layer is progressively substituted by a much more adherent $CeO_2 \cdot 2H_2O$ layer.

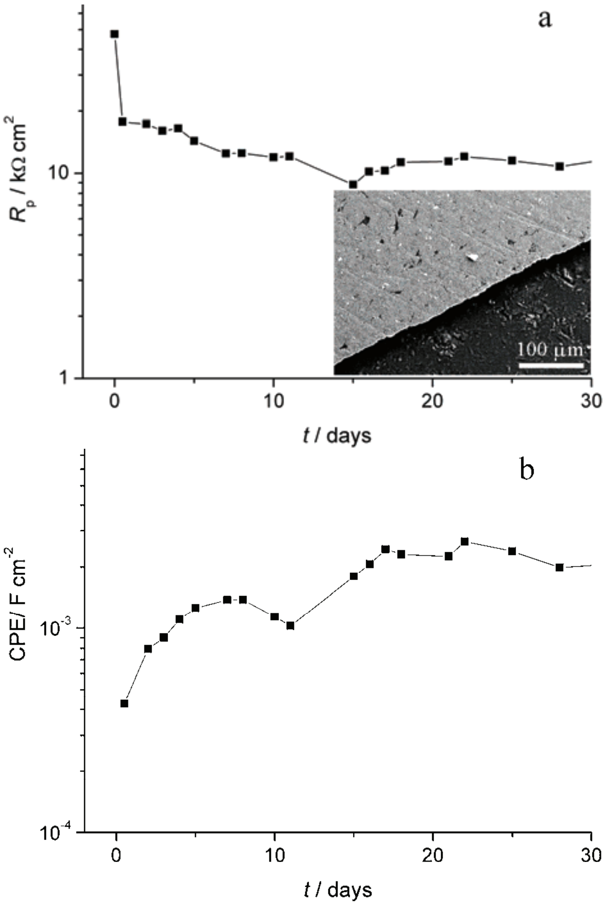

Fig. 8. The time dependences of a) pore resistance, R_p and b) constant phase element, CPE, for CeCC deposited for 20 min and post-treated, during exposure to a 0.5 mol dm^{-3} NaCl solution (inset shows cross-sectional SEM micrograph of CeCC).

The Nyquist plots in complex plane of alkali-etched AA6060 during different exposure times, as well as that of CeCC, given for comparison, are shown in Fig. 9a.

The relatively small impedance value of the alkali-etched AA6060, measured after immersion in the corrosive agent could be attributed to the cracked gel structure, illustrated in Fig. 9b. In the following days (Fig. 9a), the impedance increased gradually. The increase in impedance value with immersion time can be related to the gel wetting and self-healing (crack sealing) and the growth phenomena. On the other hand, it can be seen that already after 12 days of exposure to the NaCl solution, the resistance of the CeCC approached the resistance of the alkali-etched AA6060. Thus, after about 2 weeks, the impedance value of the CeCC attained the impedance value of the alumina gel layer. This result suggests that the CeCC degrades with time, and provides only temporary corrosion protection to the AA6060 alloy, which could be expected for such a thin film in such an aggressive corrosion agent as 0.5 mol dm^{-3} NaCl solution.

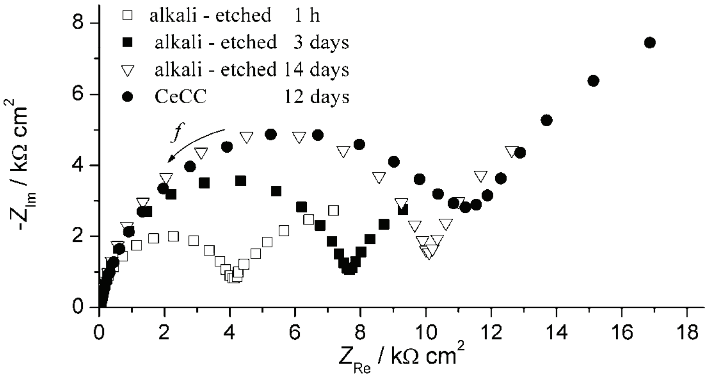

(a)

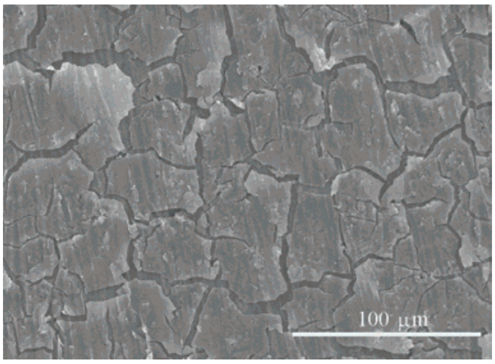

(b)

Fig. 9. a) Nyquist plots for alkali-etched AA6060 after different exposure times to 0.5 mol dm^{-3} NaCl solution and b) for CeCCs and microphotograph of alkali-etched AA6060.

CONCLUSIONS

Cerium conversion coatings (CeCCs) were deposited on AA6060 by immersion in an acidified aqueous solution $CeCl_3$ for 5 and 20 min at room temperature. To accelerate the deposition kinetics, H_2O_2 was added. Cracked layers with non-homogeneous and defect structures were produced. A subsequent post-treatment in a phosphate solution contributed to crack sealing, which improved the protective qualities of the coatings. The layers quality was evaluated from a corrosion perspective using linear sweep voltammetry and EIS, to assess the kinetics of the corrosion process and to estimate the duration of protection in a chloride-containing environment (0.5 mol dm^{-3} NaCl). The CeCCs increased the corrosion resistance of AA6060, slowing down the anodic and cathodic reaction rates with respect to the bare AA6060. The longer deposition time was more effective. However, the EIS study indicated that CeCCs provided only short term protection (2 weeks) to the AA6060 alloy.

Acknowledgment. This research was financed by the Ministry of Education, Science and Technological Development, of the Republic of Serbia (Grant Nos. III 45019 and III 45012).

ИЗВОД

ЕЛЕКТРОХЕМИЈСКЕ МЕТОДЕ ЗА ИСПИТИВАЊЕ КОРОЗИОНЕ СТАБИЛНОСТИ ПРЕВЛАКА НА БАЗИ ЦЕРИЈУМА ДОБИЈЕНИХ ПОТАПАЊЕМ НА ЛЕГУРИ АА6060

БОРЕ В. ЈЕГДИЋ[1], ЉИЉАНА С. ЖИВКОВИЋ[2], ЈОВАН П. ПОПИЋ[3], ЈЕЛЕНА Б. БАЈАТ[4]
и ВЕСНА Б. МИШКОВИЋ-СТАНКОВИЋ[4]

[1]Институт Гоша, Милана Ракића 35, 11000 Београд, [2]Институт за нуклеарне науке Винча, Универзитет у Београду, п. пр. 522, 11001 Београд, [3]ИХТМ – Центар за електрохемију, Универзитет у Београду, Његошева 12, Београд и [4]Технолошко–металуршки факултет, Универзитет у Београду, Карнегијева 4, п. пр. 3503, 11120 Београд

Наношење превлака потапањем у раствор је једноставна и економски прихватљива метода за припрему конверзионих превлака на бази церијума на металним супстратима, које су добра замена за токсичне хроматне превлаке. У овом раду превлаке на бази церијума су нанесене на алуминијумску легуру АА6060 из воденог раствора церијум-хлорида на собној температури. Испитиван је утицај времена потапања и утицај накнадног третмана у фосфатном раствору на микроструктуру и заштитна својства добијених превлака. Дужим потапањем су добијене дебље али нехомогене превлаке. Накнадни третман је повољно утицао на затварање прскотина, што је у сагласности са измереном већом корозионом отпорношћу у поређењу са превлакама без третмана. Превлаке добијене дужим наношењем су показале бољу корозиону заштиту од превлака добијених краћим наношењем. Корозиона стабилност превлака је испитивана у агресивној хлоридној средини (3,5 % NaCl) методама спектроскопије електрохемијске импеданције (СЕИ) и линеарне волтаметрије. Детаљно је праћено корозионо понашање превлака са временом деловања корозионог агенса. Поређења ради, СЕИ анализа је спроведена и за легуру АА6060 без превлаке. Резултати истраживања потврђују да добијене превлаке на бази церијума представљају добру корозиону заштиту легури АА6060. Међутим, чак и квалитетнија превлака (20 мин потапања и накнадно третирана у фосфатном раствору) обезбеђује легури краткорочну заштиту у агресивној средини услед своје мале дебљине.

(Примљено 12. децембра 2012, ревидирано 17. јануара 2013)

REFERENCES

1. R. L. Twite, G. P. Bierwagen, *Prog. Org. Coat*. **33** (1998) 91
2. M. Bethencourt, F. J. Botana, J. J. Calvino, M. M. Marcos, M. A Rodrıguez-Chacon, *Corros. Sci*. **40** (1998) 1803
3. S. A. Kulinich, A. S. Akhtar, *Russ. J. Non-Ferr. Met.* **53** (2012) 176
4. *Innovative pre-treatment techniques to prevent corrosion of metallic surfaces*, European Federation on Corrosion Publications, Eds. L. Fedrizzi, H. Terryn, A. Simões, Woodhead Publishing Ltd., Cambridge, 2007
5. D. Balgude, A. Sabnis, *J. Sol–Gel Sci. Technol*. (2012) 124
6. M. L. Zheludkevich, J. Tedim, M. G. S. Ferreira, *Electrochim. Acta* **82** (2012) 314
7. B. R. W. Hinton, D. R. Arnott, N. E. Ryan, *Met. Forum* **7** (1984) 211
8. B. R. W. Hinton, D. R. Arnott, N. E. Ryan, *Met. Forum* **9** (1986) 162
9. B. F. Rivera, B. Y. Johnson, M. J. O'Keefe, W. G. Fahrenholtz, *Surf. Coat. Tech.* **176** (2004) 349
10. L. Wilson, B. R. W. Hinton, Patent WO 88/06639, 1988
11. A. Decloroy, J. Petitjean, *Surf. Coat. Tech*. **194** (2005) 1
12. W. Pinc, S. Geng, M. O'Keefe, W. Fahrenholtz, T. O'Keefe, *Appl. Surf. Sci*. **255** (2009) 4061
13. J. Stoffer, T. J. O'Keefe, M. O'Keefe, E. L. Morris, S. Hayes, P. Yu, A. Williams, B. Rivera Vasquez, X. Lin, US Patent 7,048,807 B2, May 23, 2006
14. J. Tang, Z. Han, Y. Zuo, Y. Tang, *Appl. Surf. Sci*. **257** (2011) 2806
15. J. Creus, F. Breyault, C. Rebere, M. Gadouleau, *Surf. Coat. Tech*. **200** (2006) 4636
16. J. A. Hill, T. Markley, M. Forsyth, P. C. Howlett, B. R. W. Hinton, *J. Alloys Comp*. **509** (2011) 1683
17. B. Y. Johnson, J. Edington, M. J. O'Keefe, *Mater. Sci. Eng., A* **361** (2003) 225
18. W. Pinc, P. Yu, M. O'Keefe, W. Fahrenholtz, *Surf. Coat. Tech.* **203** (2009) 3533
19. H. Zhang, Z. Zuo, *Appl. Surf. Sci*. **254** (2008) 4930
20. C. M. Rangel, T. I. Paiva, P. P. da Luz, *Surf. Coat. Techn*. **202** (2008) 3396
21. A. de Frutos, M. A. Arenas, Y. Liu, P. Skeldon, G. E. Thomson, J. De Damborenea, A. Conde, *Surf. Coat. Tech.* **202** (2008) 3797
22. W. G. Fahrenholtz, M. J. O'Keefe, H. Zhou, J. T. Grant, *Surf. Coat. Tech.* 155 (2002) 208
23. B. Y. Johnson, J. Edington, A. Wiliams, M. J. O'Keefe, *Mater. Charact*. **54** (2005) 41
24. S. Joshi, W. G. Fahrenholtz, M. J. O'Keefe, *Appl. Surf. Sci*. **257** (2011) 1859
25. D. K. Heller, W. G. Fahrenholtz, M. J. O'Keefe, *Corros. Sci*. **52** (2010) 360
26. D. K. Heller, W. G. Fahrenholtz, M. J. O'Keefe, *J. Electrochem. Soc*. **156** (2009) C400
27. A. J. Aldykewicz, H. S. Isaacs, A. J. Davenport, *J. Electrochem. Soc*. **142** (1995) 3342
28. A. E. Hughes, J. D. Gorman, P. J. K. Paterson, *Corros. Sci.* **38** (1996) 1957
29. D. Lau, A. M. Glenn, A. E. Hughes, F. H. Scholes, T. H. Muster, S. C. Hardin, *Surf. Coat. Tech.* **203** (2009) 2937
30. P. Campestrini, H. Terryn, A. Hovestad, J. H. W. de Wit, *Surf. Coat. Tech*. **176** (2004) 365
31. A. Conde, M. A. Arenas, A. de Frutos, J. de Damborenea, *Electrochim. Acta* **53** (2008) 7760
32. M. Bethencourt, F. J. Botana, M. J. Cano, M. Marcos, *Appl. Surf. Sci.* **189** (2002) 162
33. M. Bethencourt, F. J. Botana, M. J. Cano, M. Marcos, *Appl. Surf. Sci*. **238** (2004) 278
34. M. Bethencourt, F. J. Botana, M. J. Cano, M. Marcos, J. M. Sanchez-Amaya, L. Gonzales-Rovira, *Corros. Sci.* **50** (2008) 1376
35. H. Allachi, F. Chauket, K. Draoui, *J. Alloys Comp*. **491** (2010) 223

36. M. Dabalà, L. Armelao, A. Buchberger, I. Calliari, *Appl. Surf. Sci.* **172** (2001) 312
37. J. Hu, X. H. Zhao, S. W. Tang, W. C. Ren, Z. Y. Zhang, *Appl. Surf. Sci*. **253** (2007) 8879
38. S. W. Tang, J. Hu, X. H. Zhao, *Corros. Sci.* **53** (2011) 2636
39. H. D. Johansen, C. M. A. Brett, A. J. Motheo, *Corros. Sci*. **63** (2012) 342
40. L. P. Troeger, E. A. Starke, *Mater. Sci. Eng., A* **227** (2000) 102
41. B. M. Jović, U. Č. Lačnevac, V. D. Jović, L. M. Gajić-Krstajić, N. V. Krstajić, *J. Serb. Chem. Soc.* **77** (2012) 211
42. Ž. Jovanović, J. B. Bajat, R. M. Jančić-Heinemann, M. Dimitrijević, V. B. Mišković--Stanković, *Prog. Org. Coat.* **66** (2009) 393
43. A. Janković, S. Eraković, A. Dindune, Dj. Veljović, T. Stevanović, Dj. Janaćković, V. Mišković-Stanković, *J. Serb. Chem. Soc*. **77** (2012) 1609
44. A. Pepe, M. Aparicio, S. Ceré, A. Duràn, *J. Non-Cryst. Solids* **348** (2004) 162
45. A. E. Hughes, J. D. Gorman, P. R. Miller, B. Q. Sexton, P. J. K. Paterwon, R. J. Taylor, *Surf. Interface Anal.* **36** (2004) 290.

Journal of the Serbian Chemical Society
JSCS-info@shd.org.rs • www.shd.org.rs/JSCS

J. Serb. Chem. Soc. *78* (7) 1013–1022 (2013)
JSCS–4477

UDC 628.3:546.47'74/.76'56'815:
66.061:628.336:546.264–31
Original scientific paper

Subcritical and supercritical fluid extraction of heavy metals from sand and sewage sludge

ERDAL YABALAK* and AHMET MURAT GIZIR

Department of Chemistry, Faculty of Arts and Science, Mersin University, Mersin TR-33343, Turkey

(Received 21 March, revised 15 September 2012)

Abstract: Demetalization of Pb, Ni, Zn, Cu and Cr heavy metal ions from sea sand and real samples of sewage sludge by subcritical water and supercritical carbon dioxide was investigated. Experimental parameters such as temperature, pressure, extraction time in the static and dynamic mode and sampling were optimized in order to determine the suitable conditions for high removal of metals. The best extraction efficiencies were obtained using acetyl acetonate as a chelating agent in both subcritical water and supercritical CO_2 extractions for real and artificial samples. Samples collected from extraction system using both subcritical water and supercritical carbon dioxide were analyzed by inductively coupled plasma mass spectrometry (ICP-MS). The highest recoveries obtained from real samples for Cr, Cu, Ni, Pb and Zn were 77.25, 95.1, 84.82, 94.92 and 98.39 %, respectively, using the chelating agent in the subcritical water extraction.

Keywords: subcritical water; supercritical carbon dioxide; demetalization; heavy metal extraction; sewage sludge; sea sand.

INTRODUCTION

Metal waste contamination is a big threat for the environment and human health.[1–4] There are several methods for monitoring and clean up metal contaminated soils.[5,6] Traditional extraction methods, such as BCR, Tessier, *etc*., have been used for decades, but these methods are time consuming and environmentally unacceptable.[7–10] In addition, analytical difficulties are encountered when employing sequential extraction methods. In addition, these methods involve the use significant amounts of environmentally unacceptable chemicals.

Previous research showed that in order to obtain higher recoveries of selected metal ions, the use of nitric acid-modified water as an extraction solution is the most effective.[11] The acid is stronger than water in solubilizing metals

---

* Corresponding author. E-mail: yabalakerdal@gmail.com

doi: 10.2298/JSC120321123Y

from sewage sludge and various matrixes. Enhancing the nitric acid concentration has a positive effect on the extraction recoveries. Nevertheless, it was shown that concentrations higher than 4 % caused clogging of the extraction system, including tubes, filters and valves.[12,13] Morales-Muñoz *et al.* tested various HNO_3 acid concentrations as an extraction solvent modifier in order to optimize the method and obtain the best recoveries. They obtained that the optimum value was 1 %.[14] Therefore, a solution of 1 % nitric acid was used in the study. Thus, an initial experiment that was performed with 1 % nitric acid for optimizing the method and blank experiments confirmed that concentrations higher than 1 % introduced difficulties and decreased recoveries.

Subcritical water extraction (SbWE) and supercritical carbon dioxide extraction (SCE) are promising alternatives to conventional solvent extraction, as not only do they remove heavy metals, but also the morphology and structure matrix is retained.

Carbon dioxide and water are an environmentally acceptable solvent due to their low cost, and non-toxic and non-flammable nature and solubility characteristics, which are changeable by varying the temperature and pressure. Therefore, the SbWE is the efficient technique which nowadays constantly applied by researchers for its beneficial properties such as the solubility capability, mass transfer properties, diffusion coefficient etc.[15]

In the recent years, the vast majority of supercritical fluid extractions have focused on the use of supercritical carbon dioxide ($scCO_2$) to extract metals as some metal complex, because carbon dioxide has low toxicity and is environmentally acceptable.[16]

Subcritical water, which is usually sufficient to produce the desired physicochemical properties, exhibits moderate polarities and suitable solvent properties at temperatures between 100 and 374 °C and high enough pressure to maintain the water in the liquid state.[16,17] The dielectric constant of water, which is a measure of polarity, decreases dramatically when it is heated under sufficient pressure to maintain the liquid state.[18,19] For example, dielectric constant (ε) of water is 80 at ambient temperatures, but decreases to ≈30 at 250 °C.[19] Thus, water at high temperature behave as a non-polar solvent; hence, it can be employed to extract organometallic compounds. At ambient conditions, low polarity organic compounds are poorly soluble in water, but increasing the temperature increases the solubility of non-polar organic compounds. Thus, low polarity organic compounds could be dissolved in supercritical water ($T > 647$ K and $p > 22.0$ MPa), but unfortunately its reactive and corrosive nature makes supercritical water impractical for analytical applications, due to the high temperature and pressure.[20] Hawthorne *et al.* used water as an extraction solvent to extract polycyclic aromatic hydrocarbons (PAH) at subcritical and supercritical conditions.[18] Likewise, Akinlua *et al.* used subcritical water for trace metal extraction from petroleum source rock.[21] Many organic complexing agents have been used in previous studies of supercritical fluid extraction and pressurized hot water extraction (PHWE) of heavy metals.[22–25]

The solubility of metal ions in the fluids is crucial. However, by converting charged metal ions into neutral metal chelates using organic chelating agents, this solubility can be enhanced.[26–32] Thus, the selection of suitable agents is critical in the chelating-SCE of metal ions.[33] Acetyl acetonate (AcAc) and its metal chelates dissolve in subcritical water and supercritical CO_2.[34,35]

Although various methods including different additives widely applied for the extraction of heavy metals, few data are available for the extraction of sewage sludge with subcritical water or supercritical carbon dioxide using the beta diketone AcAc.[36,37]

Thus, AcAc was used as a chelating agent in the present study, which was aimed at the development of a fast, a cheap and an environmentally friendly method for the demetalization of soils using subcritical water and supercritical CO_2 extraction methods. The heavy metals (Cu, Cr, Ni, Pb and Zn) were extracted from an artificial sample and a CRM (Certificated Reference Material) sewage sludge sample in the presence and absence of the metal chelating agent AcAc.

EXPERIMENTAL

Chemicals and apparatus

The certificated sewage sludge reference material (LGC 6181, Laboratory of the Government Chemist (LGC), Teddington, Middlesex, TW11 0LY, UK) contains $Cu(NO_3)_2$, $Cr(ClO_4)_3$, $Ni(NO_3)_2$, $Pb(NO_3)_2$ and $Zn(NO_3)_2$ in certain quantities obtained from LGC. Standard metal salts, *i.e.*, $Cu(NO_3)_2$, $Cr(ClO_4)_3$, $Ni(NO_3)_2$, $Pb(NO_3)_2$ and $Zn(NO_3)_2$, and sea sand (extra pure), which were used for the artificial experiments, were obtained from Merck. Ultra-pure HNO_3 was purchased from Sigma-Aldrich. Chelating agent (acetyl acetonate) was procured from J. T. Baker. Ultra-pure water (18 MΩ cm), which was used in the SbWEs and dilution procedures, was obtained from a Millipore Milli-Q Advantage A10 system.

All extractions were performed using a special stainless steel cylindrical extractor (100 mm × 5 mm i.d.). Both ends of the column were covered with 0.45 µm mesh size filters for the prevention of particulates. A solution of 1 % nitric acid was used as the extraction solvent for the SbWE experiments, while neat CO_2 was used for the supercritical CO_2 extraction (SCE) experiments. The experimental set-up as shown in Fig. 1 was used for both the SbWE and supercritical CO_2 extraction experiments. The fluids were delivered in the constant pressure mode at a specific value using a Teledyne ISCO 260 D series pump.

An Agilent 7500ce ICP-MS instrument (Tokyo, Japan), equipped with a collusion/reaction cell in the form of octopole reaction system (ORS), was used for the analysis of Cu, Cr, Ni, Pb and Zn metal ions in the extracted samples. The utilized argon gas was of spectral purity (99.998 %). The external standard calibration method was applied to all determinations, using Li, Sc, Ge, Y, In, Tb and Bi internal standard mixture (in 2 % HNO_3 matrix). National Institute of Standards and Technology (NIST) single element reference standards were used to construct ten-point calibration curves.

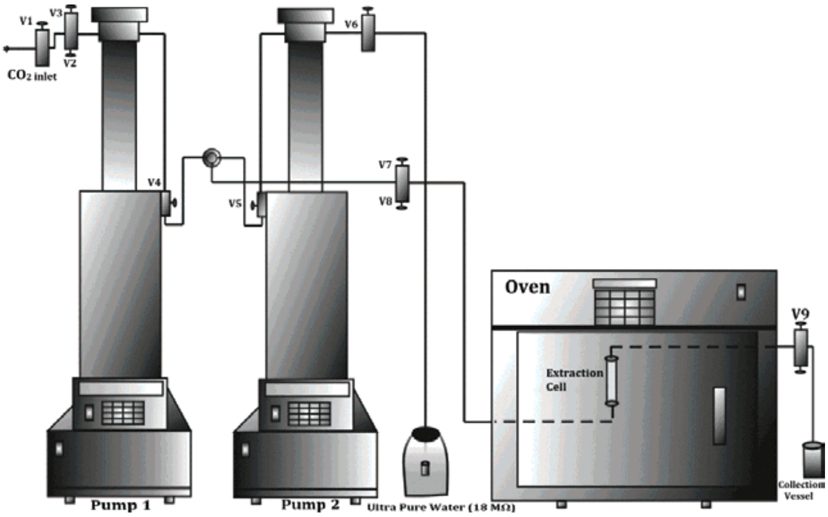

Fig. 1. Schematic diagram of extraction system (V1: CO_2 tube filling valve, V2 and V3: pressure regulation valve, V4: pump 1 filling valve, V5 and V6: pump 2 filling valve, V7 and V8: fluid transfer valve, V9: emptying/collecting valve).

The ICP-MS instrument was operated under the following parameters; RF power 1500 W, plasma gas 15 L min^{-1}, auxiliary gas flow at 1 L min^{-1}, nebulizer pump 0.1 rps, measurement time 0.5 s, make-up gas 0.13 L min^{-1}.

Pre-tests of sampling

For determining trace metal residue derived from the chemicals and apparatus, extra pure sea sand was used as a blank. Initial experiment was performed with subcritical water and supercritical carbon dioxide and the metals of interest were not detected in collected solutions.

Procedure

The artificial samples were prepared by adding 400 µL of a 500 ppm concentrated metal salt solution to 1.000 g of sea sand. Likewise, 1.000 g of sewage sludge was used for the CRM samples. The sample was placed in extraction cell and 200 µL of the chelating agent (acetyl acetonate) was added and covered by glass wool. The extraction cell was screwed on, and the cell was placed into the oven and pressurized with fluid (water in SbWE and carbon dioxide in SCE). After static mode extraction (30 min), the exit valve was opened and during dynamic mode extraction, the extracts were collected in ultra-pure water modified by 1 % HNO_3. 5 mL of water was used in the SbWE and 200 cm^3 of CO_2 was used in the SCE for each experiment. Acetyl acetonate (AcAc) was used as a chelating agent. Experiments were performed in the presence and absence of the chelating agent under the same extraction conditions. Each experiment was repeated three times under the same conditions and the average recovery and standard deviation values were calculated. SCE experiments were performed at 90 °C, 120 bar; 80 °C, 110 bar and 70 °C, 100 bar. The SbWE experiments were also performed at 110 °C, 70 bar; 120 °C, 80 bar and 130 °C, 90 bar in the constant pressure mode.

RESULTS AND DISCUSSION

In order to optimize the SCE and SbWE methods, Pb^{2+} was used as a reference metal. The parameters affecting both SCE and SbWE, namely, the amount of chelating agent, the extraction time and the optimum pressure–temperature, were investigated in order to attain the best recoveries. It was observed that density, which can be varied by changing the temperature and pressure, is one of the most influential factors affecting the extraction step and its increase had a positive effect on the recovery of the analytes. The other influencial factor affecting the extraction is the addition of chelating agent on the samples, especially for the SCE. It was found that the recovery of Pb^{2+} increased by using the chelating agent AcAc and with increased temperature–pressure (Table 1).

TABLE I. Removal of Pb^{2+} added to sea sand by SCE or SbWE in the absence (a) or presence (b) of AcAc; initial amount: 500 ppm

SCE					SbWE				
p bar	t °C	CO_2 density[41] g mL^{-1}	a	b	p bar	t °C	Water density[42] g/mL	a	b
100	70	0.248	16.8±2.6	46.7±4.5	70	110	0.95407	76.6±1.1	95.3±0.9
110	80	0.258	17.2±1.4	52.6±2.2	80	120	0.94680	79.5±0.9	96.3±0.8
120	90	0.264	20.1±1.8	57.4±3.8	90	130	0.93918	83.6±1.3	97.6±1.2

Extraction of artificial Pb^{2+}

Artificial extractions of Pb^{2+} from sea sand were performed by SCE and SbWE at selected temperature with and without AcAc and the obtained recoveries were compared with each other. Artificial extractions of Pb^{2+} from sea sand were performed by SCE at 70 °C, 100 bar (d_{CO_2} = 0.248 g mL^{-1}); 80 °C, 110 bar (d_{CO_2} = 0.258 g mL^{-1}) and 90 °C, 120 bar (d_{CO_2} = 0.264 g mL^{-1}) and by SbWE at 110 °C, 70 bar (d_{H_2O} = 0.95407 g mL^{-1}), 120 °C, 80 bar (d_{H_2O} = = 0.94680 g mL^{-1}) and 130 °C, 90 bar (d_{H_2O} = 0.93918 g mL^{-1}) both with and without AcAc. The recoveries are given in Table I. It was observed that enhancing the density of CO_2 and decreasing the density of water, especially using the chelating agent, increased the extraction yields.

SCE of artificial samples and CRM samples

Effective extractions of the selected metals were performed by SCE from CRM samples and the best result was obtained at 90 °C, 120 bar (d_{CO_2} = 0.264 g mL) for each metal with AcAc (Table II). In the absence of the chelating agent, the extraction yields were not good enough for efficient demetalization. The highest recovery was obtained for Pb^{2+} (50.2±2.4) at 90 °C, 120 bar with the chelating agent (Table II). It was observed that an enhanced density mostly scaled up the recoveries and that without the chelating agent no satisfactory yield was obtained. Solubilities of the organo-metallic compounds played a key role in determining the extraction efficiencies. Dissolution and extraction of the insoluble metal compounds from CRM samples depended on the chelation ability of the chelating agent.[28] Using AcAc, enhanced the recoveries for each metals and enhanced temperature–pressure improved the yields.

TABLE II. Removal of metals from artificial and CRM samples by SCE in the absence (a) or presence (b) of AcAc; initial amount: 100 ppm

Ion	a			b		
	100 bar, 70 °C	110 bar, 80 °C	120 bar, 90 °C	100 bar, 70 °C	110 bar, 80 °C	120 bar, 90 °C
Extraction yields of metals from artificial samples, %						
Cr^{3+}	9.3±0.9	9.9±1.4	10.0±1.2	31.0±1.2	37.4±2.6	40.2±2.3
Cu^{2+}	8.9±1.4	10.7±1.8	11.6±1.5	31.9±2.4	40.0±2.8	45.4±2.5
Ni^{2+}	12.4±1.6	17.3±1.7	18.1±2.1	27.6±2.9	43.6±2.7	47.5±4.3
Pb^{2+}	13.6±0.8	15.6±1.1	18.60±1.2	41.4±1.3	45.1±1.8	50.2±2.4
Zn^{2+}	13.1±0.3	14.1±0.5	15.1±1.0	45.2±0.9	47.1±1.3	48.2±5.4
Extraction yields of metals from CRM samples, %						
Ion	a			b		
	100 bar, 70 °C	110 bar, 80 °C	120 bar, 90 °C	100 bar, 70 °C	110 bar, 80 °C	120 bar, 90 °C
Cr^{3+}	6.2±0.9	7.1±0.9	7.9±1.3	27.9±2.8	28.2±2.9	28.6±2.0
Cu^{2+}	9.2±2.7	9.3±1.5	10.6±2.1	26.2±1.7	32.1±2.0	35.8±1.8
Ni^{2+}	10.6±3.1	12.5±1.8	13.2±1.4	22.5±4.5	35.6±1.6	39.4±0.9
Pb^{2+}	9.5±1.4	10.9±2.8	12.3±2.0	36.4±0.3	42.1±0.8	45.3±0.4
Zn^{2+}	9.6±2.7	11.8±2.0	12.6±1.9	31.2±1.0	40.8±2.9	42.1±1.1

The direct extraction of metal ions using neat supercritical CO_2 without the addition of a chelating agent is extremely inactive because of the necessity of charge neutralization and the weak solute–solvent interaction. Whereas, when the metal ions are chelated with organic ligands, they become quite soluble in $scCO_2$. Similarly, direct extraction of metal ions by subcritical water without the addition of the chelating agent is highly inefficient in comparison with extraction using a chelating agent.[38,39] Generally, higher yields were obtained in the extraction of sea sand samples compared with CRM samples for almost all metals because of the solute–solute and solute–matrix interactions which caused reduced yields in the CRM samples.[23] The matrix composition plays an important role in the efficiency of the extraction of heavy metals by supercritical and subcritical fluids. The artificial metals are held on the surface of the sea sand crystals during artificial sample extractions.[28] The difference between the results of Pb extraction yields (%) in Tables I and II for the single element (57.4 %) and multi mixed element (50.2 %) suggests that extraction of this metal from CRM was dependent on the chemical form and matrix interaction. Therefore, the extraction of Pb from sea sand was facilitated compared to CRM. Thus higher recoveries could be obtained in the extraction of artificial samples.

SbWE of artificial samples and CRM samples

The extraction yields shown in Table III clearly demonstrated that SbWE was a more effective method than SCE method. The highest recoveries obtained from real samples for Cr, Cu, Ni, Pb and Zn were 77.25, 95.1, 84.82, 94.92 and 98.39 %, respectively, when the chelating agent was employed. The lowest recovery was obtained for Cr (52.4±2.6) at 110 °C, 70 bar (d_{H_2O} = 0.95407 g mL^{-1}) in the absence of the chelating agent. It was found that the efficiency of SbWE was increased in the presence of the ligand.

TABLE III. Removal of metals from artificial and CRM samples by SbWE in the absence (a) or presence (b) of AcAc

Extraction yields of metals from artificial samples, %							
Ion	Initial amount ppm	a			b		
		70 bar, 110 °C	80 bar 120 °C	90 bar, 130 °C	70 bar 110 °C	80 bar, 120 °C	90 bar 130 °C
Cr^{3+}	100	52.4±2.6	54.8±1.8	56.5±2.3	78.1±2.3	79.4±1.9	83.6±4.5
Cu^{2+}	100	62.6±1.9	63.4±2.4	67.8±2.9	93.5±1.4	96.4±1.7	96.8±1.4
Ni^{2+}	100	58.7±2.5	58.5±2.2	69.4±3.4	85.1±1.8	86.3±2.7	90.6±1.2
Pb^{2+}	100	69.2±3.2	71.8±1.5	74.9±2.9	93.5±1.4	94.6±0.7	96.6±0.7
Zn^{2+}	100	72.9±2.9	74.7±2.6	72.5±1.8	97.9±1.6	98.1±0.6	96.4±0.9
Extraction yields of metals from CRM samples, %							
Ion	Initial amount ppm	a			b		
		70 bar, 110 °C	80 bar, 120 °C	90 bar, 130 °C	70 bar, 110 °C	80 bar, 120 °C	90 bar, 130 °C
Cr^{3+}	78	69.4±5.4	60.6±4.5	64.7±3.4	71.2±12.6	73.2±9.4	77.2±4.9
Cu^{2+}	354	73.7±1.3	80.2±1.7	86.7±1.6	84.2±2.6	90.2±3.8	95.1±3.4
Ni^{2+}	45	64.9±4.6	72.6±5.9	73.6±6.7	81.0±6.2	82.3±10.3	84.8±12.0
Pb^{2+}	105	80.4±2.5	85.7±3.1	86.6±4.1	92.0±7.7	92.9±4.4	94.9±7.0
Zn^{2+}	1100	86.4±0.5	89.4±1.8	83.8±2.0	96.7±0.5	98.4±1.8	94.7±4.6

The reduced viscosity, efficient surface tension properties of subcritical water and diffusion coefficients of solutes in subcritical water allow for favorable mass transfer properties. Changing the temperature–pressure had a large effect as it altered the physicochemical properties of analytes and fluids. Thus, SbWE could be performed in the demetalization of various matrixes.[40]

The chelating ligand formed stable organometallic complexes with the metal ions. The organometallic complex dissolved readily in the subcritical water. Thus, the extraction of the heavy metals was simplified *via* their conversion to ligand–metal complexes.

High extraction yields were obtained in the SbWE extraction of the CRM samples both with and without the chelating agent (Table III). However greater recoveries were obtained using AcAc. The matrix interaction that caused reduced yields in the SCE was not effective in the SbWE. Thus, the extraction yields showed that SbWE was more effective than SCE. There were only small differences in the yields when the SbWE was performed at different temperatures. Hence, temperature was less influential than the chelating agent (AcAc) in improving the yields during SbWE.

CONCLUSIONS

The effective conditions for elevated recoveries of heavy metals from real and artificial samples were investigated. It was observed that subcritical water is a more effective fluid compared to supercritical CO_2 for the extraction of heavy metals from various matrixes, although SbWE requires more harsh conditions than SCE. The density of supercritical CO_2 increased and that of water decreased with increasing temperature–pressure. Thus, the diffusivity of subcritical water, and the solvation and penetrating power of both improved and higher recoveries were obtained at elevated temperature–pressure in SbWE and SCE

The most popular environmentally friendly techniques, SCE and SbWE, for the extraction of trace metals, such as Pb, Ni, Zn, Cu and Cr, from sewage sludge and sea sand using the chelating agent AcAc were compared. It was shown some amounts of the metals could be extracted by SCE and almost the total amount of metals present in the samples could be extracted by SbWE from sea sand and real samples in a short time compared to traditional methods, such as BCR and Tessier.

Acknowledgements. The authors are grateful to the Mersin University Research Fund (Project No: BAB-FBE KB (EY) 2009-10 YL).

ИЗВОД

СУБКРИТИЧНА И СУПЕРКРИТИЧНА ФЛУИД ЕКСТРАКЦИЈА ТЕШКИХ МЕТАЛА ИЗ ПЕСКА И ОТПАДНОГ МУЉА

ERDAL YABALAK and AHMET MURAT GIZIR

Department of Chemistry, Faculty of Arts and Science, Mersin University,
Mersin TR-33343, Turkey

Испитивана је екстракција јона тешких метала Pb, Ni, Zn, Cu и Cr из морског песка и реалних узорака отпадног муља помоћу субкритичне екстракције водом и суперкритичне угљен-диоксидом. Оптимизовани су експериментални параметри као што су температура, притисак, време екстракције у статичком и динамичком режиму и узорковање, ради одређивања погодних услова за уклањање метала. Највећа ефикасност екстракције са реалним и синтетичким узорцима је добијена коришћењем ацетил-ацетоната као хелирајућег агенса, у оба типа екстракција, субкритичној водом и суперкритичној угљен-диоксидом. Узорци добијени после екстракције анализирани су применом индуктивно спрегнуте плазме са масеном спектрометријом (ICP-MS). Највише вредности процента приноса, добијене за реалне узорке, за Cr, Cu, Ni, Pb и Zn, износиле су

77,25, 95,1, 84,82, 94,92 и 98,39 %, са хелирајућим агенсом, субкритичном екстракцијом водом.

(Примљено 21.марта, ревидирано 15 септембра 2012)

REFERENCES

1. J. O. Nriagu, *Environ. Pollut*. **50** (1988) 139
2. I. Thornton, *Appl. Geochem*. **2** (1993) 203
3. J. W. C. Wong, N. K. Mak, *Environ. Technol*. **18** (1997**)** 109
4. N. S. Duzgoren-Aydın, C. S. C. Wong, A. Aydin, Z. Song, M. You, X. D. Li, *Environ. Geochem. Health* **28** (2006) 375
5. C. N. Mulligan, R. N. Yong, B. F. Gibbs, *Eng. Geol*. **60** (2000) 193
6. H. M. Chen, C. R. Zheng, C. Tu, Z. G. Shen, *Chemosphere* **41** (2000) 229
7. A. Tessier, P. G. C. Campbell, M. Bisson, *Anal. Chem*. **51** (1979) 844
8. C. M. Davidson, A. L. Duncan, D. LittleJohn, A. M. Ure, L. M. Garden, *Anal. Chim. Acta* **363** (1998) 45
9. M. A. Stylianou, D. Kollia, K. J. Haralambous, V. J. Inglezakis, K. G. Moustakas, M. D. Loizidou, *Desalination* **215** (2007) 73
10. C. R. M. Rao, A. Sahuquillo, J. F. Lopez Sanchez, *Water Air Soil Poll*. **189** (2008) 291
11. E. Priego-López, M. D. Luque de Castro, *Talanta* **58** (2002) 377
12. V. Fernández-Pérez, M. M. Jiménez-Carmona, M. D. Luque de Castro, *Analyst* **125** (2000) 481
13. M. M. Jiménez-Carmona, V. Pérez-Fernández, M. J. Gualda-Bueno, J. M. Cabanás-Espejo, M. D. Luque de Castro, *Anal. Chim. Acta* **395** (1999) 113
14. S. Morales-Muñoz, J. L. Luque-García, M. D. Luque de Castro, *Spectrochim. Acta, B* **58** (2003) 159
15. J. Kronholm, H. Kari, M. L. Riekkola, *Trend. Anal. Chem*. **26** (2007) 396
16. M. Z. Özel, M. D. Burford, A. A. Clifford, K. D. Bartle, A. Shadrin, N. G. Smart, N. D. Tinker, *Anal. Chim. Acta* **346** (1997) 73
17. E. Moreno, J. Reza, A. Trejo, *Polycycl. Aromat. Comp*. **27** (2007) 239
18. S. B. Hawthorne, Y. Yang, D. J. Miller, *Anal. Chem*. **66** (1994) 2912
19. Y. Yang, B. Søren, B. H. Steven, D. J. Miller, *Anal. Chem*. **67** (1995) 4571
20. S. Meredith, S. Curren, J. W. King, *Anal. Chem*. **73** (2001) 740
21. A. Akinlua, M. Roger, R. M. Smith, *Talanta* **81** (2010) 1346
22. J. Wang, W. D. Marshall, *Anal. Chem*. **66** (1994) 1658
23. S. Wang, Y. Lin, C. M. Wai, *Sep. Sci. Technol*. **38** (2003) 2279
24. L. Di Palma, P. Ferrantelli, F. Medici, *J. Environ. Manage*. **77** (2005) 205
25. K. E. Laintz, C. M. Wai, C. R. Yonker, R. D. Smith, *J. Supercrit. Fluids* **4** (1991) 194
26. C. M. Wai Y. Lin, R. D. Brauer, S. Wang, W. F. Beckert, *Talanta* **40** (1993) 1325
27. C. M. Wai, *Anal. Sci*. **11** (1995) 165
28. C. M. Wai, S. Wang, *J. Chromatogr., A* **785** (1997) 369
29. C. M. Wai, S. Wang, *J. Biochem. Bioph. Methods* **43** (2000) 273
30. S. Wang, S. Elshani, C. M. Wai, *Anal. Chem*. **67** (1995) 919
31. Y. Lin, C. M. Wai, *Anal. Chem*. **66** (1994) 1971
32. K. E. Laintz, C. M. Wai, C. R. Yonker, R. D. Smith, *Anal. Chem*. **22** (1992) 2875
33. J. Sunarso, S. Ismadji, *J. Hazard. Mater*. **161** (2009) 1
34. F. L. Anthony, N. H. Brian, J. B. Thomas, *Inorg. Chem*. **34** (1995) 5781

35. J. Starý, J. O. Liljenzin, *Pure Appl. Chem*. **54** (1982) 2557
36. J. Murphy, C. Erkey, *Ind. Eng. Chem. Res*. **36** (1997) 5371
37. C. Erkey, *J. Supercrit. Fluids* **17** (2000) 259
38. Y. Lin, R. D. Brauer, K. E. Laintz, C. M. Wai, *Anal. Chem*. **65** (1993) 2549
39. Y. Lin, N. G. Smart, C. M. Wai, *Trend. Anal. Chem*. **14** (1995) 123
40. L. Ramos, E. M. Kristenson, U. A. T. Brinkman, *J. Chromatogr., A* **975** (2002) 3
41. *SF-Solver (TM) Program*, Isco Inc., 4700 Superior St., Lincoln, NE, 68504
42. *Steam Tables Online*, http://www.steamtablesonline.com/steam97web.aspx (accessed in July 2013).

Journal of the Serbian Chemical Society
JSCS-info@shd.org.rs • www.shd.org.rs/JSCS

J. Serb. Chem. Soc. *78* (7) 1023–1034 (2013)
JSCS–4478

UDC 66.095.13:547.587.52+547.261:
547.269.3+547.533+544.973
Original scientific paper

A study of the esterification of caffeic acid with methanol using *p*-toluenesulfonic acid as a catalyst

JUN WANG[1]*, SHUANGSHUANG GU[1], NA PANG[1], FANGQIN WANG[1] and FUAN WU[1,2]**

[1]*School of Biology and Chemical Engineering, Jiangsu University of Science and Technology, Zhenjiang 212018, P. R. China and* [2]*Sericultural Research Institute, Chinese Academy of Agricultural Sciences, Zhenjiang 212018, P. R. China*

(Received 2 August, revised 24 September 2012)

Abstract: Caffeic acid (CA) could be considered as an important natural antioxidant. However, the low solubility and stability of CA in various solvent systems is a major limiting factor governing its overall application in the lipid industry. However, the synthesis of methyl caffeate (MC) using CA and methanol is a feasible way to improve its lipophilicity. Herein, the reaction conditions and kinetic parameters for the synthesis of MC using *p*-toluenesulfonic acid (PTSA) as a catalyst were investigated, and the product was confirmed by liquid chromatography–mass spectrometry (LC–MS), Fourier transform infrared (FTIR) and nuclear magnetic resonance (NMR) spectroscopy, and melting point analysis. The highest yield of MC catalyzed by PTSA attained 84.0 % under the optimum conditions as follows: molar ratio of methanol to CA of 20:1, reaction temperature of 65 °C, mass ratio of catalyst to substrate of 8 %, and a reaction time of 4 h. The esterification kinetics of CA and methanol is described by the pseudo-homogeneous second order reversible model. The relationship between temperature and the forward rate constant gives the activation energy of 17.5 kJ mol^{-1}. These results indicated that PTSA possesses high catalytic activity in the synthesis of MC, which is an efficient catalyst suitable for MC production in the chemical industry.

Keywords: caffeic acid; catalysis; esterification; kinetics; methyl caffeate; *p*-toluenesulfonic acid.

INTRODUCTION

Caffeic acid (CA) is one of the most widely distributed hydroxycinnamate and phenylpropanoid metabolites in plant tissues and agricultural wastes.[1,2] Recently, CA, as a natural antioxidant, has received increasing attention with regard to its applications in the food, health, cosmetic and pharmaceutical industries because of its numerous biological activities, such as anti-mutagenic, anti-

---

Corresponding authors. E-mails: *jimwang_js@hotmail.com; **fuword@163.com

doi: 10.2298/JSC120802101W

proliferative and anti-oxidant activities.[3–5] However, CA exhibits low solubility and stability in various solvent systems, thus it is necessary to enhance its practical applicability by improving its solubility.[6] The strategy of esterification of hydrophilic CA with lipophilic molecules, such as aliphatic alcohols, could be employed to alter its solubility in hydrophobic media.[7–9] In addition, the synthesis of alkyl esters can significantly improve their function.[10,11] For example, it was found that alkyl esters of CA have a higher antioxidant activity and lipophilicity than CA to protect neuronal PC12 cells against oxidative stress.[12] Therefore, it is advantageous to synthesize alkyl esters of caffeic acid based on both their biological function and potential application.

The classical methods for the esterification of CA, such as Fischer esterification, Wittig and one-pot reactions,[13–15] require tedious operations and generate by-products. Nowadays, a simple reactive approach appeared, *i.e.*, the direct esterification of CA with alcohols. Shin *et. al.* described an esterification of CA in the presence of methanol and sulfuric acid to prepare methyl caffeate (MC). In the reaction, the reaction time was 10 h and the yield achieved was up to 71 %.[13] Sulfuric acid has been widely used as an acid catalyst in a large variety of industrial chemical processes. However, sulfuric acid generally shows weak catalytic activity and requires high reaction temperatures and long reaction time.[16] In addition, the use of sulfuric acid is hazardous and requires special energy-inefficient processes for the treatment of the waste acid.[17] Thus, there is an urgent necessity to find a valid and simple catalyst and esterification system for the efficient synthesis of MC.

Recently, it was shown that *p*-toluenesulfonic acid (PTSA) has the potential to be used as a substitute for conventional acidic catalytic materials.[18] It is characterized by the mildness of the reaction conditions, inexpensive chemical and the excellent functional group tolerance, allowing the formation of the corresponding esters in good to excellent yields.[19] For instance, Jagdale *et al.* performed hydroarylation of cinnamic acids with anisoles and phenols mediated by PTSA under metal and solvent-free conditions, affording 3-(4-methoxyphenyl)--3-phenylpropanoic acids and dihydrocoumarins, respectively, in high yields with excellent selectivity.[20] Therefore, the use of PTSA as a catalyst is potentially attractive for the synthesis of MC.[21] However, a major concern of this system is its sensitivity and instability, because the esters of CA are readily oxidized.[2] Moreover, nowadays, the pseudo-homogeneous model of esterification is a competent kinetic model for predicting an esterification system, taking into account that it is a less complex model.[22,23] Hence, it is necessary to study the reaction conditions and kinetic parameters for an efficient synthesis of MC catalyzed by PTSA.

In the present study, using PTSA as the catalyst, the factors that strongly affect the yield of MC (namely, the reaction temperature, catalyst loading, the mole ratio of methanol to CA, and the ratio of molecular sieve to methanol) were explored and the corresponding esterification kinetic parameters of CA with methanol were obtained by the pseudo-homogeneous model. Liquid chromategraphy–mass spectrometry (LC-MS), Fourier transform infrared (FTIR) and nuclear magnetic resonance (NMR) spectroscopy, and melting point analysis were used to identify MC in the synthesis product.

EXPERIMENTAL

Materials and reagent

CA (purity > 98 %) was purchased from Nanjing Zelang Pharmaceutical Sci. & Tech. Co. Ltd. (Nanjing, China). Methanol (HPLC grade) and PTSA were purchased from Sinopharm Chemical Reagent Co. Ltd. (Shanghai, China). All other employed solvents and reagents were of analytical grade. Water was purified using an Elga Purelab Option-Q purifycation system (Elga Labwater, High Wycombe, Bucks, UK) and had a resistance greater than 18.0 MΩ cm.

General procedure for MC synthesis

The MC synthesis was performed in 5 mL screw-capped vials containing CA and methanol. The substrate was weighed accurately and the reaction was realized by the addition of PTSA. The reactions were generally performed under the following condition: 1 mM of CA, 20 mM of methanol, 2 % molecular sieves and 6 % PTSA were mixed and reacted at 60 °C under stirring (120 rpm). About 20 μL aliquots of the well-stirred reaction mixture were withdrawn at intervals for analysis.

Kinetics experimental procedure

CA and PTSA were charged into 5 mL screw-capped vials, and then methanol was added. This was taken as zero time for a run. The initial mole ratio of CA and methanol was 1:20, and the total volume of the reactant was 0.8 mL. About 20 μL of liquid sample was withdrawn from the vials at regular intervals for high performance liquid chromatography (HPLC) analysis. In a typical run, about 10 samples were taken from the system. The sample injection volume for the HPLC analysis was 20 μL. All samples were determined in triplicate.

The CA conversion and MC yield were calculated as follows:

$$\text{CA Conversion, \%}=\frac{\text{Consumptive amount of CA, mol}}{\text{Initial amount of CA, mol}}\times 100 \tag{1}$$

$$\text{MC yield, \%} = \frac{\text{Amount of methyl caffeate, mol}}{\text{Initial amount of caffeic acid, mol}}\times 100 \tag{2}$$

LC–MS and HPLC analysis

LC-PAD–MS was realized on a Thermo Fisher LC-MS system. The LC equipment comprised a Finnigan MAT Spectra System P4000 pump, an autosampler with 50 μL loop, a UV6000LP diode array detector, and a Finnigan AQA mass spectrometer. The LC separation was accomplished on a Kromasil C_{18} column (150 mm×4.6 mm, i.d.; 5 μm, W. R. Grace & Co., Deerfield, Illinois, USA) at 40 °C. The mobile phase consisted of solvent A (methanol) and solvent B (water). The samples were eluted isocratically using a 65:35 volume ratio of methanol and water at a flow rate of 1 mL min^{-1}. The wavelength range of the detection was from 200 to 400 nm. The electrospray ionization (ESI) was performed using nitrogen at a flow rate of 1.0 mL min^{-1} to assist nebulization. Selected ion monitoring (SIM) was in the negative ion mode. A capillary voltage at 1.6 kV was used and the temperature of the curved desolvation line (CDL) and heat block were both set at 200 °C. The data were processed using Xcalibur 1.2 software.

LC–UV was performed using an LB-5 pump (Beijing Satellite Manufactory, Beijing, China) with a UV detector (L-7420, Techcomp Co. Ltd., Shanghai, China) and N-2000 workstation (Hangzhou Mingtong S&T, Hangzhou, China). The reaction samples were analyzed on a C_{18} column (250 mm×4.6 mm, i.d.; 5 μm, W. R. Grace & Co., Deerfield, Illinois, USA) maintained at 30 °C. The mobile phase consisted of methanol and water (65:35 volume ratio) at a flow rate of 1.0 mL min^{-1}, and the detection wavelength was 325 nm.

FTIR, NMR and melting point analysis of MC

MC was prepared from CA as follows: a solution of CA (9 g) in methanol (100 mL) was treated with a catalytic amount of PTSA and heated at reflux for 6 h. The reaction mixture was cooled to room temperature and concentrated. The residue was dissolved in ethyl acetate and washed successively with dilute saturated aqueous $NaHCO_3$ solution, saturated aqueous NaCl, dried over $MgSO_4$, filtered and evaporated. The residue was crystallized from methanol to give a pure sample (yield 6.3 g, 70 %) as a white solid, and then was identified as MC by FTIR and NMR spectroscopy and melting point determination. Before testing, the sample was dried at 100 °C for 5 h in an oven, and then sealed in plastic bags. A sample was ground into a fine powder using an agate mortar immediately prior to analysis. The FTIR analysis was performed at room temperature on a Nicolet 560 instrument using the KBr disc technique. The ^{1}H-NMR spectra were recorded on Bruker Advance Spectrospin 400 MHz using TMS as the internal standard. The melting point analysis was performed using an Optimelt MPA100 instrument.

RESULTS AND DISCUSSION

LC–MS analysis of the reaction product of CA and methanol

Based on preliminary results, CA had been completely converted to MC after the esterification reaction of CA and methanol catalyzed by PTSA had proceeded for 5 h. The high catalytic efficiency of PTSA was proved *via* LC–MS in the present work. The LC–UV and TIC chromatograms of the reaction mixture from reaction of CA and methanol catalyzed by the PTSA are shown in Figs. 1A and 1B, respectively, which indicated that 84.0 % of the CA was effectively transformed to MC in the presence of methanol. The ESI-MS spectra of the reaction mixture are presented in Figs. 1C and 1D, which exhibit two intense peaks at m/z 179.01 and 193.07, corresponding to the deprotonated ion $[M–H]^-$ of CA and MC, respectively.[24] These results indicated that no side-products were formed during the whole reaction process catalyzed by the PTSA.

FTIR, NMR and melting point analysis

That MC was obtained in the studied reaction was confirmed by FTIR and NMR spectroscopy, and melting point analysis.

M.p.: 159–160 °C. FTIR (KBr, cm^{-1}): 3477, 3099, 2925, 1677, 1606, 1536; ^{1}H-NMR (400 MHz, DMSO-d_6, δ / ppm): 9.60 (1H, *s*, OH), 9.16 (1H, *s*, OH), 7.50 (1H, *d*, J = 15.9 Hz, α-H), 7.07 (1H, *d*, J = 2.0 Hz, Ph–H), 7.01 (1H, *dd*, J =

= 8.1 Hz, Ph–H), 6.77 (1H, *d*, *J* = 8.1 Hz, Ph–H), 6.28 (1H, *d*, *J* = 15.9 Hz, *β*-H), 3.69 (3H, *s*, CH_3).

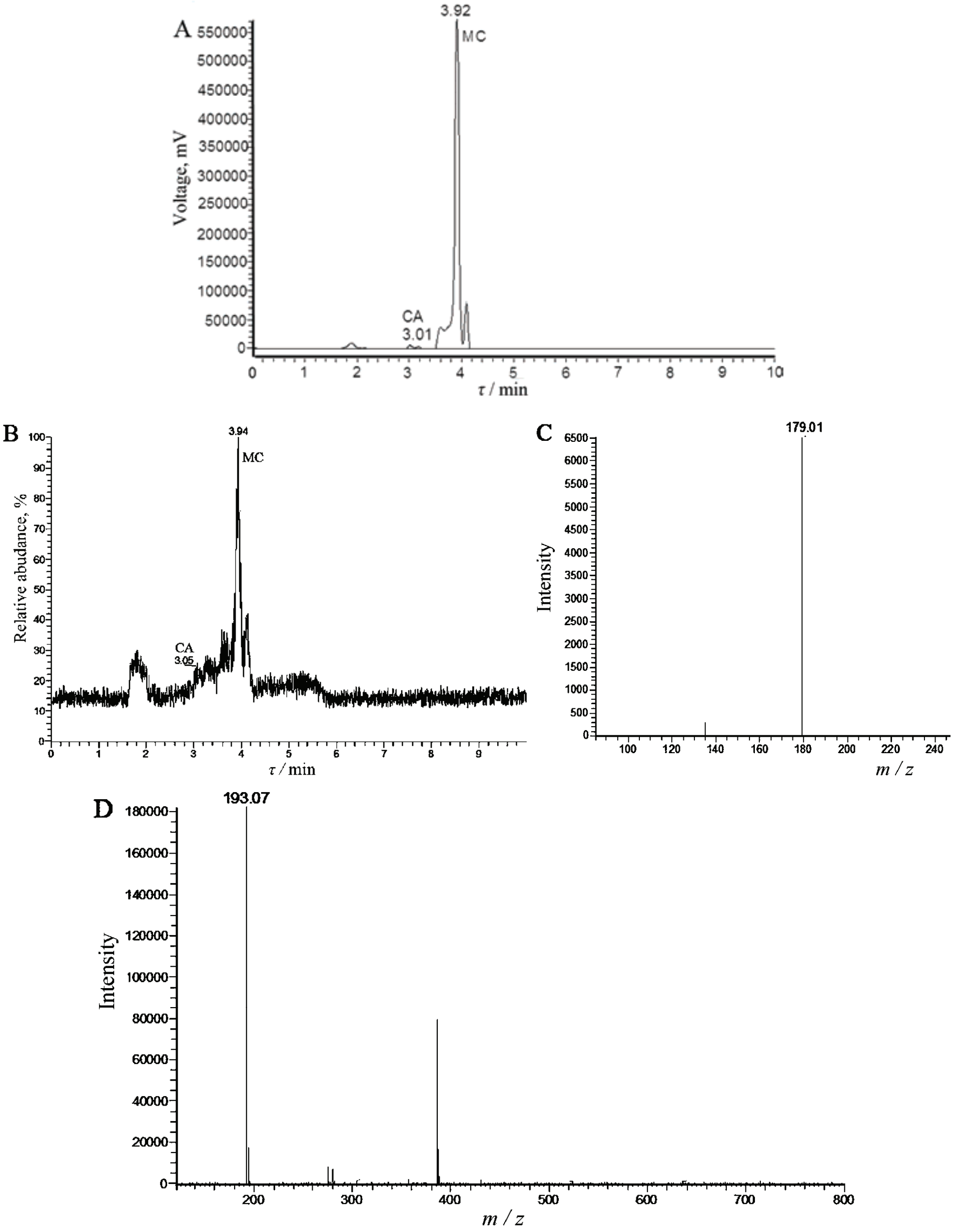

Fig. 1. Analysis of the reaction mixture after CA esterification with methanol catalyzed by PTSA: A) LC–UV chromatogram, B) TIC chromatogram, C) mass spectrogram, *m*/*z* ratio 179.01, and D) mass spectrogram *m*/*z* ratio 193.07.

Effect of mole ratio of methanol to CA on the yield of MC

The esterification reaction between CA and methanol follows a reversible path. A higher equilibrium conversion can only be obtained if the backward reaction is minimized. There are two ways to reduce the rate of backward reaction: a) to remove one of the undesired products, *i.e.*, water in the present case, continuously or b) to use one of the reactants in excess (methanol in this case).[25] In the present system, it was not easy to remove water, as the employed system was a closed system. Thus, the option of using excess methanol was employed in the present study. The change of the MC yield with the mole ratio of methanol to CA is shown in Fig. 2A. The MC yield increased from 25.8 % to 71.7 % on increasing the mole ratio of methanol to CA from 5:1 to 20:1. According to the Le Chatelier principle, the excess methanol was used to shift the equilibrium of the reversible reaction toward the direction of ester formation,[26] while any further increase exhibited an inhibitory effect on the production of MC. At a mole ratio of 50:1, the yield of MC was significantly lower because the use of too high amount of methanol could increase the water content, which arises from commercial methanol.[27] Therefore, the optimal mole ratio of methanol to CA for MC production was suggested to be 20:1.

Effect of reaction temperature on the yield of MC

The reaction temperature is one of the most important parameter affecting the MC yield during the esterification process. Six different temperatures were selected in the range of 45–70 °C. The MC yield markedly increased from 48.9 % to 78.9 % on increasing the temperature from 45 to 65 °C (see Fig. 2B). Obviously, a higher temperature results in an increase in the reaction rate and the equilibrium constant for an endothermic reaction.[17] With a further increase to 70 °C, the final yield of MC decreased to 65.4 %. These results indicated that higher temperatures could activate the substrate molecules, reduce the viscosity of the reaction mixture and lead to a higher reaction rate. However, too high a temperature leads to methanol volatilization.[28] Therefore, a temperature of 65 °C was retained in the subsequent optimization experiments.

Effect of catalyst loading on the yield of MC

To study the effect of catalyst loading on the yield of methyl ester, the reaction was performed at seven different mass ratios of catalyst to substrate (1, 2, 4, 6, 8 and 10 %), the other reaction conditions being kept constant. The results are shown in Fig. 2C, which indicates that there was a significant increase in the yield of MC as the mass ratio of catalyst to substrate increased from 0 % to 8 %, under identical conditions. The amount of PTSA influences the reaction rate because more H^+ become available when the amount of catalyst in the mixture increases.[29] Unexpectedly, when the mass ratio of catalyst to substrate was in-

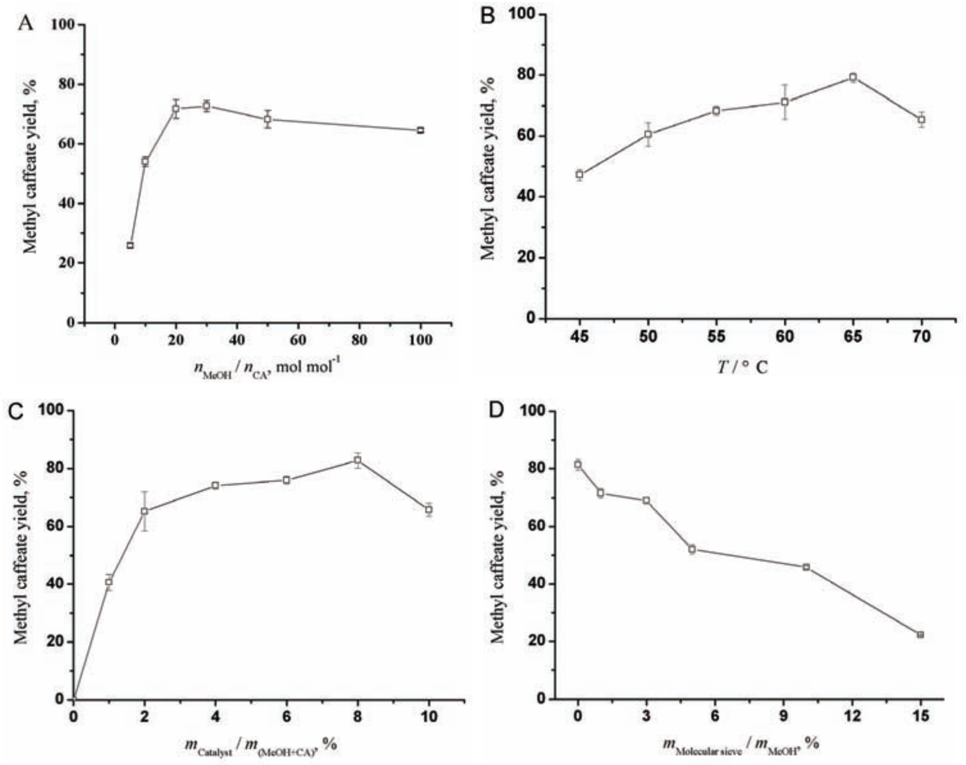

Fig. 2. The effects on the yield of MC of A) the mole ratio of methanol to CA (5:1 to 100:1) at a mass ratio of catalyst to substrate of 6 % and a temperature of 60 °C, B) reaction temperature, C) catalyst loading and D) mass ratio of molecular sieve to methanol, on the yield of MC catalyzed by PTSA. Reaction conditions: B) mole ratio of methanol to CA of 20:1 and a mass ratio of catalyst to substrate of 5 %, C) the catalyst loading (0 to 10 %) at a mole ratio of methanol to CA 20:1 and a temperature of 65 °C and D) the mass ratio of molecular sieve to methanol (0 to 15 %) at a molar ratio of methanol to CA of 20:1, a mass ratio of catalyst to substrate of 8 % and temperature of 65 °C.

creased to 10 %, the yield of MC decreased. Similar results were reported for the synthesis of functionalized pyrimido[4,5-*b*]quinolines and indeno-fused pyrido-[2,3-*d*]pyrimidines in water catalyzed by PTSA.[30] Therefore, the optimum mass ratio of catalyst to substrate for MC synthesis was 8 %.

Effect of mass ratio of molecular sieve to substrate on the yield of MC

Water is the second product during the esterification of CA with methanol. Thus, the water content is another important parameter in esterification reactions. Kumar *et. al.* reported that addition of molecular sieves or silica usually improves the equilibrium conversion.[16] To study the effect of the reaction water on the reaction rate, 0–15 % 3 Å molecular sieves were added to remove the water. Fig. 2D showed that the yield of MC decreased with increasing ratio of molecular sieve to methanol. This is because PTSA has strong acidic properties and could corrode the molecular sieves in some way. Kuwabara *et. al.* also reported that molecular sieves in many cases had negative effects, such as the formation of di-esters and degradation of unstable substances.[31] Therefore, the employment of molecular sieves to remove the formed water is not suitable here.

Kinetics of the esterification of CA with methanol in the presence of PTSA

The effect of the reaction time on the esterification of CA with methanol catalyzed by PTSA at different temperatures is shown in Fig. 3A. With increasing time, the conversion of CA increased rapidly, which reflects the synthesis ability and stability of MC in the PTSA-catalyzed reaction system. After an esterification time of 4 h, the conversion of CA reached a stable value. Therefore, the optimal reaction time was 4 h. The highest yield of MC was 84.0 % under the optimum conditions as follows: mole ratio of methanol to CA of 20:1, reaction temperature of 65 °C, reaction time of 4 h, and mass ratio of catalyst to substrate of 8 %.

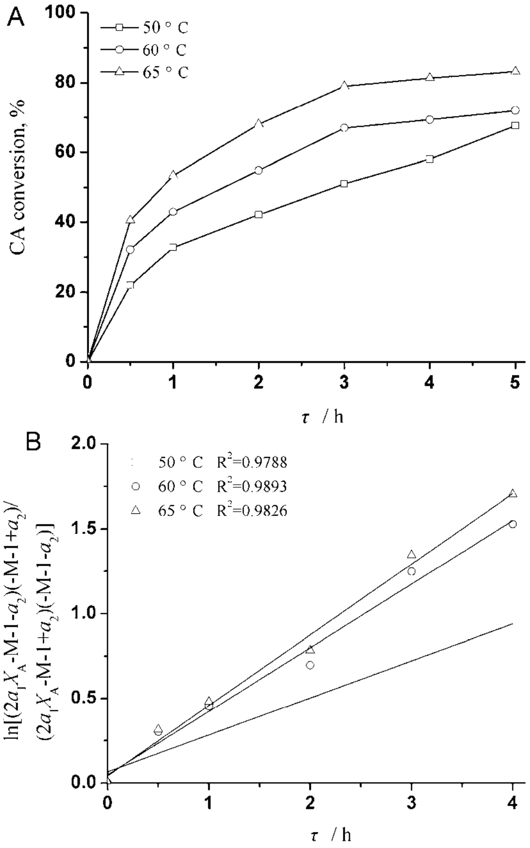

Fig. 3. Second order reversible model for the calculation of the reaction rate constants at different reaction temperatures.

The pseudo-homogeneous model does not take into account the sorption effect into the catalyst in a reactant medium.[32,33] If the reaction mixture is considered as a single liquid phase, the performance of the pseudo-homogeneous model could be considered as a satisfactory tool to correlate the esterification of CA with methanol in the presence of PTSA as a catalyst.

The esterification of CA with methanol using PTSA as a catalyst is represented as follows:

$$\mathrm{A} + \mathrm{B} \underset{k_{-1}}{\overset{k_1}{\rightleftarrows}} \mathrm{E} + \mathrm{W} \tag{3}$$

where A is CA, B is methanol, E is MC and W is water. This reaction can be considered a second order reaction. Therefore, the rate equation can be written as follows:

$$r_\mathrm{A} = \frac{\mathrm{d}c_\mathrm{A}}{\mathrm{d}t} = k_1 c_\mathrm{A} c_\mathrm{B} - k_{-1} c_\mathrm{E} c_\mathrm{W} \tag{4}$$

where c_A, c_B, c_E and c_W are the concentrations of CA, methanol, MC and water, respectively. k_1 is the forward rate constant and k_{-1} is the backward rate constant.

From the relationship of c_A and the extent of conversion of CA, x_A:

$$-\frac{\mathrm{d}c_\mathrm{A}}{\mathrm{d}t} = c_\mathrm{A0}\frac{\mathrm{d}x_\mathrm{A}}{\mathrm{d}t}$$

as well as the correlations of the changes in B, E and W to A:

$$c_\mathrm{A} = c_\mathrm{A0}(1 - x_\mathrm{A})$$
$$c_\mathrm{B} = c_\mathrm{B0}(M - x_\mathrm{A})$$

and

$$c_\mathrm{E} = c_\mathrm{W} = c_\mathrm{A0} x_\mathrm{A}$$

where c_A0 is the initial concentration of CA, c_B0 is the initial concentration of methanol and M is the concentration ratio of methanol to CA ($M = c_\mathrm{B0}/c_\mathrm{A0}$).

Thus, Eq. (4) becomes:

$$\frac{\mathrm{d}x_\mathrm{A}}{\mathrm{d}t} = c_\mathrm{A0}[k_1(1 - x_\mathrm{A})(M - x_\mathrm{A}) - k_{-1}x_\mathrm{A}^2] \tag{5}$$

At equilibrium, $\mathrm{d}c_\mathrm{A}/\mathrm{d}t = 0$ and thus, the equilibrium constant (K_e) can be calculated from:

$$K_\mathrm{e} = \frac{k_1}{k_{-1}} = \frac{x_\mathrm{Ae}^2}{(1 - x_\mathrm{Ae})(M - x_\mathrm{Ae})} \tag{6}$$

x_Ae is the conversion of CA at equilibrium stage, and K_e is the equilibrium constant.

If Eq. (6) is integrated and rearranged, the following equation in its linear form is obtained:

$$\ln\left[\left(\frac{2a_1x_A - M - 1 - a_2}{2a_1x_A - M - 1 + a_2}\right)\left(\frac{-M - 1 + a_2}{-M - 1 - a_2}\right)\right] = a_2k_1c_{A0}t \tag{7}$$

where:

$$a_1 = \left(1 - \frac{1}{K_e}\right)$$

$$a_2 = \left[(M + 1)^2 - 4a_1M\right]^{1/2}$$

The results of plotting the left-hand-side of Eq. (7) *vs*. t are presented in Fig. 3B, from which it can be seen that straight lines passing through the origin were obtained. All straight lines gave a good linear correlation lying in the R^2 range of 0.979–0.989. This clearly shows that the proposed kinetic model is appropriate for this reaction. The forward reaction rate constant, k_1, was obtained from the slope of the lines in Figure 3B at different temperatures. The backward rate constants $k_{–1}$ could be calculated using the correlation of the forward rate constant and the equilibrium constant, as in Eq. (7). All forward and backward rate constants at the different reaction temperatures are given in Table I.

TABLE I. Estimated forward and backward rate constants (L mol^{-1} min^{-1}) at different reaction temperatures

Run	Reaction temperature, °C	Forward rate constant, k_1	Backward rate constant, k_{-1}
1	50	0.219	2.992
2	60	0.376	1.749
3	65	0.417	4.344

The dependence of the forward rate constant on the reaction temperature is described by the Arrhenius Law, as given in Eq. (8):

$$k_1 = Ae^{-E/RT} \tag{8}$$

where, A is the pre-exponential factor, E is the activation energy, R is the idea gas constant and T is the reaction temperature (K).

The Arrhenius–Van’t Hoff plot of the forward rate constant in the temperature range 50–65 °C gives the coefficient of linearity of 0.940. The slope could be applied to calculate the activation energy. The activation energy is 17.5 kJ mol$^{–1}$, which confirms that PTSA possesses a high catalytic activity in the synthesis of MC.

CONCLUSIONS

The reaction conditions and kinetic parameters for the efficient synthesis of MC by esterification of CA by methanol using PTSA as a catalyst were first investigated. The results indicated that the highest attained yield of MC was 84.0 % under the optimum conditions, *i.e.*, reaction time of 4 h, reaction temperature of 65 °C, mole ratio of methanol to CA of 20:1, and mass ratio of catalyst to substrate of 8 %. A pseudo-homogeneous second order reversible model was demonstrated to justify the experimental data. The model provided good agreement with the experimental kinetic results. The activation energy of the reaction was 17.5 kJ mol^{-1}, which indicates that PTSA possesses high catalytic activity in the synthesis of MC.

Acknowledgements. This work was sponsored by Natural Science Foundation of Jiangsu Province (BK2009213), National Natural Science Foundation of China (21206061), China Postdoctoral Science Foundation funded projects (2012M510124, 2013T60505), Qing Lan Project of Jiangsu Province, Postdoctoral Science Foundation Funded Project of Jiangsu University (1143002085), Graduate Innovation Project of Jiangsu Province (2012JSSPITP1482), Graduate Innovation Project of Jiangsu University of Science and Technology, Research Projects of Jiangsu University of Science and Technology (35211002, 33201002), and Modern Agro-industry Technology Research System of China (CARS-22).

The authors have declared no conflict of interest.

ИЗВОД

ИСПИТИВАЊЕ РЕАКЦИЈЕ ЕСТЕРИФИКАЦИЈЕ КОФЕИНСКЕ КИСЕЛИНЕ СА МЕТАНОЛОМ У ПРИСУСТВУ *p*-ТОЛУЕНСУЛФОНСКЕ КИСЕЛИНЕ КАО КАТАЛИЗАТОРА

JUN WANG[1], SHUANGSHUANG GU[1], NA PANG[1], FANGQIN WANG[1] и FUAN WU[1,2]

[1]School of Biology and Chemical Engineering, Jiangsu University of Science and Technology, Zhenjiang 212018, P.R. China и [2]Sericultural Research Institute, Chinese Academy of Agricultural Sciences, Zhenjiang 212018, P.R. China

Кофеинска киселина (КК) представља важан природни антиоксидант. Слаба растворљивост и стабилност КК у различитим растварачима представља главни ограничавајући фактор свеукупне примене у индустрији липида. Због тога синтеза метил-кофеата (МК) из КК и метанола представља могући начин да се побољша липофилност. У оквиру рада, прво су испитани реакциони услови и кинетички параметри синтезе МК користећи *p*-толуенсулфонску киселину (PTSA) као катализатор. У овом раду су прво испитивани реакциони услови и кинетички параметри при синтези МК и за идентификацију производа су коришћене методе LC–MS, FTIR, NMR и анализа тачке топљења. Највећи остварени принос МК у присуству PTSA је био 84 %, а оптимални реакциони услови су били: молски однос метанол: КК 20:1, реакциона температура 65◦°C, масени однос катализатор : супстрат 8 %, и реакционо време 4 h. Реакција естерификације КК метанолом је описана ревирзибилним моделом псеудо-хомогеног другог реда. На основу зависности константе k_1 од температуре активациона енергија износи 17,5 kJ mol^{-1}. Резултати показују да PTSA поседује каталитичку активност у синтези МК, као и да је ефикасан катализатор погодан за синтезу МК у хемијској индустрији.

(Примљено 2. августа, ревидирано 24. септембра 2012)

REFERENCES

1. J. Fu, K. Cheng, Z. Zhang, R. Fang, H. Zhu, *Eur. J. Med. Chem.* **45** (2010) 2638

2. J. Wang, D. Lu, H. Zhao, X. Ling, B. Jiang, P. Ouyang, *Afr. J. Biotech.* **8** (2009) 1416
3. Y. Tsai, S. Chiou, K. Chan, J. Sung, S. Lin, *LWT – Food Sci. Technol.* **46** (2012) 169
4. T. Nagaoka, A. H. Banskota, Y. Tezuka, I. Saiki, S. Kadota, *Bioorg. Med. Chem.* **10** (2002) 3351
5. A. O. Aytekin, S. Morimura, K. Kida, *J. Biosci. Bioeng.* **111** (2011) 212
6. H. Chen, Y. Twu, C. J. Chang, Y. Liu, C. Shieh, *Ind. Crop Prod.* **32** (2010) 522
7. K. Uwai, Y. Osanai, T. Imaizumi, S. Kanno, M. Takeshita, M. Ishikawa, *Bioorg. Med. Chem.* **16** (2008) 7795
8. J. Wang, S. Gu, L. Zhang, F. Wu, X. Guo, *Acta Crystallogr., E* **67** (2011) O2871
9. S. Gu, J. Wang, F. Pan, N. Pang, F. Wu, *Acta Crystallogr., E* **68** (2012) O557
10. X. S. Zhou, J. B. Liu, W. F. Luo, Y. W. Zhang, H. Song, *J. Serb. Chem. Soc.* **76** (2011) 1607
11. Z. Knezevic-Jugovic, D. Bezbpadica, Z. Jakovijevic, S. Brankovic-Dimitrijevic, D. Mijin, *J. Serb. Chem. Soc.* **73** (2008) 1139
12. J. Garrido, A. Gaspar, E. M. Garrido, R. Miri, M. Tavakkoli, S. Pourali, L. Saso, F. Borges, O. Firuzi, *Biochimie* **94** (2012) 961
13. K. Shin, I. Kim, Y. Park, J. Ha, J. Choi, H. Park, Y. S. Lee, K. Lee, *Biochem. Pharmacol.* **68** (2004) 2327
14. F. de Campos Buzzi, C. L. Franzoi, G. Antonini, M. Fracasso, V. C. Filho, R. A. Yunes, R. Niero, *Eur. J. Med. Chem.* **44** (2009) 4596
15. S. M. Fiuza, C. Gomes, L. J. Teixeira, M. T. Girão Da Cruz, M. N. D. S. Cordeiro, N. Milhazes, F. Borges, M. P. M. Marques, *Bioorg. Med. Chem.* **12** (2004) 3581
16. A. Kumar, S. S. Kanwar, *Bioresour. Technol.* **102** (2011) 2162
17. Y. Feng, B. He, Y. Cao, J. Li, M. Liu, F. Yan, X. Liang, *Bioresour. Technol.* **101** (2010) 1518
18. L. Xiao, C. Xia, J. Chen, *Tetrahedron Lett.* **48** (2007) 7218
19. G. Le Bras, O. Provot, J. Peyrat, M. Alami, J. Brion, *Tetrahedron Lett.* **47** (2006) 5497
20. A. R. Jagdale, A. Sudalai, *Tetrahedron Lett.* **48** (2007) 4895
21. Y. H. Kuo, M. J. Su, US 20090143397 (2009)
22. E. Ö. Akbay, M. R. Altıokka, *Appl. Catal. A* **396** (2011) 14
23. B. Bessling, J. Löning, A. Ohligschläger, G. Schembecker, K. Sundmacher, *Chem. Eng. Technol.* **21** (1998) 393
24. Y. Lu, L. Y. Foo, H. Wong, *Phytochemistry* **52** (1999) 1149
25. V. G. Deshmane, P. R. Gogate, A. B. Pandit, *Ultrason. Sonochem.* **16** (2009) 345
26. C. Su, C. Fu, J. Gomes, I. Chu, W. Wu, *AIChE J.* **54** (2008) 327
27. L. H. Chin, A. Z. Abdullah, B. H. Hameed, *Chem. Eng. J.* **183** (2012) 104
28. Y. Feng, A. Zhang, J. Li, B. He, *Bioresour. Technol.* **102** (2011) 3607
29. M. C. de Jong, R. Feijt, E. Zondervan, T. A. Nijhuis, A. B. de Haan, *Appl. Catal., A* **365** (2009) 141
30. G. K. Verma, K. Raghuvanshi, R. Kumar, M. S. Singh, *Tetrahedron Lett.* **53** (2012) 399
31. K. Kuwabara, Y. Watanabe, S. Adachi, K. Nakanishi, R. Matsuno, *Biochem. Eng. J.* **16** (2003) 17
32. J. Lilja, D. Y. Murzin, T. Salmi, J. Aumo, P. Mäki-Arvela, M. Sundell, *J. Mol. Catal., A* **182–183** (2002) 555
33. B. K. Adnadjević, J. D. Jovanović, *Chem. Eng. Technol.* **35** (2012) 761.

Journal of the Serbian Chemical Society
version electronic
JSCS-info@shd.org.rs • www.shd.org.rs/JSCS

J. Serb. Chem. Soc. 78 (7) 1035–1043 (2013) UDC 547.21+542.92:504.53.054+665.73/.75
JSCS–4479 *Original scientific paper*

Degradability of *n*-alkanes during *ex situ* natural bioremediation of soil contaminated by heavy residual fuel oil (mazut)

MUFTAH MOHAMED ALI RAMADAN[1], TATJANA ŠOLEVIĆ KNUDSEN[2#],
MALIŠA ANTIĆ[3#], VLADIMIR P. BEŠKOSKI[1,2#], MIROSLAV M. VRVIĆ[1,2#],
JAN SCHWARZBAUER[4] and BRANIMIR JOVANČIĆEVIĆ[1,2*#]

[1]*Faculty of Chemistry, University of Belgrade, Studentski trg 12–16, P. O. Box 158, 11001 Belgrade, Serbia,* [2]*Center of Chemistry, Institute of Chemistry, Technology and Metallurgy, University of Belgrade, Njegoševa 12, 11001 Belgrade, Serbia,* [3]*Faculty of Agriculture, University of Belgrade, Nemanjina 6, 11081 Belgrade, Serbia and* [4]*Institute of Geology and Geochemistry of Petroleum and Coal, Lochnerstrasse 4–20, 52056 Aachen, Germany*

(Received 29 August, revised 09 October 2012)

Abstract: It is well known that during biodegradation of oil under natural geological conditions, or oil pollutants in the environment, degradation of hydrocarbons occurs according to a well-defined sequence. For example, the major changes during the degradation process of *n*-alkanes occur in the second, slight and third, moderate level (on the biodegradation scale from 1 to 10). According to previous research, in the fourth, heavy level, when intensive changes of phenanthrene and its methyl isomers begin, *n*-alkanes have already been completely removed. In this paper, the *ex situ* natural bioremediation (non-stimulated bioremediation, without addition of biomass, nutrient substances and biosurfactant) of soil contaminated with heavy residual fuel oil (mazut) was conducted during a period of 6 months. Low abundance of *n*-alkanes in the fraction of total saturated hydrocarbons in the initial sample (identification was possible only after concentration by the urea adduction technique) showed that the investigated oil pollutant was at the boundary between the third and the fourth biodegradation level. During the experiment, an intense degradation of phenanthrene and its methyl-, dimethyl- and trimethyl-isomers was not accompanied by the removal of the remaining *n*-alkanes. The abundance of *n*-alkanes remained at the initial low level, even at end of the experiment when the pollutant reached one of the highest biodegradation levels. These results showed that the non-stimulated biodegradation of some hydrocarbons, despite their high biodegradability, had not proceeded completely to the end, even at final degradation stages. Under the condition of reduced availability of some hydrocarbons, microorganisms tend to opt for the less biodegradable but more accessible hydrocarbons.

---

* Corresponding author. E-mail: bjovanci@chem.bg.ac.rs
\# Serbian Chemical Society member.
doi: 10.2298/JSC120829106A

Keywords: *ex situ* bioremediation; soil; heavy residual fuel oil; *n*-alkanes; degradability.

INTRODUCTION

Biodegradation and the removal of oil-type pollutants (crude oil and refinery products of petroleum refining) from the environment are difficult to be classified in one category. Oil is a very complex mixture of hydrocarbons, but also nitrogen, sulfur and oxygen compounds (NSO). Each class of compounds, and often individual compounds as well, require special study aimed at defining the type of microorganisms and optimal conditions for microbial degradation.[1,2]

Knowledge about the rate of microbial degradation of individual organic compounds in oil is mostly based on organic geochemical research. As early as 1984, Volkman *et al*. classified oils into 9 groups according to their degree of biodegradation.[3] Biodegradation begins with the degradation of lower *n*-alkanes ($< n$-C_{15}), while maximum degraded oils, with completely degraded steranes and dominated by diasteranes and demethylated hopanes, belong to the ninth group. In their research, these authors interpreted biodegradation of oil mainly through the biodegradation of *n*-alkanes, isoprenoid alkanes and polycyclic alkanes.

In 2003, Head *et al*. completed the classification of oils according to the biodegradation level, comparing the degradability of a larger number of classes of organic compounds.[4] First, they included mono- and tri-aromatic steroids as well as phenanthrene with its methyl isomers. According to these authors as well, biodegradation of *n*-alkanes starts on the first level. Only in the last phases, do the degradation of mono- and tri-aromatic steroids, gammacerane, oleanane, C_{21} and C_{22} steranes, tricyclic terpanes, diasteranes, diahopanes and norhopanes begin. Among these compounds, only C_{21} and C_{22} steranes and tricyclic terpanes can be removed completely.

For the degradation of some compounds, microorganisms and conditions for degradation are unknown, and these compounds are considered non-biodegradable. This is especially true for compounds in the fraction of NSO-compounds.[5]

In this study, *ex situ* natural microbial degradation of soil contaminated with heavy residual fuel oil (mazut) was conducted during a period of 6 months. The fate of the *n*-alkanes in the pollutant was monitored. Namely, the main transformations during the degradation process of *n*-alkanes, which are the dominant hydrocarbons in most oils and oil-type pollutants, occur during the second, slight and the third, moderate level (on the biodegradation scale from 1 to 10).[4] According to previous research, in the fourth, heavy level, when intensive changes of phenanthrene and its methyl isomers begin, the *n*-alkanes had already been completely removed. However, in the samples investigated in the present study, at the very beginning of the biodegradation experiment, *n*-alkanes within the fraction of saturated hydrocarbons were present in amount close to the detection limit. The question arose as to what their fate would be in case of their minimum availability to the microorganisms.

EXPERIMENTAL

The *ex situ* natural biodegradation (non-stimulated bioremediation, without addition of biomass, nutrient substances and biosurfactant) of a soil contaminated with heavy residual fuel oil (mazut) was conducted. The crude oil-polluted soil was excavated contaminated soil from an energy power plant that, due to a breakdown, had been polluted for a year with heavy fuel oil and sediment from a heavy oil reservoir.

The crude oil-polluted soil (approximately 150 t; 210 m^3) was uniformly distributed over 300 m^3 of not rinsed sand from the Sava River (settlement Ostruznica, Serbia). Sawdust from poplar, beech and oak (approx. 60 m^3) was added in order to not only increase the retention water capacity, but also as an alternative, additional carbon (C) substrate. The entire material (volume of approx. 600 m^3), defined as the substrate for biodegradation, was homogenized, and then formed into a biopile shape with dimensions of 75 m×20 m×0.4 m (length, width, height), with bulldozers. Immediately after mixing, approximately 10 m^3 of the biopile mixture was set aside on the same waterproof asphalt surface to be used as a substrate for monitoring the natural biodegradation. The experiment was conducted in autumn and winter with average daily temperatures ranging from 25 to –10 °C. However, due to the intensive microbiological activity, the temperature of the soil was stable, above 25 °C. After mixing, the biopile was covered with polyethylene foil to prevent loss of temperature and the direct influence of the weather conditions on the bioremediation substrate.

From the polluted soil, a consortium of hydrocarbon degrading microorganisms was isolated and individual components were identified. Analytical Profile Index (API-Biomerieux) tests were conducted with isolated cultures of the microorganisms and the following were identified: *Pseudomonas aeruginosa*, *Rhodococcus* sp., *Pseudomonas* sp., *Pseudomonas fluorescens*, *Sphingomonas paucimobilis*, *Pseudomonas luteola*, *Achromobacter denitrificans*, *Stenotrophomonas maltophilia* and *Aeromonas hydrophila*. The number of microorganisms was determined by plating appropriate serial dilutions on agar plates incubated at 28 °C. The media used were nutrient agar for total chemoorganoheterotrophs (TC) and a mineral base medium[6] containing 2 g of standard D2 diesel fuel in 1 L of medium[7] for hydrocarbon degraders (HD). The results are presented in Table I. More detailed characteristics of the investigated mazut-polluted soil were presented in a previous paper.[8]

TABLE I. Content of microorganisms (CFU g^{-1}) in the investigated oil-polluted sample; TC – total chemoorganoheterotrophs; HD – hydrocarbon degraders; CFU – colony-forming unit

Specimen	Polluted soil	Substrate for biodegradation
TC	1.2×10^6	9.7×10^5
HD	2.7×10^5	5.6×10^4

During six-month time interval, samples were taken five times (07/09/2009 – P1; 06/10/2009 – P2; 09/11/2009 – P3, 12/01/2010 – P4 and 18/03/2010 – P5).

The organic substance from the 5 soil samples was extracted with chloroform (HPLC grade, J. T., USA) using a Soxhlet apparatus.

From these extracts, the hydrocarbons (saturated and aromatic) were isolated by column chromatography: the extracts were saponified with a 5 % solution of KOH in methanol and after standing overnight, neutralized with 10 % hydrochloric acid. The products were dissolved in a mixture of dichloromethane (containing 1 % methanol) and hexane (1:40), and separated by column chromatography on alumina and silica gel. The hydrocarbon fractions were eluted with hexane (saturated hydrocarbons) followed by dichloromethane (aromatic hydrocarbons). A detailed description of the analytical procedure was discussed in previous papers.[9,10]

Hydrocarbons were analyzed by the gas chromatography–mass spectrometry (GC–MS) techniques. An Agilent 7890N gas chromatograph fitted with a HP5-MS capillary column (30 mm×0.25 mm, 0.25 μm film; temperature program: 80 °C for 0 min; then 2 °C min^{-1} to 300 °C and held for 20 min) with helium as the carrier gas (flow rate 1 cm^3 min^{-1}) was used. Detailed analyses of the target compounds were conducted in the single ion monitoring mode (SIM), comprising the following ion chromatograms: 178 (phenanthrene), 192 (methyl-phenanthrenes), 206 (dimethyl-phenanthrenes) and 220 (trimethyl-phenanthrenes). A detailed description of the instrumental techniques was discussed in a previous paper.[11]

The saturated hydrocarbon mixture was separated into *n*-alkane and branched and cyclic alkane fractions by urea adduction.[12] The *n*-alkanes in the urea adducts were analyzed by gas chromatography (GC). The gas chromatographic analyses were conducted on a GC8000 instrument (Fisons Instruments, Italy) equipped with a 30 m×0.25 mm i.d.×0.25 μm film ZB1 fused silica capillary column (Phenomenex, Germany). The chromatographic conditions were as follows: 1 μL split/splitless injection at 80 °C oven temperature (injector temperature 270 °C, splitless time 60 s), 3 min hold, then programmed at 5 °C min^{-1} to 300 °C. The carrier gas was hydrogen at a velocity of 40 cm s^{-1}.

RESULTS AND DISCUSSION

Total ion chromatograms (TICs) of saturated hydrocarbon fractions isolated from the oil pollutant at the beginning of the biodegradation (P1) and after 6 months (P5), at the end of the experiment, are shown in Fig. 1. In similar samples, P1 and P5, the peaks originating from *n*-alkanes were of very low intensity. Based on these chromatograms, a precise conclusion about the extent of microbial degradation of the investigated oil pollutant could not be made.

Mass fragmentograms of phenanthrene, methyl-, dimethyl- and trimethyl--phenanthrenes obtained by GC–MS analysis of aromatic fractions isolated from extracts of samples P1–P5 are shown in Fig. 2. In the initial sample (P1), the distributions of these aromatic hydrocarbons were typical for oil. Considering the fact that most of *n*-alkanes in the initial sample have already been degraded (Fig. 1), and that phenanthrene and its methyl-isomers were still preserved, it could be concluded that the investigated sample of oil pollutant was at the third, moderate level of the Head scale of oil biodegradation at the beginning of the experiment.[4]

In the samples from P1 (the beginning of *ex situ* natural bioremediation, 7th September 2009) to P5 (the end of the experiment, 18th March 2010), a gradual degradation of phenanthrene and its methyl-, dimethyl- and trimethyl-isomers was registered (Fig. 2). On the scale from 1 to 10 of the Head classification of oils according to biodegradation level,[4] sample P5 can be classified as > 6, the severe level.

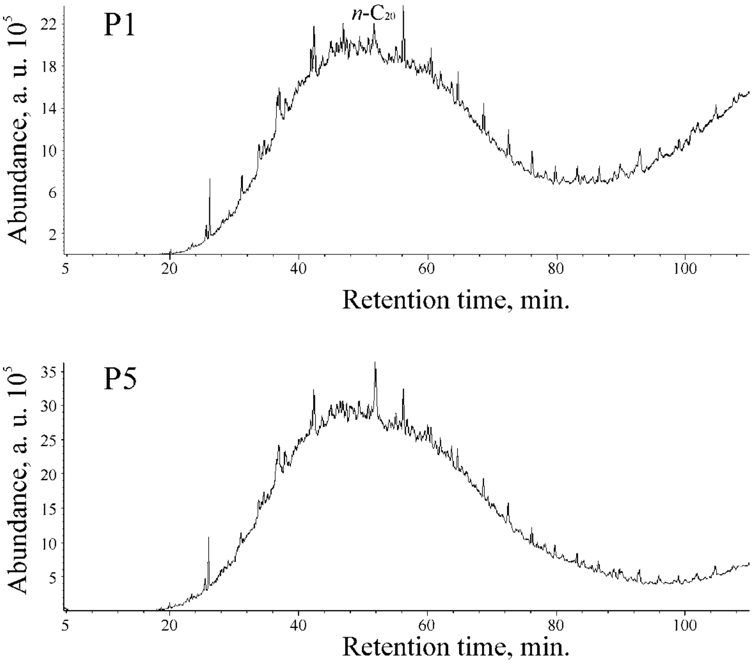

Fig. 1. Total ion chromatograms (TICs) of the saturated hydrocarbon fractions isolated from the oil pollutant. P1 (beginning of the experiment) and P5 (after the six-month bioremediation).

Considering the fact that in the initial sample, the amount of *n*-alkanes within the saturated hydrocarbons fraction was very low (Fig. 1), these compounds were concentrated by urea adduction technique to facilitate their analysis. Due to their ability to form channel inclusion compounds with urea molecules, *n*-alkanes can be successfully concentrated, *i.e.*, separated from branched, cyclic and polycyclic alkanes in a mixture of saturated hydrocarbons.[12]

Parallel with the mass fragmentograms of phenanthrene and its methyl-isomers, gas chromatograms of the urea adduct from samples P1–P5 are given in Fig. 2. Although the amount of *n*-alkanes within the total mixture of saturated hydrocarbons, both at the beginning and at the end of the experiment, was very low (Fig. 1), they were successfully concentrated by the urea adduct technique. Accordingly, in the gas chromatograms of all the investigated samples, a homologous series of alkanes, ranging from C_{16} to C_{31} and maximizing at *n*-C_{20}, was identified. It is noticeable that the abundance and the distribution of the *n*-alkanes during the biodegradation of the oil pollutant did not change. Considering the fact that phenanthrene and its methyl-isomers, although less biodegradable compounds, were efficiently degraded from samples P1 to P5, this observation was surprising. According to the generally accepted principles of oil biodegradation,[3,4,13] *n*-alkanes should have already been completely removed at the biodegradation level 4 and 5.[4] Due to this, it could be stated that their appearance in sample P5, which is obviously at a biodegradation level > 6, was unexpected.

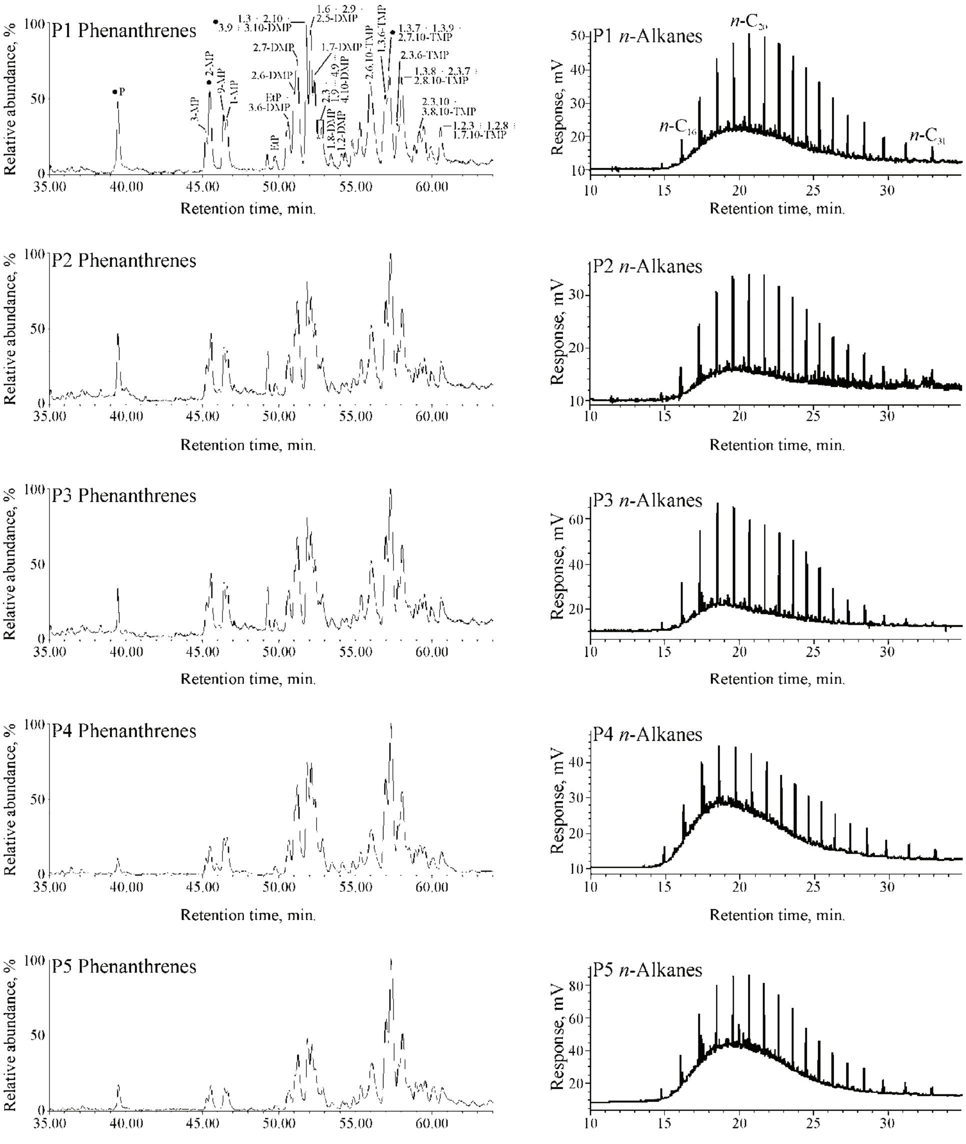

Fig. 2. Mass fragmentograms of phenanthrene (P), methyl-phenanthrenes (MP), dimethyl-phenanthrenes (DMP) and trimethyl-phenanthrenes (TMP), obtained by gas chromatography–mass spectrometry (GC-MS) analysis (using the Single Ion Monitoring, SIM method) of the aromatic fractions and the gas-chromatograms (GC) of the urea adducts of the saturated fractions (*n*-alkanes), isolated from the oil-type pollutants taken from the soil during the six-month biodegradation, P1–P5.

n-Alkanes are significantly more biodegradable compounds than aromatic hydrocarbons, including phenanthrene and its methyl-isomers. However, the results obtained in this study undoubtedly show that under conditions of reduced availability of a certain class of compounds, microorganisms opt for those that are, although less biodegradable, more accessible, *i.e*. those that are found in higher amounts in a substrate. In this case, the reason for lower biodegradability might be the smaller amounts of *n*-alkanes in the pollutant. On the other hand, this observation could also be caused by their protection by incorporation, *i.e*., the formation of inclusions with non-biodegradable components, such as humic substances or fulvic acids, present in recent sediments as native organic compounds.

CONCLUSIONS

The *ex situ* natural biodegradation (non-stimulated bioremediation, without the addition of biomass, nutrient substances and biosurfactant) of soil contaminated with heavy residual fuel oil (mazut) was conducted during a period of 6 months. The low abundance of *n*-alkanes in the total saturated hydrocarbons fraction in the initial sample (identification was only possible after concentration by the urea adduction technique) showed that the investigated oil pollutant was at the boundary between the third and the fourth biodegradation level on the Head biodegradation scale from 1 to 10.[4] During this experiment, intensive degradation of phenanthrene and its methyl-, dimethyl- and trimethyl-isomers was not accompanied by the complete removal of remaining *n*-alkanes. Contrary to expectations, the abundance of *n*-alkanes remained at the initial low level even at the end of the experiment when the pollutant attained a degradation level > 6.

According to these results, it can be concluded that during biodegradation of oil pollutant, under the condition of reduced availability of a certain class of compounds (caused by their low amount), microorganisms opt for those which are more accessible, *i.e*., those which are found in a substrate in higher amounts, even if these compounds are less biodegradable.

Acknowledgments. We thank the Ministry of Education, Science and Technological Development of the Republic of Serbia (Projects 176006 and III 43004) and the Alexander von Humboldt Foundation (Germany) for supporting this research.

ИЗВОД

ДЕГРАДАБИЛНОСТ НОРМАЛНИХ АЛКАНА ЗА ВРЕМЕ *EX SITU* ПРИРОДНЕ БИОРЕМЕДИЈАЦИЈЕ ЗЕМЉИШТА ЗАГАЂЕНОГ МАЗУТОМ

MUFTAH MOHAMED ALI RAMADAN[1], ТАТЈАНА ШОЛЕВИЋ KNUDSEN[2], МАЛИША АНТИЋ[3], ВЛАДИМИР П. БЕШКОСКИ[1,2], МИРОСЛАВ М. ВРВИЋ[1,2], JAN SCHWARZBAUER[4] и БРАНИМИР ЈОВАНЧИЋЕВИЋ[1,2]

[1]Хемијски факултет, Универзитет у Београду, Студентски трг 12–16, 11001 Београд, [2]Центар за хемију, Институт зе хемију технологију и металургију, Његошева 12, 11001 Београд, [3]Пољопривредни факултет, Универзитет у Београду, Немањина 6, 11081 Београд и [4]Institute of Geology and Geochemistry of Petroleum and Coal, Lochnerstrasse 4–20, 52056 Aachen, Germany

Добро је познато да се у току биодеградације нафте у природним геолошким условима, или нафтног загађивача у животној средини, деградација угљоводоника одиграва према дефинисаном распореду. На пример, главне промене у процесу разградње нормалних алкана дешавају се у току другог, „благог“, и трећег, „умереног“, ступња (на скали биодеградације од 1 до 10). Према досадашњим истраживањима, у четвртом ступњу, када почињу интензивне промене фенантрена и његових метил изомера, нормални алкани су већ у потпуности уклоњени. У овом раду у току периода од 6 месеци извођена је *ex situ* природна биоремедијација (нестимулисана биоремедијација без додатка биомасе, хранљивих састојака и биосурфактаната) земљишта загађеног мазутом. Ниска обилност нормалних алкана у фракцији укупних засићених алкана у почетном узорку (идентификација је била могућна тек након концентровања помоћу карбамида) показала је да је испитивани нафтни загађивач на граници између трећег и четвртог ступња биодеградације. Током експеримента, интензивну разградњу фенантрена и његових метил, диметил и триметил изомера није пратило уклањање остатка нормалних алкана. Њихова обилност је остала на почетном, ниском нивоу и на крају експеримента када је загађивач достигао један од највиших степена биодеградације. Добијени резултати су показали да се разградња појединих угљоводоника упркос њиховој високој биодеградабилности не одиграва до потпуног краја ни у завршним фазама деградације. У условима њихове смањене доступности, микроорганизми се опредељују за теже деградабилне, али доступније угљоводонике.

(Примљено 29. августа, ревидирано 9. октобра 2012)

REFERENCES

1. W. Fritsche, M. Hofrichter, *Biotechnology*, Vol. 11b, 2nd ed., H. J. Rehm, G. Reed, Eds., Wiley–VCH, New York, USA, 2008, p. 144
2. J. D. Van Hamme, A. Singh, O. P. Ward, *Microbiol. Mol. Biol. Rev.* **67** (2003) 503
3. J. K. Volkman, R. Alexander, R. I. Kagi, G. W. Woodhouse, *Geochim. Comochim. Acta* **47** (2983) 785
4. M. Head, D. Martin Jones, S. R. Larter, *Nature* **426** (2003) 344
5. K. E. Peters, J. M. Walters, J. M. Moldowan, *The Biomarker guide: biomarkers and isotopes in the petroleum exploration and earth history*, Vol 2, Cambridge University Press, Cambridge, UK, 2005, p. 658
6. C. Loser, H. Seidel, A. Zehnsdorf, U. Stottmeister, *Appl. Microbiol. Biotechnol.* **49** (1998) 631
7. I. D. Bossert, L. M. Shor, D. S. Kosson, in *Manual of Environmental Microbiology*, C. J. Hurst, R. L. Crawford, G. R. Knudsen, M. J. McInerney, L. D. Stetzenbach, Eds., ASM Press, Washington, D.C., 2002, pp. 934

8. V. Beškoski, G. Gojgić-Cvijović, J. Milić, M. Ilić, S. Miletić, T. Šolević, M. M. Vrvić, *Chemosphere* **83** (2011) 34
9. B. Jovančićević, P. Polić, M. M. Vrvić, G. Sheeder, M. Teschner, H. Wehner, *Environ. Chem. Lett.* **1** (2003) 73
10. B. Jovančićević, M. Antić, T. Šolević, M. Vrvić, A. Kronimus, J. Schwarzbauer, *Environ. Sci. Pollut. Res.* **12** (2005) 205
11. M. Novaković, M. A. R. Muftah, T. Šolević Knudsen, M. Antić, V. Beškoski, G. Gojgić-Cvijović, M. Vrvić, B. Jovančićević, *Environ. Chem. Lett.* **10** (2012) 287
12. E. Evans, G. Kenny, W. Meinschein, E. Bray, *Anal. Chem.* **29** (1957) 1858
13. H. Huang, B. F. J. Bowler, T. B. P. Oldenburg, S. R. Larter, *Org. Geochem.* **35** (2004) 1619.

Journal of the Serbian Chemical Society
JSCS-info@shd.org.rs • www.shd.org.rs/JSCS

J. Serb. Chem. Soc. 78 (7) 1045–1053 (2013) UDC 504.53:504.06+581.5+635.01:546.3
JSCS–4480 *Original scientific paper*

Impact of urban gardening in an equatorial zone on the soil and metal transfer to vegetables

JEAN AUBIN ONDO[1,2]*, PASCALE PRUDENT[1], CATHERINE MASSIANI[1], RICHARD MENYE BIYOGO[2], MARIANE DOMEIZEL[1], JACQUES RABIER[3] and FRANÇOIS EBA[2]

[1]Aix-Marseille Université, CNRS, LCE, FRE 3416, 13331 Marseille, France, [2]Ecole Normale Supérieure, Laboratoire Pluridisciplinaire des Sciences, B.P. 17009 Libreville, Gabon and [3]Equipe BBE, UMR-CNRS/IRD 6116 IMEP, Aix-Marseille université, case 97, 3, place Victor-Hugo, 13331 Marseille cedex 03, France

(Received 15 September 2012)

Abstract: This study was aimed at assessing the impact of urban agriculture on physicochemical properties of the soil and the metal uptake by some leafy vegetables cultivated in urban soils of Libreville, Gabon. Cultivated and uncultivated topsoil and vegetable samples were collected from two urban garden sites, and analyzed. The results showed that there was strong acidification and a decrease in the concentrations of nutrients and metals in soils due of agricultural practices. The metal transfer to plants was important, with the exception of iron. The non-essential metals cadmium and lead were not detectable in the plant tissues. Amaranth accumulated more metals than other vegetables. Amaranth and Roselle were vegetables that preferentially concentrated metals in their leaves and could, therefore, be used for metal supplementation in the food chain.

Keywords: soil acidification; trace metals; leafy vegetables; bioconcentration factor; translocation factor.

INTRODUCTION

Population growth forecasts for year 2030 indicate that the world population will increase and reach 9 billion inhabitants. This growth will particularly occur in the urban areas of developing countries, creating a situation of exploding alimentary needs.[1] In response to this considerable challenge, urban agriculture, which was almost insignificant thirty years ago, has developed in and around cities and has reached a phase of rapid expansion in developing countries. Therefore, it is important to assess the impact of this practice on urban soils and the nutritional quality of cultivated vegetables. International trade regulatory rules and guidelines are being developed in many countries across the world to

---

* Corresponding author. E-mail: laplus_ens@yahoo.fr
doi: 10.2298/JSC120915116O

prevent, monitor and control soil pollution.[2,3] For instance, the European Economic Commission was asked to elaborate guidelines for member states and competent regional authorities to revise the EU directive on sludge and elaborate a new directive on composting. Although transfer of trace metals from the soil to plants has often been mentioned,[4,5] to date, only a few studies have been conducted on this issue in West and Central Africa.[6–8]

The mobility of metals in soils and their absorption and bioaccumulation in vegetables depend on many factors, such as the climate, the bio-physicochemical properties of the soils, the type of vegetable cultivated, *etc*.[9] In urban areas, the proximity to roads and many factories can modify the physicochemical properties of and metal speciation in soil.

The aim of this study was to assess the impact of agriculture on the properties of soils in Libreville and the transfer of metal elements from the soils to vegetables.

MATERIAL AND METHODS

This study was conducted in two market gardening areas of Libreville between January and March 2008. The city is situated in West Gabon (9°25′ east longitude and 0°27′ north latitude). The two study sites, Alibandeng and PK8, are located in the north and east of Libreville, respectively. The climate type is equatorial. The annual rainfall varies from 1,600 to 1,800 mm. The average temperatures oscillate between 25 and 28 °C with minima (18 °C) in July and maxima (35 °C) in April, with a humidity of 80 to 100 %.

The oldest sites of vegetable production around Libreville were selected (16 years old). The first one, Alibandeng is located nearby the airport, and the other one, PK8 is beside the National Road 1. Both are densely populated flat and swampy zones. The Alibandeng soil is made of raw minerals of non-climate origin, formed on marine sands from the Quaternary era, whereas the ferralitic soil of PK8 is strongly altered and desaturated.[10]

Three cultivated soil samples and three uncultivated soils samples in each area were randomly collected with a stainless steel shovel. The samples were put in plastic bags immediately and stored at −4 °C. They were air-dried, crushed in a mortar, sieved through a 100-mesh sieve (2 mm), then crushed with a tungsten-carbide blade grinder and subsequently sieved through a 0.2 mm titanium mesh. The soil properties were assessed according to Association Française de Normalisation (AFNOR) protocols.[11] They included: particle size, pH, total organic carbon (*TOC*), total Kjeldahl nitrogen (*TKN*), assimilatable phosphorus (*P*), and cation exchange capacity (*CEC*). Considering, the average content of carbon in soil organic matter of 58 %, a conversion factor of 1.724 was used to calculate the percentage of organic matter (*OM*) from the content of organic carbon.[12]

Plant samples were collected at maturation. They were washed with distilled water and with de-ionized water to eliminate air-borne pollutants and soil particles, dried in air and then at 70 °C until constant weight, finely ground (0.2 mm) and kept in plastic bags. Amaranth (*Amaranthus cruentus*) and lettuce (*Lactuca sativa*) were collected at the Alibandeng site and roselle (*Hibiscus sabdariffa*), amaranth, Chinese cabbage (*Brassica chinensis*) and lettuce at the PK8 site.

The soil and plants samples were mineralized at 150 °C for 1 h in a microwave mineralizer using *aqua regia* (1/3 HNO_3+2/3 HCl) and a mixture of nitric acid, hydrogen peroxide and ultra-pure water with a volume proportion ratio 2:1:1, respectively. The mineralization products were filtered through a 0.45 μm mesh and the metals were analyzed by ICP-AES (Spectra 2000 Jobin Yvon).

The mobile fraction of the metal in the soils was extracted with 0.05 M EDTA at pH=7 and analyzed by ICP-AES.[13]

The capacity of plants to uptake metals from soils can be assessed using the bioconcentration factor (*BCF*), defined as:[14]

$$BCF = \frac{\text{Metal concentration in dry plant (mg kg}^{-1}\text{)}}{\text{Metal concentration in soil (mg kg}^{-1}\text{)}} \tag{1}$$

The transfer capacity of metal elements between the roots and aerial parts of a plant can be defined by the translocation factor (*TF*) given by:[15]

$$TF = \frac{\text{Metal concentration in aerial part (mg kg}^{-1}\text{)}}{\text{Metal concentration in roots (mg kg}^{-1}\text{)}} \tag{2}$$

Statistical tests were realized with the XLSTAT package under EXCEL. Similarity between samples was verified with a one-way analysis of the variance (ANOVA). A 0.05 level of probability was used for the statistical significance level.

RESULTS AND DISCUSSION

The physicochemical characteristics of the soil samples are presented in Table I. The two control soils were neutral. Alibandeng soil is sandy with low elevated organic matter (*OM*), nitrate test kit (*NTK*) and *P* levels. The water retention capacity of this soil is lower than that of the PK8 soil, which is siltier and exhibits more *OM*, *NTK* and *P* levels. Thus, the PK8 site seems more appropriate for agriculture than Alibandeng. In each site, the agricultural practices have led to a significant soil acidification. The cultivated soils are more acidic, and have higher levels of *NTK*, silt, *OM*, *P* and clay than the control soils. The fertilizers used were urea, and nitrate, phosphate and potassium (NPK) salts. These data agree with a comprehensive review of from 57 studies in Africa that showed a trend of negative balances for nutrients due of agricultural practices.[16]

TABLE I. Physicochemical properties of soils of Alibandeng and PK8; numbers followed by the same letter, a, b, c, d, e, f, g, h, i or j, in each row are not significantly different at $p < 0.05$ by the Student's *t*-test

Soil		pH	*CEC*	Sand	Silt	Clay	*OM*	*NTK*	*P*
			meq/100 g			g kg^{-1}			mg kg^{-1}
Alibandeng	Control	6.9^{a}	2.8^{d}	914^{a}	53^{b}	39^{a}	25.7^{c}	0.80^{b}	0.10^{b}
	Cultivated	4.3^{b}	4.8^{c}	935^{a}	22^{b}	35^{c}	22.2^{c}	0.66^{bc}	< 0.05
PK8	Control	7.1^{a}	13.6^{a}	545^{b}	278^{a}	178^{b}	68.3^{a}	3.07^{a}	5.6^{a}
	Cultivated	4.1^{b}	7.5^{b}	587^{b}	268^{a}	135^{c}	29.8^{b}	0.49^{c}	< 0.05

In urban soils, trace metals such as cadmium, copper, manganese, lead and zinc are good indicators of soil contamination arising from gasoline, vehicle exhausts, car components, industrial emissions, *etc*.[17,18] Pseudo-total and EDTA-extractable metal levels in the soils are presented (in mg kg^{-1} of dry weight) in Table II. They were higher in the PK8 soils than the Alibandeng soils and were significantly decreased at Alibandeng for Pb and Zn ($p < 0.001$), and at PK8 for Cu, Fe, Mn, Pb and Zn ($p < 0.001$). Metal levels in the cultivated soils were lower than or in ranges of those found in other agricultural soils of West African countries.[7,8] The soil acidity, as well as erosion and mineral fertilizers (particularly urea) have a strong influence on the mobility of ions and their uptake by plants, and decrease the soil metal concentrations.[19,20]

TABLE II. Pseudo-total and mobile metals in soils of Alibandeng and PK8 (expressed in mg kg-1 of dry weight); numbers followed by the same letter, a, b, c or d, in each row are not significantly different at $p < 0.05$ by the Student's *t*-test

Metal		Alibandeng control	Control PK8	Cultivated Alibandeng	Cultivated PK8
Cu	Pseudo-total	3.15^{c}	22.24^{a}	2.72^{c}	9.81^{b}
	Mobile	0.39^{c}	2.03^{a}	0.06^{c}	1.08^{b}
Fe	Pseudo-total	15011^{bc}	44841^{a}	8856^{c}	16332^{b}
	Mobile	2587^{b}	4225^{a}	208^{c}	1646^{b}
Mn	Pseudo-total	55.6^{c}	448.4^{a}	39.6^{c}	278.9^{b}
	Mobile	2.8^{b}	30.5^{a}	2.3^{b}	22.9^{a}
Pb	Pseudo-total	55.0^{b}	110.6^{a}	7.3^{c}	19.6^{c}
	Mobile	4.9^{b}	11.7^{a}	0.3^{b}	2.5^{b}
Zn	Pseudo-total	75.5^{b}	218.2^{a}	8.2^{c}	25.4^{c}
	Mobile	7.5^{b}	21.3^{a}	0.4^{c}	1.7^{bc}

The rate of element absorption by a plant depends on the cultivated plant, the soil properties and the mobility of the metals in the soil.[21] The results showed that the mobile (or EDTA-extractable) metal levels in this study followed the order Fe > Mn ≈ Zn > Pb > Cu in the control soils and Fe > Mn > Zn > Cu > Pb in the cultivated soils. The mobile metal levels varied from 0.4 to 10.9 mg kg^{-1} for Cu, from 31 to 361 mg kg^{-1} for Fe, from 2.3 to 95.0 mg kg^{-1} for Mn, up to 19.9 mg kg^{-1} for Pb and from 0.5 to 41.5 mg kg^{-1} for Zn. These values showed an important mobile fraction of Cu (13.7–46.8 % of its pseudo-total concentration in the soil), a moderate mobile fraction for Mn (3.9–30.3 %), Pb (3.6–19.2 % in the control soils), Zn (6.7–17.8 %) and a low value for Fe (0.2–2.5 %). It is possible that the addition of EDTA to the soils increased the phytoavailability of the metals by forming water-soluble chelate–metal complexes.[21,22] Cu, Pb and Zn were more mobile in the control soils, and Fe and Mn were more mobile in the cultivated soils than in the uncultivated soils. With the exception of Fe in the cultivated soils, the metals were more mobile in the silty soils than in the sandy soils. This result does not reflect the capacity of retention of metals, which is more important in loamy soils than in sandy soils. Indeed, Zhang and Zhang found that the contents of clay, organic carbon, total P, total Pb, total Cu and total Zn in silty soils were higher than sandy soils.[23]

The metal concentrations in the vegetables based on their dry weight are given in Table III. The concentrations of Cd and Zn were below the detection limits (0.30 and 2.36 mg kg^{-1}, respectively). Moreover, the Cd and Pb concentrations were low in the studied plants and these non-essential metals could not contaminate the food chain. The concentrations of Cu, Fe, Mn and Zn in vegetables ranged from 3.4 to 21.6 mg kg^{-1} for Cu, 319 to 3.777 mg kg^{-1} for Fe, 34 to 555 mg kg^{-1} for Mn and 29 to 176 mg kg^{-1} for Zn. The differences in the metal concentrations between the vegetables implied that the uptake capacity of the metals depended on the vegetable and the soil. The highest concentrations were found in the roots of lettuce from Alibandeng and the cabbage from PK8 for Cu and Fe, respectively; in amaranth leaves from Alibandeng for Mn; in amaranth leaves and roots from Alibandeng for Zn (Table III). Zinc concentrations were significantly higher in the vegetables from Alibandeng than those from PK8 were. These results confirmed the high uptake capacity of amaranth as was found previously in other studies.[14,21] The capacity of amaranth to accumulate more Mn and Zn than lettuce when grown on Alibandeng soil but not on PK8 soil probably reflects differences in the inherent crop growth characteristics.[7] The order of metal accumulation in the different parts of the plants depended on the studied species. When the entire plant is considered, the metal concentrations were Fe > Mn > Zn > Cu.

TABLE III. Metal levels in leaves, roots and entire plant cultivated at Alibandeng and PK8 (expressed in mg kg^{-1} of dry weight); numbers followed by the same letter, a, b, c, d, e, f, g, h, i or j, in each row are not significantly different at $p < 0.05$ by the Student's *t*-test

Soil	Plant	Part	Cu	Fe	Mn	Zn
Alibadeng	Lettuce	Leaves	8.64^{bcdef}	701.4^{cde}	170.7^{c}	117.1^{b}
		Roots	21.56^{a}	2229.1^{b}	69.5^{hi}	122.1^{b}
		Entire plant	11.47^{b}	1034.8^{cd}	149.4^{cd}	118.6^{b}
	Amaranth	Leaves	9.69^{bcde}	318.5^{e}	554.5^{a}	156.0^{a}
		Roots	10.83^{b}	2108.6^{b}	114.2^{ef}	175.7^{a}
		Entire plant	9.08^{bcdef}	678.7^{de}	370.1^{b}	152.1^{a}
PK8	Lettuce	Leaves	5.86^{fgh}	478.6^{e}	62.3^{hij}	45.0^{c}
		Roots	10.33^{bc}	1867.8^{b}	79.4^{ghi}	49.4^{c}
		Entire plant	6.58^{efgh}	749.6^{cde}	63.6^{hij}	44.4^{c}
	Amaranth	Leaves	11.46^{b}	1044.1^{cd}	89.7^{fgh}	49.3^{c}
		Roots	9.01^{bcdef}	2122.8^{b}	77.4^{ghi}	42.9^{c}
		Entire plant	9.82^{bcd}	1136.3^{cd}	75.6^{ghi}	45.2^{c}
	Cabbage	Leaves	3.42^{h}	479.8^{e}	48.1^{ij}	28.7^{c}
		Roots	7.47^{cdefg}	3776.9^{a}	92.6^{fgh}	42.9^{c}
		Entire plant	4.26^{fgh}	1206.2^{c}	57.1^{hij}	31.3^{c}
	Sorrel	Leaves	6.00^{fg}	705.9^{cde}	133.4^{de}	30.8^{c}
		Roots	7.08^{defg}	756.7^{cde}	34.2^{j}	30.0^{c}
		Entire plant	6.16^{fgh}	679.5^{cd}	106.3^{efg}	31.7^{c}

A comparison between the determined metal concentrations based on plant dry weight with those in the literature showed that the lowest Zn concentration in vegetables from Alibandeng found in the present study was obviously higher than those reported elsewhere.[24–26] In addition, the highest Mn concentration in found in this study was higher than those reported elsewhere.[24,25] The amount of Fe in the leaves of vegetables of Libreville gardens was higher than the vegetable Fe in other urban gardens in Africa.[25,26] However, the Cu concentration in the leaves was within the ranges of Cu concentrations in Africa and China.[7,24–26]

Cu, Fe, Mn and Zn are essential metals and have known biological functions. Zinc is well known to be essential for the somatic growth of children.[27] It constitutes about 33 mg kg^{-1} of an adult body mass and it is essential as a constituent of many enzymes involved in several physiological activities, such as protein synthesis and energy metabolism.[28] Manganese ions activate numerous enzymes in plant cells. The most important role of this element in green plants is its involvement in the process of decomposition of water molecules with the release of oxygen. Copper is essential for photosynthesis and mitochondrial respiration, carbon and nitrogen metabolism, oxidative stress protection and is required for cell wall synthesis. Iron is one of the key elements for normal enzyme functions, especially those involved in redox processes, such as the synthesis of porphyrin, reduction of nitrite and sulfate, and N_2-fixation.[29]

The metal concentrations in plants depend mainly on their concentrations in the soil on which they grew or were cultivated.[29] Thus, it is important to assess the transfer from soil to plant. The *BCF* and *TF* values for metal concentrations in the entire plants are presented in Table IV. The metal *BCF* values differed between vegetable species and between sites for a same species. This indicates a difference in uptake selectivity. The *BCF* values for Mn and Zn were 34 and 10 times higher for amaranth from Alibandeng than for amaranth from PK8, respectively. For all metals, high *BCF* values were measured in the plants from Alibandeng. This suggested that the metals were more bioavailable in the Alibandeng soils than in the PK8 soils. Alibandeng has mostly sandy soils. Sandy soils are most likely to release metals, such as Mn and Zn. Brazauskiene *et al*.[30] showed that soils with sandy texture savannas had low retention capacity of metals, such as Zn and Cu. It is thus probable that metal leaching is more important at Alibandeng than at PK8. The *BCF* data obtained in the present study followed the order Zn > Mn > Cu > Fe > Pb in Alibandeg and Zn > Cu > Mn > > Fe > Pb in PK8 (Table IV). The soil–plant metal transfer seems enhanced in Alibandeng compared to PK8. Accumulator plants exhibited *BCF* values > 1. The high *BCF* values for Cu, Mn and Zn for amaranth confirmed that this vegetable accumulates metals and could be used as food crop for the supplementation of Zn for example in the case of deficiency in this metal. Indeed, in many parts of the developing world, most Zn is provided by edible parts of plants with high phytic acid, a potent inhibitor of Zn absorption.[31] Zn deficiency is widespread in developing countries, but it is under-recognized due to lack of sensitive biomarkers of the Zn status.[32]

The ranges of *TF* values were 0.4–1.3 for Cu, 0.1–0.9 for Fe, 0.5–4.9 for Mn, and 0.7–1.0 for Zn. The *TF* of Mn was generally near to or above 1, showing that Mn could be taken up more readily in vegetables leaves than other metals. On the other hand, with exception of Fe in amaranth, the *TF* values for the metals in roselle and amaranth were near to or above 1, showing an easy metal uptake in these leafy vegetables. Both the *BCF* and *TF* values were near to or above 1 for Cu in amaranth from PK8, Mn in lettuce and amaranth from Alibandeng, and Zn in all plants, with exception of cabbage from PK8 (Table IV). It is, therefore, probable that amaranth, lettuce and roselle are useful plants for metal phytoextraction.[33] A study on plants cultivated in jars under controlled conditions is foreseen to verify this hypothesis. However, these are edible plants, so attention must be paid to the toxic levels of metals in these plants.

CONCLUSIONS

Agricultural practices in the market gardens of Libreville have led to a high acidification of the soils, a decrease in the soil fertility parameters and a loss of metal elements. These practices did not increase the levels of toxic metals in the soils. Arranged in decreasing order, the concentrations of the metals in the entire plants were Fe > Mn > Zn > Cu > Pb. All these concentrations are below the toxicity tolerance thresholds for leafy vegetables. Of the studied plants, *Amaranthus cruentus* and *Hibiscus sabdariffa* exhibited the best metal accumulation and translocation to the leaves, the consumable part of these plants. As these vegetables are widely consumed throughout West Africa, laboratory and field studies would be necessary to determine the capacity of these plants to accumulate toxic metals, such as Pb or Cd in polluted area.

Acknowledgements. Financial assistance to the first author by the Gabonese Government is acknowledged. The authors thank Prof. Patrick Höhener and Dimitra Ondo for their constructive comments.

ИЗВОД

УТИЦАЈ ГРАДСКОГ БАШТОВАНСТВА НА ЗЕМЉИШТА И ТРАНСФЕР МЕТАЛА КОД ПОВРЋА У ЕКВАТОРИЈАЛНОЈ ЗОНИ

JEAN AUBIN ONDO[1,2], PASCALE PRUDENT[1], CATHERINE MASSIANI[1], RICHARD MENYE BIYOGO[2], MARIANE DOMEIZEL[1], JACQUES RABIER[3] и FRANÇOIS EBA[2]

[1]Aix-Marseille Université, CNRS, LCE, FRE 3416, 13331 Marseille, France, [2]Ecole Normale Supérieure, Laboratoire Pluridisciplinaire des Sciences, B.P. 17009 Libreville, Gabon и [3] Equipe BBE, UMR-CNRS/IRD 6116 IMEP, Aix-Marseille université, case 97, 3, place Victor-Hugo, 13331 Marseille cedex 03, France

Циљ ове студије је оцена утицаја обраде земљишта у граду на физичкохемијске карактеристике земљишта и узимања метала од стране неког лиснатог поврћа узгајаног у земљишту у градској средини Либервила у Габону. Сакупљени су и анализирани узорци биљака и узорци површинског слоја култивисаног и некултивисаног земљишта из градских башта на две локације. Резултати су показали да је дошло до снажне ацидификације и смањења концентрација нутријената и метала у овим земљиштима, због начина обраде земљишта. Пренос метала је био значајан, осим у случају гвожђа. Неесенцијални метали кадмијум и олово нису били детектовани у ткивима биљака. Амарант је акумулирао више метала него друго поврће. Испоставило се да амарант и хибискус преференцијално концентришу метале у лишћу, те стога могу бити коришћени као суплементи метала у ланцу исхране.

(Примљено 15. септембра 2012)

REFERENCES

1. M. N'Dienor, *PhD Thesis*, Institut National Agronomique Paris-Grignon, France, 2006
2. M. J. McLaughlin, R. E. Hammon, R. McLaren, G. Speir, T. W. Rogers, *Aust. J. Soil Res.* **38** (2000) 1037
3. *Towards a thematic strategy for soil protection*, Commission of the European Communities, Communication from the Commission to the Council, the European Parliament, the Economic and Social Committee and the Committee of the Regions, Brussels, Belgium, 2002
4. Y. J. Cui, Y. G. Zhu, R. H. Zhai, D. Y. Chen, Y. Z. Huang, Y. Qiu, J. Z. Liang, *Environ. Int*. **30** (2004) 785
5. Y. Yang, F. S. Zhang, H. F. Li, R. F. Jiang, *J. Environ. Manage*. **90** (2009) 1117
6. K. J. Kouakou, Y. A. Bekro, A. E. Sika, D. Baize, D. O. Dogbo, M. Bounakhla, F. Zahry, P. Macaigne, *Eur. J. Sci. Res*. **21** (2008) 471
7. J. O. Agbenin, M. Danko, G. Welp, *J. Sci. Food Agric*. **89** (2009) 49
8. M. W. Pasquini, *Sci. Total Environ*. **354** (2006) 43
9. R. K. Sharma, M. Agrawal, F. M. Marshall, *Environ. Pollut.* **154** (2008) 254
10. M. Delhumeau, *Notice explicative N° 36. Carte pédologique de reconnaissance à 1/200000. Feuille Libreville-Kango*, ORSTOM Ed., Paris, France, 1969, p. 51
11. AFNOR, *Qualité des sols. Recueil de normes françaises*, Afnor, Ed., Paris, France, 1994, p. 533
12. O. Abollino, M. Aceto, M. Malandrino, E. Mentasti, C. Sarzanini, F. Petrella, *Chemosphere* **49** (2002) 545
13. P. Quevauviller, *Trends Anal. Chem*. **17** (1998) 289
14. E. T. Tyokumbur, T. Okorie, *Biol. Trace Elem. Res*. **140** (2011) 215
15. H. Deng, Z. H. Ye, M. H. Wong, *Environ. Pollut*. **132** (2004) 29
16. J. G. Cobo, G. Dercon, G. Cadisch, *Agr. Ecosyst. Environ*. **136** (2010) 1
17. M. D. Marjanovic, M. M. Vukcevic, D. G. Antonovic, S. I. Dimitrijevic, D. M. Jovanovic, M. N. Matavulj, M. D. Ristic, *J. Serb. Chem. Soc*. **74** (2009) 697
18. I. Grzetic, R. H. A. Ghariani, *J. Serb. Chem. Soc*. **73** (2008) 923
19. J. A. Ondo, *PhD Thesis*, Aix-Marseille Université, France, 2011
20. S. Razic, S. Dogo, L. Slavkovi, *J. Serb. Chem. Soc.* **71** (2006) 1095
21. B. Kos, H. Grcman, D. Lestan, *Plant Soil Environ*. **49** (2003) 548
22. N. Finzgar, B. Kos, D. Lestan, *Plant Soil Environ*. **52** (2006) 25
23. M. Zhang, H. Zhang, *J. Environ. Sci.* **22** (2010) 598
24. Q. Yang, Y. Xu, S. Liu, J. He, F. Long, *Ecotox. Environ. Safety* **74** (2011) 1664

25. E. I. Uwah, N. P. Ndahi, F. I. Abdulrahman, V. O. Ogugbuaja, *J. Environ. Chem. Ecotox*. **3** (2011) 264
26. T. C. E. Mosha, H. S. Laswai, I. Tetens, *Nutrition* **55** (2000) 185
27. M. Kaji, Y. Nishi, *Growth Genet. Horm.* **22** (2006) 1
28. N. Jalbani, F. Ahmed, T. G. Kazi, U. Rashid, A. B. Munshi, A. Kandhro, *Food Chem. Toxicol.* **48** (2010) 2737
29. J. Zivkovic, S. Razic, J. Arsenijevic, Z. Maksimovic, *J. Serb. Chem. Soc.* **77** (2012) 959
30. D. M. Brazauskiene, V. Paulauskas, N. Sabiene, *J. Soil. Sediment.* **8** (2008) 184
31. E. Frossard, M. Bucher, F. Mächler, A. Mozafar, R. Hurrell, *J. Sci. Food Agr.* **80** (2000) 861
32. M. Olivares, F. Pizarro, S. de Pablo, M. Araya, R. Uauy, *Nutrition* **20** (2004) 205
33. W. J. Fitz, W. W. Wenzel, *J. Biotechnol.* **99** (2002) 259.

Journal of the Serbian Chemical Society
version electronic
JSCS-info@shd.org.rs • www.shd.org.rs/JSCS

J. Serb. Chem. Soc. *78* (7) 1055–1077 (2013)
JSCS–4481

UDC 661.183.6+54–145.2+544.723+
544.4:632.95
Original scientific paper

Extractive efficacy for acephate of microwave synthesized zeolitic materials: equilibrium and kinetics

BHAVNA A. SHAH[1]*, AJAY V. SHAH[2] and PIYUSH Y. JADAV[1]

[1]Department of Chemistry, Veer Narmad South Gujarat University, Surat-395007, Gujarat, India and [2]Science and Humanity Department, Polytechnic, Vidyabharti trust, Umrakh, Bardoli-394345, Gujarat, India

(Received 30 May, revised 23 November 2012)

A*bstract*: The present investigation deals with the utilization of Bagasse fly ash (BFA), a sugar industry waste, and a zeolitic material (MZBFA) synthesized from BFA by a combined conventional and microwave reflux method as adsorbents for the extraction of acephate (ACP), an organophosphorus pesticide, from aqueous solution. The synthesized adsorbents were characterized using various techniques, such as Fourier-transform infrared (FTIR) spectroscopy, powder X-ray diffraction (PXRD) analysis and scanning electron microscopy (SEM). The effects of various experimental parameters were investigated using a batch adsorption technique for the extraction of ACP. The extent of removal increased with decreasing initial ACP concentration and particle size of the adsorbent. The adsorption was fast and equilibrium was established within 90 min. Pseudo-first-order, pseudo-second-order, Bangham and intra-particle diffusion models were used to fit the experimental data. The pseudo-second-order rate equation was able to provide a realistic description of the adsorption kinetics. Equilibrium isotherms were analyzed by the Freundlich, Langmuir, Dubinin–Radushkevich and Tempkin isotherm Equations. The Langmuir Equation was found to represent the equilibrium data the best. A thermodynamic study showed that the adsorption of ACP on MZBFA was higher than that on BFA. The results indicate that such Zeolitic materials could be employed as low cost alternatives to BFA in wastewater treatment for the removal of pesticides.

Keywords: ACP; adsorption; isotherm; kinetics; zeolite.

INTRODUCTION

In recent years, the application of organophosphorus pesticides to agricultural crops and other land areas has increased manifold. India is the largest consumer of pesticides of the South Asian countries with 44.5 % consumption of the

---

* Corresponding author. E-mail: bhavna606@gmail.com
doi: 10.2298/JSC120530146S

total pesticides for cotton crops alone.[1] Substantive application of pesticides may cause accumulation in the hydrological systems[2] and in food crops.[3,4] The leaching runoff from agricultural and forest lands, deposition from aerial applications, and discharge of industrial wastewater are responsible for water contamination.[5]

Pesticides are considered to be potential chemical mutagens and potential chronic health hazards.[6] Considerable evidence has been accumulated indicating contamination of natural water resources globally, including India.[7] The Poison information Center in National School of Occupational Health (NIOH), Ahmadabad, India, reported that organophosphorus compounds are responsible for maximum number of poisoning (73 %) among all agricultural pesticides.[7] Patients of acute organophosphorus poisoning have been reported to suffer from problems such as vomiting, nausea, miosis, excessive salivation, blurred vision, headache, giddiness and disturbance in consciousness.[8]

Acephate, *N*-(methoxy-methylsulfanylphosphoryl)acetamide, is one of the ten most important organophosphorus insecticides in terms of sales volume. It has been extensively used in cotton crop cultivation. Surface and ground water contamination have been observed due to the presence of acephate. For evaluation of environmental waters and water resources for preparation of drinking water, highly sensitive methods for the determination of organophosphorus pesticides in surface water, ground water and drinking water are required. In the European Union, a maximum allowable concentration of 0.1 $\mu g\ L^{-1}$ for each individual (organophosphorus) pesticide in drinking water is in force. In the Netherlands, for aquatic ecosystems, the maximum allowable risk level for organophosphorus pesticides varies from 0.0007 to 23 $\mu g\ L^{-1}$.[9] Therefore, effective methods of pesticide removal from water are urgently needed. However, the wide ranges of pesticides, insecticides and herbicides in use make research extremely difficult for producing a single method for their removal. Several methods, either independent or in conjunction with others, have been used for the removal of pesticides, and these include chemical oxidation with ozone,[8] photodegradation,[10] UV irradiation,[11] biological degradation[11] and adsorption.[12–20] Adsorption on activated carbon is the most widely spread technology used for water treatment.[21] However, the commercially available carbon is not economically feasible on the large scale due to its high cost. For this reason, many industrial, agricultural, natural, and synthetic materials, such as bagasse fly ash (BFA), carbon cloth, porous polymeric adsorbents, wheat-residue black carbon, resin, lignin, wood charcoal, waste tire rubber granules, *etc.*, have been converted into inexpensive activated carbons for this purpose.[21]

Despite many studies on the chemical modification of cellulose, only a few investigated the modification of bagasse fly ash. In view of all these facts, attempts were made to convert bagasse fly ash, a waste material of the sugar industry, into an inexpensive and effective adsorbent, such as zeolite. BFA is currently used as a filler in building materials. It was used previously for chemical oxygen demand (COD) reduction of sugar mill and paper mill effluents.[22] Various researchers utilized it for the adsorptive extraction of phenolic compounds,[23] metals[24,25] and dyes.[26] However, from the survey of the literature, no information for the adsorptive removal of ACP pesticide by BFA and a zeolitic material (MZBFA) synthesized from BFA could be found.

The main objective of this paper were: *i*) to study the feasibility of using BFA and MZBFA as adsorbents for the removal of ACP pesticide, *ii*) to determine the physicochemical characteristics and thermal stability of BFA and MZBFA, *iii*) to determine the various parameters affecting the sorption, such as pH, adsorbent dose, initial concentration, contact time and temperature, *iv*) to evaluate the usefulness of various kinetic models, *viz*. pseudo-first-order, pseudo-second-order, Bangham and intra-particle diffusion models and *v*) to determine the applicability of linear and non-linear forms for various isotherm models (*i.e.*, the Freundlich,[27] Langmuir,[28] Dubinin–Radushkevich[29] and Tempkin models[30]).

EXPERIMENTAL

Preparation of adsorbents

In the present investigation, BFA was collected from a local sugar mill, Shree Khedut Sahkari Khand Udhyog Mandali Ltd., located at Bardoli, Gujarat, India. All of the reagents used in these investigations were supplied by Merck and Rankem as analytical grade reagents. Initially, the raw BFA obtained from the sugar mill was washed thoroughly with double distilled water to avoid the presence of foreign impurities and dried in sunlight for 8 and then 4 h in hot air oven at 353±5 K. The washed and dried material was sieved through a 200-μm mesh sieve to eliminate the larger particles. The dried BFA material, sieved through 200 μm mesh sieve was suspended into 3 M NaOH solution (8:1 liquid:solid ratio) for partial microwave irradiation at the earlier stages (15 min) followed by conventional heating (165 min) in a round bottom flask equipped with a reflux condenser and stirrer at a reaction temperature of 373±5 K. Microwave experiments were realized using a microwave oven (Q-ProM, Germany). After the hydrothermal reaction, the treated BFA was allowed to cool to room temperature. The resultant zeolite was washed with distilled water to remove excess sodium hydroxide, filtered and dried at 373±10 K in a hot air oven. The zeolization of bagasse fly ash by microwave heating was reported to be useful for shortening the reaction time (from hours or days down to minutes).

Instrumental techniques

A UV–Visible spectrophotometer (UV-1601, Shimadzu, Japan) was used to detect ACP. The pH measurements were made using a pH meter (PICO$^+$, Labindia pH meter, India). The Fourier-transform infrared (FTIR) spectra of the samples were recorded on a FTIR spectrophotometer (Thermo Nicolet IS10, Thermo Scientific Ltd., Switzerland). The specific surface area and pore volume of the adsorbents were determined using the Brunauer–Emmett–Teller (BET)[31] and Barret–Joyner–Halenda (BJH)[32] nitrogen adsorption and desorption methods at 77 K using a Micromeritics automatic surface area analyzer (Gemini 2360, Shimadzu, Japan). The chemical composition of each adsorbent was examined by the X-ray fluorescence method (X-ray XDL-B, Fischer scope, Japan). The moisture contents of the adsorbents were determined using a Karl-Fischer (1204R of VMHI, Metrohm Ltd., USA) instrument. The powder X-ray diffraction (PXRD) patterns of the adsorbents were obtained using a Panalyticals X-Pert Pro instrument employing nickel filtered Cu K_α (λ = 1.54060 Å) radiation. The density of the adsorbent was determined by pycnometery. The point of zero charge was calculated by the mass titration method.[33]

Adsorbate

High purity (99.1 %) ACP pesticide (obtained from United Phosphorous Ltd., India) was used as the adsorbate in the present study. The characteristics of ACP pesticide are listed in Table I. ACP is white crystalline powder with a strong mercaptan-like odor. Since ACP is hygroscopic, it was preserved in a dry atmosphere. An accurately weighed quantity of ACP was dissolved in distilled water to prepare stock solutions. The ACP solution was allowed to stand for some time until the absorbance of the solutions remained unchanged. Experimental solutions of desired pesticide concentration were obtained by successive dilutions.

TABLE I. The physical and chemical characteristics of ACP

Pesticide name	Abbreviation	IUPAC Name	λ_{max} nm	Empirical formula	Molecular mass, g mol^{-1}
Acephate	ACP	*N*-(methoxy-methylsulfanyl-phosphoryl)acetamide	214	$C_4H_{10}NO_3PS$	183.17

Analytical measurements

The UV–Vis spectrum of a standard solution ACP was recorded to determine its maximum absorbance (λ_{max}), which was found to be at 214 nm. A calibration curve for ACP was plotted between the absorbance 214 nm and the concentration of standard ACP solutions. The ACP concentrations were calculated from the calibration curve.

Batch experimental studies

To study the effect of important parameters on the adsorptive removal of ACP, batch experiments were conducted. For each experimental run, 50 mL of ACP of known concentration, pH and the known amount of the BFA and MZBFA were taken in a 100 mL brown colored glass bottle. The mixture was agitated in an incubator shaker at a constant speed of 150 revolutions per min. Samples were withdrawn at appropriate time intervals and the withdrawn samples were filtered and spectrophotometrically analyzed for the residual ACP concentration. Experiments were performed at initial pH values ranging from 2–10; controlled by the addition of 1 M HCl or 1 M NaOH solutions. For optimum amount of adsorbents per unit mass adsorbate, a 50 mL ACP solution was contacted with different amounts of adsorbents (1–6 g L^{-1}) until equilibrium was attained. Kinetics of adsorption was determined by analyzing adsorptive uptake of the ACP from the aqueous solution at different time intervals. For adsorption isotherms, ACP solutions of different concentrations (50–200 mg L^{-1}) were agitated with known amount of adsorbents until equilibrium was achieved. The residual ACP concentration was then determined. Blank runs, with only the adsorbents in 50 mL of distilled water were conducted simultaneously under similar conditions to account for any adsorption by either the container or the filter material. Each experiment was repeated three times and the mean values were taken.

RESULTS AND DISCUSSION

Characterization of adsorbents

Characteristics of adsorbents were determined by proximate analysis and physicochemical properties. Results are presented in Table II. The formation mechanism of zeolitic material from BFA was previously proposed as follows: dissolution of SiO_2 and Al_2O_3, particularly from the glass phase, into the alkaline solution, decomposition of aluminosilicate gel as zeolite precursor, and crystallization of zeolite. In present study, mechanism of zeolization is mainly separated into three terms. The first step is dissolution of SiO_2 and Al_2O_3 into the alkaline solution at 0–15 min. After 15 min, an intermediate aluminosilicate gel forms by the deposition of dissolved Si and Al species, which is the prematerial of zeolite crystals covering the external surface of BFA particles. The intermediate gel begins to change into zeolite *via* a dissolution–reprecipitation process at 40 min and the capture of sodium ions to neutralize the negative charge on the aluminate in the zeolite structure when zeolite crystal growth occurred. Zeolization was enhanced by partial microwave irradiation in the early stages of reaction because microwave can rapidly heat up an aqueous solution. Another reason may be assigned to active water generated by the break up of hydrogen bonds under microwave irradiation. The active water molecules, isolated H_2O molecules, should freely attack Si–O and Al–O bonds so to enhance the dissolution of the glass phase on the fly ash particles. The particle size of synthesized MZBFA and native BFA were determined by a Mastersizer 2000 particle size analyzer. The particle size distributions specify that majority of particles lies below 58.55 µm (95 %) in case of MZBFA, while in BFA majority of particles lies below 150.62 µm (95 %). The surface area of BFA and MZBFA were determined by the BET nitrogen adsorption method. The specific surface area obtained by the instrument for BFA and MZBFA were 99.14 and 328.30 $m^2 g^{-1}$ respectively. This indicates that the surface area of zeolitic adsorbent had been increased significantly during treatment. The mass titration results for BFA and MZBFA are shown in Fig. 1. The pH_{pzc} values obtained by mass titration method were 8.18 and 9.09 pH for BFA and MZBFA, respectively.

TABLE II. Physicochemical properties of BFA and MZBFA

Characteristics	Obtained values	
	BFA	MZBFA
Proximate analysis, mass %		
Loss on drying	11.95±0.2	13.74±0.2
Moisture content	10.36±0.3	12.25±0.3
Ash content	72.85±0.2	67.74±0.2
Physical properties		
Specific density	1.888±0.02	2.036±0.02

TABLE II. Continued

Characteristics	Obtained values	
	BFA	MZBFA
Physical properties		
Bulk density, g mL^{-1}	1.725±0.02	1.983±0.02
Dry density, g mL^{-1}	1.081±0.02	1.225±0.02
Void ratio	0.747	0.662
Porosity, fraction	0.428	0.398
pH$_{pzc}$	8.18±0.05	9.09±0.05
BET Surface area	99.14	328.30
Composition, mass %		
SiO_2	46.35	43.54
Al_2O_3	19.99	18.90
Fe_2O_3	5.89	2.99
CaO	4.97	3.17
MgO	4.83	4.12
Na_2O	4.17	7.24
K_2O	3.74	2.35

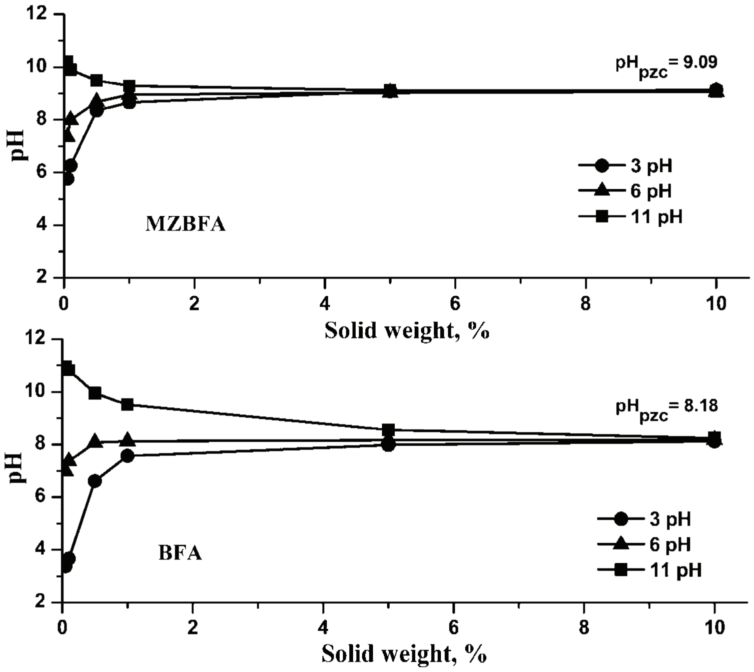

Fig. 1. Mass titration curves of BFA and MZBFA.

FT-IR Analysis

FT-IR spectra of the adsorbents, shown in Fig. 2, exhibit a broad band at about 3400 cm^{-1} indicating the presence of both free and hydrogen bonded OH groups on the adsorbent surface; the stretching is due to both silanol groups (Si–OH) and adsorbed water on the surface of adsorbents. The 1033.97, 676.67 and 475.33 cm^{-1} bands are due to the asymmetric stretching vibration of the internal tetrahedra, the symmetric stretching vibration and the bending vibration modes of T–O bonds in the TO_4 tetrahedra (where T = Si or Al), respectively. The band at 1097.31 cm^{-1} of BFA was shifted to 1033.97 cm^{-1} in MZBFA, confirming the tetrahedral coordination of aluminum in the zeolite skeleton. In MZBFA, the shift of the symmetric stretching band at 797.53 to 792.61 cm^{-1} of the internal tetrahedral (TO_4) of the amorphous aluminosilicates formed by the reaction of dissolved Si^{4+} and Al^{3+} confirmed the formation of zeolite phases.[34,35] The amount of improved tetrahedral sites of the aluminosilicate skeleton of the zeolite can be seen by the decreased frequency of the asymmetric stretching vibration of the tetrahedral. The band at about 1646.21 and 1456.34 cm^{-1} are ascribed to deformation of the –OH vibration of absorbed water and the bending vibration of interstitial water.[34]

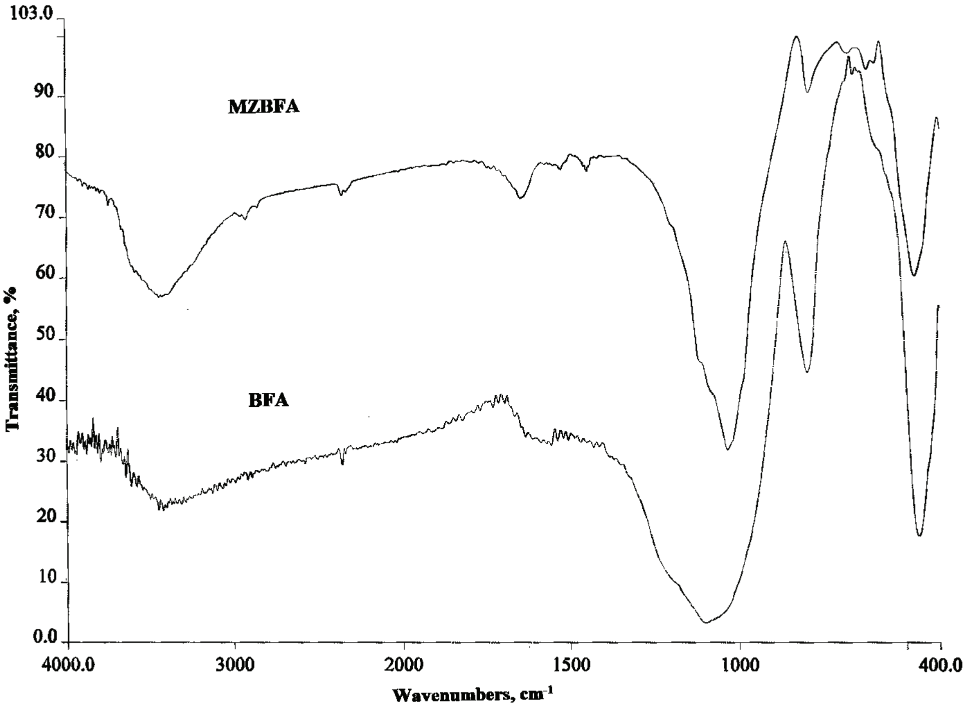

Fig. 2. FTIR Spectra of BFA and MZBFA.

PXRD Analysis

The identification of corresponding crystalline and mineralogical characteristics of adsorbents were made from powder X-ray diffraction patterns by comparing the diffraction data against a database provided by “Joint Committee on Powder Diffraction Standards”.[36] The low hump at lower diffraction angle in the BFA diffraction patterns shown in Fig. 3 indicates the presence of a glass phase.[37] BFA exhibited the presence of α-quartz as the major part and other amorphous materials.[36] The PXRD pattern of MZBFA showed that the hump at lower diffraction angle was suppressed. The newly observed intense peaks at 2θ 26.54 and 43.09° can be ascribed to the formation of zeolites in MZBFA. The X-ray diffraction patterns of MZBFA confirmed the presence of zeolite P (Phillipsite, JCPDS 39-0219) and zeolite X (JCPDS 28-1036) as the major minerals as indicated from their high intensities as seen in Fig. 3. Analcime (JCPDS 76-0901), zeolite A (JCPDS 14-90), chabazite (JCPDS 12-0194) and ZSM 12 (JCPDS 15-274) were present as minor minerals.

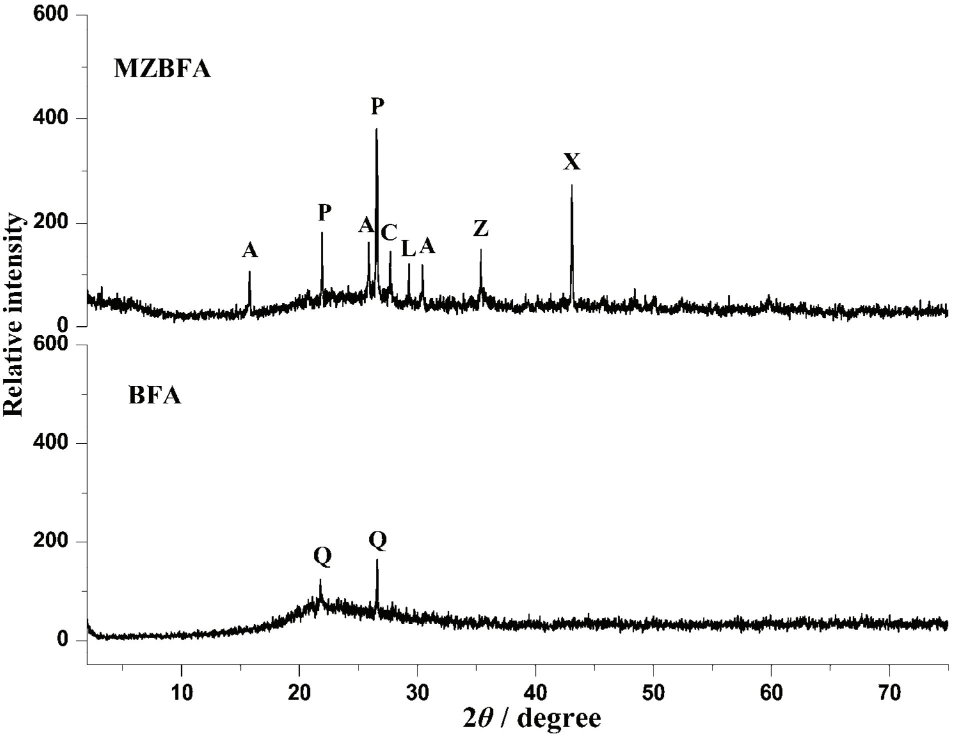

Fig. 3. PXRD Patterns of BFA and MZBFA. (P = phillipsite, X = zeolite X, A = analcime, L = zeolite A, Z = ZSM-12, C = chabazite and Q = α-quartz).

Morphology of the adsorbents

The SEM photomicrographs of both the adsorbents at 5.00 KX magnifications are presented in Fig. 4. The SEM image of BFA before hydrothermal reaction mostly contains non-crystalline glass, with a loose structure and posses smooth surface particle with no pits because the surface is covered by an aluminosilicate glass phase. The particles of MZBFA appeared to be more fluffy and porous. The SEM photomicrograph of MZBFA shows clear crystalline forms with compact structures and honeycomb aperture and holes. The MZBFA image shows the development of extended folded strands with deeper pits; with interior voids. The SEM photomicrograph of the pesticide loaded adsorbents shown in Fig. 4 reveals that the layered strands become diminished, showing that the adsorption of the pesticide created a more compact nature and spherical beads fill up the surface showing very intense pesticide adsorption on the surface throughout. In the case of MZBFA, agglomeration of particles forming clusters could be expected due to its softer porous texture.

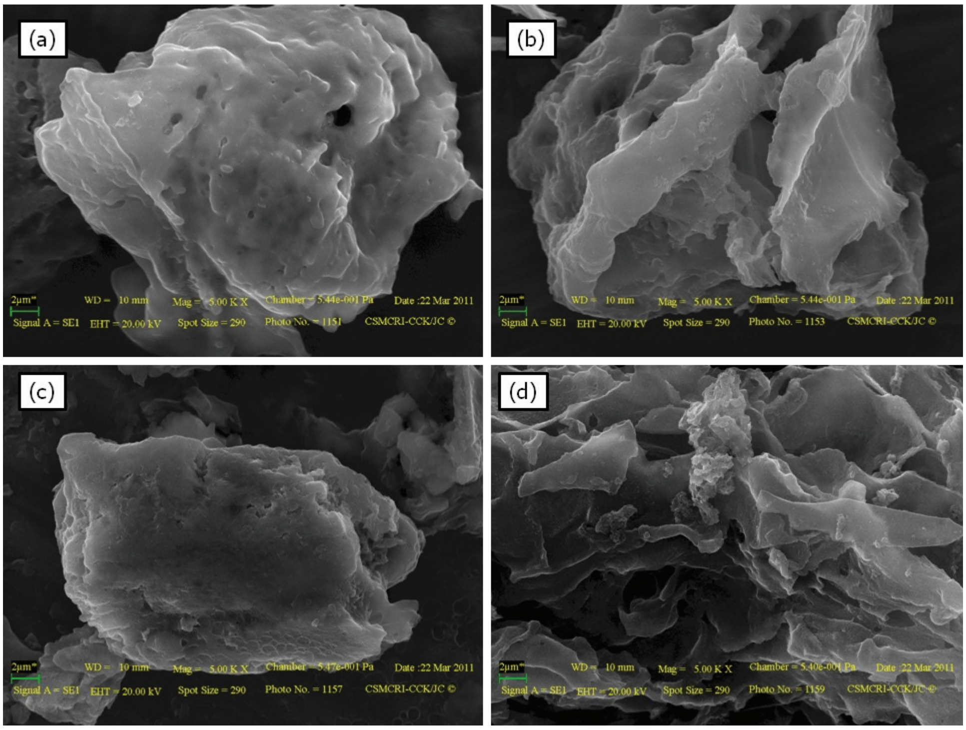

Fig. 4. SEM Micrographs of a) BFA, b) MZBFA, c) ACP-loaded BFA and d) ACP-loaded MZBFA at 5000× magnification.

Effect of pH

The adsorption of ACP by BFA and MZBFA was studied over a pH range of 2–10 at 298 K for 6 h. The initial ACP concentration was 125 mg L^{-1} and the adsorbent doses were kept at 0.15 g 50 mL^{-1}. The effects of pH on the adsorptive removal of ACP by the adsorbents are shown in Fig. 5. The pK_a of ACP is 8.35

and ACP exists in molecular form below this pH. The pH_{pzc} of the MZBFA increased to 9.09 from 8.18 in case of BFA, due to the alkaline hydrothermal treatment, which enables the utilization of MZBFA over a wide pH range, suitable for the adsorption of pesticides. At acidic pH values, the adsorption affinities of the adsorbents toward ACP are high due to dispersive interactions that are promoted in solutions of pH below the pH_{pzc} of the adsorbents. The percentage removal of ACP was maximum at acidic pH (pH 2), decreased with further increase in pH (up to pH 6) for both adsorbents and after pH 6 a trivial increase was observed up to 10 pH. At $pH < pH_{pzc}$, the negatively charged silica sites of the adsorbent are neutralized by H^+, thereby reducing hindrance to the diffusion of ACP ions. For the pH below 4, a significantly high electrostatic attraction exists between the positively charged surface of the adsorbent and appreciably ionized ACP. At pH 6, the partially charged ACP exhibits minimum adsorption on both adsorbents. As the pH of the system increases, the negative charge of adsorbent increases which results in high electrostatic repulsion between the solute molecules and between the solute and adsorbent surface. The percentage removal of ACP by BFA and MZBFA were 23±1 % and 33±1 %, respectively, at pH 2 after 6 h. The higher adsorption capacity of MZBFA compared to BFA in acidic solutions was due to the microporous structure of MZBFA, where ACP can be intensively adsorbed by the micropore-filling mechanism.[38]

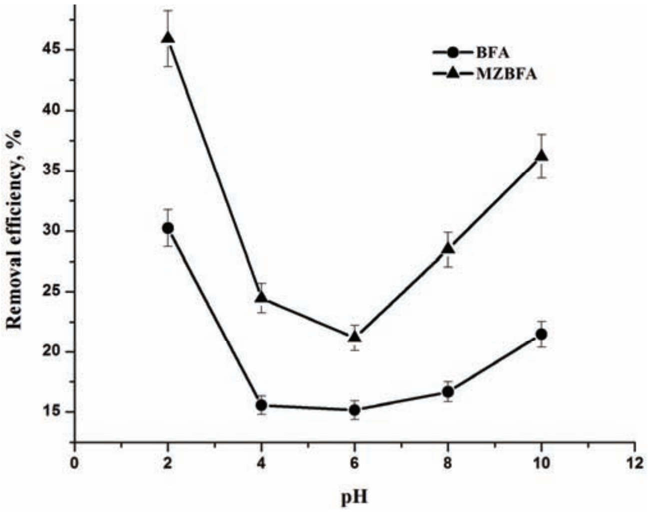

Fig. 5. Effect of pH (conc. = 125 mg L^{-1}, dose = 3 g L^{-1}, pH = 2–10, temperature = 298 K, time = 6 h) on the adsorption of ACP by BFA and MZBFA.

Effect of adsorbent dosage and acephate concentration

Initially, the rate of removal of ACP was found to be rapid, after which it slowed down as the dose concentration was increased, as shown in Fig. 6. The removal efficiency became almost constant and no significant change was observed in the removal of ACP above 0.2 g 50 mL^{-1} in the solution. Thus, the results obtained from this section of the experiments indicated 37±1 and 56±1 % removal of ACP was observed by BFA and MZBFA, respectively, at a dose of 4 g L^{-1}. At higher doses, the remaining ACP concentration in the solution was expected to be very low, so it experiences high resistance to mass transfer.

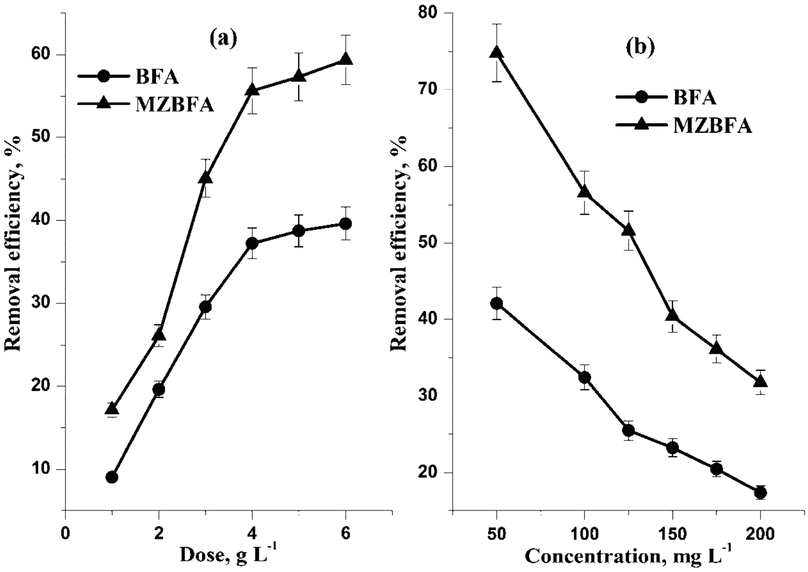

Fig. 6. a) Effect of adsorbent dosage (c = 125 mg L^{-1}, dose = 1–6 g L^{-1}, pH 2, temperature, 298 K, time, 5 h) and b) acephate concentration (c = 50–200 mg L^{-1}, dose = 3 g L^{-1}, pH 2, temperature, 298 K, time, 5 h) on the adsorption of ACP by BFA and MZBFA.

A given mass of adsorbent can adsorb only a fixed amount of adsorbate. Thus, the initial concentration of adsorbate solution is very important. The effect of the initial pesticide concentration on the removal by both the adsorbents is shown in Fig. 6. However, the amount of pesticide adsorbed per unit adsorbent mass increased with decreasing initial pesticide concentration due to the decrease in resistance to the uptake of solute from the pesticide solution. The curves indicate that the uptake efficiency of ACP by MZBFA was higher compared to that of BFA.

Effect of contact time

The effect of contact time on the adsorption of ACP by the adsorbents was studied for a period of 24 h for an initial pesticide concentration of 125 ppm at 298 K and pH 2. ACP solutions were kept in contact with the adsorbents for 24 h although no significant variation in the residual ACP concentration was detected after a contact time of 5 h. Thus, after 5 h contact time, a steady-state approximation was assumed. The effect of the contact time on the adsorption of ACP is presented in Fig. 7. The contact time curve shows that the pesticide removal was rapid in the first 90 min. An early and rapid uptake of pollutant and the establishment of equilibrium in a short period signify the efficacy of an adsorbent for its use in wastewater treatment. The curves indicate possible monolayer coverage of the surface of adsorbents by the pesticide. In between these two uptake stages, the rate of adsorption was found to be nearly constant. This is understandable from the fact that a large number of vacant surface sites were available for adsorption during the initial stages, and after a lapse of time, the remaining vacant surface sites were difficult to occupy due to repulsive forces between the solute molecules on the solid and in the bulk phases. Saturation of BFA occurred at 25±1 % adsorption, while for MZBFA, it occurred at 53±1 % adsorption. The resulting data shows that MZBFA has a greater potential to adsorb ACP than BFA. This may be due to the higher surface area and larger pore volume of MZBFA as compared to BFA.

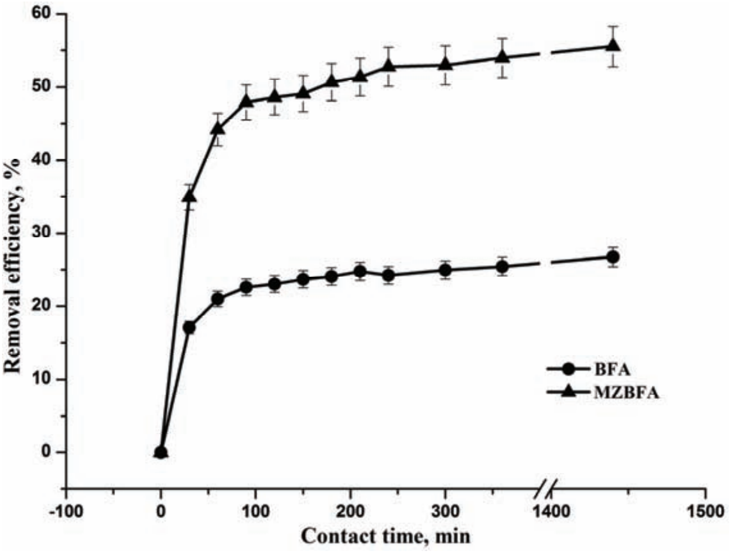

Fig. 7. Effect of contact time (c = 125 mg L^{-1}, dose = 3 g L^{-1}, pH 2, temperature, 298 K, time, 24 h) on the adsorption of ACP by BFA and MZBFA.

Effect of temperature and thermodynamic parameters

The adsorption of ACP on both the adsorbents was investigated at five different temperatures (293, 303, 313, 323 and 333 K). The uptake of ACP increased with increasing temperature, indicating the process is endothermic in nature.

Thermodynamic parameters were evaluated from Van't Hoff plots (not shown) for the adsorption of ACP onto BFA and MZBFA. The results are summarized in Table III. The change in enthalpy, ΔH^0, and change in entropy, ΔS^0, were evaluated from the slope and intercept, respectively, of the equation:

$$R\ln K_\mathrm{d} = \frac{-\Delta G^0}{T} = \Delta S^0 - \frac{\Delta H^0}{T} \tag{1}$$

where, K_d is the distribution coefficient; ΔH^0 is the enthalpy change, kJ mol^{-1}; ΔS^0 is the entropy change, J K^{-1} mol^{-1}; R is the gas constant, 8.314 J mol^{-1} K^{-1} and T is the temperature, K.

The spontaneity of the adsorption process was ensured by the decrease in the Gibbs free energy, ΔG^0, of the systems. The negative values of ΔG^0 indicate that the adsorption process becomes more spontaneous with increasing temperature, which favors the adsorption process. The positive values of ΔH^0 were in the range of 6.04–7.40 kJ mol^{-1}, *i.e.*, lower than 20 kJ mol^{-1}, confirming the endothermic nature of the overall adsorption process and also the adsorption to be physical rather than chemical linking through weak attraction forces.[39,40] The positive value of ΔS^0 corresponds to an increase in the degree of freedom of the adsorbed species, signifying weak interaction between ACP and the adsorbents.[40] However, if the adsorption process is influenced by cylindrical and convective diffusion, the adsorption capacity will increase with temperature.[41] Furthermore, it may be due to an increase in the equilibrium constant with increasing temperature.

TABLE III. Thermodynamic parameters for the adsorption of ACP on BFA and MZBFA

Pesticide	$-\Delta G^0$ / kJ mol^{-1}					ΔH^0 kJ mol^{-1}	ΔS^0 J mol^{-1} K^{-1}
	T / K						
	293	303	313	323	333		
BFA	7.199	7.811	8.309	8.660	9.028	6.035	45.48
MZBFA	9.217	9.698	10.24	10.94	11.43	7.403	56.58

Adsorption equilibrium studies

To optimize the design of an adsorption system for the adsorption of ACP, it is important to establish the most appropriate correlation for the equilibrium curves. Various linear and non-linear isotherm equations have been used to describe the equilibrium nature of adsorption. Some of these equations are the Freundlich,[27] Langmuir,[28] Dubinin–Radushkevich[29] and Tempkin[30] Equations. The models for characterization of the equilibrium distribution relate the quantity of solute adsorbed at equilibrium per unit weight of adsorbate, (q_e, mg g^{-1}) and the concentration of the solute remaining in the solution at equilibrium (c_e, mg L^{-1}).

The Freundlich isotherm[27] is derived by assuming a heterogeneous surface with a non-uniform distribution of heat of adsorption over the surface. The Freundlich isotherm was tested using the following linear equation:[27]

$$\log q_\mathrm{e} = \log K_\mathrm{f} + 1/n \log c_\mathrm{e} \tag{2}$$

where q_e is the amount adsorbed (mg g^{-1}), c_e is the equilibrium concentration of the adsorbate (mg L^{-1}), and K_f and n are the Freundlich constants related to adsorption capacity and adsorption intensity, respectively. The values of R^2 for this model, Table IV, show that the Freundlich Equation presents the poorest fit of the experimental data compared to the other isotherm equations. Values of the heterogeneity factor $n > 1$ would indicate conformity of the data to the formation of a multilayer at the adsorbent surface. The reported data of adsorption of ACP on soil shows $K_\mathrm{f} = 0.21$ and $n = 0.55$ which indicates multilayer formation is not possible in soil.[42] The value of n for the adsorption of ACP was higher for MZBFA (4.48) than for BFA (3.38).

The Langmuir Equation[28] can be used in following linearized form:

$$1/q_\mathrm{m} = 1/Q_0 + 1/Q_0 B c_\mathrm{e} \tag{3}$$

where q_m is the amount adsorbed (mg g^{-1}), c_e is the equilibrium concentration of the adsorbate (mg L^{-1}), and Q_0 and B are the Langmuir constants related to maximum adsorption capacity and energy of adsorption, respectively.

TABLE IV. Isotherm parameters for the adsorption of ACP on BFA and MZBFA

Isotherms	Adsorbent	Parameter values			
		q_m / mg g^{-1}	B / dm^3 mg^{-1}	R_L	R^2
Langmuir	BFA	13.699	0.044	0.155	0.990
	MZBFA	22.727	0.122	0.062	0.996
Freundlich		K_f / dm^3 g^{-1}	n	–	R^2
	BFA	10.328	3.38	–	0.875
	MZBFA	106.170	4.48	–	0.855
D–R		X_m / mg g^{-1}	B / mol^2 J^{-2}	E / kJ mol^{-1}	R^2
	BFA	8.166	5.1×10^{-4}	0.313	0.933
	MZBFA	15.975	1.5×10^{-4}	0.572	0.988
Tempkin		K_T / dm^3 mg^{-1}	B_1	–	R^2
	BFA	0.541	2.738	–	0.891
	MZBFA	3.107	3.677	–	0.860

Table IV indicates that the Langmuir model gave high quality fitting with correlation coefficient values R^2 0.990 to 0.996, *i.e.*, closer to unity than the other isotherms for the adsorption of ACP on BFA and MZBFA, indicating that the adsorption data better fits to the Langmuir isotherm model. Using the Langmuir model, the monolayer capacity of the adsorbents follows the order: MZBFA (22.73 mg g^{-1}) > BFA (13.70 mg g^{-1}). An essential characteristic of the Langmuir isotherm is that can be expressed in terms of a dimensionless separation factor, R_L, that was less than unity for both absorbents, which evidences that the adsorptions were favorable under the applied conditions. The relatively smaller value of R_L for adsorption by MZBFA than by BFA indicates that the adsorption was more feasible in the former case.

The Dubinin–Radushkevich (D–R) isotherm model[29] assumes that the mechanism of adsorption in micropores is pore-filling in nature, rather than layer-by-layer formation of a film on the walls of the pores. In order to appreciate the nature – physical or chemical – of the adsorption process, the isotherms data were analyzed by the (D–R) model, expressed by the following equation:[29]

$$\ln q_e = \ln X_m - \beta\varepsilon^2 \tag{4}$$

where q_e is the amount adsorbed (mg g^{-1}), X_m is the D–R monolayer capacity, β is the activity coefficient related to mean sorption energy, and ε is the Polanyi Potential, which is given by:

$$\varepsilon = RT \ln(1/c_e) \tag{5}$$

where R is the gas constant (kJ mol^{-1} K^{-1}), T is temperature (K), and c_e is the equilibrium concentration of the adsorbate (mg L^{-1}). When ln q_e is plotted against ε^2, a straight line is obtained. The slope of the plot gives the value of β and the intercept yields the value of the sorption capacity, X_m (8.17–15.97 mg g^{-1}), as shown in Table IV. The value of β is related to sorption energy, E, *via* the following relationship:

$$E = \frac{1}{\sqrt{-2\beta}} \tag{6}$$

The magnitude of the adsorption energy, E, is related to the reaction mechanism. If E is in the range of 8–16 kJ mol^{-1}, the adsorption is governed by ion exchange. In the case of $E < 8$ kJ mol^{-1}, physical forces may affect the sorption mechanism. The calculated values E for the systems examined in the present study were found to be < 8 kJ mol^{-1} (Table IV), which indicates that the adsorption of ACP in the studied adsorbate–adsorbent systems was physical in nature.

The Tempkin isotherm[30] contains a factor that explicitly takes into account adsorbate species–adsorbent interactions. This isotherm assumes that: *i*) the heat of adsorption of all the molecules in the layer decreases linearly with coverage due to adsorbate species–adsorbent interactions and *ii*) the sorption is characterized by a uniform distribution of binding energies, up to some maximum binding energy. Thus:

$$q_e = B_1 \ln K_T + B_1 \ln c_e \tag{7}$$

where $B_1 = RT\,b^{-1}$ and K_T are constants. K_T is the equilibrium binding constant (L mol^{-1}) corresponding to maximum binding energy and constant B_1 is related to the heat of sorption. A plot of q_e *vs*. ln c_e enables the determination of the isotherm constants K_T and B_1.

The values of K_T and B_1 obtained from the Tempkin plots of q_e *vs*. ln c_e are presented in Table IV. The R^2 value obtained for MZBFA is very close to its value for the Freundlich isotherm. This indicates that the heat of sorption of all the molecules in the layer decreases linearly with coverage due to adsorbent–adsorbate interactions. Thus, the adsorption of ACP on MZBFA could be characterized by a uniform distribution of the binding energies, up to some maximum binding energy.

The non-linear fitting of all four isotherms for the BFA and MZBFA adsorbents are presented in Fig. 8. The non-linear curves of the isotherms also indicate

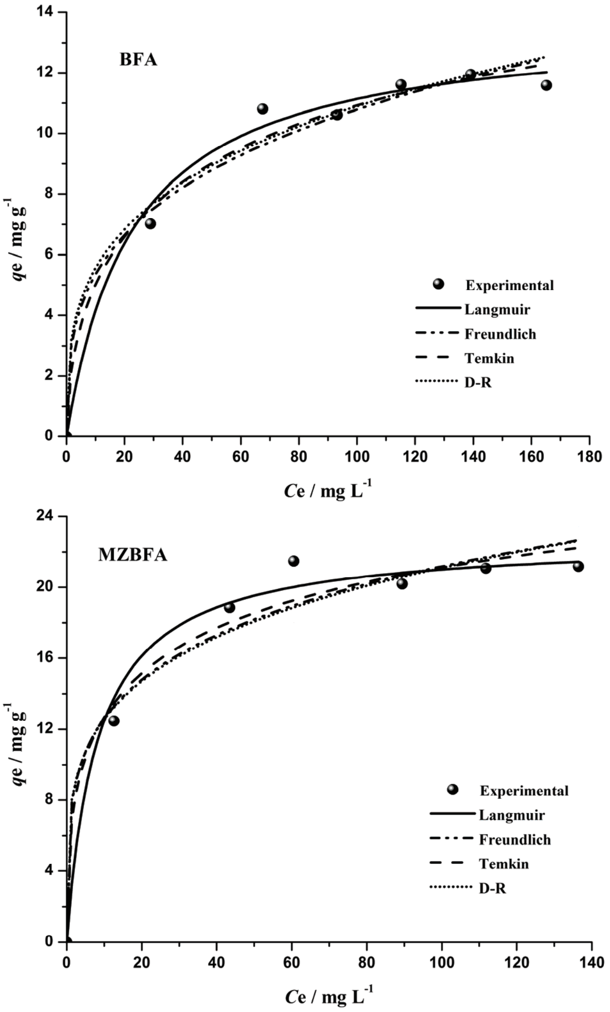

Fig. 8. Isotherms obtained using the non-linear method for the sorption of ACP onto BFA and MZBFA.

that of all four isotherms, the Langmuir Isotherm best fitted the experimental data. No matter what type of error distribution compromised the data; non-linear regression always produced accurate and efficient estimates of the parameters.[43] The adsorption equilibrium data of ACP onto both the adsorbents followed the order Langmuir > D–R > Tempkin ≥ Freundlich.

Adsorption kinetics

In order to investigate the adsorption process of ACP onto the adsorbents, four kinetic models were used, *i.e.*, the Lagergren pseudo-first-order,[44] the pseudo-second-order,[45] the Bangham[46] and the intra-particle diffusion[47] models. The pseudo-first-order kinetics model assumes that the rate of change of adsorbate uptake with time is directly proportional to the difference in the saturation concentration and the amount of solute uptake with time. The Lagergren Equation is given by:[44]

$$\log\left(q_\mathrm{e}-q_t\right)=\log q_\mathrm{e}-\left(\frac{k_\mathrm{f}}{2.303}\right)t \tag{8}$$

where, q_t and q_e (mg g^{-1}) are the amounts of ACP adsorbed at time t (min) and at equilibrium, respectively, and k_f is the pseudo-first-order rate constant (min^{-1}) of the reaction.

A plot of log (q_e – q_t) *vs*. t, was drawn to express the Lagergren first order kinetics model (Fig. 9). The kinetic parameters calculated from the slope and intercept are given in Table V. These values indicate that the adsorption rate was very fast at the beginning of the adsorption for both adsorbents. The values of the equilibrium adsorption capacity, q_e, were well below the monolayer capacities found by the Langmuir equilibrium isotherm model. The q_e values suggested that the adsorption process was not a true first order reaction.

The rate of pseudo-second-order reaction is expressed by the following equation:[45]

$$\frac{t}{q_t}=\frac{1}{(k_\mathrm{s}q_\mathrm{e}^2)}+\frac{1}{q_\mathrm{e}}t \tag{9}$$

where k_s is the rate constant of pseudo-second-order adsorption (g mg^{-1} min^{-1}) and $k_\mathrm{s}q_\mathrm{e}^2=h$ can be regarded as the initial sorption rate (mg g^{-1} min^{-1}). The initial sorption rate, h; the equilibrium adsorption capacity, q_e; and the pseudo-second-order constant, k_s, can be determined experimentally from the slope and intercept of a plot of t/q_t *vs*. t (Fig. 9). The kinetic parameters along with the correlation coefficients for the pseudo-second-order kinetic model are listed in Table V. The obtained results revealed that the initial adsorption rate, h was fast and that the adsorption mechanism was somewhat complex and not a single step process. The correlation coefficients are closer to unity for the pseudo-second-order kinetics than those for the pseudo-first-order kinetic model. Therefore, the adsorption of ACP by BFA and MZBFA could be approximated more appropriately by the pseudo-second-order kinetic model than by the pseudo-first-order kinetic model.

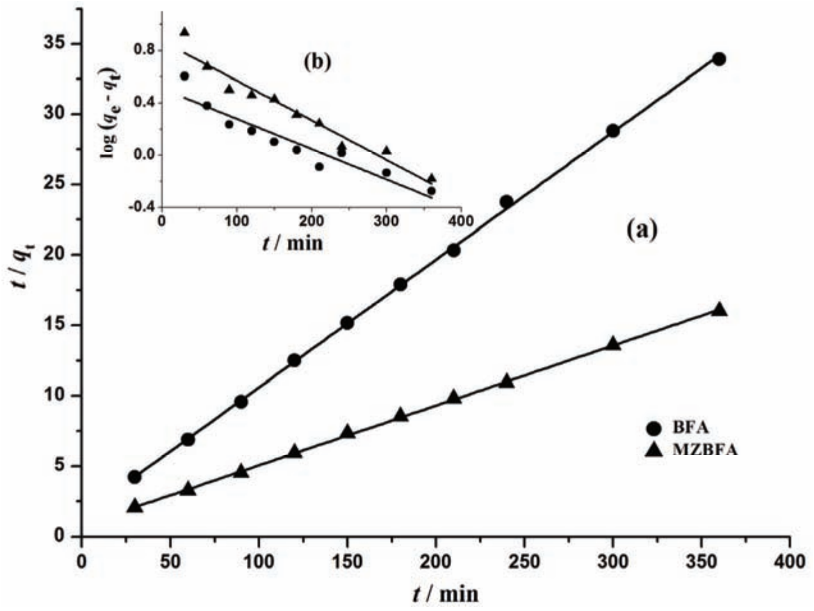

Fig. 9. a) Pseudo-second-order kinetic model (t/q_t *vs*. time) and b) pseudo-first-order kinetic model (log ($q_e - q_t$) *vs*. time) on the adsorption of ACP by BFA and MZBFA (c = 125 mg L^{-1}, dose = 3 g L^{-1}, temperature, 298 K).

TABLE V. Kinetic parameters for the removal of ACP by BFA and MZBFA

Pseudo-first order						
Adsorbent	q_e / mg g^{-1}	k_f×10^3 / min^{-1}	R^2			
BFA	3.236	4.606	0.897			
MZBFA	7.447	6.909	0.950			
Pseudo-second order						
Adsorbent	q_e / mg g^{-1}	k_s ×10^3 / g mg^{-1} min^{-1}	h / mg g^{-1} min^{-1}	R^2		
BFA	11.111	5.364	0.060	0.999		
MZBFA	23.810	2.227	0.053	0.999		
Bangham						
Adsorbent	α	k_0 / g	R^2			
BFA	0.165	0.577	0.903			
MZBFA	0.216	1.141	0.909			
Intraparticle diffusion						
Adsorbent	$k_{id,1}$ / mg g^{-1} min$^{-1/2}$	I_1 / mg g^{-1}	R^2	$k_{id,2}$ / mg g^{-1} min$^{-1/2}$	I_2 / mg g^{-1}	R^2
BFA	0.582	4.017	0.974	0.114	8.465	0.888
MZBFA	1.367	7.290	0.972	0.290	17.120	0.947

The kinetic data were further employed to gain insight into the slow step occurring in the present adsorption system and to check whether the adsorption process was diffusion controlled by using the Bangham Equation:[46,48]

$$\log\log\left(\frac{c_0'}{c_0' - q'm'}\right) = \log\left(\frac{K_0 m'}{2.303\ V}\right) + \alpha\ \log t \tag{10}$$

where c_0' is the initial concentration of adsorbate in solution (mmol L^{-1}), V is the volume of the solution (mL), m' is the weight of the adsorbent (g L^{-1}), q' is the amount of adsorbate retained at time t (mmol g^{-1}), and α and k_0 are constants. The values of constants α (<1) and k_0 are given in Table V. The double logarithmic plot (Fig. 10) according to above equation did not yield perfect linear curves (R^2 = 0.903 and 0.909 for removal of ACP by BFA and MZBFA, respectively, because the diffusion of adsorbate into the pores of the sorbents was not the only rate controlling step.

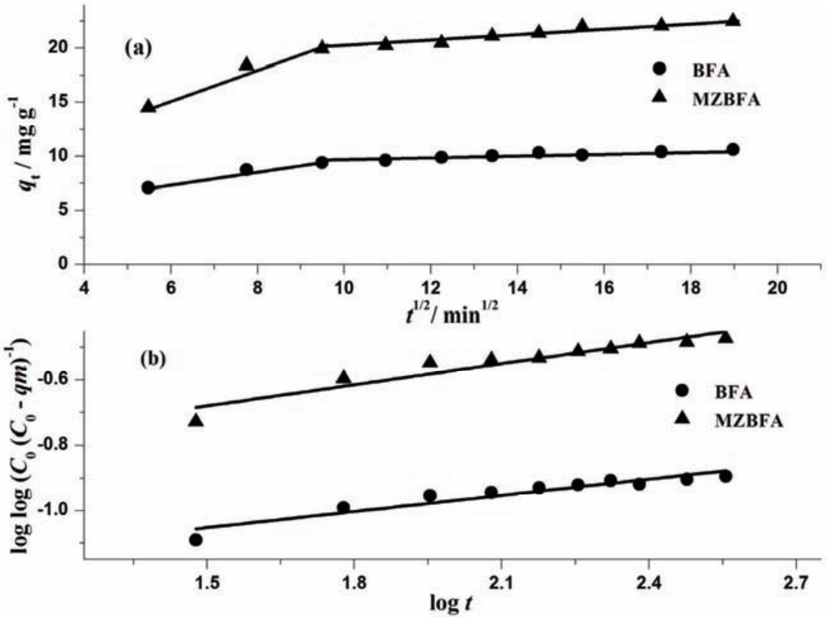

Fig. 10. a) Intra-particle diffusion plots and b) Bangham plots on the adsorption of ACP by BFA and MZBFA (c = 125 mg L^{-1}, dose = 3 g L^{-1}, temperature, 298 K).

The possibility of intra-particle diffusion resistance affecting adsorption was explored by use of the intra-particle diffusion model.[47] Intra-particle diffusion was characterized using the relationship between specific sorption (q_t) and the square root of time ($t^{1/2}$). This relation is expressed as follows:[47]

$$q_t = k_{id} t^{1/2} + I \tag{11}$$

where q_t is the quantity of ACP adsorbed at time t (mg g^{-1}) and $k_{\rm id}$ is the intra-particle diffusion rate constant (g mg^{-1} min$^{-1/2}$); a plot of q_t *vs*. $t^{1/2}$ should be a straight line with a slope $k_{\rm id}$ and intercept I when the adsorption mechanism follows an intra-particle diffusion process. The value of the intercept gives an idea about the thickness of boundary layer, *i.e*., the larger the intercept, the greater is the boundary layer affect.[49] Plots of mass of ACP pesticide adsorbed per unit mass of adsorbent, q_t, *versus* $t^{1/2}$ are presented in Fig. 10. The deviations of the straight lines from the origin may be due to differences in rate of mass transfer in the initial and final stages of adsorption.[50] Furthermore, such deviations of the straight lines from the origin indicate that pore diffusion is not the sole rate-controlling step,[51] as was deduced earlier by the Bangham Equation. From Fig. 10, it may be seen that there are two separate regions – the first straight portion is attributed to macropore diffusion (phase I) and the second linear portion to micropore diffusion (phase II).[52] These show only the pore diffusion data. Phase I is attributed to the instantaneous utilization of the most readily available adsorption sites on the adsorbent surface. Phase II may be attributed to the very slow diffusion of the adsorbate from the surface film into the micropores, which are the least accessible adsorption sites. This also stimulates a very slow rate of migration of adsorbate from the liquid phase on to the surface of the adsorbents. That the values of $k_{\rm id,2}$ are lower than those of $k_{\rm id,1}$ implies that ACP diffuses into the pores of the adsorbents. As the diffusion resistance increases with time, the diffusion rate decreases. Thus, the adsorption is a multi-step process involving transport of ACP to the surface of the adsorbents followed by its diffusion into the interior of the pores.

CONCLUSIONS

MZBFA was formed by the hydrothermal alkaline treatment of BFA. The microwave irradiation of the reaction solution was effective in enhancing the zeolitization. This was assign to the stimulated dissolution of SiO_2 and Al_2O_3 from BFA by the rapid heating rate and probably by the strong attack of the glass phase by the active water molecules. On the other hand, microwave heating in the middle stage significantly retarded the formation of zeolite. This was caused by impeded nucleation in the intermediate aluminosilicate gel. Therefore, early-stage microwave heating followed by conventional heating was effective in enhancing the zeolization from Bagasse fly ash. The microwave heating was a very effective method of modifying the porosity and the surface chemistry of BFA. In addition, after microwave treatment, the surface of MZBFA remained in a more reactive state and thus exhibited a higher adsorption capacity. The adsorbents were characterized by the FTIR, PXRD and SEM techniques and possessed improved morphological and adsorption properties. The PXRD analysis data confirmed the formation of zeolites P and X as the major minerals.

Batch experiments revealed that solute removal was favored at lower solute concentrations, increased contact time, increased adsorbent dose and higher temperature at the acidic pH of 2. Equilibrium was attained in 240 min for a dose of 3 g L^{-1} and an ACP concentration of 125 mg L^{-1}. A thermodynamics study proved that the adsorption process was endothermic and spontaneous. The kinetics of the adsorption process was found to follow the pseudo-second-order kinetic model. The Langmuir isotherm fitted the batch experimental data, indicating monolayer coverage of the outer surface of the adsorbents by ACP molecules. MZBFA showed a higher adsorption capacity for ACP than the native BFA. The mass transfer and rate expression studies confirmed that the rate of adsorption was associated with mass transfer from the bulk liquid to the external surface of the particles and intra-particle diffusion from the adsorbent surfaces.

The results demonstrated that BFA, which has a very low economic value, might be effectively used for the synthesis of zeolitic materials that exhibited extractive efficacy for ACP from aqueous solutions.

ИЗВОД

ЕФИКАСНОСТ ЕКСТРАКЦИЈЕ АЦЕФАТА МИКРОТАЛАСНО СИНТЕТИСАНИМ ЗЕОЛИТИМА: РАВНОТЕЖА И КИНЕТИКА

BHAVNA A. SHAH[1], AJAY V. SHAH[2] и PIYUSH Y. JADAV[1]

[1]*Department of Chemistry, Veer Narmad South Gujarat University, Surat-395007, Gujarat, India* и
[2]*Science and Humanity Department, Polytechnic, Vidyabharti trust, Umrakh, Bardoli-394345, Gujarat, India*

Приказано је истраживање примене Bagasse летећег пепела (Bagasse fly ash, BFA), одпадног материјала у индустрији добијања шећера из шећерне трске, као и зеолитног материјала (MZBFA), синтетисаног из BFA комбиновањем конвенционалног и микроталасног рефлукс метода, као адсорбента за екстракцију ацефата – ACP (органофосфорног пестицида) из водених раствора. Синтетисани адсорбент је карактерисан различитим методама, као што су FTIR, PXRD и SEM. Утицај експерименталних параметара истраживан је применом шаржних адсорпционих техника за екстракцију ACP. Показано је да се степен екстракције повећава са смањењем почетне концентрације ACP, као и са смањењем величине честица адсорбента. Процес је брз и равнотежа се успоставља у времану од 90 min. Експериментални подаци су фитовани моделима псеудо-првог и псеудо-другог реда, *Bangham*-овим моделом, као и моделом интра-честичне дифузије. Моделом псеудо-другог реда је могућ реалан опис кинетике процеса адсорпције. Од више промењених модела, равнотежне податке најбоље описује Ленгмирова (*Langmuir*) изотерма. Термодинамичка анализа показује да је адсорпија ACP већа на MZBFA него на BFA. Може се закључити да је синтетисани зеолит јефтина и погодна алтернатива *Bagasse* летећем пепелу као адорбенту за уклањање пестицида из отпадних вода.

(Примљено 30. маја, ревидирано 23. новембра 2012)

REFERENCES

1. N. P. Agnihotri, *Pesticide: Safety Evaluation and Monitoring*, All India Coordinated Project (AICRP) on Pesticide Residues; Indian Agricultural Research Institute, New Delhi, India, 1999, p. 132

2. M. T. Meyer, E. Thurman, in *Herbicide Metabolites in Surface Water and Groundwater*, M. T. Meyer, E. Thurman, Eds., *ACS Symp. Ser*. **630** (1996) 1
3. A. Adeyeye, O. Osibanjo, *Sci. Total Environ.* **231** (1999) 227
4. C. Hura, M. Leanca, L. Rusu, B. A. Hura, *Toxical Lett.* **107** (1999) 103
5. K. James, W. D. Guenzi, *Pesticides in Soil and Water*, Soil Science Society of America, Madison, WI, 1986
6. C. Bolognesi, G. Morasso, *Trends Food Sci. Technol.* **11** (2000) 182
7. I. Ali, C. K. Jain, *Curr. Sci.* **75** (1998) 123
8. F. J. Beltrán, J. F. Garcia-Araya, B. Acedo, *Water Res.* **28** (1994) 2153
9. *Milieukwaliteitsnormen bodem, water, lucht*, in *(Inter)national normen stoffen*, Ministerie van Volkshuisvesting, Ruimtelijke Ordening en Milieu (Ministry of Housing, Spatial Planning and the Environment), VROM, 1997 (in Dutch)
10. A. Topalov, B. Abramovic, D. Monlar-Gabor, J. Csanadi, O. Arcson, *J. Photochem. Photobiol., A* **140** (2001) 249
11. C. Zwiener, L. Weil, R. Niessner, *Int. J. Anal. Chem.* **58** (1995) 247
12. J. B. Weber, H. D. Coble, *J. Agric. Food Chem.* **16** (1968) 475
13. M. A. El-bid, O. A. Aly, *Water Res.* **11** (1977) 611
14. V. K. Gupta, I. Ali, in Adsorbents for water treatment: Low cost alternatives to carbon, in Encyclopedia of Surface and Colloid Science, A. Hubbard, Ed., Marcel Dekker, New York, 2002, p. 136
15. H. Jian-Ying, A. Takako, O. Yutaka, M. Takeshi, M. Yasumoto, *Water Res.* **32** (1998) 2593
16. V. K. Gupta, I. Ali, *Water Res.* **35** (2001) 33
17. V. K. Gupta, I. Ali, S. Suhas, V. K. Saini, *J. Colloid Interface Sci.* **299** (2006) 556
18. V. F. Domingues, G. Priolo, A. C. Alves, M. F. Cabral, C. Delerue-Matos, *J. Environ. Sci. Health, B* **42** (2007) 649
19. J. Boucher, L. Steiner, I. W. Marison, *Water Res.* **41** (2007) 3209
20. M. Akhtar, S. M. Hasany, M. I. Bhanger, S. Iqbal, *Chemosphere* **66** (2007) 1829
21. I. Ali, V. K. Gupta, *Nat. Protoc.* **1** (2006) 2661
22. V. C. Srivastava, *M. Tech. Dissertation*, Indian Institute of Technology Roorkee, India, 2003
23. I. D. Mall, S. Tewari, N. Singh, I. M. Mishra, in Proceeding of the eighteenth international conference on solid waste technology and management, Philadelphia, PA, USA, 2003, p. 23
24. V. K. Gupta, C. K. Jain, I. Ali, M. Sharma, V. K. Saini, *Water Res.* **37** (2003) 4038
25. V. K. Gupta, I. Ali, *Sep. Purif. Technol.* **18** (2000) 131
26. B. A. Shah, A. V. Shah, H. D. Patel, *Environ. Prog. Sustain. Energy* **30** (2011) 549
27. H. Freundlich, *Z. Phys. Chem.* **57** (1906) 384
28. I. Langmuir, *J. Am. Chem. Soc.* **40** (1918) 1361
29. M. M. Dubinin, E. D. Zaverina, L. V. Radushkevich, *Zh. Fiz. Khim.* **21** (1947) 1351
30. M. J. Temkin, V. Pyzhev, Acta Physicochim. URSS **12** (1940) 217
31. S. Brunauer, P. H. Emmett, E. Teller, *J. Am. Chem. Soc*. **60** (1938) 309
32. E. P. Barrett, L. G. Joyner, P. P. Halenda, *J. Am. Chem. Soc*. **73** (1951) 373
33. J. S. Noh, J. A. Schwarz, *Carbon* **28** (1990) 675
34. D. Vucinic, I. Miljanovic, A. Rosic, P. Lazic, *J. Serb. Chem. Soc.* **68** (2003) 471
35. Y. Wang, Y. Guo, Z. Yang, H. Cai, Q. Xavier, *Sci. China, D* **46** (2003) 967
36. *Joint committee on powder diffraction standards*, Index Inorganic to the powder diffraction file, Publication PDIS-211, Newton Square, PA, 1971

37. M. Inada, H. Tsujimoto, Y. Eguchi, N. Enomoto, J. Hojo, *Fuel* **84** (2005) 1482
38. B. Pan, W. Du, W. Zhang, X. Zhang, Q. Zhang, B. Pan, L. Lv, Q. Zhange, J. Chen, *Environ. Sci. Technol.* **41** (2007) 5057
39. A. Bhatnagar, *J. Hazard. Mater.* **139** (2007) 93
40. E. Tutem, R. Apak, C. F. Unal, *Water Res.* **32** (1998) 2315
41. I. D. Mall, V. C. Srivastava, M. M. Swamy, B. Prasad, I. M. Mishra, *Colloids Surf., A* **272** (2006) 89
42. *Pesticide Properties Database*, http://sitem.herts.ac.uk/aeru/footprint/en (September 2011)
43. Y. S. Ho, G. F. Malash, M. I. El-Khaiary, *Desalination* **257** (2010) 93
44. S. Lagergren, *Kungl. Svenska Vetenskapsakad. Handl.* **24** (1898) 1
45. Y. S. Ho, G. McKay, *Process Biochem.* **34** (1999) 451
46. E. Tutem, R. Ape, C. F. Unal, *Water Res*. **32** (1998) 2315
47. W. J. Weber Jr., J. C. Morris, J. Sanit. *Eng. Div. Proceed. Am. Soc. Civil Eng.* **89** (1963) 31
48. B. A. Shah, A. V. Shah, R. R. Singh, N. B. Patel, *J. Environ. Sci. Health, A* **44** (2009) 880
49. K. Kannan, M. M. Sundaram, *Dyes Pigm.* **51** (2001) 25
50. K. K. Panday, G. Prasad, V. N. Singh, *Environ. Technol. Lett.* **50** (1986) 547
51. V. J. Poots, G. McKay, J. J. Healy, *J. Water Pollut. Control Fed.* **50** (1978) 926
52. S. J. Allen, G. McKay, Y. H. Khader, *Environ Pollut.* **56** (1989) 39.